School of Electronics and Computer Science
University of Southampton

AN INVESTIGATION INTO THE STRUCTURE AND PROPERTIES OF POLYETHYLENE OXIDE NANOCOMPOSITES

PhD Thesis

by

Martin Reading

2010

ABSTRACT

Polymer nanocomposites have attracted great interest over many years, because of the enhanced properties exhibited by such systems. However, it is only recently that the electrical characteristics of this class of material have begun to be studied in detail. Whenever fillers are added to a host polymer matrix, dispersion is of critical importance since, while a well dispersed nanophase may be beneficial, poor dispersion can have negative consequences. Hence, for the nanocomposites to be used appropriately and provide the best properties, a method for observing the dispersion within the matrix is useful. Despite this, evaluating the dispersion of nano-additives in the bulk is far from straight forward using conventional solid-state materials characterization techniques.

This study set out to consider the influence of nano-additives on the physical, thermal and electrical properties of poly(ethylene oxide) systems. The initial objective is to investigate the extent to which dispersion of nanofillers and effect of host molecular weight can be inferred from rheological analysis. This investigation covers many systems based upon polyethylene oxide (PEO); PEO blends, thermally aged PEO and PEO composites with montmorillonite (MMT), micro/nano silicon dioxide (SD/nSD) and boehmite fillers (BO). The study continued from dispersion and solution characterisation onto thermal and electrical properties. The effects of additives and treatment on the crystallisation kinetics and thermal transitions are considered. Polymers are most well known for their electrically insulating properties, therefore electrical analysis into AC breakdown and dielectric spectroscopy were also performed.

The research has shown that rheology is capable of producing well dispersed PEO nanocomposites. Addition of fillers during the rheology phase produced the expected monotonic increase in viscosity apart from boehmite, which formed a very viscous gel after reaching a threshold loading. Large drops in thermal transitions were observed for the composite samples. All fillers caused a large increase in breakdown strength at higher loadings, except boehmite which caused the breakdown strength to decrease, an effect discussed in detail.

TABLE OF CONTENTS

ABBREVIATIONS AND SYMBOLS

PEO – Polyethylene oxide

PE – Polyethylene

20k – PEO of molecular weight 20,000 $gmol^{-1}$

100k – PEO of molecular weight 100,000 $gmol^{-1}$

400k – PEO of molecular weight 400,000 $gmol^{-1}$

1M – PEO of molecular weight 1,000,000 $gmol^{-1}$

4M – PEO of molecular weight 4,000,000 $gmol^{-1}$

PPHP – Parts per hundred polymer (aka % weight added)

PPHW – Parts per hundred water (aka % weight added)

MMT – montmorillonite clay

SD – micro silicon dioxide

nSD – nano silicon dioxide

BO – boehmite

DW – distilled water

DSC – differential scanning calorimetry

FTIR – fourier transform infra-red

T_g / T_m / T_c – Glass, melting and crystallisation transition temperatures

$T_{1/2}$ – Arbitrary value between T_g and T_m

τ – Shear stress

τ_0 – Yield stress

μ_p – Plastic viscosity

$\dot{\gamma}$ – Shear rate

c – a constant

K_c – Consistency value

n_p – Power index representing the deviation from Newtonian behaviour

α_t – Time dependent parameter

μ_∞ – Apparent viscosity at a very high shear rate

$\dot{\gamma}_0$ – Shear rate correction factor

K_p – Parameter related to viscosity

n_o – Distortion parameter

a, b, c – 3 parameter hyperbolic parameters

η – Viscosity / scale Weibull parameter

η_0 – Zero shear rate viscosity

η_∞ – Limiting viscosity at high shear rates

λ – Time constant

i – A specific molecular species

r – The highest degree of polymerisation possible

k_{ij} – Individual rate constant

n_i – Number of molecules of species i

ΔH – Enthalpy of fusion

ρ_c – Density of crystalline portion

ρ_l – Density of liquid portion

$\lambda(t)$ – Relative untransformed fraction at time t

N' – Steady states nucleation rate per unit of untransformed mass

$w(t,\tau)$ – Mass of a given centre at time t

N – Nucleation rate

V_c – Instantaneous crystallinity volume fraction

V_∞ – Final crytallinity volume fraction

n – Avrami index

n_d – Dimensionality of growing crystals

n_n – Time dependence

G – Growth rate

K – Avrami parameter

T – Avrami time parameter

K_3 – Avrami calculated value

f – A fraction

U^* – Activation energy

T_∞ – Temperature at which all motion ceases

Δh_f – Heat of fusion

f_c – Correction factor

T_m^0 – Melting point of a very large crystal

ε^* – Complex permittivity

ε_S – Static low frequency permittivity

ε_∞ – Permittivity at the high frequency limit

E_L – Local electric field

E – Applied field

E_O – Amplitude of electric field

ω – Angular frequency

D and D_0 – Displacements

δ – Phase lag in displacement

ε' and ε'' – Real relative permittivity and imaginary permittivity

ε_r – Relative permittivity

τ_t – Relaxation time of medium

σ – Conductivity

f_r – Frequency

ε_0 – Permittivity of a vacuum

t – Time to breakdown

V – Voltage

x and x_t – Time of failure and threshold time under which no failures can occur

α – Weibull parameter / MHS parameter

β – Weibull parameters

$P_f(x)$ – Cumulative probability of failure at time x

a – Lower bound / MHS equation parameter

b – Upper bound

γ – Weibull location parameter

$L(\theta)$ – Likelihood function for parameter vector θ

$\tilde{\upsilon}$ – Wavenumber

λ_l – Wavelength

h – Planck constant

c – Speed of light in a vacuum

E_b – Electrical breakdown strength

V_c – Coefficient viscosity

V_d – Differential viscosity

T1 and T2 – De Kee parameters

M – Molar mass

M_w – Molecular weight

ΔH_c' and ΔH_m' – Raw enthalpy values

ΔH_c and ΔH_m – Corrected enthalpy values

χ_c – Crytallinity

m and c – Viscosity regime constants

NOMENCLATURE

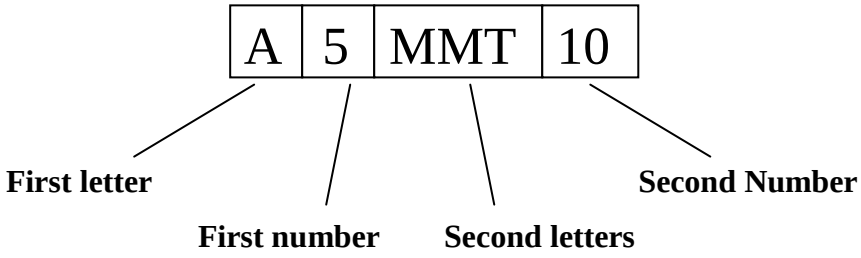

First letter: Represents molecular weight of PEO

A = 100,000 $gmol^{-1}$

B = 400,000 $gmol^{-1}$

C = 1,000,000 $gmol^{-1}$

First number: Represents the weight ratio of PEO added per hundred water (PHW), with such values as: 1, 2, 5, 10.

Second letters: Represent the filler present, if any

MMT = aluminium pillared montmorillonite

SD = micro sized silicon dioxide

nSD = nano sized silicon dioxide

BO = boehmite

Second number: Represents the weight ratio of filler added per hundred polymer (PHP), with such values as: 1, 2, 5, 10, 25, 50, 100

Some example sample names,

A5 - is 5 PPHW of 100,000 $gmol^{-1}$ PEO

B1MMT5 - is 1 PPHW of 400,000 $gmol^{-1}$ PEO with 5 PPHP of MMT

B10SD5 - is 10 PPHW of 400,000 $gmol^{-1}$ with 5 PPHP of SD

A10nSD50 - is 10 PPHW of 100,000 $gmol^{-1}$ with 50 PPHP of nSD

C1BO100 - is 1 PPHW of 1,000,000 $gmol^{-1}$ with 100 PPHP of BO

AUTHOR DECLARATION

I, Martin Reading, declare that the thesis entitled "An Investigation into the Structure and Properties of Polyethylene Oxide Nanocomposites", and the work presented in the thesis are both my own and have been generated by me as a result of my own original research. I confirm that:

- This work was done wholly in candidature for a research degree at the University of Southampton;

- Where any part of this thesis has previously been submitted for a degree or any other qualification at the University of Southampton or any other institution, that this has been clearly attributed;

- Where I have consulted the published work of others, this is always clearly attributed;

- Where the work of others has been quoted the source is always given, and with the exception of such quotations this thesis is entirely my own work;

- I have acknowledged all main sources of help;

- Where the thesis is based on work done by myself jointly with others, I have made clear exactly what contributions were my own;

- Parts of this work have been published as:

1. M. Reading and A. S. Vaughan, *IEEE Conference CEIDP 2008, Quebec City,* 37-40, 2008
2. M. Reading and A. S. Vaughan, *IEEE Conference CEIDP 2008, Quebec City,* 579-582, 2008
3. M. Reading and A. S. Vaughan, *IOP 2nd UHVnet Colloquium, Glasgow*, 2009
4. M. Reading and A. S. Vaughan, *IOP Dielectrics Conference, Reading*, 2009
5. M. Reading and A. S. Vaughan, *ISH Conference 2009, Cape Town*, 2009
6. M. Reading and A. S. Vaughan, *IEEE Conference CEIDP 2009, Virginia Beach*, 2009
7. M. Reading and A. S. Vaughan, *IEEE Conference ICSD 2010, Potsdam,* 2010
8. M. Reading and A. S. Vaughan, *IEEE Conference CEIDP 2010, West Lafayette,* 2010

Signed: _ Date: _ _ _ _ _ _ _ _ _ _ _ _

ACKNOWLEDGEMENTS

I would like to thank my supervisor, Professor Alun S. Vaughan, for his enthusiasm, patience, and general support throughout my PhD. I would also like to thank Professor Paul Lewin for his guidance and undeniable passion for PEO based insulator systems. Without their help this thesis could not have been possible.

I am also grateful to many of the other members of the EPE group working in the Tony Davies High Voltage Laboratory who provided advice, interesting discussions and technical support over the years, in particular, Dr Ian Hosier and Dr Gabriele Gherbaz. Their help and advice was greatly appreciated.

However most of all I would like to thank my wife, Jen, for being a constant inspiration and supporting me through the highs and lows that are inevitable when doing a PhD. She has always been on hand to offer support, guidance and encouragement when I've needed it the most. I will love you always.

Also, a special thanks goes to my fellow PhD students whom I worked alongside: Richard Chippendale, Nicola Freebody, Alex Holt, Jack Hunter, David Mills, Ramizi Mohamed, James Pilgrim, Trung Nam Tran and Celia Yeung. I wish you all the best!

Chapter 1: INTRODUCTION

1.1 Polymer Nanocomposites

A polymer is composed of a long chain of repeated monomers. The most common technological polymers are plastics, however there are other forms such as cellulose, a naturally occurring polymer found in plants. The term polymer has been used since the early 1830s and was first coined by Jons Jakob Berzelius [1]. However, a true understanding was not attained until the 1920s and, since then, some of the most famous polymers have been developed, such as – Nylon, polyethylene, Teflon and silicones [2]. Engineering plastics can be created from a single polymer, or by adding a second phase, eg an inorganic mineral, to form a composite. In this way it is possible to enhance key properties to render the base polymer more suitable for use in a particular application. For example Haque et. al. [3] investigated mechanical and thermal properties of glass/epoxy nanocomposites with added nanoclays such as MMT. They found significant improvements in mechanical properties with addition of 1% organo silicate nanoparticles.

While polymer composites have a long history, a critical advance in the subject occurred in the early 1990s when research at Toyota showed the benefits that can result from reducing the size of the included mineral phase. This work led to the concept of a nanocomposite, interest in which has increased at a rapid rate ever since [4]. Polymer nanocomposites are frequently found in everyday life, from personal computers through to car manufacturing. With the correct addition of filler the composite can have better properties than an unfilled equivalent [5]. An example of this is work by Chiang et. al. [6], who found that epoxy nanocomposites with a silica filler possessed far better thermal stability at higher temperatures and superior flame retardance. Many other instances exist where composites have provided greater properties than virgin polymers. Another example is the investigation into mechanical and water-barrier properties of an unsaturated polyester resin gel coat system with addition of organoclay performed by Jawahar et. al. [7]. It was found that addition of

organoclay increased mechanical tensile strength by 55% and also an increase in water-barrier properties.

Typically polymer nanocomposites are composed of ~5% nanometric filler within the polymeric matrix, where the term nanometric is used to indicate that at least one dimension of the filler is ~10 nm in size. Then, three situations are possible. The first is where the nanofiller has one dimension that falls within the nanometer range and, consequently, takes the form of a sheet; examples include mica sheets, such as the ones used by Jarvela and Jarvela [8] in their investigation of polypropylene compounding. The second is where two dimensions fall in the nanometer range; examples include carbon nanotubes which are a popular choice in nanocomposites [9-11]. An example is the investigation by Jun et. al. [12] which involved creation of a nanofiber from poly(ethylene oxide) with carbon nanotubes. The third is where all three dimensions are in the nanometer range, which is termed an isodimensional configuration [13-14].

1.2 Polymer Properties

Synthetic polymers are one of the newest discoveries in a great line of materials development. The first advancement in the materials field was the discovery of base metals and methods of purifying them, such as iron, copper and lead. It was then discovered that creating alloys of these metals would create a material with different properties, such as alloying carbon with iron to create steel. Further developments around alloying and metals continued until the discovery of synthetic polymers. Plastics could be considered to be one of the most important discoveries over the last few hundred years, with society today using variations in almost every part of life. For example, since 1950, 1 billion tons of plastic have been used [15].

Polymers and plastics have been hugely successful in a multitude of areas for many reasons. For packaging, for example, they are light, strong, easily moulded, cost effective, re-usable and flexible in their application. All of these characteristics represent improvements on previous technologies such as glass and metal. As

discussed previously, polymers in particular are capable of being manipulated and altered to create many unique materials for different uses.

An important concept of polymers is crystallisation. Polymers can be largely crystalline, fully amorphous or a combination of the two. The major bulk commodity plastics, polyethylene and polypropylene, fall into this final category and are therefore described as being semicrystalline. The long chains of repeating monomers form stacks of parallel chains called lamellae. It is believed that these lamellae are comprised of chains folding back on themselves, explained well by Keller [16], and theorised by Keller, Till [17] and Fischer [18] in 1957. Figure 1.1 shows such a stack of lamellae made from the polymer chains folding back on themselves and highlights the crystalline and amorphous parts.

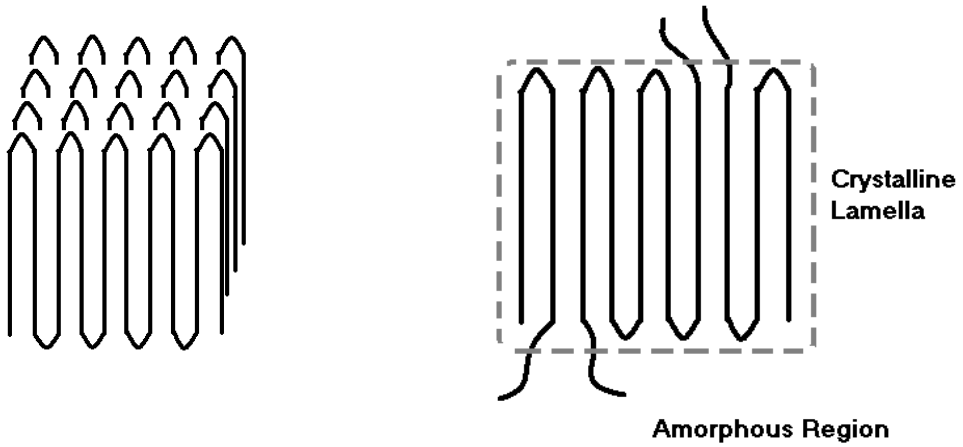

FIGURE 1.1 : A lamella formed by folding chains (left), with the crystalline and amorphous regions labelled (right)

When a semicrystalline polymer is melted and subsequently cooled it frequently crystallises to form a morphology composed of spherical superstructures called spherulites [19-20]. These symmetric structures grow from a central point when several lamellae form together as a nucleus. The lamellae then grow outwards at a linear rate, as shown by Takayanagi and Yamashita [21] and many others [22-24]. The rate of growth of these spherulites is dependent on the crystallisation temperature and mobility effects within the system. Figure 1.2 shows the spherulite growth rate as a function of temperature. With reference to figure 1.2, the region from T_g to $T_{1/2}$ is considered as region 1, with the region $T_{1/2}$ to T_m^0 as region 2.

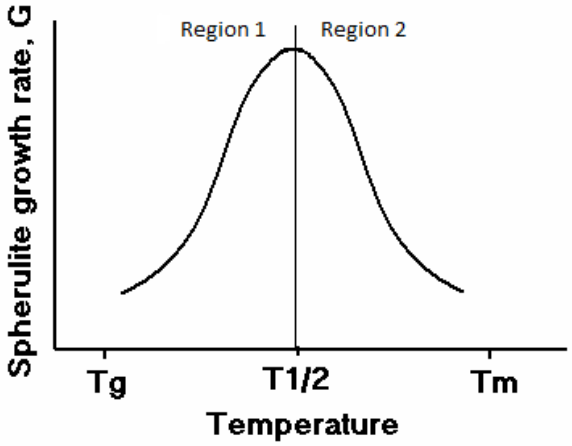

FIGURE 1.2 : Spherulite growth rate temperature dependence. Reproduced from Gedde [25].

There are two processes here; the thermodynamic drive for the polymer to crystallise, and the mobility of the polymer chains. The thermodynamic drive, sometimes referred to as the undercooling, can be defined as $\Delta T = T_m^0 - T_c$, where T_m^0 is the melting temperature of a perfect crystal. Therefore the thermodynamic drive increases as the T_c is lowered. The mobility of the chains within the system does the opposite, with the chains having more kinetic energy with increasing temperature. The combination of these two processes dictates the spherulite growth rate.

In region 1 between T_g – $T_{1/2}$, lower crystallising temperatures create more thermodynamic drive, but without sufficient mobility, the growth rate is still low. Higher crystallising temperatures, peaking at $T_{1/2}$, still exhibit a fairly high thermodynamic drive but with much increased mobility, causing the growth rate to reach a maximum. Then in region 2 at high crystallising temperatures the mobility of the system is high, however little thermodynamic drive exists causing the crystal growth rate to be low.

1.2.1 Electrical Properties of Polymers

Despite the excellent mechanical benefits of using polymers, this should not overshadow the dielectric benefits. Metals have strong electronic conductivity, whereas polymers do not, underlying their use as excellent insulators. Nevertheless, although the bulk conductivity of most polymers is low, more subtle effects can be

observed, such as space charge, and experimental techniques have been developed to evaluate electrical breakdown strength, dielectric loss and permittivity [26]. However, the dielectrics of polymers is still an area of much interest, for example, the cause of electrical breakdown in polymers has drawn many theories from scientists and engineers, as discussed in Appendix 1.

A material with such adaptable physical and electrical qualities is a fantastic basis from which engineers can generate advanced composite materials. Such composites are filtering throughout society helping to improve equipment, the environment and life for mankind. For example, the development of composite materials allowed the production of the Airbus A380 aircraft, a 525 seat jetliner, currently the largest in the world [27]. Another example would be the increasingly common fibre reinforced polymer composites (FRPC) used in many advanced engineering structures, from aircraft and automobiles through to civil buildings and biomedical equipment [28].

1.3 Structure and Property Dependence

The properties of a material depend on its composition and structure. This strong dependence underlines the importance of dispersion within nanocomposites. A poorly mixed nanocomposite will show a larger variation in properties across the material compared to a well mixed composite [29-30]. A good example of poor dispersion causing a decline in material performance can be seen in the work of Moczo et al. [31] where a decrease in fracture resistance with increasing aggregation was observed in polypropylene-$CaCO_3$ composites. They also noted that aggregation increased with increasing filler content and decreasing particle size for their investigations. Similarly, better dispersion can increase properties further [30]. Vaughan et. al. [32] found that well-dispersed MMT-polyethylene composites displayed enhanced nucleation and Ramanathan et. al. [33] found that better dispersion of their graphite/PMMA composites provided better mechanical, thermal and electrical properties.

In the case of nanoclays, addition of the filler to a polymer matrix can result in three main formations, shown in figure 1.3. Unmixed- the polymer and composite are separate, with agglomerations of clay. Intercalated- the main layered additive is still

intact with polymer chains beginning to penetrate the agglomerations and disperse between the clay platelets. Exfoliated- the filler and polymer are completely mixed.

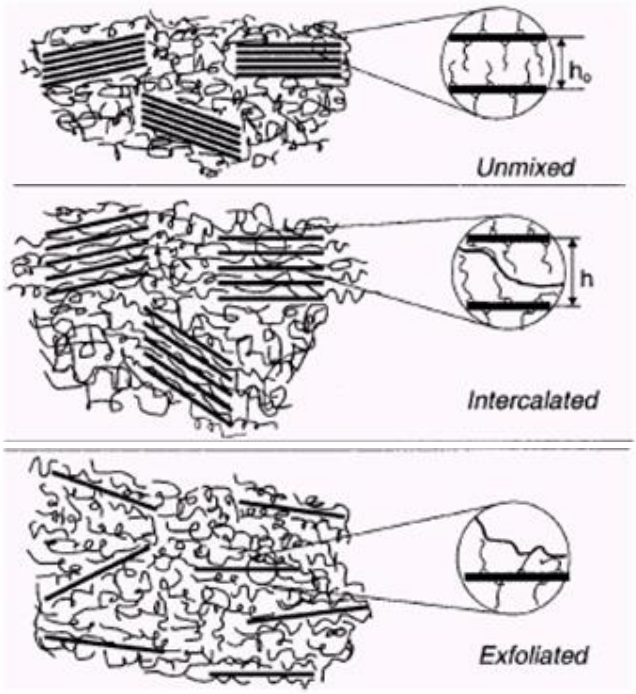

FIGURE 1.3 : The three general formations of a clay filler within a polymer; unmixed, intercalated and exfoliated [34]

1.4 Polymer Customisation

The polymeric architecture is a highly flexible one that can be adapted in many ways to meet specific requirements. For example, the incorporation of an additive into a polymer can modify its characteristics. Commonly used additives include antioxidants, nucleating agents, plastisizers, crosslinkers and fillers. In the case of nanocomposites, a large proportion of the fillers used are clays, such as the sodium montmorillonite clay added by Grunlan et. al. [35] to their modified poly(vinyl alcohol). The main advantageous effect of the clay in this case was a reduction in oxygen permeability.

With the inclusion of a second monomer during the chemical synthesis phase, a different polymer with different characteristics is created. These so-called copolymers can be random, blocks or branched [2,36-37], shown in figure 1.4.

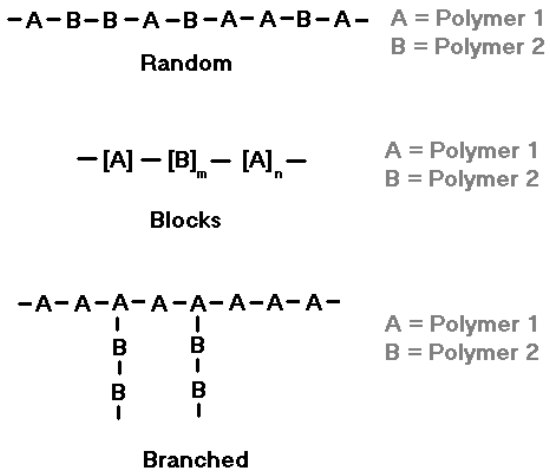

FIGURE 1.4 : Types of Copolymers

Increasing the chain length of polymers tends to increase mechanical strength [38], increase the glass transition temperature, T_g [39], and decrease the molecular mobility. These effects can be explained by the increase in chain interactions that serve to constrain the individual chains in position and resist deformation [38]. Polymers can have varying degrees of crystallisation, which can be altered by adjusting the molecular architecture or through processing [40-41]. If crystallisation is increased, the polymers tend to be stronger and more rigid, however this can lead to brittleness [42-43].

Branches can be introduced during polymerisation, possibly by using a condensation reaction [44]. Long branch chains usually increase the strength, general toughness and T_g of the polymer. Short chains on the branches do the opposite and cause disruption to the organisation. For example, in HDPE there is a low degree of branching and it is relatively stiff, while in LDPE there are variable length branches and it is flexible [26,45]. Cross-linking is a method whereby chemical bonds are created between different chains in the polymer. This process was first developed for rubbers using sulphur (known as vulcanisation). Just like branching, cross-linking tends to increase the strength, toughness and T_g of the polymer [45-47].

Plasticizers, such as acetylated monoglycerides, [48] are low molar mass compounds that are chemically similar to the main polymer and which, simplistically, serve to separate the main polymer chains. The resulting conformations result in enhanced molecular mobility, flexibility and reduced inter-chain interactions. Although the classic example of this is PVC, another good example of using plasticizers is in the construction of car dashboards. In a car they need to be firm and inflexible, however in the process of fitting them it is beneficial for them to be the opposite. Therefore a plasticizer is used during fitting to enable the plastic dashboard to be fitted into place easily. The plasticizer is designed to evaporate after fitting and hence leave a firm, inflexible dashboard behind. This plasticizer evaporation is normally the cause of the "new car smell" that people notice when purchasing new cars. The use of a plasticizer greatly increases flexibility and lowers T_g [49].

Methods such as those described above provide considerable scope for customising a polymer. For this investigation several methods will be used to observe such effects on the host polyethylene oxide (PEO) system; altering the chain length (molecular weight) of the PEO and adding a nano-clay are considered in detail.

1.5 Aims of this Thesis

For many polymers used in the creation of nanocomposites, the filler and the matrix are incompatible or weakly interacting. This leads to addition of, possibly undesirable, chemicals to improve the state of dispersion. This makes it difficult to deconvolute the real fundamental nanocomposite effects due to the complications introduced with the chemical compatibiliser. PEO however, is highly polar and thus compatible with a large range of chemical compounds and polar nanofillers. Also many engineering polymers are either crystalline (eg. Polyethylene), or liquid (eg. Epoxy), whereas PEO easily crystallises producing particularly large spherulites but is also readily soluble in polar solvents, therefore making it a good model for studying both forms.

For example, dispersing fillers such as MMT into PE is difficult and a compatibiliser is normally needed, a process outlined by Vaughan [50] and shown in figure 1.5. To allow an exfoliated structure the compatibiliser expands the galleries and allows the

polymer to diffuse in. Using such a compatibiliser often makes the process more complicated, less cost effective and more time consuming. For a model system these are all undesired characteristics. Since PEO is polar and hydrophilic, addition of fillers should require no comparable compatibiliser to achieve a high level of dispersion. This allows creation of materials with a maximum possible compatibility to observe the true fundamental effects of the fillers.

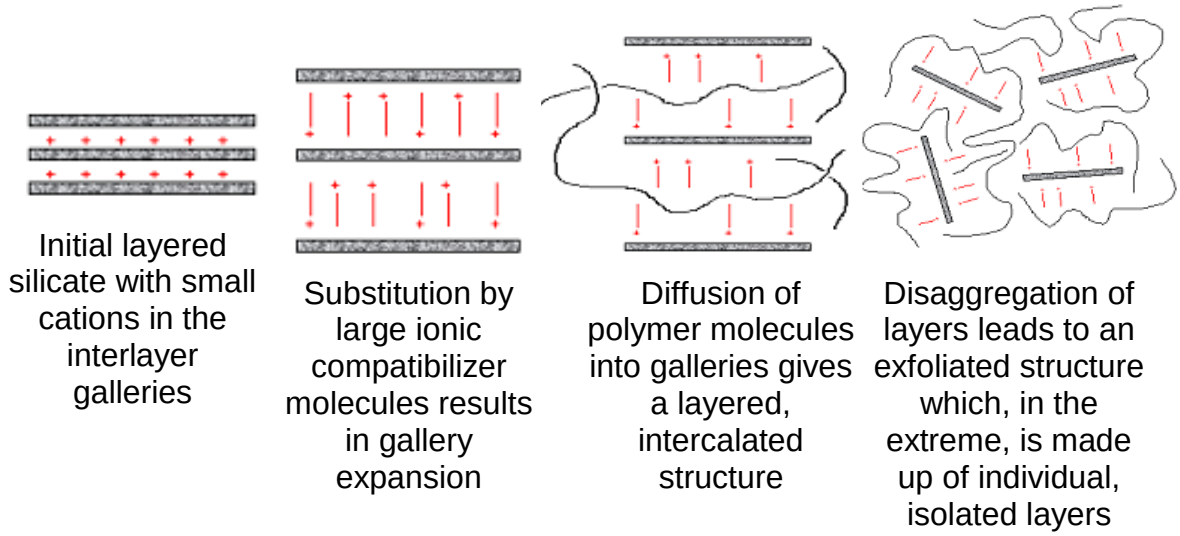

FIGURE 1.5 : Polyethylene – MMT dispersion using a compatibilizer. Reprinted from [50]

The focus of this research has therefore been to investigate the properties of polyethylene oxide and PEO nanocomposites. One of the most important factors that affects the properties of a composite is the dispersion of any fillers present. As mentioned, poor filler dispersion can severely reduce the materials properties, whereas a well-dispersed system can show increases in almost any area, dependent on the filler used. The overall aim was therefore to produce and test several PEO composites with a high level of dispersion for structure, thermal or electrical property changes. Objectives set for this research were;

- Produce a material with different shear histories and varying degrees of filler dispersion, using compatible fillers of varying geometries; platelet, spherical and rod-like

- Explore the rheological response of the PEO nanocomposites to confirm whether this is related to the dispersion state of the nanofiller, and the effect of addition of the fillers
- Explore the shear rate-shear stress and calculated shear rate-viscosity data, and compare to any existing theoretical models
- Explore the structure of the PEO composites using optical microscopy, observe the crystallisation process and thermal transitions and the effect of fillers on these
- Explore the dielectric properties and insulation qualities of PEO nanocomposites

1.6 Thesis Contents

Chapter 1 provides a basic introduction to polymer nanocomposites, their properties and their property dependence.

Chapter 2 provides the theory behind all experimental techniques used, as well as any theoretical models used for comparison.

Chapter 3 provides details on experimental procedures followed, preliminary experimental data and experimental conditions chosen.

Chapters 4-8 contain the results from all experimentation performed, along with comparison to known models, comparison to previous work by other authors, theories for behaviour observed and general analysis.

Chapter 9 summarises the findings from this work and draws conclusions as well as suggesting areas of further study.

Chapter 2: THEORY

2.1 Mechanical Properties - Rheology

Rheology is a term used to describe the study of the deformation and flow of matter, mostly liquids, under the influence of stresses. While the main aim is to characterise fluid or solid properties, when dealing with a system containing additives, rheometry can also be used to aid in mixing as well as providing flow data [51-52]. An example of this is work by Feger et. al. [53]. They found that a torque rheometer greatly outperformed a 3-roll-mill system with respect to dispersion, requiring only 15 minutes to reach the same mixing index that took the 3-roll-mill 2 hours to achieve.

Rheometry was also used by Bar-Chaput et. al. [54] when dispersing a carbon filler in polymers. They found that particle-particle and matrix-filler interactions should be considered when modelling their system. They also drew attention to three main types of dispersion- rupture, erosion and collision which they discuss in detail [54]. Comparing experimental data to theoretical models will also be beneficial for understanding mobility and flow kinetics. For example, De Kee [55] and Zhu [56] used their constitutive model on couette flow (flow of liquid between two surfaces where one moves relative to the other, such as a cup-bob rheometer) of non-Newtonian liquids, while Coppola et. al. [57] used the Milner-McLeish model to describe the zero shear viscosity in their experiments. Rheology of Polymeric systems [58] provides an excellent overview of a range of models.

In previous investigations, many different models have been used to represent shear rate-shear stress and shear rate-viscosity data, many of which are only applicable for certain materials or situations. For this investigation many models were considered and tested, some empirical and some relating to flow dynamics theory, but only the two most promising models for each were applied in detail. The models tested but not found to be applicable for these samples are detailed in table 2.1. The chosen models are detailed over the next few pages. Graphical representations of some of the models are shown in figure 2.1.

Model	Equation	Definitions
Bingham [59]	$\tau = \tau_0 + \mu_p \dot{\gamma}$	τ_0 - yield stress (Pa) μ_p - plastic viscosity (Pa.s) $\dot{\gamma}$ - shear rate (s^{-1}) c – constant K_c – consistency n_p – power index representing the deviation from newtonian behaviour α_t - time dependent parameter μ_∞ - apparent viscosity at very high shear rate $\dot{\gamma}_0$ – shear rate correction factor
Modified Bingham [60]	$\tau = \tau_0 + \mu_p \dot{\gamma} + c\dot{\gamma}^2$	
Casson [61]	$\sqrt{\tau} = \sqrt{\tau_0} + \sqrt{\mu_p \dot{\gamma}}$	
Herschel-Bulkley [62]	$\tau = \tau_0 + K_c \dot{\gamma}^2$	
Robertson-Stiff model [62-63]	$\tau = K_c \left(\dot{\gamma}_0 + \dot{\gamma}\right)^{n_p}$	
Basic De Kee [56,58]	$\tau = \tau_0 + \mu_p \dot{\gamma} e^{-\alpha_t \dot{\gamma}}$	

TABLE 2.1 : A number of rheological models

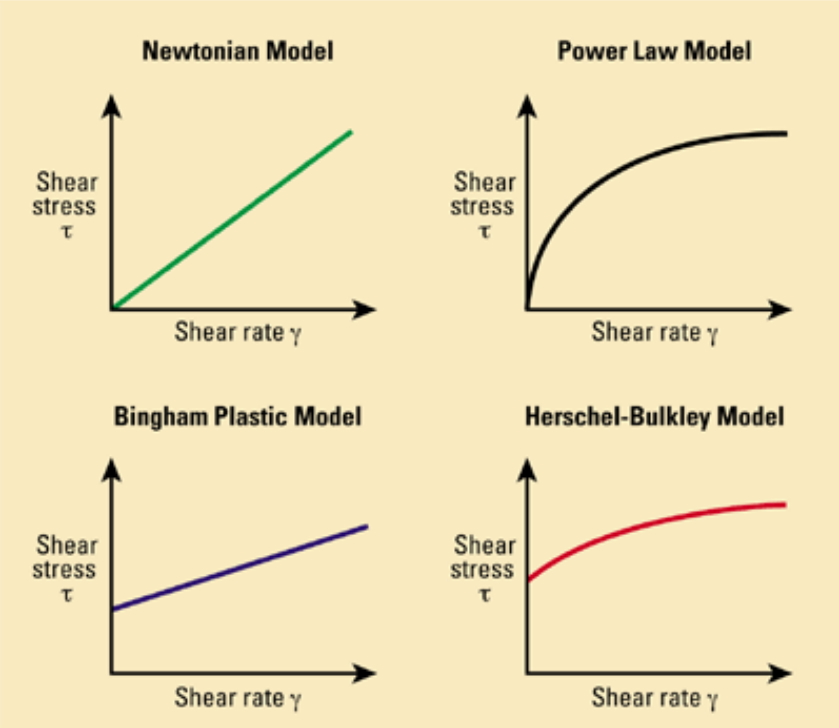

FIGURE 2.1 : Shear rate-shear stress plots of some of the more popular rheological models. Reprinted from the *Schlumberger Oilfield Glossary* [64]

It was observed that;

- The Bingham model worked well for near-newtonian samples but poorly for others.
- The modified Bingham model was a vast improvement, giving an accurate fit.
- The Casson model was deemed to be most appropriate for solutions that increase in viscosity as the shear rate is increased (shear thickening samples)
- The Herschel Bulkley model fitted with a very small τ_0 but with relatively large errors
- The Robertson-Stiff model fitted well using a shear rate correction factor
- The De Kee model gave an acceptable fit.

2.1.1 Dependence of Shear Stress on Shear Rate

The key parameters determined in rheology are shear stress (Pa) and shear rate (s^{-1}) from which, material viscosity (Pa.s) can be determined. When performing rheometry on solutions, 'flow curves' can be generated for the material by plotting shear stress

against shear rate. The shape of the curve on this graph shows the type of viscosity for the liquid. A Newtonian liquid exhibits a linear dependence whereas non-Newtonian liquids will curve away either above or below the Newtonian line [65].

Pseudoplastic liquids are quite common and their shear rate/shear stress curve starts in the same format as a Newtonian liquid, but then curves below the linear straight line. Dilatent liquids display the opposite, curving above the Newtonian line [66]. Pseudoplastic materials can be observed to have a decreasing viscosity with increasing shear rate, a phenomenon known as shear thinning, caused by a decrease in the entanglement density. For example, poly(ethylene oxide) (PEO) solutions end-capped with carbon alkanes tested by Ma et. al. [67] were seen to shear thin, as well as PEO-anionic polyacrylamide blends, as shown by MacFarlane et. al. [68] when characterising flocculated kaolinite pulps. Also, some fluids display an increase in viscosity over time during a period of constant shear stress, these are called rheopectic fluids, an example being printer ink.

One of the simplest models to account for non-Newtonian behaviour was proposed by Ostwald-de Waele [69]. This can be expressed mathematically as the power law equation shown below.

$$\tau = K_p \dot{\gamma}^{n_o} \tag{2.1}$$

Here, τ represents shear stress, $\dot{\gamma}$ represents shear rate, K_p is a parameter related to viscosity (larger K represents higher viscosity) and n_o is a parameter defining the measure of distortion from a Newtonian fluid [69]. Although previous work by Lewandowska [70] showed that data on polyacrylamide followed the Ostwald power law, preliminary results suggested that it does not describe the behaviour of PEO particularly well. Rather, the following empirical 3 parameter hyperbolic function suggested by Matheson [71], shown in equation 2.2, represented the shear stress-shear rate experimental data with excellent accuracy. Here, τ is the shear stress, $\dot{\gamma}$ is the shear rate and *a, b, c* are parameters. Differentiation of equation 2.2 leads to equation 2.3, which provides a means of obtaining viscosity data since *Viscosity = Shear stress / Shear rate*.

$$\tau = \frac{a\dot{\gamma}}{b + \dot{\gamma}} + c\dot{\gamma} \tag{2.2}$$

$$\frac{d\tau}{d\dot{\gamma}} = \frac{ab}{(b + \dot{\gamma})^2} + c \tag{2.3}$$

2.1.2 Dependence of Viscosity on Shear Rate

The Carreau model [58] describes the shear rate dependence of viscosity and analysis is based on equation 2.4. However, Carreau assumed that as $\dot{\gamma}$ tends to infinity, η_∞ tends to zero, and with this assumption equation 2.5 is used.

$$\frac{\eta - \eta_\infty}{\eta_o - \eta_\infty} = \left[1 + (\lambda\dot{\gamma})^2\right]^{\frac{n-1}{2}} \tag{2.4}$$

$$\eta = \eta_o\left[1 + (\lambda\dot{\gamma})^2\right]^{\frac{n-1}{2}} \tag{2.5}$$

Here, η_o is the zero shear viscosity, η_∞ is the limiting viscosity at high shear rates, λ is a time constant, n is a dimensionless parameter and $\dot{\gamma}$ is the shear rate. Equation 2.5 shows that as the shear rate, $\dot{\gamma}$, tends to zero the shear rate viscosity, η, tends to η_o. Figure 2.2 shows that the slope is represented by n-1 and when n=1 the whole equation reduces to a Newtonian fluid. For instances where n<1 it describes shear thinning. By comparing collected data to a Carreau model, it should firstly be possible to check that the Carreau model is representative, and secondly help to understand the physical processes present [58].

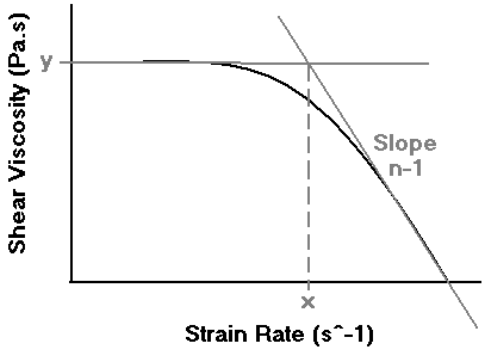

FIGURE 2.2 : Carreau model on a Stress-Strain curve

Another viscosity model is the De Kee model, using four parameters and the sum of two exponentials with addition of a single value, shown in equation 2.6.

$$\eta = \eta_1 e^{-t_1\dot{\gamma}} + \eta_2 e^{-(0.1)t_1\dot{\gamma}} + \eta_\infty \tag{2.6}$$

Here, η_1, η_2 and η_∞ are viscosity quantities. The two exponentials represent two relaxation methods. In the De Kee model, the second relaxation time is assumed to be $1/10^{th}$ the size of the first relaxation time. This dependence could be removed later to test a free-fit model. De Kee showed that the model provided a good fit to data from Ashare [58].

2.1.3 Dependence of Viscosity on Temperature

It is known that the atoms present in the fluid are moving randomly by Brownian motion at a speed determined by their energy. Increasing the temperature will increase the speed of the particles, and hence increase the number of particle interactions or 'collisions'. The kinetic theory of gases states that addition of energy increases the number of particle interactions and so the viscosity of the gases increases with temperature. In this theory, several assumptions are made;

- The gas consists of a large enough number of small, spherical and elastic particles, each with a set mass, that statistical treatment can be applied
- The particles are in constant Brownian motion and collide with other particles
- Interactions between particles (excluding collisions) are negligible
- The average distance between particles is far larger than the size of the particles

Comparing this theory for gases to liquids, the same particle interactions occur but due to the closer proximity of particles, additional attractive cohesive forces come into effect. The cohesive force, or attraction between same-type molecules, explains surface tension in liquids. Increasing both the cohesive forces and particle interactions increase the viscosity. However, increasing the temperature increases the number of collisions and decreases the cohesive forces. As the cohesive forces reduce, the

resistance to shear stress of the liquid decreases, while increasing particle collisions will cause the resistance to shear stress to increase.

To determine which of the forces prevails with increasing temperature, their relative size must be considered along with their individual response to the temperature change. If the increase in particle collisions dominates then the viscosity will increase, in the same way that it does for a gas. However if the cohesive forces dominate then the viscosity will drop. In actual fact, the usual net result is that with increasing temperature the cohesive forces dominate over the particle collisions and the viscosity of the solution decreases.

2.1.4 Polymer Ageing, Oxidation and Chain Scission

Engineering materials are often assessed for their physical, electrical and thermal properties to ascertain their suitability for a task. However one main factor to be considered is the lifetime of the material. In this respect, the lifetime is the time the material is capable of performing its task before its properties degrade such that it can no longer fulfil its duty. Degradation of properties over time is termed ‘ageing’ and can seriously affect the reliability of engineered structures; hence in some cases putting lives at risk. Ageing is an important practical part of materials research and hence draws a large amount of interest from the scientific community. One such long-term investigation was into the constituent materials of an aircraft in service for 24 years performed by Harlow et. al.[72]. Ageing is frequently addressed in journals such as the *Journal of Materials Processing Technology, Polymer Journal* and *Materials Chemistry and Physics Journal.*

Allara [73] has performed considerable research into types of chemical degradation and ageing. He explained that chemical degradation is a process whereby exposure to certain environmental conditions, such as, an additive or impurity within the composite, exposure to air (oxidation), exposure to sunlight, water vapour or gas presence, causes chemical changes within the material. Chemical degradation is said to often be relatively slow, possibly due to the difficulty encountered with penetration of chemical agents and radiation etc. An example of ageing degradation would be the

absorption of UV or thermal energy causing weaker bonds to rupture, and possibly for new bonds to form in their place. These bond-breaking processes may occur in polymer backbones to lower the average length of chains and/or in pendant group bonds which can have a severe effect on the material's characteristics and properties. Another is the possibility for bond forming to other polymer chains to create a crosslinked material or to increase molecular weight.

There are many methods employed to detect the method of thermal ageing and to test the altered properties of such materials. One of the most obvious signs of polymer ageing is a visible colour change, caused by the alternating single-double bonds between the carbons in the backbone causing de-localisation of electrons, however this is often observed too late for practical purposes. Akhavan et. al. [74] found that when thermally ageing their polymerised 3-nitratomethyl-3-methyloxetane (PolyNIMMO) samples they observed gas bubbles, a colour change and a viscosity change. In particular their samples held at 100 ^{0}C were seen to show no colour change with up to 4 days ageing, but then passed through a dark yellow, orange and finally finishing as a reddish brown after 28 days. Many polymeric materials have been tested for ageing using conventional characterization equipment such as; mechanical strength tensile tests [75], thermal transition and specific heat capacity experiments [76], dielectric spectroscopy [77] and FTIR [78].

Chain scission is a form of polymer ageing whereby the backbone chains of the polymer are severed leaving smaller chains behind. Early work by Kuhn [79] and Simha [80] in the 1930's and early 1940's detailed theories into statistical models to obtain molecular weight averages for random scission of polymer chains like this. Such breaking of chains is said to be due to the oxygen present attacking the polymeric chain, producing alkoxy and peroxy radicals which extract a hydrogen atom from the chain leading to scission and resulting in a decrease in molecular weight and formation of carbonyl end groups [81]. Theoretically, chain scission can occur in three modes; 1) random scission whereby the chain can be broken anywhere along the backbone; 2) central scission whereby the chain can only be broken at the centre of the backbone; 3) gaussian scission whereby the probability distribution of chain scission is distributed as a Gaussian curve around the midpoint of the chain [82]. Several polymer degradation models have been proposed for chain scission, one

such model, shown in equation 2.7, was proposed by Basedow et. al. [83]. Here dn_i/dt is the reaction rate of the species i, k_{ij} is the individual rate constant, n_i is the number of molecules of species i and r is the highest degree of polymerization under consideration.

$$\frac{dn_i}{dt} = -\left(\sum_{j=1}^{i-1} k_{ij}\right) n_i + \left(k_{i+1,1} + k_{i+1,i}\right) n_{i+1} + \ldots + \left(k_{r,i} + k_{r,r-1}\right) n_r \ldots \tag{2.7}$$

2.2 Thermal Properties

The melting point T_m of a polymer describes the transition of its crystalline lamellar regions into amorphous ones. The energy required to melt the sample is termed the enthalpy of fusion ΔH. The crystallisation temperature T_c describes the reverse, a change of amorphous regions to crystalline ones. The glass transition temperature T_g describes a second order transition that amorphous regions undergo where they change from rubbery and viscous above the T_g to solid and brittle below the T_g. The T_g can be altered using branching, cross-linking or the addition of a plasticizer [84]. It is worth noting that after the T_g the heat capacity is higher, shown in figure 2.3, hence the requirement for a higher heat input to continue the steady temperature rise. Also, only the amorphous portion of the polymer undergoes the glass transition and only the crystalline portion undergoes the melting transition [85].

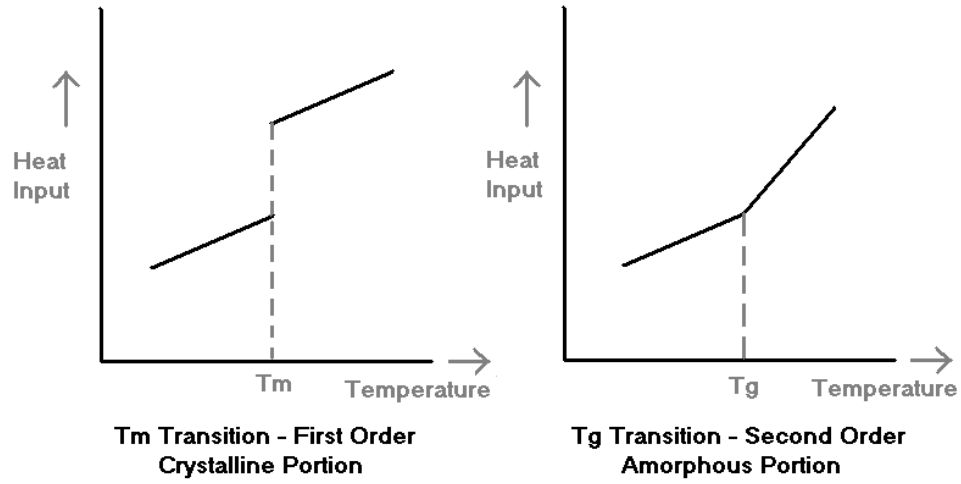

FIGURE 2.3 : T_m and T_g thermal transitions

2.2.1 Differential Scanning Calorimetry

The theory behind DSC is based on the three transitions (T_m/T_c/T_g) that polymers can undergo. Figure 2.4 shows these three transitions for a standard semi-crystalline polymer, with temperature on the *x* axis and endothermic heat flow on the *y* axis, as the sample is heated at a constant rate.

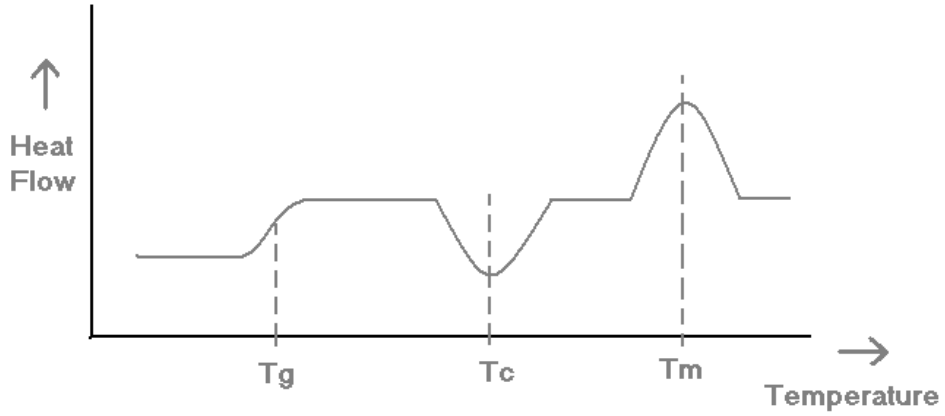

FIGURE 2.4 : A non-specific polymer undergoing three thermal transitions

Below the T_g, in the 'glassy region', the thermal energy available is not enough to allow rotation about single bonds in the polymer backbone. This explains their hard and brittle qualities at these temperatures. Above this temperature, the molecules have increasing thermal energy and mobility. This increase continues until the T_m where the thermal energy is sufficient for the crystalline structure to melt. When crystallising from the melt, the heat flow drops as crystallisation is an exothermic process, unlike melting which is endothermic. The area of this T_c dip equals the latent energy of crystallisation [84]. A simplified power compensated DSC can be seen in figure 2.5.

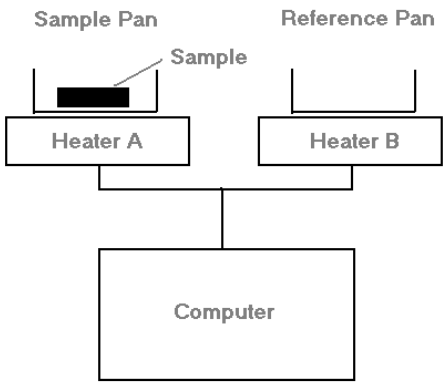

FIGURE 2.5 : A basic view of a Differential Scanning Calorimetry set-up

Here the computer monitors both pans and controls the heaters to ensure the pans are the same temperature. Therefore, during an increasing temperature scan, when the sample pan reaches the samples T_m the sample will begin to melt. At this point the pan temperature will no longer rise at the same rate as the reference pan. The computer will detect this and increase the output from heater A to compensate. Observing the increase in heater output can aid in identifying and analysing the transition.

2.2.2 Hyper DSC

Using DSC to calculate the thermal transitions of the PEO samples is actually fairly complex. For many samples the technique of hyper DSC has been successfully employed [86], where the scan rate chosen is the highest possible, eg. 500 ^{0}C/min for Saklatvala et. al. [87], to increase the sensitivity of detecting the initiation of the transition. Despite Saklatvala finding that the hyper method provided little improvement in accuracy over other DSC techniques, this method has certain virtues, notably, in eliminating dynamic reorganisation processes [88-89]. However, when using such high scan rates, the DSC may not have constant control. As explained well by Lorenzo et. al. [90], when reaching a particularly high or low temperature, the DSC can lose control and any data collected be of questionable validity. They went on to explain that for isothermal crystallisation/melting, if the scan rate is reduced too much the sample will begin to crystallise/melt before the DSC has reached the specified temperature. This will be considered further in the Avrami section.

For thermal transitions the most important aspect is ensuring that the highest possible scan speed is used whilst avoiding excessive thermal lags or the DSC losing control. For melting traces around 50 ^{0}C there was no problem and the DSC could cope with rates ranging from 10-100 ^{0}C/min. However for the crystallisation traces the scan rate could only reach 30 ^{0}C/min for some samples. Therefore during experimentation, care was taken to ensure the highest scan rate was used whilst maintaining control for each individual sample.

2.2.3 Avrami analysis

Avrami analysis can be applied to isothermal crystallisation data to aid in understanding the crystallisation kinetics of a material [25,91]. Lorenzo et. al. [90] showed that assuming the polymer to be a 2 phase model, with ρ_c and ρ_l representing the density of the crystalline portion and liquid (amorphous) portion respectively then the initial equation 2.8 can be re-written as equation 2.9. Here, $\lambda(t)$ is the relative untransformed fraction at time t. N' is the steady state nucleation rate per unit of untransformed mass and $w(t,\tau)$ is the mass of a given centre at time t. Therefore at t = 0, $\lambda(t)$ = 1 and the specimen is fully amorphous.

$$1-\lambda(t)=\int_0^t w(t,\tau)N'(\tau)\lambda(\tau)dt \tag{2.8}$$

$$1-\lambda(t)=\frac{\rho_c}{\rho_l}\int_0^t V(t,\tau)N(\tau)\lambda(\tau)dt \tag{2.9}$$

In equation 2.9, $N(\tau)$ is the nucleation frequency per untransformed volume and $V(t-\tau)$ is the volume of a given centre at time t, rather than its mass. It should be noted that the transformation is initiated at time τ where $\tau \leq t$ and that in absolute terms the degree of crystallinity of a sample is always lower than 100%. To solve this details on the nucleation and growth rates are needed.

In general, accommodating for volume changes and incomplete crystallisation, the following general formula can be derived:

$$1-\frac{\nu_c}{\nu_\infty}=\exp\left[-K\left\langle 1-\nu_c\left(\frac{\rho_c-\rho_l}{\rho_l}\right)\right\rangle t^n\right] \tag{2.10}$$

Here, V_c and V_∞ are the instantaneous and final crystallinity volume fractions, ρ_c and ρ_l are the crystal phase density and the melt phase density, and n is dependent on the dimensionality of the crystallisation, whether the nucleation is thermal or athermal

and the form of linear crystal growth. This equation is quite complex, a common simplified version, with an induction time t_0, can be derived:

$$1 - \frac{\nu_c}{\nu_\infty} = \exp\left(-K(t - t_0)^n\right) \tag{2.11}$$

Here, (V_c / V_∞) is the relative volumetric transformed fraction, n is the Avrami index and K is the overall crystallisation rate constant containing contributions from both nucleation and growth kinetics. For an ideal homopolymer, Avrami theory is expected to fit accurately to the end of the primary crystallisation before impingement of spherulites begins at around 50%. The Avrami index, n, represents the dimensionality of the evolving objects, shown in equation 2.12. Keller et. al. [92] gave a first principles derivation of the Avrami parameters, with table 2.2 showing some derived n values for varying systems. (Athermal nucleation is based on a system where all evolving entities are simultaneously nucleated at t = 0) [93-94].

$$n = n_d + n_n \tag{2.12}$$

Where, n_d is the dimensionality of growing crystals eg. 1, 2 or 3 and n_n represents the time dependence where 0 means instantaneous crystallisation and 1 means sporadic nucleation. It should be noted that these values can all be non-integral. Therefore, a polymer nucleating sporadically creating spherulites has an Avrami index ≈ 4. While the same polymer supercooled with instantaneous crystallisation has an index of 3.

System	Nucleation	n value
Fibrillar	Athermal	1
Fibrillar	Thermal	2
Laminar spherulitic	Athermal	2
Laminar spherulitic	Thermal	3
Spherical spherulitic	Athermal	3
Spherical spherulitic	Thermal	4

TABLE 2.2 : Typical *n* values with respect to system and nucleation method [95]

Lorenzo et. al. [22] provide a good guide to common pitfalls when performing isothermal DSC scans and Avrami analysis. Following their advice, the classical equation can be adapted to allow for an induction time, t_0, by simple substitution as shown in equation 2.11. Complete DSC crystallisation runs are preferred, since incomplete runs require a projection method, usually either a horizontal line from a point after the crystallisation to a point at the beginning of the crystallisation at t_0, or drawing a line between the local maxima before and after the exothermic curve. Figure 2.6 shows an ideal crystallisation curve, whereas the graphs in figure 2.7 show an incomplete crystallisation curve caused by the sample beginning to crystallise before the T_c is reached, along with two varying methods of calculating subsequent Avrami data.

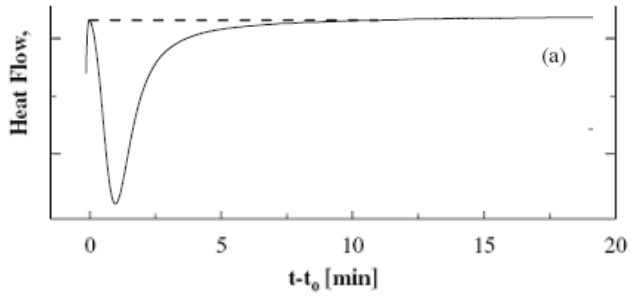

FIGURE 2.6 : An ideal isothermal crystallisation curve for Avrami analysis. Reprinted from [90]

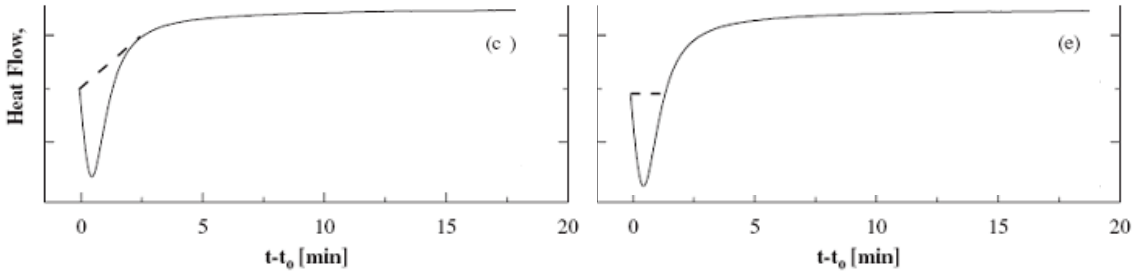

FIGURE 2.7 : The Booth-Hay Method (left) and Scott-Ramachandrarao Method (right). Reprinted from [90]

By performing an isothermal DSC scan, a curve similar to that shown in figure 2.8 is obtained. Software can then be used to ascertain the percentage crystallinity of the sample as a function of time by dividing the curve into segments representing percentage of crystallised material up to 50%. An Avrami curve can then be generated, shown in figure 2.9. With the assumptions that the nucleation occurs

randomly and homogeneously, and that the growth is linear and occurs in all directions, the Avrami equation 2.13 can be applied.

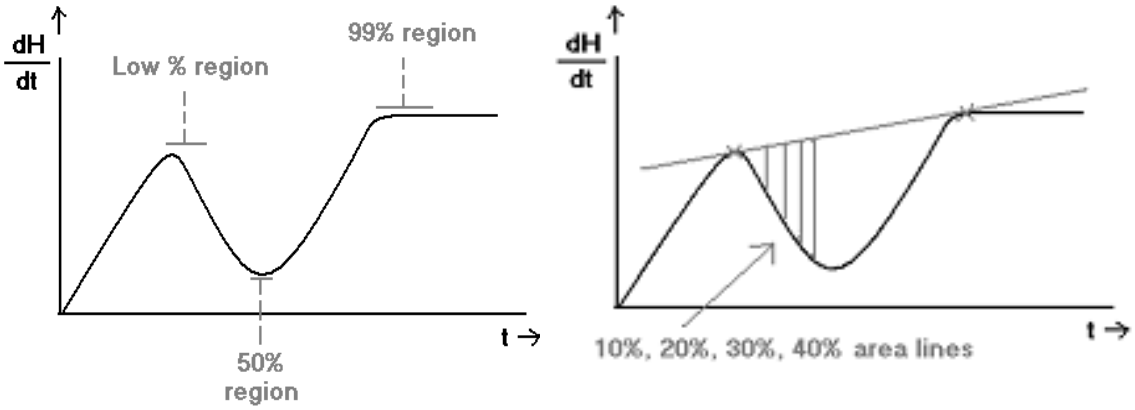

FIGURE 2.8 : An isothermal crystallisation curve (left) and curve with segments representing percentage of sample crystallised (right)

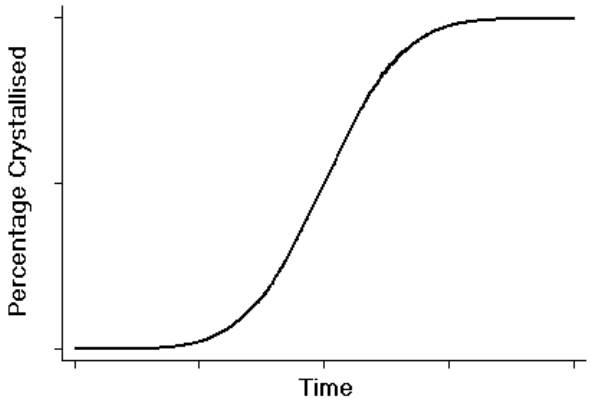

FIGURE 2.9 : A characteristic S-shape Avrami curve

$$f = 1 - [\exp(-\{K * (t - T)^n\})] \qquad (2.13)$$

Vaughan [96], amongst others, showed that by fitting this function to data values *n*, *K* and *T* are calculated, where *T* here relates to the induction time t_0 used previously in equation 2.11. To make the data comparable, since *K* has units min^{-n}, K_3 values are calculated using equation 2.14 for athermal spherulitic crystallisation [97-98]. To calculate a growth rate, *G*, equation 2.15 is generally considered to be the most acceptable method [99-103], which expresses the growth rate dependence on crystallisation temperature. This was first published by Hoffman and Lauritzen in detail [104-106].

To calculate an experimental value however, observation of the radius of growing spherulites during crystallisation using optical microscopy can be employed [95]. Plotting these values provides a linear relationship, shown in figure 2.10, the gradient of which is the respective *G* value for that T_c. Plotting the *G* values obtained against T_c produces a curve similar to that shown in the right of figure 2.10. K_3 constitutes an effective three dimensional crystallization rate constant that depends on two factors; the number of nucleation sites per unit volume and the rate of subsequent crystal growth. The Williams-Landau-Ferry theory covers the thermal activation, detailed in Appendix 4.

$$K_3 = \frac{4}{3}\pi N G^3 = K_{exp}^{(\frac{3}{n})} \tag{2.14}$$

$$G = G_0 \exp\left[\frac{-U^*}{R(T - T_\infty)}\right] \exp\left[\frac{-K_g}{T(\Delta T) f}\right] \tag{2.15}$$

Here, U^* is the activation energy associated with the segmental jump rate in polymers, T_∞ is the temperature (hypothetically) at which all motion associated with viscous flow ceases, *G* is the growth rate and *f* can be defined by equations 2.16, derived by Hoffman et. al. [107] and 2.17 [103]. From Suzuki and Kovacs [108], T_∞ was found to be approximately 30 ^{0}K less than the T_g.

$$\Delta f = \Delta h_f - T\Delta S_f = \Delta h_f - \frac{T(\Delta h_f)}{T_m^0} = \frac{\Delta h_f (\Delta T)}{T_m^0} \tag{2.16}$$

$$\Delta f = \left[\frac{\Delta h_f (\Delta T)}{T_m^0}\right] f_c \tag{2.17}$$

Where, $$f_c = \frac{2T}{T_m^0 + T}$$

Here, Δh_f is the heat of fusion, Δf is the bulk free energy of fusion, f_c is the correction factor and T_m^0 is the melting point of a crystal with very large *l* (crystal dimension). Details of this derivation and usage can be found at [103].

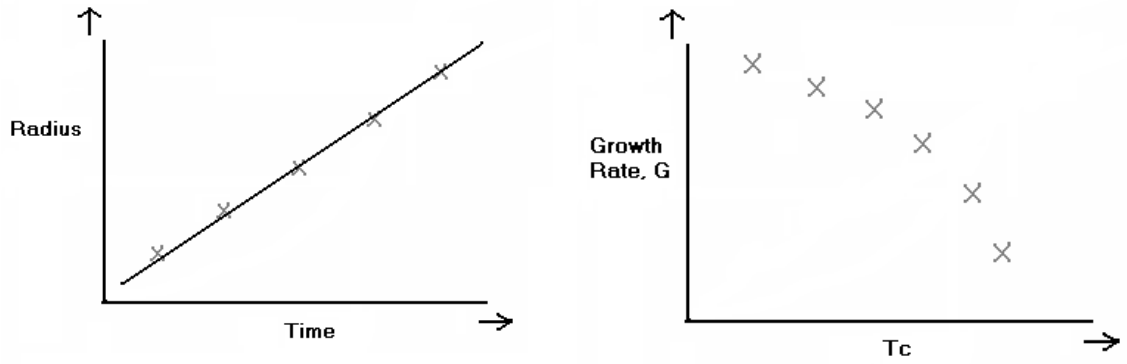

FIGURE 2.10 : The linear growth rate of spherulites (left) and a curve of growth rates plotted against increasing T_c (right)

To calculate a value for T_m^0 a plot of T_m verses T_c can be generated, with the point at which T_m is equal to T_c, also said to be T_m^0, shown in figure 2.11. This is called the Hoffman-Weeks method and is widely used [109-111].

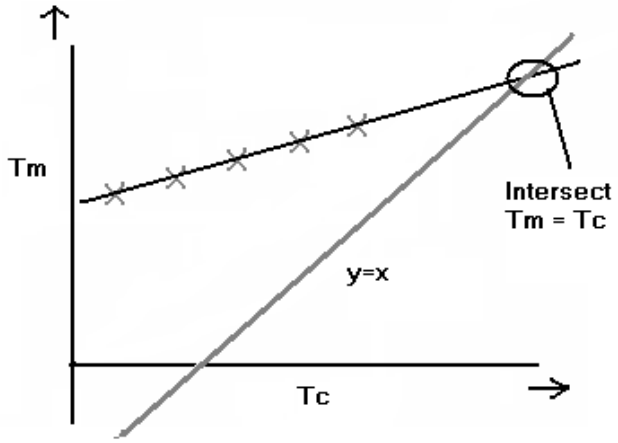

FIGURE 2.11 : Hoffman-Weeks method for calculating T_m^0

Using experimental or calculated values this entire process can provide nucleation rate data, hence information on the crystallisation kinetics of the material and any effects that addition of fillers may have.

2.3 Electrical Properties

One method for analysing the electrical properties of a material is dielectric spectroscopy. However to perform this type of analysis a gold coat should first be applied to the same. A schematic diagram showing a gold sputter coater is presented in figure 2.12. The sample is underneath a gold head or foil in the main chamber, which is then sealed and held at a vacuum. The gold is then negatively charged and argon gas is released into the chamber. An electric field is then applied across the chamber, which results in ionisation of the argon atoms to create positive ions, which are accelerated and bombard the gold electrode, ejecting gold atoms that are deposited onto the sample.

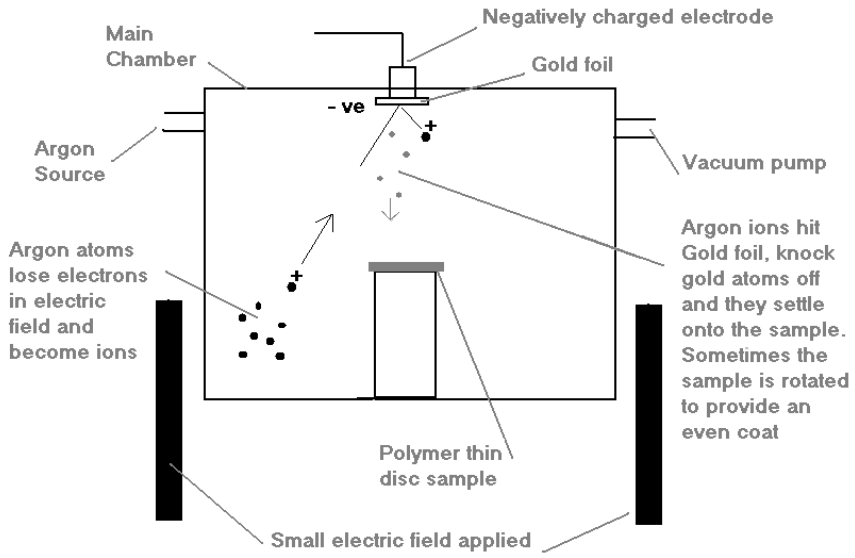

FIGURE 2.12 : An example gold sputter coater

For dielectric spectroscopy, the coating process is repeated for both sides of the sample, great care being taken to ensure that a small annular region at the edge of the sample remains uncoated, to avoid pure conduction across the electrodes. In this study an Emitech K550X sputter coater was used. The K550X is primarily designed to provide metallic coatings for SEM microscopy, however is also suitable for coating for dielectric purposes [112]. The deposition rate of the coater when using gold is shown in figure 2.13.

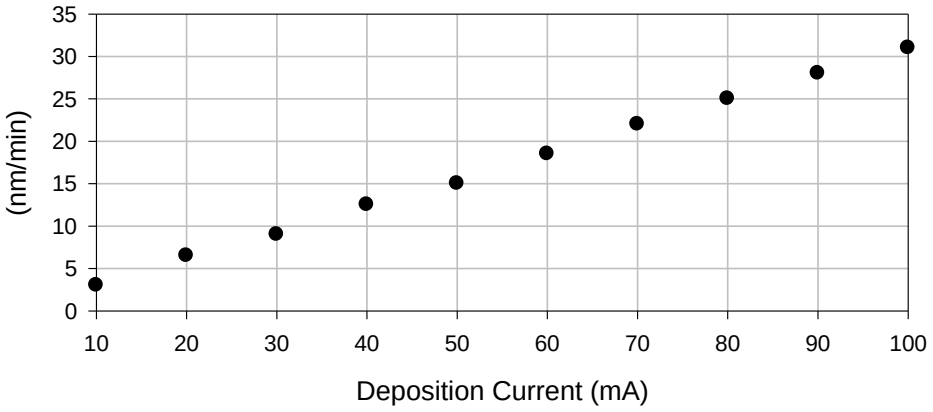

FIGURE 2.13 : Deposition rate of gold given by *Emitech K550X manual*

A series of experiments were performed that involved coating glass slides using varying current/time settings and measuring the resulting surface resistance to determine the optimum set-up. It was decided that an acceptably small resistance was 10 Ω since this gave a low noise-to-signal ratio during initially testing. The results of the resistance experiments can be seen in Appendix 2.

Polymers are popular dielectric insulators and therefore part of this investigation is based upon the interaction between an applied electric field and the dipole moments present in the material. In dielectric spectroscopy, the properties of the sample are generally measured as a function of frequency, other variables being temperature and the magnitude of the applied field. There are two main types of dielectric mechanisms – relaxations and resonance [26, 113-115].

When a material is placed between two oppositely charged plates the positive charges move towards the negative electrode and vice versa, polarising the material. In isotropic materials, the small dipole moments are aligned in the direction of the field created by the plates and the global polarisation is a vector quantity resulting from the magnitude and direction of these individual moments. The three main types of molecular polarisation are electronic, atomic and orientational, shown in figure 2.14. Electronic occurs when the electric field causes slight displacement of electrons. Atomic is where the electric field distorts the arrangements of the atoms in a molecule. Orientational is where the molecules possess permanent dipole moments and they align to the direction of the applied field giving a net polarisation [116]. Hill et. al. [117] provide a good method for listing these effects, reprinted below.

High

Frequency

1) Electric Polarisation. This occurs in neutral atoms at higher frequencies. The electric field slightly displaces the electron relative to the nucleus. It is therefore a resonance effect. This displacement is very small but can react to very high frequencies and is responsible for refracting light. It occurs as the electric force and restoration forces oppose each other and find an equilibrium.

2) Atomic Polarisation. Occurs at a lower frequency than electric. Here the electric field distorts the arrangement of atomic nuclei in a molecule or lattice. The movement displayed here is much slower, due to the larger mass being moved, than that in the electric polarisation and hence cannot occur at high frequencies. The magnitude of the atomic polarisation is usually 10% that of the electric magnitude.

3) Orientational Polarisation. This can be broken down into – dipole relaxation, ionic relaxation and dielectric relaxation. With an applied field any permanent or induced dipoles present will align to the fields direction. Hence once aligned a net polarisation is created in that direction. This process is slow but can make a very large contribution.

Low

Frequency

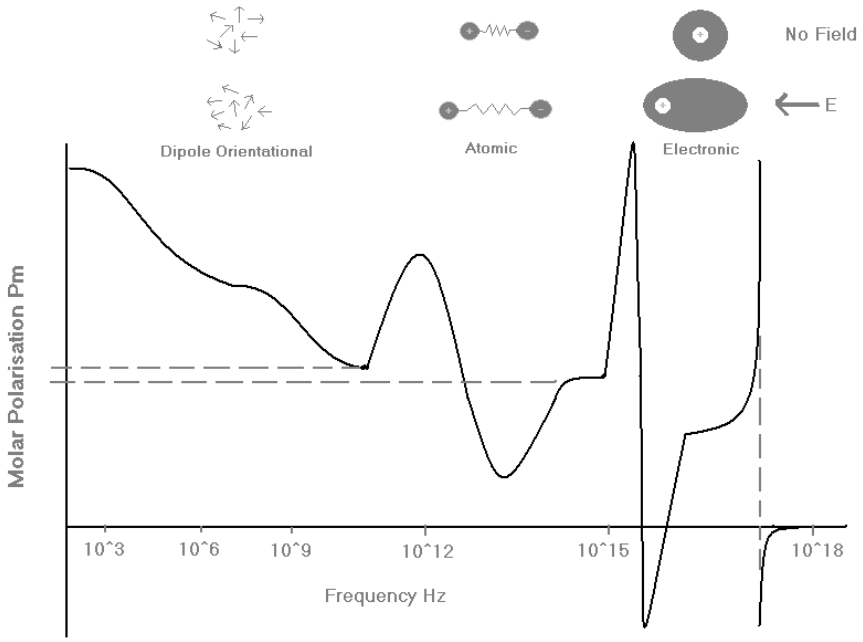

FIGURE 2.14 : Graphical representation of three dielectric effects.

Reprinted from Blythe [26]

Blythe and Bloor [26] explain that the orientation of molecular dipoles is relatively slow, but given sufficient time within an electric field, the orientation will reach an equilibrium at which maximum polarisation is achieved. The observed dielectric constant at this equilibrium is known as the static dielectric constant ε_S and if no time

is allowed for the orientation of dipoles then the instantaneous relative permittivity, ε_∞, will be low and due to deformational effects. They continue by defining an alternating electric field E with amplitude E_0 and angular frequency ω across a dielectric material, shown in equation 2.18.

$$E = E_o \cos\omega t \tag{2.18}$$

This produces polarisation and at high enough frequencies the dipole orientation will lag behind the applied field, producing a phase lag δ. This can be written as equation 2.20 with electric displacements D and D_0, with D_1 and D_2 defined in equation 2.21.

$$D = D_o \cos\omega t - \delta \tag{2.19}$$

$$D = D_1 \cos\omega t + D_2 \sin\omega t \tag{2.20}$$

$$D_1 = D_0 \cos\delta \qquad \text{add others} \qquad D_2 = D_0 \sin\delta \tag{2.21}$$

Blythe and Bloor [26] then defined the two relative permittivities, shown in equations 2.22 and 2.23 with the relationship between the two said to be $\varepsilon'' / \varepsilon' = \tan\delta$. From these a complex relative permittivity can be defined, shown in equation 2.24.

$$\varepsilon' = \frac{D_1}{(\varepsilon_o E_o)} \tag{2.22}$$

$$\varepsilon'' = \frac{D_2}{(\varepsilon_o E_o)} \tag{2.23}$$

$$\varepsilon^* = \varepsilon' - i\varepsilon'' \tag{2.24}$$

A population of ideal, non-interacting dipoles respond to an alternating electric field with a single dielectric relaxation, called a Debye relaxation, usually expressed as equation 2.25. A common medium that shows a single debye relaxation, when scanned up to a frequency of 1 GHz, is water [118-119].

$$\varepsilon^*(\omega) = \varepsilon_\infty + \frac{\varepsilon_s - \varepsilon_\infty}{1 + i\omega\tau_t} \tag{2.25}$$

Here, $\varepsilon^*(\omega)$ is the complex permittivity of the medium as a function of frequency, ω is equal to $2\pi f$, ε_∞ is the permittivity at the high frequency limit, ε_s is the static low frequency permittivity and τ_t is the relaxation time of the medium. Having collected dielectric spectroscopy data it is also possible to then calculate conductivity values for the medium [120-121]. This is performed using equations 2.26 and 2.27 below.

$$\varepsilon'' = \frac{\sigma}{\omega} \tag{2.26}$$

$$\sigma = 2\pi f_r \varepsilon_r \varepsilon_0 \tan\delta \tag{2.27}$$

Here, σ is the conductivity, f_r is the frequency, ε_r is the relative permittivity and ε_0 is the permittivity of vacuum (known to be 8.85 x10^{-12} F/m).

When observing the dielectric response of a multi-component system interfacial polarisation should also be considered. The effect of non-uniformity within samples or impurities within the host material, such as a filler within a polymer, is referred to as the Maxwell-Wagner effect, or Maxwell-Wagner polarisation [26]. Cracks and voids within the sample are noted to produce a drop in relative permittivity, whereas impurities with different conductivities and permittivites will cause a build-up of charge over time at the interfacial regions [26]. In 1914, Wagner [355], defined that a conductive impurity present in a highly insulating material would cause a dielectric relaxation said to be indistinguishable in form from that given by the Debye equation [26], shown in equation 2.25. The experimental implications of Maxwell-Wagner polarisation would be the addition of a large frequency-dependent contribution to the dielectric response, caused by the build-up of charge at the interfacial regions, most notably at low frequencies. Therefore for this investigation, a large increase in dielectric response may be expected at low frequencies.

2.3.1 AC Electrical Breakdown

AC ramp breakdown testing is experimentally simple and involves imposing a linearly increasing voltage across the sample until failure occurs. The international standards relating to data collection for electrical breakdown are: ASTM D149 and IEC 80243. There are many theories about the underlying mechanisms behind electrical breakdown and numerous electrical, thermal and mechanical theories have been proposed (see Appendix 1). Since polymers are good insulators, the empirical electrical breakdown strength is particularly important.

To simplify the electrical breakdown process, thin uniform thickness discs are used for testing. The thickness is noted and an increasing voltage is then applied to the target samples and a time to breakdown measurement, *t*, or voltage at breakdown, *V* is recorded. With these values the material can be given an average breakdown strength, although fitting a function to the data is deemed more useful [122]. An example is a 2-parameter Weibull distribution [123], shown in equation 2.28, given that $x \geq x_t$.

$$P_f(x) = 1 - \exp\left[-\frac{(x - x_t)}{\alpha} \right]^{\beta} \tag{2.28}$$

Here, $P_f(x)$ is the cumulative probability of failure at time x, x_t is a threshold time under which no failures can occur, α and β are the location (approximately the average time, x) and shape parameters (describes the spread of the data). With the apparatus shown in figure 2.15, breakdown times, x, are recorded and the resulting data analysed using the Weibull 7++ software package, assuming a 2-parameter Weibull distribution [124]. When performing such data analysis, there are two functions that can be explored; the probability density function (PDF), $f(x)$, shown in figure 2.16, and the cumulative distribution function (CDF), $F(x)$ [125-126].

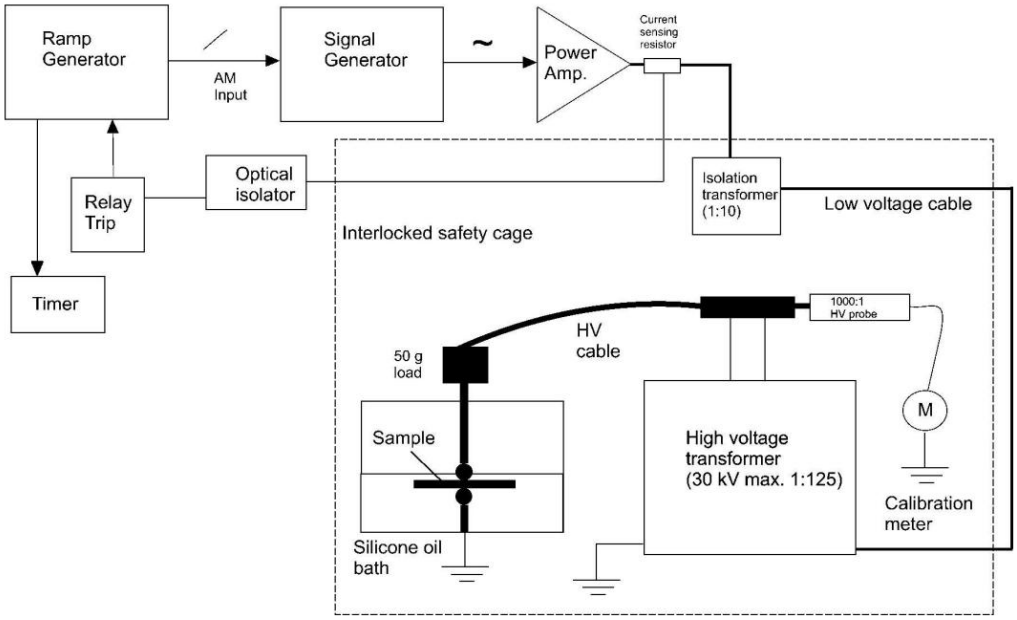

FIGURE 2.15 : Schematic diagram of the breakdown equipment, reprinted from [95]

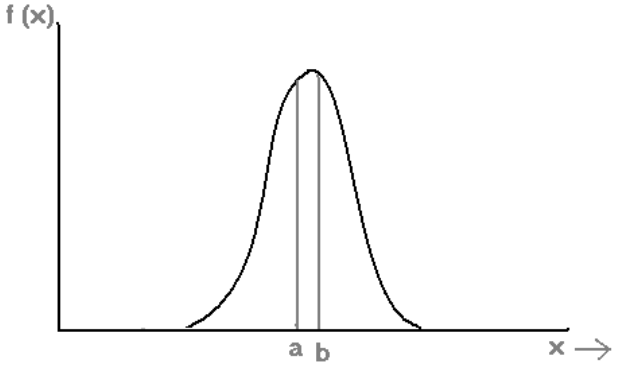

FIGURE 2.16 : A graphical representation of a Probability Density Function, PDF

With reference to figure 2.16, the PDF can be described:

$$P(a \le x \le b) = \int f(x)dx \tag{2.29}$$

Where, *b* and *a* are the upper and lower bounds respectively given that the probability function is positive for all positive values of x. Then the probability that *x* takes a value between *a* and *b* is the area between the *a* and *b* x-axis values under the PDF. For a CDF we can say the following,

$$F(x) = P(X \leq x) = \int_0^X f(s)ds \tag{2.30}$$

For a given *x*, *F(x)* is the probability that the observed value of *X* will be at most *x*. Limits of integration depend on the domain of *f(x)*. The relationship between the PDF and CDF can be represented as follows,

$$F(x) = \int_{-\infty}^{x} f(s)ds \tag{2.31}$$

Weibull suggested three distributions, with three, two or one parameter, shown in equations 2.32, 2.33 and 2.34 respectively, to model life data [125]. In general, the one parameter Weibull fails to fit experimental data accurately and the three parameter is considered to "over-parameterise", giving little improvement in the fit and the addition of an unwarranted extra parameter. This is the belief of many researchers, such as Chunsheng et. al. [127], who investigated the three Weibull equations and found the two-parameter to be the preferred choice. The three parameter Weibull distribution is defined is as follows:

$$f(t) = \left(\frac{\beta}{\eta}\right)\left(\frac{(t-\gamma)}{\eta}\right)^{\beta-1} \exp\left[-\frac{(t-\gamma)}{\eta}\right]^{\beta} \tag{2.32}$$

Here, β is the shape parameter ≥ 0, η is the scale parameter ≥ 0 and γ is the location parameter given that *f(t)* ≥ 0, *t* ≥ 0 or γ and that γ takes a value between $-\infty$ and ∞. For the two parameter distribution γ is assumed to be zero, resulting in equation 2.33 and for the one parameter distribution β is assumed to be a constant, *C*.

$$f(t) = \left(\frac{\beta}{\eta}\right)\left(\frac{t}{\eta}\right)^{\beta-1} \exp\left[-\frac{t}{\eta}\right]^{\beta} \tag{2.33}$$

$$f(t) = \left(\frac{C}{\eta}\right)\left(\frac{t}{\eta}\right)^{C-1} \exp\left[-\frac{t}{\eta}\right]^{C} \tag{2.34}$$

Once a distribution has been selected to fit to the data, the spread of the data can be calculated. Rather than simple residuals, a more accurate method is often used- upper and lower confidence bounds [128]. Two sided confidence bounds will represent a region where a certain percentage of the population lies [129]. For example, a set of 90% confidence bounds would contain the population as shown in figure 2.17.

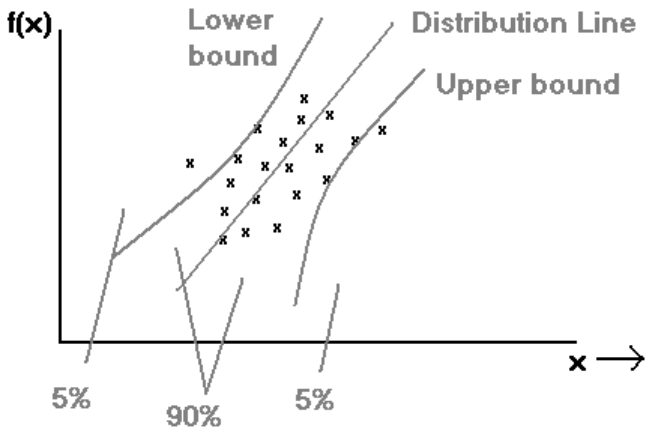

FIGURE 2.17 : An example of a breakdown distribution and confidence bounds

Confidence bounds are similar to error bars and give a graphical representation of the spread in the data. They are very often used when performing Weibull analysis to gauge the variation in breakdown strength across a sample, such as by Vaughan et. al. [130] and Mann et. al. [131]. There are two main types of confidence bounds – Fisher matrix and Maximum Likelihood. Fisher matrix confidence bounds are sometimes considered to be too optimistic, therefore Maximum Likelihood bounds were used [125]. Maximum Likelihood is also considered a simpler method than the Fisher matrix but takes more computer power. It is based on, [124]

$$-2\times\ln\left[\frac{L(\theta)}{L\left(\hat{\theta}\right)}\right]\geq X^{2}_{\alpha,k} \qquad (2.35)$$

Where, $L(\theta)$is the likelihood function for unknown parameter vector θ, $L(\hat{\theta})$ is the likelihood function calculation at estimated vector $\hat{\theta}$, $X^2_{\alpha,\,k}$ is a statistic with a

probability, α and k are degrees of freedom where k is the number of quantities jointly estimated.

Within this investigation the electrical breakdown strength and dielectric properties of PEO systems are determined. As previously stated, there are many theories and methods of breakdown hypothesised; short overviews of the most common electrical breakdown theories are given in Appendix 1.

2.4 Structure and Composition using Polarised Optical Microscopy

A basic method for observing the structure of a material's surface is by optical microscopy. With the development of SEM, TEM etc. optical microscopy is used less for maximum magnification structure analysis. However, due to the simplicity of optical systems, their ease of use, production of colour images and that many conclusions can be drawn about the structure of a system at these magnifications, optical microscopy is still a core imaging technique. The first optical microscopes were simply based upon one converging lens for magnification, such as those used by the Dutch pioneering microscope scientist Van Leeuwenhoek in the 17th century. Since then the technique has been greatly refined, mostly through the use of multiple lenses rather than only one.

Microscopes of today can often be operated in either reflection or transmission mode, altering the position of the light source. For thin samples the transmission mode is often used as light is passed from under the sample, up through the sample and into the optical system. For thicker samples where the amount of transmitted light is insufficient to give detailed images, reflection is used with the light source above the sample. In polarised optical microscopy, the light source of the microscope produces natural un-polarised light, which is passed through a polarizer to produce a single-plane (hence polarised) wave. This light is then passed through the sample, splitting into two components – the ordinary and extra-ordinary rays which travel through the sample at different speeds. This splitting of light is called bifringence and results in the two split rays having a phase difference before recombining to form one ray after passing through the sample. This ray then passes through an analyser, which detects

the change in polarisation of the ray due to the bifrigence within the sample. This is useful when studying spherulites [19,132-133], therefore particularly relevant for PEO since it crystallises to give particularly large spherulites, since the long polymer chains that align in the lamella act as linear polarisers. Therefore when their orientations coincide with one of the optical crossed polarisers little light is transmitted creating the dark regions of the maltese cross.

Following on from this, the theory and subsequent usage of etching and scanning electron microscopy is detailed in Appendix 5.

2.4.1 Fourier Transform Infrared Spectroscopy

Fourier transform infra-red spectroscopy (FTIR) is a variation on infrared spectroscopy; the use of the infrared region of the electromagnetic spectrum to observe the interaction of light with matter. Covering any combination of near (14000-4000 cm^{-1}), mid (4000-400 cm^{-1}) and far (400-10 cm^{-1}) infrared regions to observe the rotation or vibration of molecules, or combinations of these. Depending on the responses from this vibrational spectroscopy, the molecular structure can be determined. Some examples of the vibrational modes of simple molecules are; symmetrical stretching, anti-symmetrical stretching, scissoring, rocking or twisting etc. Figure 2.18 shows some examples of these vibrational modes when observing a CH_2 group.

FTIR and ultraviolet-visible spectroscopy (UV-Vis) are both popular techniques when observing ageing effects on materials. Hosier et. al. [134] used both techniques to characterise the ageing of dodecylbenzene (DDB) and vegetable oils. From infrared spectroscopy they observed that the DDB was oxidised significantly, exhibiting a very high dielectric loss.

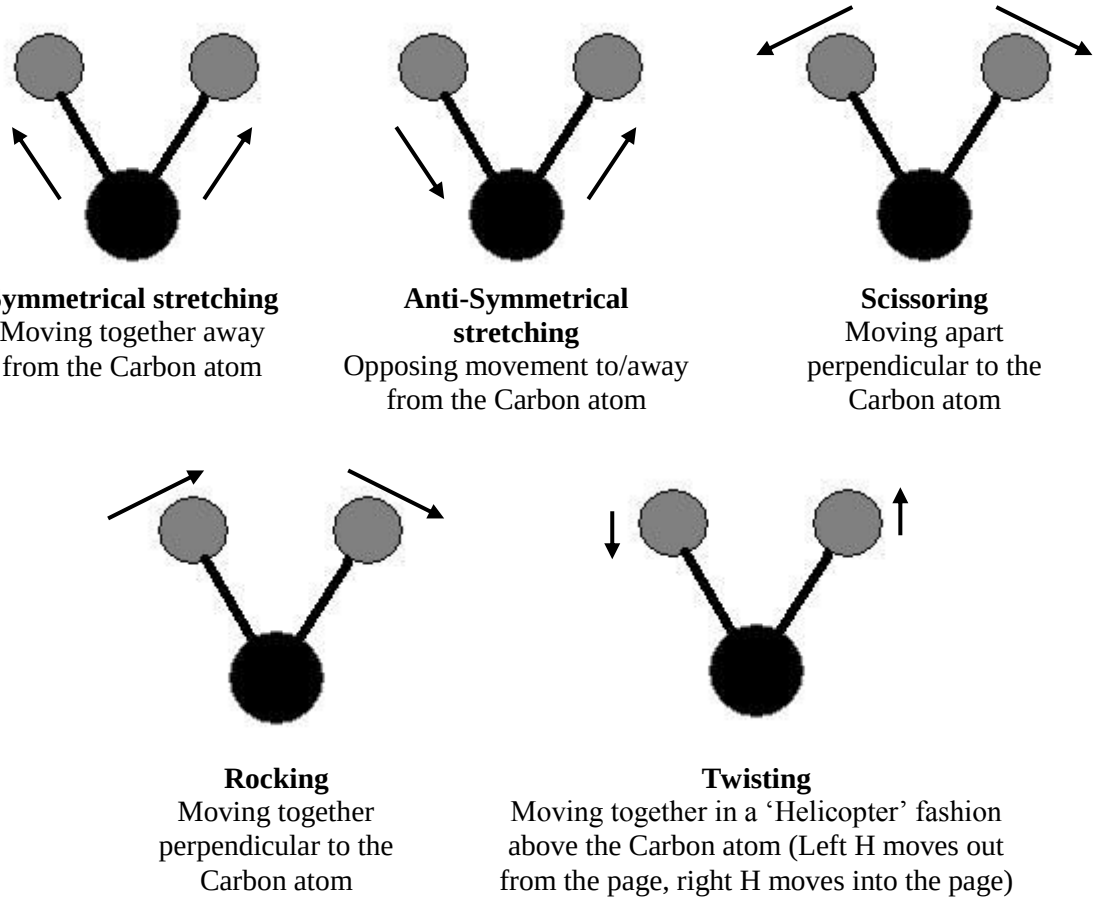

FIGURE 2.18 : Some examples of vibrational movement in a CH_2 Group

Dispersive infra-red spectroscopy is performed by splitting a beam and passing one half through the sample, while the second acts as a reference. Comparison of the dual beams, thus energy absorbed when varying the frequency, then allows vibrational analysis to determine the molecular structure. For FTIR the beam passes through an interferometer. Having passed through the sample a Fourier transform on the returning signal provides the same spectrum that would be achieved from the basic infrared spectrometer. It should be noted however that FTIR is less reliable, but is faster than conventional IR since information on all frequencies is collected simultaneously [135].

FTIR data are usually presented using either absorbance or transmission as a function of wavenumber [136]. Equation 2.36 shows the relationship between wavenumber and wavelength, and the energy-wavenumber relationship is shown in equation 2.37, where $\tilde{\upsilon}$ is the wavenumber in cm^{-1}, λ_l is the wavelength in cm, E_n is the energy, h is the planck constant and c is the speed of light in vacuum (3.00×10^8 m/s).

$$\tilde{\upsilon} = \frac{1}{\lambda_1} \tag{2.36}$$

$$E_n = hc\tilde{\upsilon} \tag{2.37}$$

From this it is clear that as the wavenumber increases the energy increases. FTIR is mostly used to assess the positions of the vibrational modes with respect to wavenumber, however it has been previously used to successfully determine the concentration of the analyte using Beer's law [137-138], also known as the Beer-Lambert or Beer-Lambert-Bouguer law, originating from [139-141]. The height of the peak is directly proportional to the concentration of the analyte, therefore calibrating using standard samples with known analyte concentrations, FTIR can be used to detect the concentration of the analyte in a variety of samples [135]. This law however, has limited applications, working only when the measured value of absorbance varies linearly with concentration, hence ignoring any chemical effects present [142]. A good overview of the Beer-Lambert-Bouguer law can be found at [143].

Chapter 3: EXPERIMENTAL

3.1 Materials

Polyethylene Oxide (PEO) is one of the most studied hydropolymers, drawing great interest from the scientific community. Investigations have involved degradation, solution behaviour, clustering etc.[144-147]. PEO comprises of linear macrochains consisting of different electronegativity elements: carbon and oxygen, and is defined as a hydrocarbon with full formula shown in equation 3.1. PEO is hydrophilic and the mechanism for solubility revolves around hydrogen bonding between the chain and water molecules. PEO crystallinity was found by Maclaine et. al. [148] to reach a maximum at a molecular weight of 6000 g mol^{-1}. The 5 molecular weight PEO's used in this investigation were in powder form provided by Sigma-Aldrich; 20,000 $gmol^{-1}$, 100,000 $gmol^{-1}$, 400,000 $gmol^{-1}$, 1,000,000 $gmol^{-1}$ and 4,000,000 $gmol^{-1}$. These were chosen to represent three molecular weights that cover the viscosity range of the rheometer at a 5 PPHW loading, then with one molecular weight chosen above and one below this range.

$$-\left[CH_2-CH_2-O\right]_n- \tag{3.1}$$

PEO has many applications in industry areas such as – cosmetics, medicine, crosslinked hydrogels, wound healing and as an electrolyte in lithium ion batteries. [149-150]. It has also been seen to improve healing of spinal injuries in canines and nerve repair [151-152]. In crystalline solid state, PEO exists mainly in a regular 7_2 helix form (seven chemical units in two turns of the helix) with a length of 1.93 nm [153], is able to form complexes with different metal cations and since the PEO helix loops are able to trap cations and owing the high flexibility of the macrochains, the loop can be fitted to ion diameter, in a similar way to cyclic ethers [154]. These complexes are ionic conductors and can be applied as polyelectrolytes in electronic apparatus [150]. Production of PEO is achieved by reacting ethylene oxide with water, ethylene glycol or ethylene glycol oligomers [155] using a catalyst, as follows;

$$HOCH_2CH_2OH + n\left(CH_2CH_2O\right) \rightarrow HO\left(CH_2CH_2O\right)_{n+1}H \tag{3.2}$$

PEO is noted to have low thermal and photochemical stability and is easily degraded and sensitive to oxidation [156]. In particular, Fares et. al. [144] found that the main degradation process is due to C-O and C-C cleavage. PEO is highly polar, making it compatible with a variety of fillers, and crystallises to form spherulites. Lower crystallinity and lower molecular weight PEO is more resistant to oxidation as found by Schiers et. al. [157-158], who performed research into thermal oxidation of PEO. PEO is also well-known for crystallising into large spherulites, such as those shown in figure 3.1.

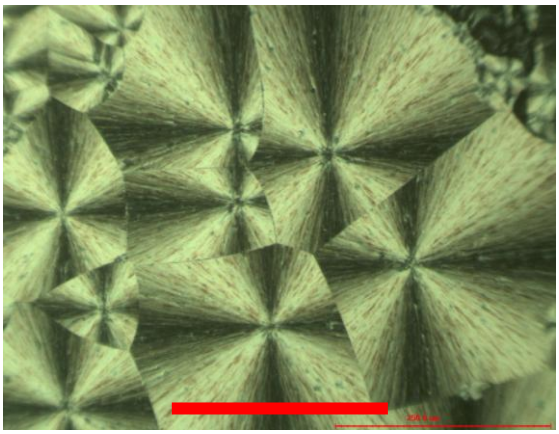

FIGURE 3.1 : PEO spherulites viewed using an optical microscope during this investigation (in transmission using crossed polars). Red scale bar is 250 μm.

Montmorillonite (MMT) is classified as part of the soft phyllosilicate clay group of the smectite family and is a platelet 2:1 system with 2 tetrahedral sheets sandwiching a central octahedral sheet [159]. MMT usually has a white or grey appearance [160] and its notable qualities include its tendency for its crystals to grow to several times their original size when added to water [161]. This growth suggests that it interacts strongly with this polar solvent. MMT has been used in a drilling clay called bentonite (aluminium phyllosilicate) and helps to increase the viscosity of water [162]. It can also be used to slow the progress of water within soils and this could be advantageous for farmers during dry seasons [162]. MMT has the standard and empirical formulae shown in equations 3.3 and 3.4. It is a non-stoichiometric compound and therefore cannot be represented by a ratio of well-defined values for each constituting element, and subsequently when considering the charges involved in equation 3.4, they will not balance.

$$SiO_2 / Al_2O_3 \tag{3.3}$$

$$(Na, Ca)_{0.33}(Al, Mg)_2 Si_4O_{10}(OH)_2 nH_2O \tag{3.4}$$

For many years MMT and other clays/clay minerals were used as filler for rubbers and plastics to reduce polymer consumption and reducing costs [163]. Other uses for MMT cover many industrial areas, such as; an effective treatment method for IBS [164], an absorbent of uric acid [165], to improve growth of fish [166] and others [167-168]. Much research has been performed using MMT as filler for materials [169-170]. A popular form of MMT for polymer research is aluminium-pillared MMT, shown in figure 3.2. This is probably due to its polar, hydrophilic nanofiller, making it particularly useful for research [171]. Previous research by Strawhecker et. al. has involved MMT and PEO, along with other polymers such as poly(vinyl alcohol) and polypropylene [172-174]. For this investigation, aluminium pillared MMT clay is used.

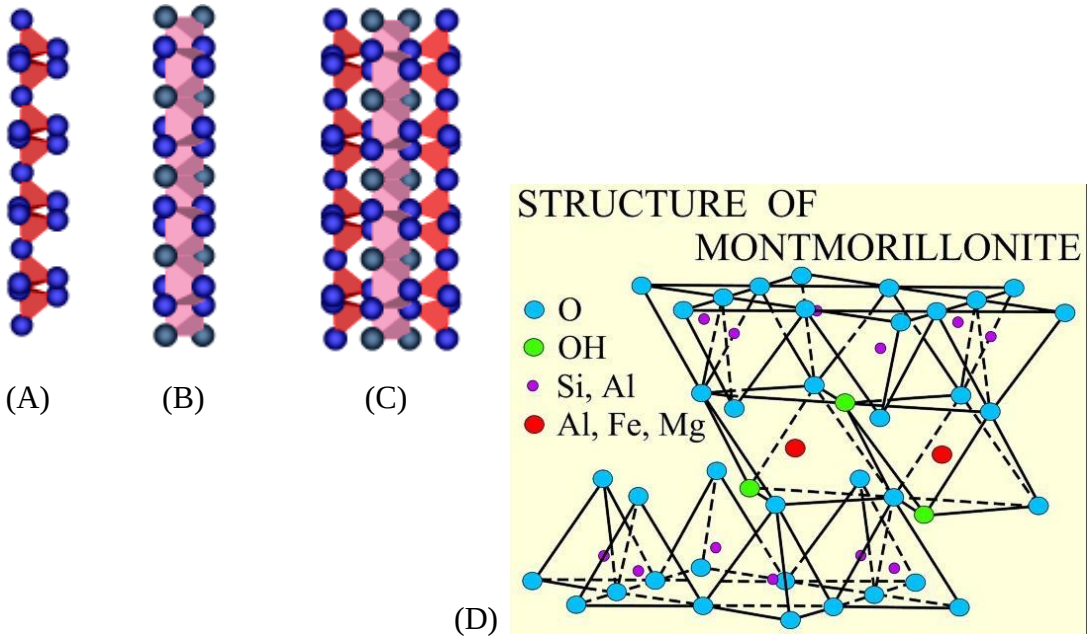

FIGURE 3.2 : Upper portion; (A) A tetrahedral sheet, (B) Octahedral sheet, (C) The tetrahedral and octahedral sheets combined to create montmorillonite. Lower portion; (D) 3D structure of MMT.

A-C reprinted from [175] and D reprinted from [176]

Silicon Dioxide (SD), also known as silica, is a physically strong oxide of silicon commonly found as sand or quartz, is the most abundant mineral in the earth's crust and is present in many types of glass, concrete etc [177], shown in equation 3.5. Another popular use of silicon dioxide is as silica gel, produced by the acidification of solutions of sodium silicate to produce a gelatinous precipitate that can be washed and dehydrated to leave a colourless microporous silica. Silica gel is well known for its ability to reduce local environmental humidity by absorbing water readily [178].

$$SiO_2 \tag{3.5}$$

When cooling silicon dioxide rapidly enough, it does not crystallise and instead solidifies as a glass. The simplest way to form silica is by exposing silicon to oxygen at ambient temperature, with a 'native oxide' layer forming on the surface of the silicon. Other methods include; low temperature oxidation at 400-450 ^{0}C shown in equation 3.6, decomposition of tetraethylorthosilicate at 680-730 ^{0}C shown in equation 3.7 or by plasma enhanced chemical vapor deposition using tetraethylorthosilicate at 400 ^{0}C shown in equation 3.8 [179].

$$SiH_4 + 2O_2 \rightarrow SiO_2 + 2H_2O \tag{3.6}$$

$$Si(OC_2H_5)_4 \rightarrow SiO_2 + H_2O + 2C_2H_4 \tag{3.7}$$

$$Si(OC_2H_5)_4 + 12O_2 \rightarrow SiO_2 + 10H_2O + 8CO_2 \tag{3.8}$$

SiO_2 forms a tetrahedral formation with strong directional covalent bonds holding four oxygen atoms at corners around a central silicon atom [180], shown in figure 3.3. The oxygen bridging bonds between the Si atoms give silica its unique properties [181]. It is difficult to define precise values for SiO_2's properties due to the high flexibility of the structure, causing wide variability of these properties. Two sizes of silicon dioxide particles were used during this investigation – micro sized SD (referred to as SD) and nano sized SD (refered to as nSD) with particle sizes 1-5 μm and 5-15 nm respectively.

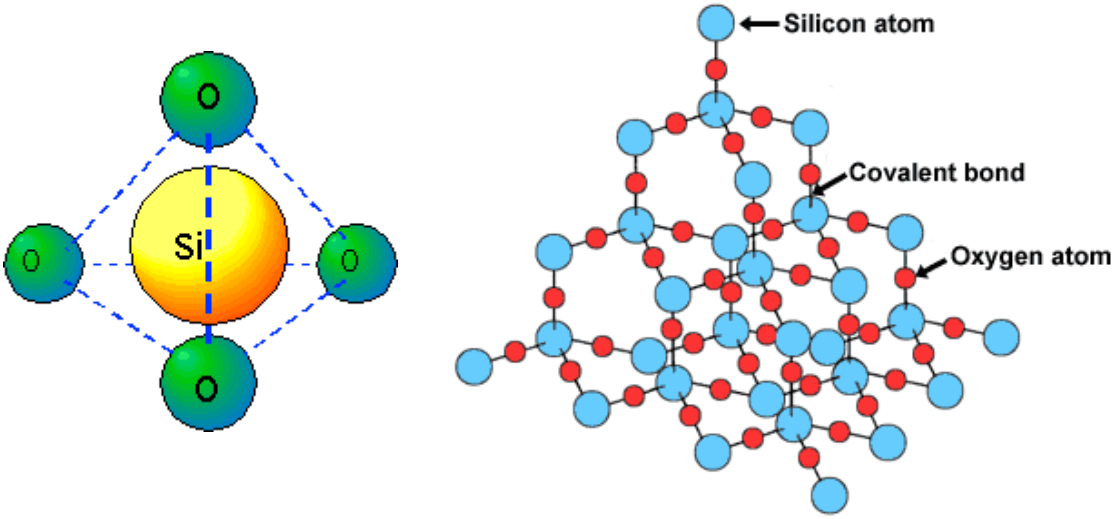

FIGURE 3.3 : A silicon atom surrounded by four oxygen atoms in a tetrahedral orientation (left) reprinted from [182], and the overall silicon dioxide structure (right) reprinted from [183].

Boehmite (BO), named after a German geologist J. Bohm, is a soft white/yellow mineral (thin films are noted to be colourless) often found in bauxite rock, the principal ore of aluminium [184-185]. Boehmite is an aluminium oxide hydroxide with an orthorhombic system of the rhombic-dipyramidal class. It therefore has 3 perpendicular 2-fold axes. The dipyramid faces consist of 4 identical faces on the top and on the bottom, these being a reflection of each other through the horizontal plane, figure 3.4 below.

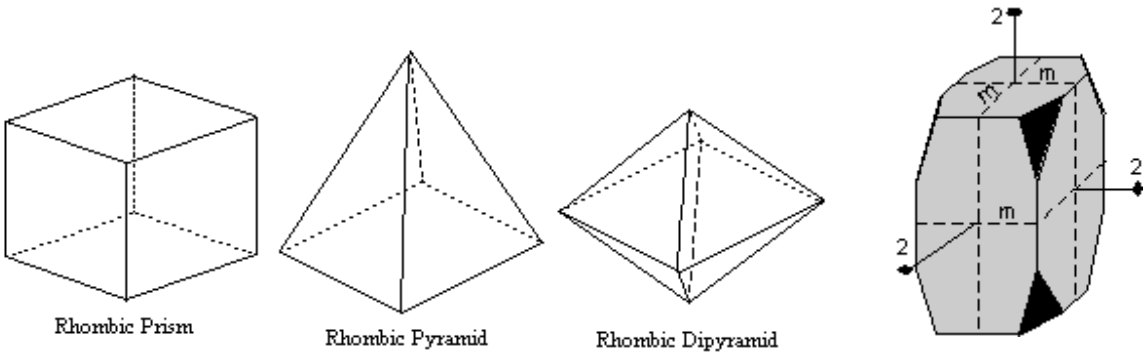

FIGURE 3.4 : Diagram of a rhombic prism, pyramid and dipyramid (left), image reprinted from [186]. A 3d image of an orthorhombic dipyramid with the dipyramid faces shaded black (right), image reprinted from [187]

Boehmite itself, with standard formulae shown in equation 3.10, is not soluble in water, however by modifying the boehmite it can be made particularly hydrophilic. Such modified aluminium oxides can be particularly hydrophilic and highly dispersible in water solutions with polymers [188]. Previous use has shown modified boehmite to alter mechanical properties, causing higher hydrophility [189-190] and porosity [191] as well as changing the photostability [192].

$$Al(OH)O \tag{3.10}$$

The boehmite used for this investigation has been modified using aluminium nitrate, a salt of aluminium and nitric acid and a strong oxidising agent. By treating the boehmite with aluminium nitrate (final composition has < 10% aluminium nitrate), shown in equation 3.11, SASOL have created a clay with a solubility of 15 g/l and increased acidity, from a ph value of 7-9 down to 3-4. This could have been achieved in a similar fashion to that produced by Mousavand et. al. [193] during their research into hydrothermal synthesis and modification of boehmite. They did this by using the hydrothermal synthesis and *in situ* surface modification techniques described in their paper, along with a pressure resistant tube, they could heat the mixture to 673 K for 10 minutes before submerging the reactor tube into a cool water bath.

$$Al(NO_3)_3 \tag{3.11}$$

3.2 Experiment Samples

One of the key differences between the commonly studied polyethylene (PE) and polyethylene oxide (PEO) is water solubility, due to the polar nature of PEO. PEO solubility gives distinct advantages as a model system, especially when adding polar fillers. Dissolving PEO into distilled water, followed by the addition of a nanofiller and the use of various mixing methods, should provide a high level of dispersion. With higher molecular weight PEO and higher polymer concentrations the samples require time to disperse, which raises an issue with water evaporation. When left to disperse, the solutions lose water and the ratio of PEO to water would slowly change.

By using weight-weight ratios for polymer and filler addition, along with weighing the entire solution in its flask, amount of water lost through evaporation can be observed and samples subsequently re-hydrated. Hand mixing solutions initially provides a basic level of dispersion, followed by rheometry to attain shear stress and viscosity data and help to disperse the solution further.

The rheometer used was a RHEOLAB MC1 Paar Physica instrument, optimised for a solution volume of 20 ml. 20 ml of distilled water weighs approximately 20 grams, therefore all solutions were created with 20 grams of distilled water and the required mass of PEO was added. Composite solutions were created by further addition of the required mass of filler as a ratio to PEO. The solutions generated were all named according to the nomenclature, which can be found after the contents pages. Samples were mixed in glass flasks, which were cleaned using hot water with commercial detergent and then rinsed with distilled water to remove ions from the detergent.

3.3 Dispersion methods

It is particularly important to disperse the filler and PEO to the highest level possible within the system. For solutions the most common mixing techniques are based around magnetic stirrer bars, stirring rods and forms of rheometry. During initial tests it was found that the magnetic stirrer bars worked well for low concentration samples but failed for the majority, since the solutions were too thick. Stirring rods were much more successful and appeared to disperse the solutions well, although with thicker samples a rod-climbing effect, called the Weissenberg effect, was observed [194]. This caused a loss of sample and also removed some of the PEO/filler from being dispersed. Recovering a sample after the stirrer bar process proved that a large amount of the specimen was lost and the dispersion was inconsistent. Rheometry however was still preferred since shear rate-shear stress data could be collected while increasing the dispersion state of the solution, despite a small amount of the solution being lost on surfaces. The PEO and fillers were added instantaneously to the flasks containing 20 g of distilled water. They were weighed, hand mixed and rehydrated if necessary.

3.4 Rheometry

In addition to providing rheological data, the rheometer should help to break up any agglomeration within the solution and provide good dispersion of the final system. The RHEOLAB MC1 is based on a spinning cylinder and a rheometer cup, designed to measure the torque acting on the spinning cylinder as a result of the viscosity of the solution in the rheometer cup, shown in figure 3.5.

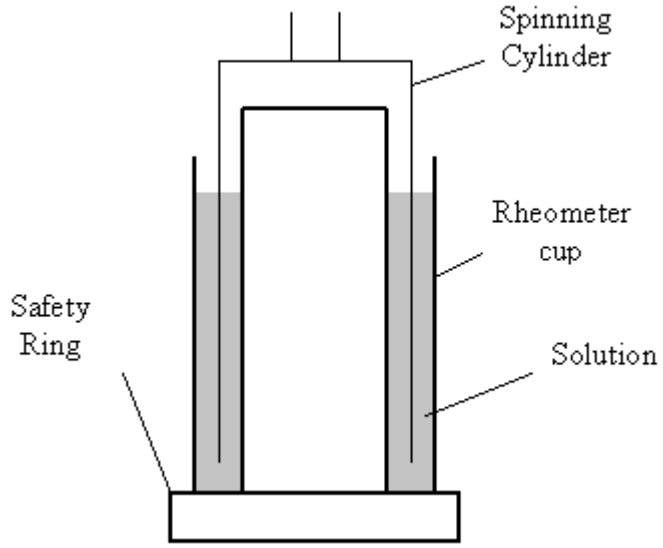

FIGURE 3.5 : Cross-section of rheometer components

The solution is poured into the rheometer cup around the centre pillar, then the spinning cylinder is lowered into the mixture and the complete assembly is attached to the rheometer. A Physica Rheologic RS 100 software package was used for instrument control, data collection and analysis. All samples were subjected to the same processes, shown below and in figure 3.6, and the same time intervals to ensure consistency

Process 0 - Preliminary manual dispersion

Process 1 - Shear stress linear ramp rate, 0.1-60 Pa

Process 2 - Shear stress held constant, 60 Pa

Process 3 - Shear stress linear ramp rate, 60-0.1 Pa

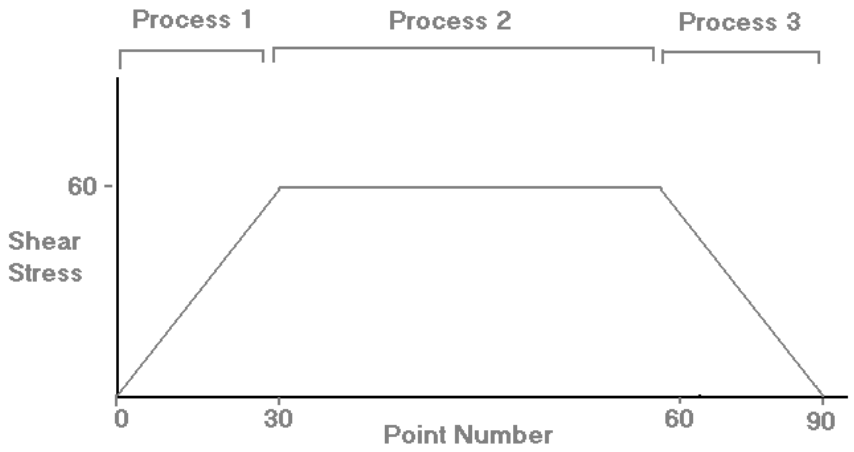

FIGURE 3.6 : Complete processing for all samples

With reference to figure 3.6, process one provides rheological characterisation of the initially prepared system. Process two then holds the system at a fixed shear stress and should achieve further dispersion followed by a ramp down as process three. If any additional dispersion has been achieved by the rheometer it should be apparent during process three. In particular, if further dispersion has been achieved the data collected in process three should differ than that from process one.

3.5 Differential Scanning Calorimetry

For DSC the previously mixed samples were stored and dried. Small samples were cut weighing 5 mg, using washed scalpel blades. The cut samples were placed into Perkin Elmer DSC cans and placed onto a hot plate set to 80 ^{0}C to melt the sample to the base of the DSC can, before a lid was added and the can sealed. The DSC equipment needs 1 hour to stabilise before measurements can be taken. The equipment set-up is shown in figure 3.7. The DSC is a power compensated Perkin-Elmer DSC 7 with Perkin-Elmer Pyris analysis software. The analyser runs the main DSC unit, which holds the sample pans, while the chiller maintains a stable background temperature in the DSC head.

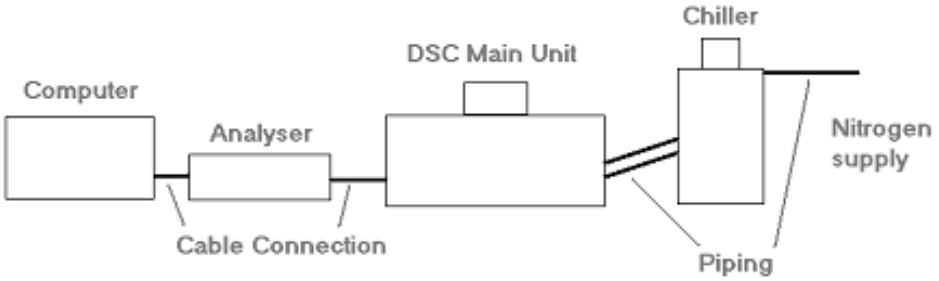

FIGURE 3.7 : Basic view of a DSC set-up

To ensure maximum possible accuracy, the DSC was calibrated before and after use. This is usually performed by testing a sample with a known thermal transition, such as the melting point [195]. Calibration for this investigation was performed using indium, with a known melting point of 156.6 ^{0}C. Starting at 140 ^{0}C, the indium was heated to 170 ^{0}C at 5, 10 and 15 ^{0}C/min. For temperature scan data this would provide the offset applicable for that specific scan speed. For isothermal scans a plot of T_m against scan rate can be extrapolated to obtain the T_m for a zero scan rate. These values are compared to the known T_m of indium and future values corrected.

To calculate the thermal transitions of samples, temperature scans were performed. Before each scan the sample was held at a fixed temperature to reduce thermal history effects. For the crystallisation temperature T_c, a scan from high-to-low temperature was employed and vice versa for the melting temperature T_m. Then full scans were taken as detailed in table 3.1, allowing for Avrami analysis.

Avrami Sample Processing
Sample held at 80^{0}C for 2 mins to remove any thermal history
Sample cooled to chosen crystallisation temperature at 100^{0}C/min
Sample held at chosen crystallisation temperature until fully crystallised
Sample cooled to 25^{0}C at 100^{0}C/min and held for 2 mins
Sample heated to 80^{0}C at 10^{0}C/min to provide a melting trace

TABLE 3.1 : DSC thermal procedure for Avrami analysis

3.5.1 Avrami analysis

The set-up defined in section 3.5 was performed to generate scans that Avrami analysis could be performed on to better understand the crystallisation and thermal processes in these materials. An example of collected data is shown in figure 3.8 as a heat flow verses temperature curve. From these data, crystallisation and melting scans can be extracted, the former being used to generate Avrami curves for up to 50% crystallisation. Fitting equation 2.13 from section 2.2.3 produced *n*, *K* and *T* values. K_3 values were then calculated using equation 2.14.

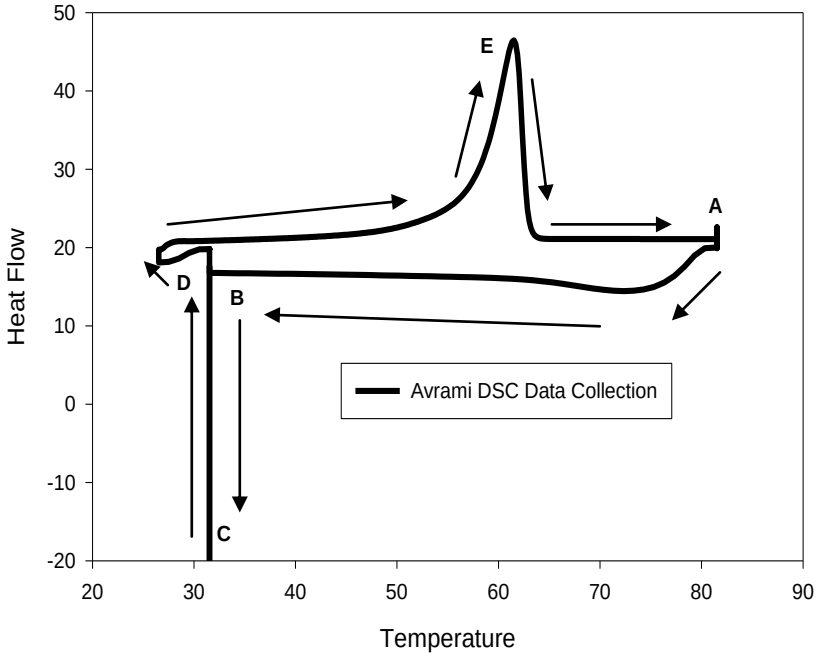

FIGURE 3.8 : A typical DSC data collection curve

With reference to figure 3.8, five regions are labelled A-E. The data collection begins at **A** with the sample held melted at 80 ^{0}C to remove any thermal history. Then the sample is rapidly cooled, hence showing a drop in the heat flow to the sample pan, down to region **B** - the chosen crystallisation temperature, which here is shown to be 31.2 ^{0}C (representing T_c = 30 ^{0}C with a 1.2 ^{0}C offset found when calibrating with indium). The sample is then held at the chosen T_c and crystallises, shown as region **C**, resulting in the large drop in heat flow required by the pan to remain a constant temperature during the exothermic process. Once the sample has finished crystallising, and the heat flow has returned to a steady rate, the sample is cooled to a

lower temperature, here chosen to be 25 ^{0}C, to ensure the sample has fully crystallised, before being heated at a steady rate up to 80 ^{0}C providing a melting trace, shown as region **D**. From the crystallisation data collected during this process, at region **C**, an Avrami curve, such as that shown in figure 3.9, is generated.

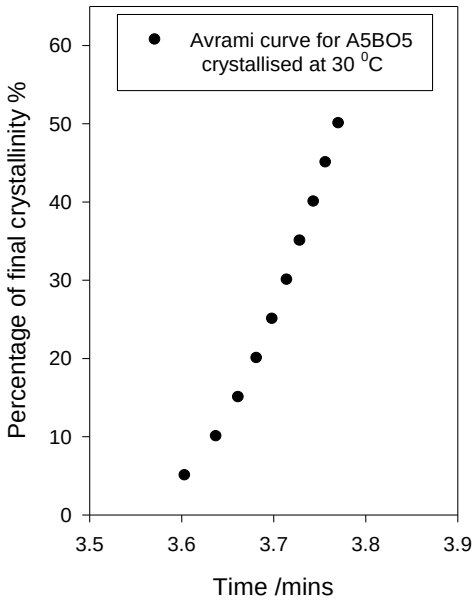

FIGURE 3.9 : An Avrami curve generated for the A5BO5 sample

3.6 Dielectric Spectroscopy

Dielectric spectroscopy experiments require thin film samples, like those used for AC breakdown measurements, although it has been found that samples around 400 μm provide better data since data collected is less related to surface effects and more from the bulk [95]. Unlike AC breakdown, dielectric loss experiments are non-destructive and thus only two samples were created for each material. To minimise surface effects, a thin gold coat was applied to each side of the thin disc sample to give improved electrode contact. The thickness and gold cross section of each sample were recorded.

For this investigation a Solartron 1296 Dielectric Interface and Schlumberger SI 1260 Impedance/phase gain analyzer were used with a choice of a custom built or commercial dielectric cell. For data collection the frequency was varied and real relative permittivity, imaginary relative permittivity and tan delta of each sample was

recorded. To increase accuracy, background scans were taken without a sample inside the cells. This background scan was subtracted from the sample data to remove contributions from the cables and external interference. Preliminary tests on samples showed the best parameters for testing, shown in table 3.2.

Parameter		**Value or Range**	
Frequency		0.01 – 1,000,000 Hz	
AC	DC bias	1 V	0 V
Integration		10 cycles	
Sample Area		Circular, 19mm dia.	
Sample Thickness		Eg. 0.59mm	

TABLE 3.2 : Parameter for dielectric spectroscopy experiments

Graphs representing the log of the real relative permittivity and log of the imaginary relative permittivity were also plotted as a function of frequency. Plots of the log tan delta against frequency were also generated.

Finally, graphs relating to a technique defined by Kenneth and Robert Cole [196] were produced, known as Cole-Cole plots. For these, the log of the real relative permittivity against imaginary relative permittivity is plotted. Such plots have been previously used by authors such as Kohli et. al. [197] during eye lens impedance studies. Cole-Cole plots form a curve, which is often the arc of a circle and can be used to determine the zero-frequency dielectric constant ε'_o and the limiting high-frequency value ε'_∞ [198]. The frequency dependence equation linked with the Cole-Cole plot is shown below.

$$\varepsilon = \varepsilon_\infty + \frac{\varepsilon_s - \varepsilon_\infty}{1 + (i\omega\tau)^\alpha} \tag{3.12}$$

Here, ε_s is the static permittivity (relative permittivity at frequency 0 Hz), ε_∞ is the permittivity at the maximum frequency, τ is the relaxation time and α is the Cole exponent, a specific value for different materials. Wei et. al. [199] provide a good background on Cole-Cole plots.

3.7 AC Electrical Breakdown

Thin film specimens for AC breakdown were prepared by melt pressing in a Grazeby Specac press equipped with a thin film attachment. One such example of pressed films would be the LDPE composites created by Bormashenko et. al. [200] with melting point of around 110 ^{o}C by pressing them at 180 ^{o}C. For polyethylene samples quenching is often achieved in water, however due to the solubility of PEO, the entire case was placed into another cooled press held at less than 5 ^{0}C, to rapidly cool the sample, a process detailed in figure 3.10.

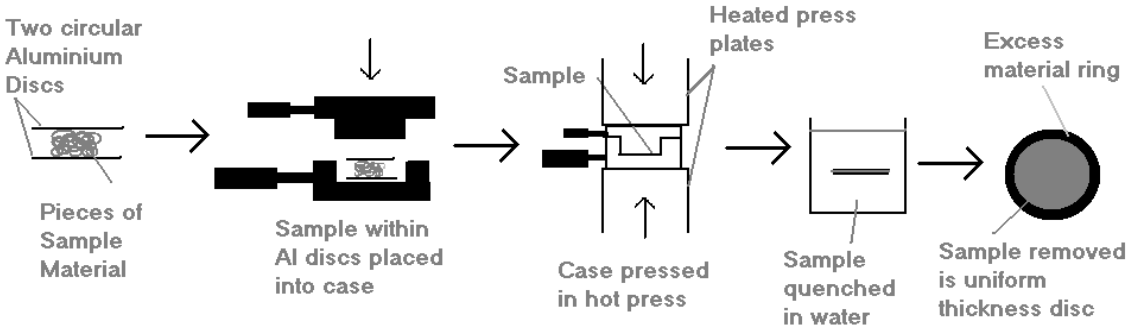

FIGURE 3.10 : Preparation of thin film discs

Since the PEO used in this study was supplied in a granular, rather than pellet form, this was initially melted in a vacuum oven to remove air and provide materials that were less likely to produce voided breakdown specimens. Then single cuttings from this block were pressed to create thin-film samples. This method was advantageous over the use of pellets, since when pressing pellets of polymers the grain boundaries between the pellets are sometimes a concern. Preliminary tests showed that each molecular weight PEO required a different time to de-gas, believed to be related to the relative molecular mobility within the system. For unfilled PEO samples, 5 g of each molecular weight were placed into Kapton cradles in glass beakers and placed into vacuum ovens at 80 ^{0}C. The de-gassing time was varied and observations of this effect are shown in table 3.3.

Sample	Time in Vac. Oven	Visual Observations
1M PEO	2 hours	Barely melted and full of air bubbles, more time needed
1M PEO	8 hours	Slightly melted but full of air bubbles, more time needed
1M PEO	24 hours	Melted sufficiently but air bubbles remaining, more time needed
1M PEO	48 hours	Fully melted and no visible air bubbles
400k PEO	2 hours	Barely melted and full of air bubbles
400k PEO	8 hours	Melted sufficiently but air bubbles visible, longer needed
400k PEO	24 hours	Fully melted and no visible air bubbles
400k PEO	48 hours	Fully melted with no viible air bubbles. Colour change from white to yellow
100k PEO	1 hour	Not melted and sample changed to a faintly yellow colour
100k PEO	2 hours	Barely melted, full of air bubbles and colour change to light yellow
100k PEO	5 hours	Mostly melted with visible air bubbles, a bright yellow colour

TABLE 3.3 : Visual observations when de-gassing PEO samples

It was noticed that obtaining 100k thin film discs without air bubbles would not be possible without the sample undergoing a thermal ageing process. To further understand the ageing process, an 8-hour aged PEO sample was used in the same experiments to gauge the effect that thermal ageing has on such properties. This knowledge would aid in determining if any thermal ageing has taken place in other samples.

After these preliminary tests it was possible to create breakdown samples of 400k and 1M without ageing by heating at 80 ^{0}C for 30 hours and 50 hours respectively. For the electrical tests (AC breakdown and dielectric spectroscopy) some reference polyethylene samples were pressed and tested for comparison. All pressed breakdown samples were numbered and labelled in a clock formation as detailed overleaf.

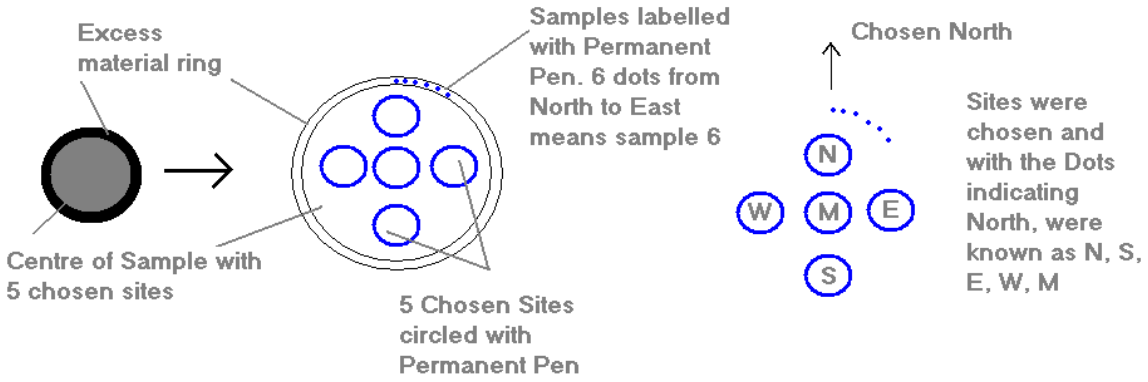

FIGURE 3.11 : Labelling of pressed thin film discs

In the test cell, as shown in section 2.3.1, the sample and 6.3 mm diameter steel ball bearing electrodes were immersed in silicone oil to prevent surface flashover. The oil was changed every day to avoid possible contamination and the ball bearings were changed after every other disc sample to avoid pitting. To check the linearity of the AC ramp rate a thick plastic plate was inserted in between the ball bearings in place of a sample before each test, and the voltage was measured as a function of time. Plotting voltage against time will confirm the linearity and alterations can be made if it is found to be non-linear. It is worth noting that all used samples were retained for reference and the AC ramp rate was kept at a constant 50 V/s.

3.8 Structure and Composition

The optical microscope used for this investigation was a Leitz Aristomet, shown in figure 3.12, using DeltaPix software connecting through a DP300 camera. Samples were viewed on cleaned glass slides using reflection and transmission modes on several magnifications. Experimental details for the etching and SEM can be found in Appendix 5.

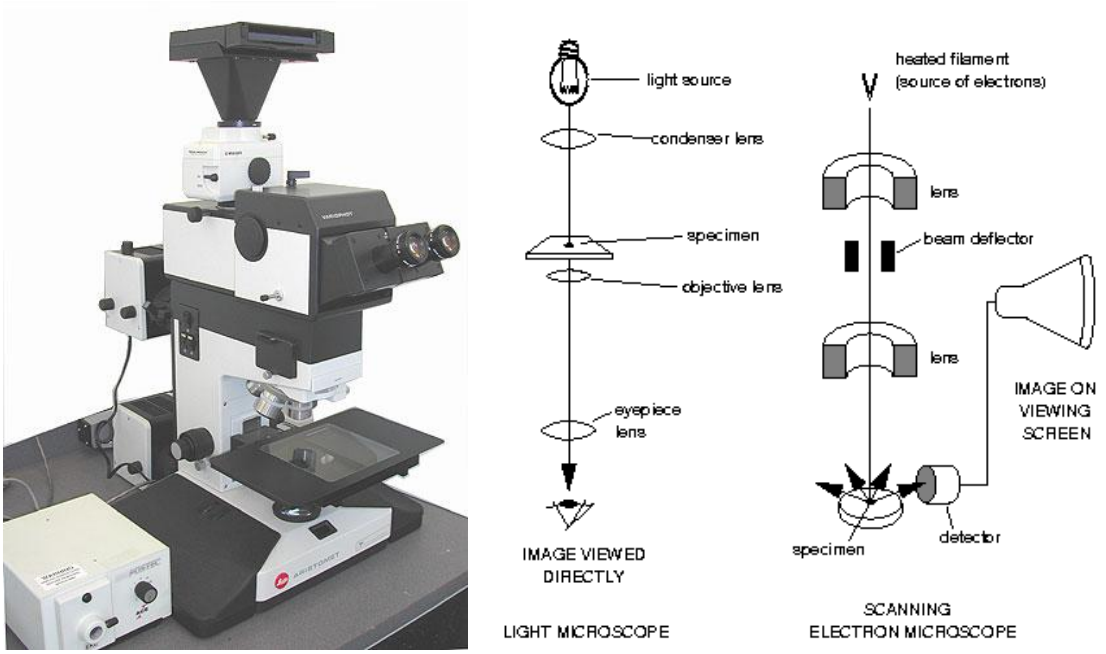

FIGURE 3.12 : The Leitz Aristomet microscope used (left) and a schematic for the optical microscope Vs a SEM microscope (right) reprinted from [201]

3.8.1 FTIR

For FTIR data collection a Nicolet 710 system was used. Samples were mounted into Nicolet sample holders and equipment given 10 minutes to stabilize before data collection using Omnic software. This software allowed collection of absorption and transmittance data, although it is known that one can be inferred from the other. Before data were collected for each sample, a background scan was taken to produce a clearer spectrum and improve accuracy. The target chamber is enclosed, but not airtight, so care was taken to limit air movement around the FTIR.

As a test of dispersion, FTIR scans were performed on several sites on several pressed samples for each material. If the dispersion within the system is poor, large variations would be seen in the spectra, however this was not the case. Transmittance data were taken first and stored as a percentage value for subsequent wavenumbers, up to the upper limit of the mid-infrared range, 4000 cm^{-1}. Absorbance data were then recorded and stored as a log of a ratio, with arbitrary units. Previous tests by Hosier et. al. [202] and initial tests for this investigation, suggest that to maintain accuracy for the absorbance data the plots are capped at 2 units.

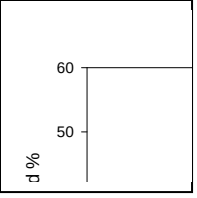

3.9 Chapter Summary

PEO was chosen as the host polymer for this investigation along with four fillers representing 3 varying geometries; MMT (a platelet system), SD and nSD (spherical particles) and BO (a rod-like system). These fillers were dispersed within PEO in solutions made from 20 g of distilled water with addition by weight as PPHW (parts per hundred water) for the polymer and as PPHP (parts per hundred polymer) for the fillers.

Rheometry should allow characterisation of the initial and final systems and to aid in dispersion. Stirring rods were not used due to losses from the Weissenberg effect. Using power compensated DSC, calibrated using indium, for 5 mg samples would allow calculation of the thermal transition temperatures and analysis of the avrami kinetics.

Dielectric spectroscopy, with varying frequency and a subtracted background for accuracy, would be used with gold coated 400 μm thick samples, chosen to increase the measurement of the bulk and reduce surface effects, to collect permittivity and loss tanδ data. AC breakdown would be used for 100 μm thick samples, chosen to reduce the overall voltage used during testing, with spherical electrodes at a rate of 50 V/s to provide breakdown data.

Thermal processing revealed the susceptibility of PEO to thermal ageing, with the 100k PEO the most easily affected. FTIR is proposed as a method to observe any major chemical changes taking place due to thermal ageing.

Optical imaging, etching and SEM are discussed as methods to analyse the structure and composition of samples.

Chapter 4: POLYETHYLENE OXIDE

4.1 Rheometry volume and temperature dependence

Before analysing the composite materials containing fillers it is necessary to characterise the unfilled material. Firstly the PEO was characterised in solution using rheology. It was expected that the volume and temperature of the solutions would affect the rheology data obtained. To gauge this effect, short experiments were performed, firstly by varying the volume of a sample from the optimal 20 ml down to 10 ml. Secondly, varying the temperature using a heat bath from room temperature (20 ^{0}C) up to 60 ^{0}C. Figure 4.1 shows that varying the volume of solutions has a large impact on the data collected. Therefore care was taken to ensure all samples were the same volume. The recorded shear stress varies as expected, since the shear stress value will be proportional to the contact surface area of the spinning cylinder/polymer solution, which is in turn proportional to the volume of solution present. This would not hold for extreme solutions, such as 25 ml or 5 ml, due to extra effects, such as the solution causing a resistive force on the top of the spinning cylinder.

Figure 4.1 also shows that increasing the temperature decreases the viscosity of the solution, by as much as 60% from 30 ^{0}C to 60 ^{0}C, at an approximate rate of 30 s^{-1} per 10 ^{0}C. Viscosity-temperature data was found to follow a basic exponential model, shown in equation 4.1 below. This equation allows calculation of the coefficients and accurate prediction of viscosities for specific temperatures. Here, η is viscosity, α_c and β_c are coefficients and T is the temperature.

$$\eta = \alpha_c \exp(-\beta_c T) \tag{4.1}$$

Both of these findings could be useful since high loading levels create solutions too viscous for this rheometer, so to characterise these solutions in further work the volume within the rheometer could be reduced or temperature increased and an offset applied.

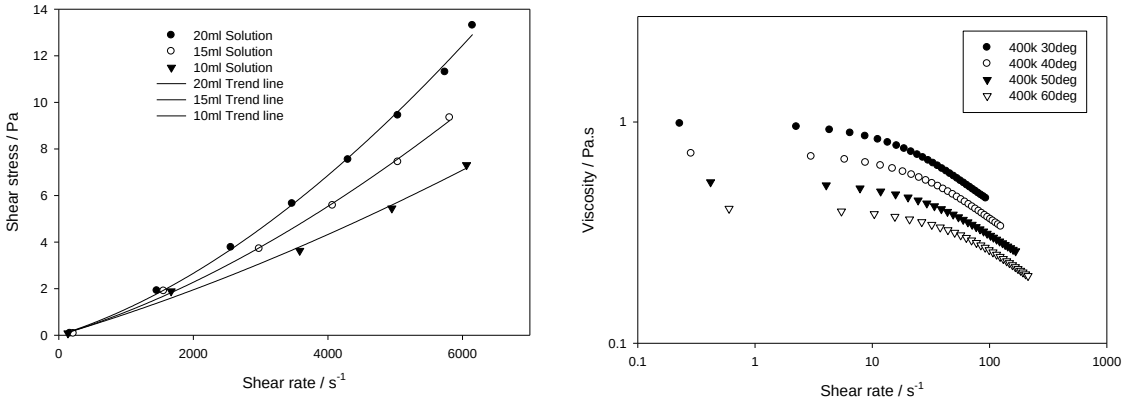

FIGURE 4.1 : Shear stress data obtained for varying volume solutions (left) and viscosity data obtained for varying temperature (right)

4.1.1 Shear rate – Shear Stress

Data collected from the samples show expected shear rate-shear stress curves, with lower percentages of PEO loadings showing an initial linear dependence, before shear thinning occurs. However, data from the lowest loading solutions have emphasised limitations to the rheometry system. Guidelines for the Rheolab equipment state that the maximum shear rate for very high accuracy data is 4000 s^{-1}, however initial experimentation suggested a limitation closer to 5000 s^{-1} before data collection completely failed, all documented in Appendix 3. Guidelines for the Rheolab apparatus express an accuracy of 1% maximum values with shear rates between 1-4000 s^{-1} and shear stresses equally accurate at 0-67 Pa. To maintain reasonable accuracy, any samples where large portions of the required data fall outside of the recommended accurate region were discounted, detailed below.

All A1 solutions (viscosity too low)
All A2 solutions (viscosity too low)
Some B1 solutions (viscosity too low)
All C10 solutions (viscosity too high)

After the first set of three processes described previously, plotting shear stress against shear rate demonstrated the repeatability of the data. Sequential testing, with and without delays, suggested good precision with the majority of variations not

exceeding 3% above or below the absolute value. This repeatability suggests that any history effects that may alter the rheometry data collected are either very small or only take effect after excessive previous testing. Nevertheless, on the first experiment for each set of data the ramp up and ramp down did not overlap, shown in figure 4.2. Ramp down shear stress values were around 8% higher than ramp up values. Similar effects have previously been reported by Daga et. al. [203] when testing laponite filled PEO solutions. They found that the viscosity was observed to be lower when descending from a high shear rate than the viscosity observed when rising from a low shear rate. They deemed this variation as due to a temporary shear re-dispersion within the solution.

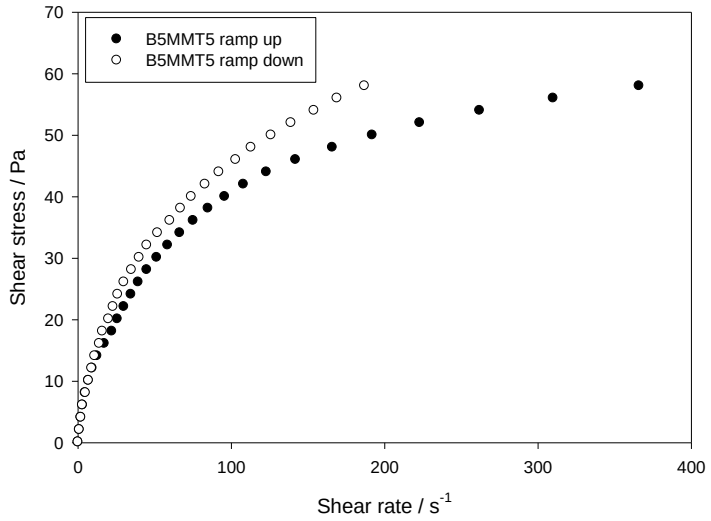

FIGURE 4.2 : Flow curve showing the difference between the ramp up and ramp down of the first run

For this investigation the variation between ramp up and ramp down data was only observed in the first set, with the ramp up data of the next set showing the same values as the ramp down data of the first set, shown in figure 4.3. This suggests that instead of a repeating shear re-dispersion occurring, such as observed by Daga et. al. [203], it is due to the achievement of further dispersion of the system during processes one and two, leading to a maximum level of dispersion for following tests.

Comparison of flow curves from the sets of data collected show that, as predicted, increasing the molecular weight of the PEO increases the viscosity. This is due to the

increased entanglement caused by the presence of longer chains. Comparison of shear rate-shear stress data to some models should allow further analysis and the calculation of viscosity values. The Ostwald de Waele power law, previously used by Rao et. al. [204] and others [205-206], was a good model to start with. Figure 4.4 shows the fit for a higher viscosity sample with MMT filler, and visually the fit appears to be good

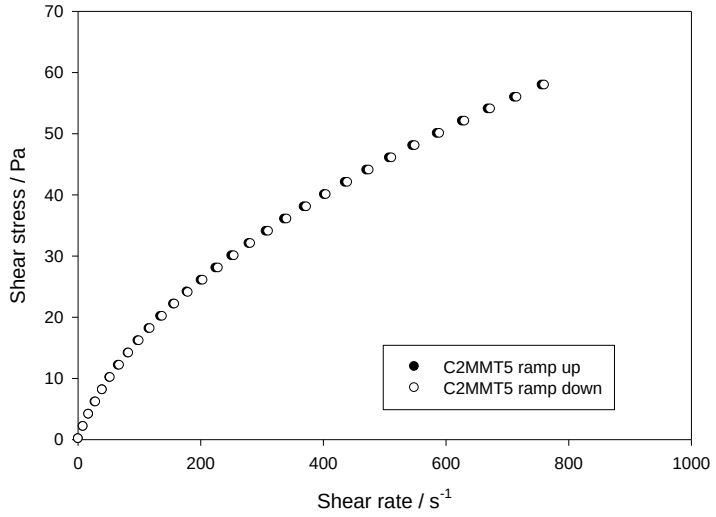

FIGURE 4.3 : Flow curve showing the repeatability of data after the first set of processes are completed

.

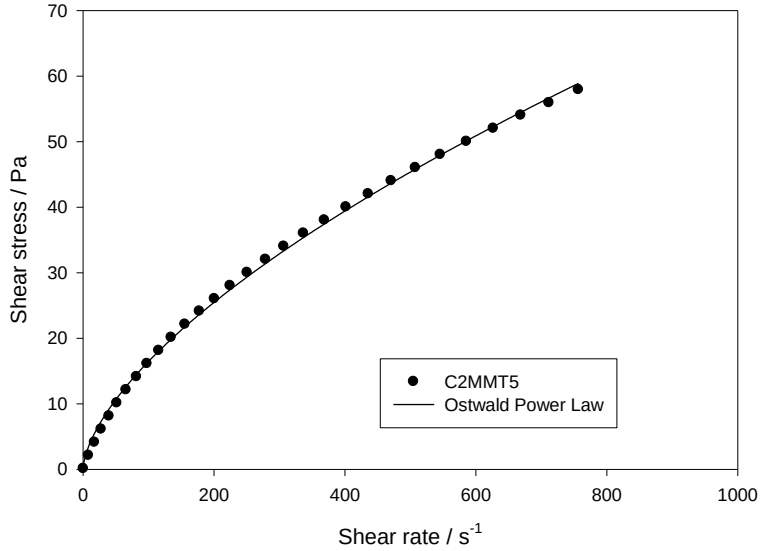

FIGURE 4.4 : A visually good fit to data using an Ostwald de Waele power law

As a method of evaluating the accuracy of the Ostwald de Waele model in representing these data sets, residuals were calculated. A residual, or 'fitting error', is a good estimate of the statistical deviation of experimental data compared to the fitted function value. Therefore by comparing the experimental values obtained against fitted values at the same shear rates, the deviation of the data sets can be analysed. This is a simple method to estimate the accuracy of a fitted function, previously used by authors such as Matheson [71] and Regan et. al. [207] in their NMR experiments. Despite the existence of other residual based accuracy calculation, such as the Godunov finite volume method [208], this simple version appears more appropriate to this function fitting.

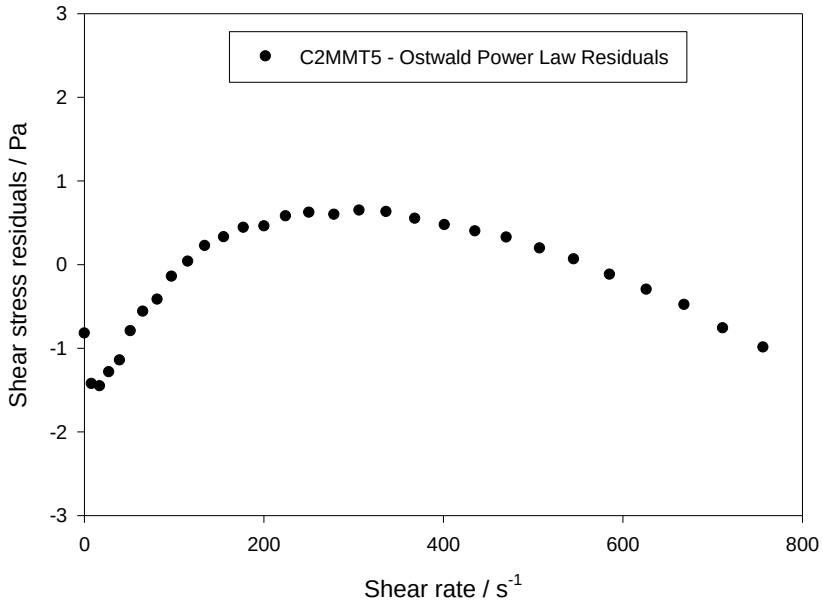

FIGURE 4.5 : Fairly large residuals show the fit to be relatively inaccurate

While the form of the Ostwald de Waele equation broadly matches that of the data, the non-random nature of the residuals indicates that it is not ideal. Previous work into residuals by Langenbach et. al. [209] showed that small, random residuals represent the highest level of accuracy. They also argued that the non-random distribution of residuals highlighted the inadequacies of a single regression equation.

In this investigation the Ostwald de Waele equation showed a better fit for the lower viscosity samples, as was expected after the work by Lewandowska [70]. However the increasing residuals were still fairly large and not randomly distributed. This

prompted the search for a better model, namely a 3 parameter hyperbolic model. This model was visually seen to fit particularly well with all viscosity data samples, as well as providing particularly small residuals, an example fit is shown in figure 4.6 with the associated residuals in figure 4.7. Despite still not being randomly distributed, the residuals from this model are around one fifth those from the Ostwald de Waele fit. Having obtained such an accurate fit with the 3 parameter hyperbolic it was possible to calculate differential viscosity data for all samples, a process described previously.

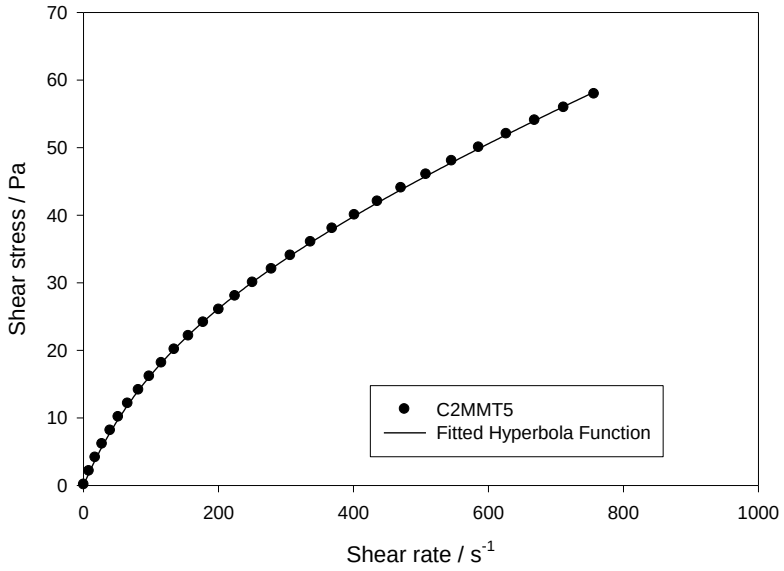

FIGURE 4.6 : Flow curve with a fitted 3 parameter hyperbolic function

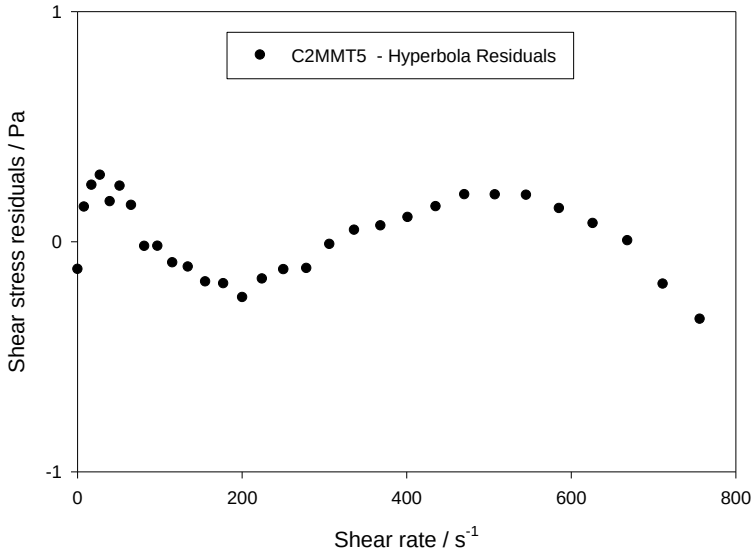

FIGURE 4.7 : Residuals for samples are smaller but still not randomly distributed

4.1.2 Shear rate – Viscosity

Close inspection of the output data from the Rheolab software suggests that the algorithm used to calculate the viscosity is calculating the coefficient of viscosity. Theory dictates that viscosity is defined as the gradient of the shear rate/shear stress curve. Mathematically we can therefore calculate the differential viscosity values, V_d. The software is dividing individual shear stress values by shear rate values to give the coefficient of viscosity, V_c, at each point, shown in equation 4.2. As figure 4.8 shows, this V_c will therefore be identical to the V_d for Newtonian liquids (and near-Newtonian liquids).

$$V_c = \frac{y_1}{x_1}, \frac{y_2}{x_2}, \frac{y_3}{x_3}, \text{etc.} \tag{4.2}$$

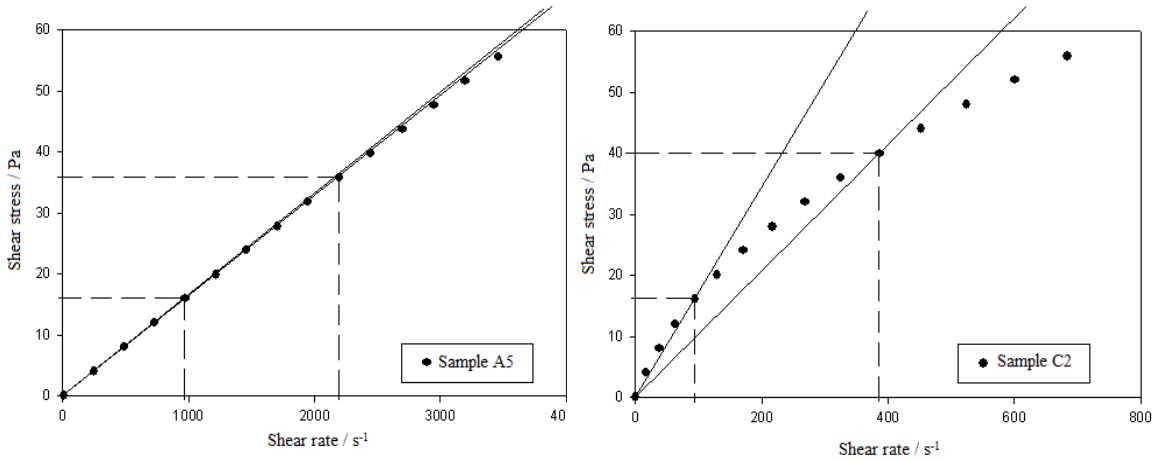

FIGURE 4.8 : Basic gradient calculation gives V_c values similar to V_d values for near-Newtonian liquids (left) but differs for non-Newtonian liquids (right)

By considering the position of the previous data point, a differential viscosity can be calculated, as shown in equation 4.3. Using this technique an accurate differential viscosity for the liquid, at that specific moment, is given. Figure 4.9 shows this, and that this method has an accuracy dependent on the frequency of the data points.

$$V_d = \frac{y_1 - 0}{x_1 - 0}, \frac{y_2 - y_1}{x_2 - x_1}, \frac{y_3 - y_2}{x_3 - x_2}, \text{etc.} \tag{4.3}$$

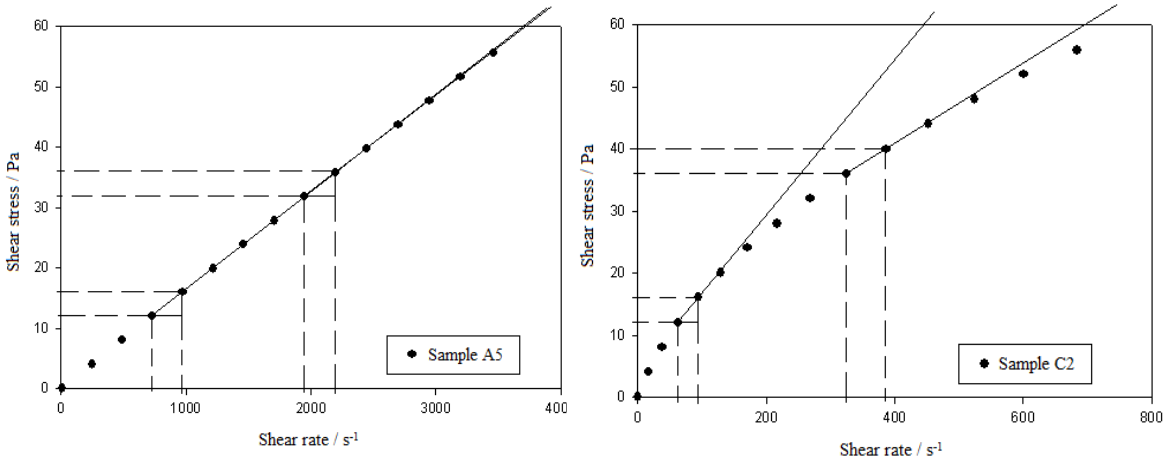

FIGURE 4.9 : By considering the previous data point, differential viscosity data is obtained for both near-newtonian (left) and non-newtonian (right) liquids

Since we are dividing the small change in *y*, (Δy), by the small change in *x*, (Δx), it is possible to use the limiting case, *dy/dx*. Therefore by fitting an accurate function to the shear rate-shear stress data, the 3 parameter hyperbolic, this can be differentiated and the subsequent equation used to generate viscosity data, mentioned in section 2.1.1. Comparing the differential viscosity data, to the software generated coefficient viscosity data, a large discrepancy is clear, depicted in figure 4.10. For this investigation differential viscosity values were used due to the uncertainty in knowing the exact calculation the software was performing.

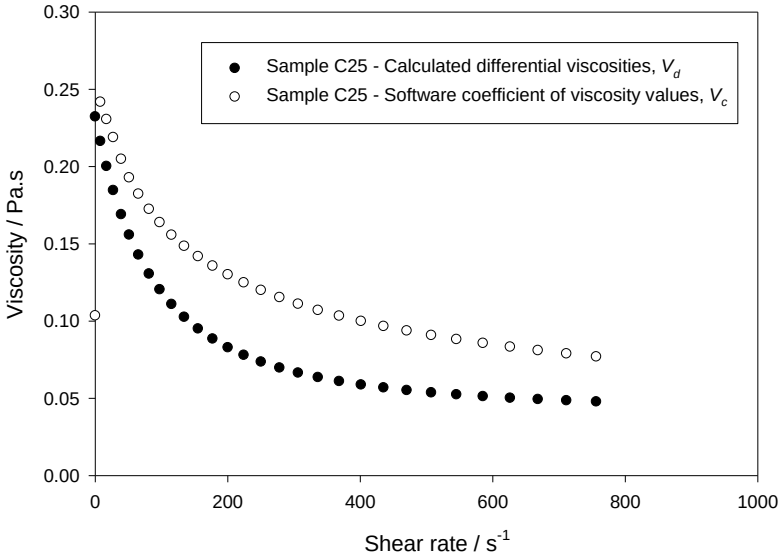

FIGURE 4.10 : A differential viscosity curve compared to the software coefficient viscosity curve. Here, the V_c values are noted to be higher than the V_d values.

With the generated viscosity values it was possible to fit models to the data sets, namely the Carreau and De Kee models. The Carreau model, known for its good reliability for solutions with shear thinning, shown by Franco et. al. [210], should represent high concentration PEO solutions, while its accuracy at low viscosities, hence near-Newtonian liquids, will likely be poor due to the nature of the equation used.

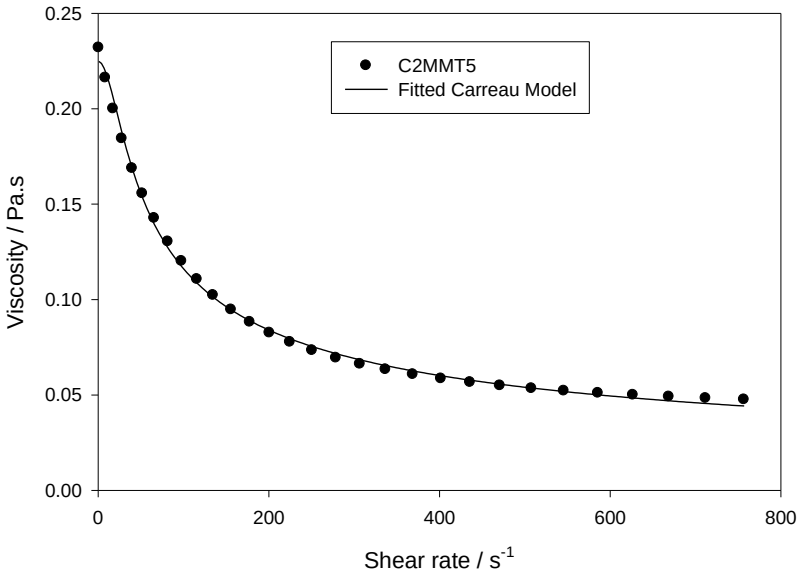

FIGURE 4.11 : A fitted Carreau model for a high viscosity C2MMT5 sample

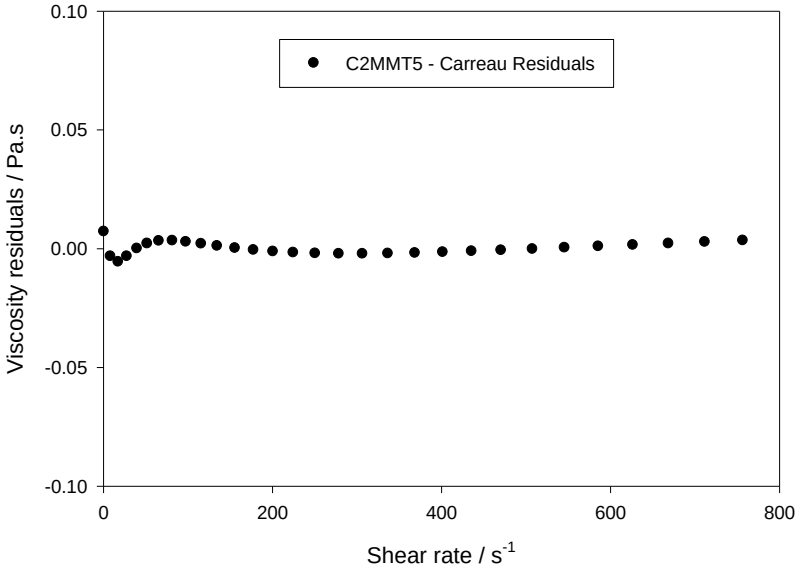

FIGURE 4.12 : The residuals for the Carreau model fit shown in figure 4.11

From figures 4.11 and 4.12 it is clear that the Carreau model does indeed fit accurately for high viscosity samples, producing small residuals. However, for lower viscosities that display less shear thinning, the model fails with some residuals up to 300% higher than the real value. Figures 4.13 and 4.14 show such a failure with a low viscosity sample. In general the Carreau model works well for higher viscosity solutions that display shear thinning, but in order to cover the whole range of viscosity samples, another model is needed.

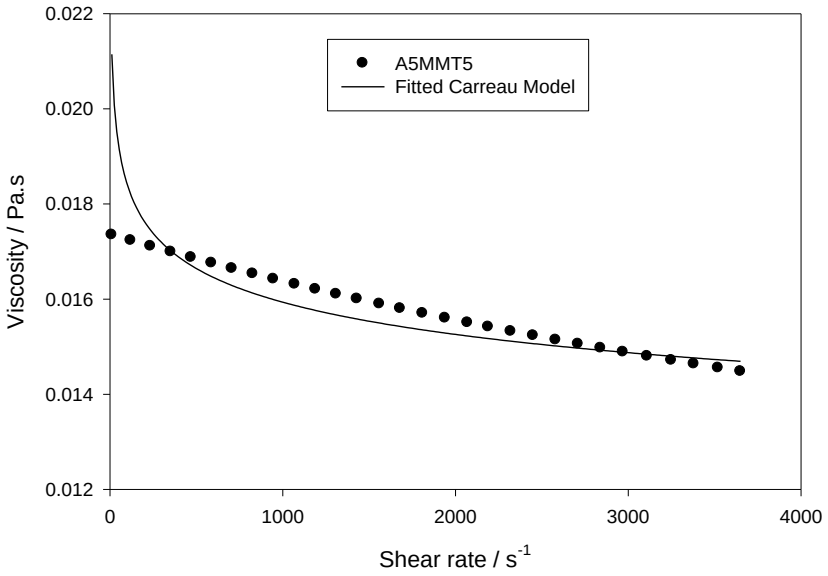

FIGURE 4.13 : The Carreau model fails for low viscosity samples

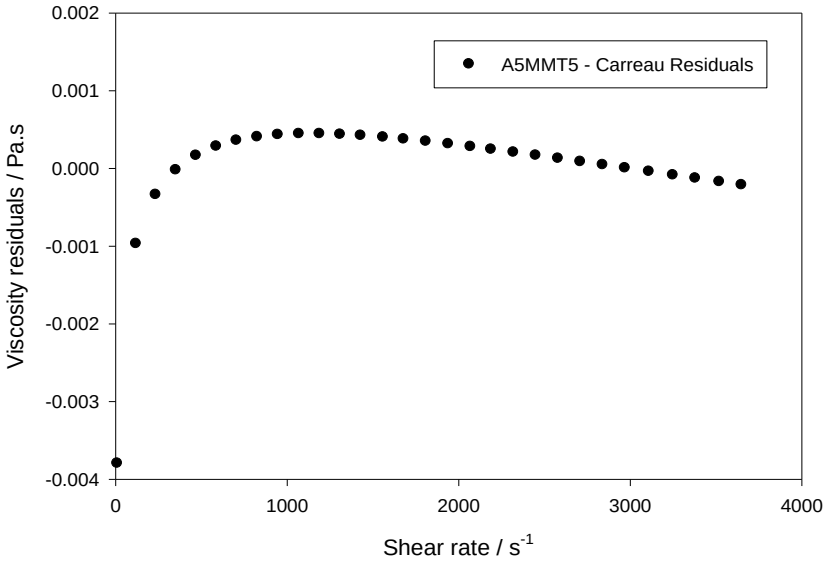

FIGURE 4.14 : The Carreau model residuals are large and non-random

With the Carreau model failing to represent the whole range of viscosities, other models were considered, such as the Bingham, Casson and Herschel-Bulkleythe models [60] before a variation of the De Kee model was applied, and after initial testing it was found to best represent the data. De Kee predicted that the double exponential model would be applicable to a large range of viscosities, such as that covered in this investigation [56,58].

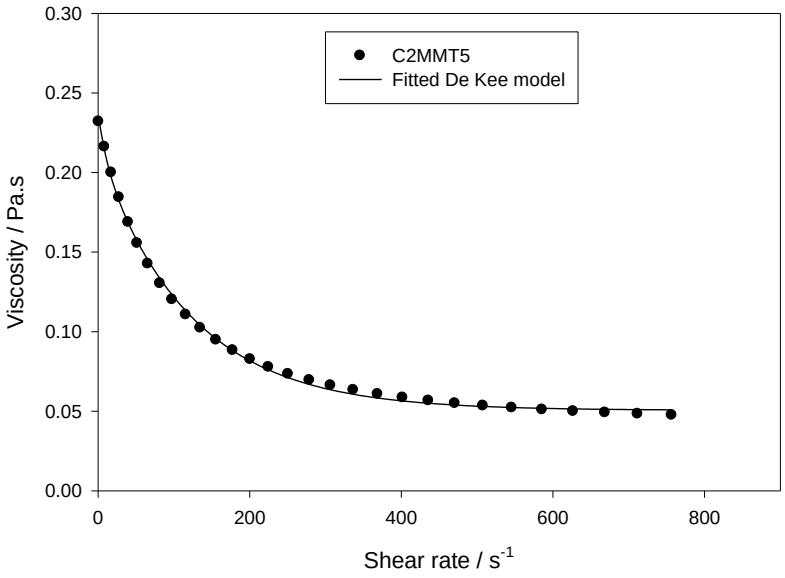

FIGURE 4.15 : A viscosity curve of a highly viscous C2MMT5 sample with a fitted De Kee function

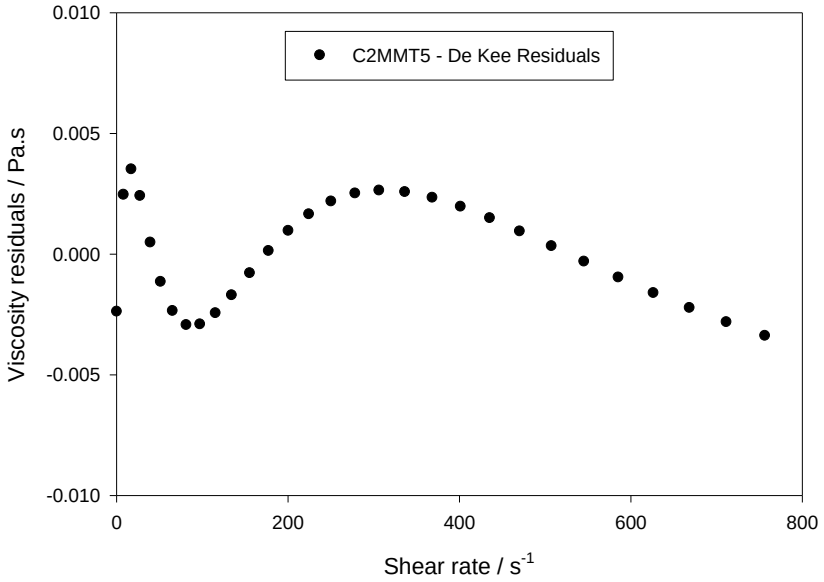

FIGURE 4.16 : The De Kee residuals for the C2MMT5 sample are non-random but relatively small

Figure 4.15 clearly shows that the double exponential De Kee model fits the high viscosity data almost as well as the Carreau model did. Despite the non-random distribution of residuals, shown in figure 4.16, their relatively small size shows an accurate fit. Figures 4.17 and 4.18 show that the De Kee, unlike the Carreau model, also fits for the low viscosity samples, producing exceedingly small residuals.

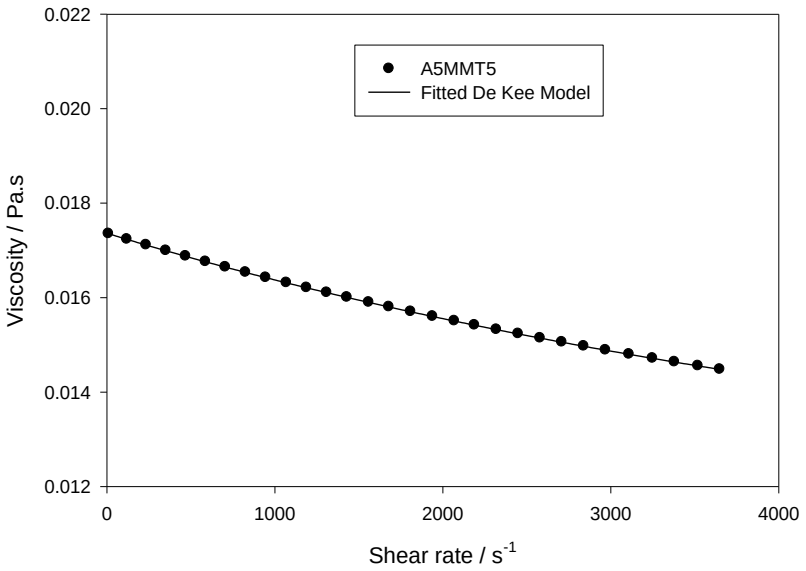

FIGURE 4.17 : A low viscosity A5MMT5 sample with a fitted De Kee model

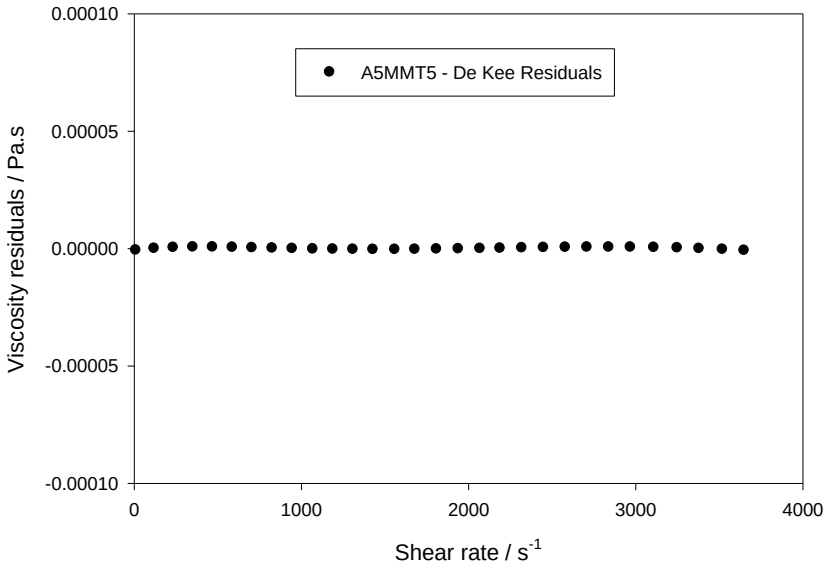

FIGURE 4.18 : The residuals for the De Kee fit shown in figure 4.17 are much smaller than those for the Carreau fit

To better analyse the accuracy of the fits above, fractional residual viscosity values were calculated by dividing the residuals by the viscosity data value. Figures 4.19 and 4.20 below shows the percentage deviation for the Carreau and De Kee fits for a high viscosity sample and a low viscosity sample respectively. It can be concluded that the De Kee and Carreau models are both appropriate at high viscosities but that only the two relaxation functions of the De Kee model are appropriate at low viscosities.

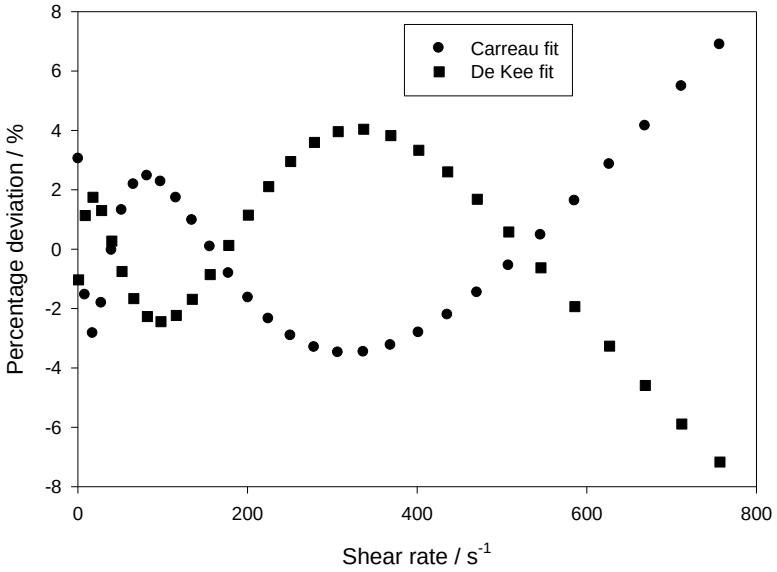

FIGURE 4.19 : Percentage deviation from fitted Carreau and De Kee models for a high viscosity C2 sample

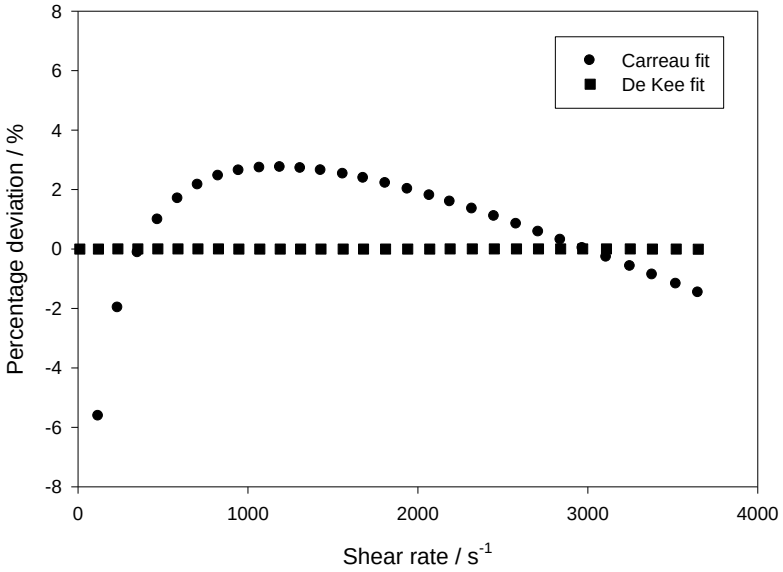

FIGURE 4.20 : Percentage deviation from fitted Carreau and De Kee models for a high viscosity C2 sample

When dealing with the whole range of viscosities it is clear that the double exponential De Kee model is far superior to the Carreau model. Where the Carreau model fails at low viscosities the De Kee model shows excellent correlation with extremely small residuals. The De Kee model also shows slightly lower residuals at high viscosities, where the Carreau model appeared to fit well. It was noted that the De Kee model shows a dependence of the second relaxation function to be $1/10^{th}$ the magnitude of the first. To test this, the second variable dependence on the first was removed. The relaxation times, some shown in table 4.1, were found to differ greatly with this dependence removed, suggesting that De Kee's observation of a $1/10^{th}$ dependence for relaxation times is not suitable for this investigation.

Sample	**T1/T2 Confined**		**T1/T2 Free-fit**		**Difference**	
	T1	T2	T1	T2	T1	T2
A5MMT10	0.00106	0.000106	0.5141	0.00011	0.51304	0.000004
A10MMT10	0.0135	0.001349	1.8117	0.00140	1.7982	0.000051
B5MMT5	0.0518	0.005179	0.0743	0.0236	0.0225	0.018421
B2MMT10	0.0103	0.001028	0.4809	0.00108	0.4706	0.000052
B10MMT5	0.0493	0.004926	0.0695	0.0180	0.0202	0.013074
C2MMT5	0.0136	0.001356	0.0193	0.00543	0.0057	0.004074
C5MMT5	0.3313	0.0331	0.4680	0.1285	0.1367	0.0954

TABLE 4.1 : De Kee confined and free fit parameters

4.1.3 Single molecular weight PEO solutions

The shear rate-shear stress data obtained for single molecular weight PEO are shown in figures 4.21-4.23. They clearly show that increasing molecular weight, hence chain length, increases the viscosity. This is due to the mobility within the system being hindered by entanglement and chain interactions. Also, increasing the amount of PEO within the system is seen to increase the gradient, hence viscosity, of the solutions as expected. Interestingly, two solutions were found to have similar flow curves: the A5 and B2 samples.

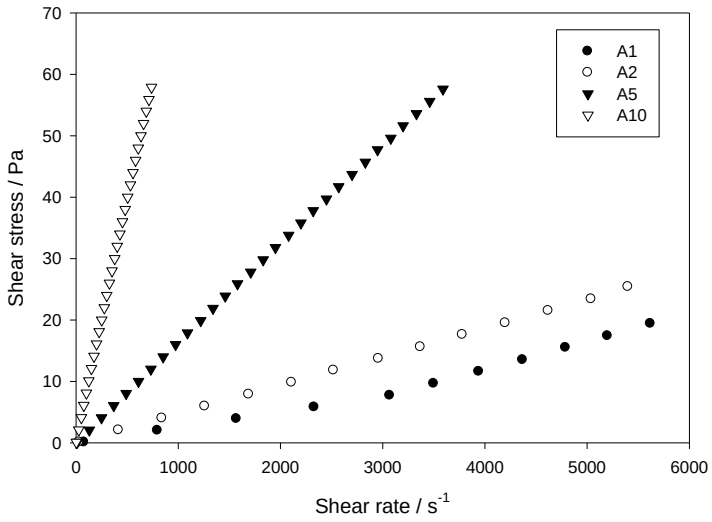

FIGURE 4.21 : The shear rate – shear stress data for 100k PEO solutions

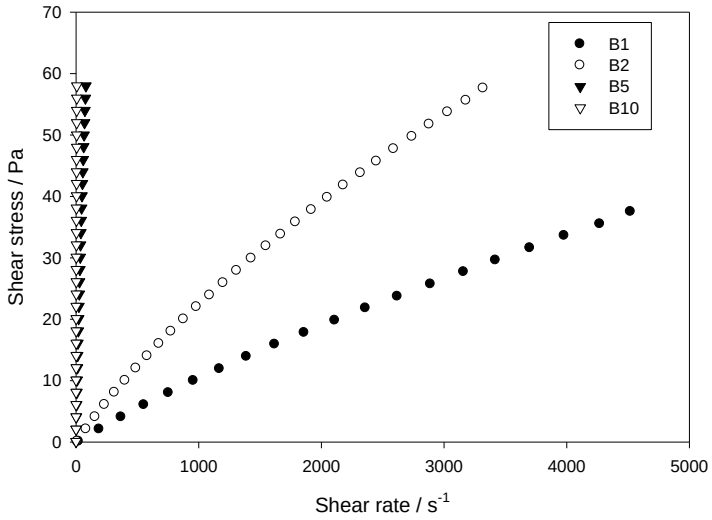

FIGURE 4.22 : The shear rate – shear stress data for 400k PEO solutions

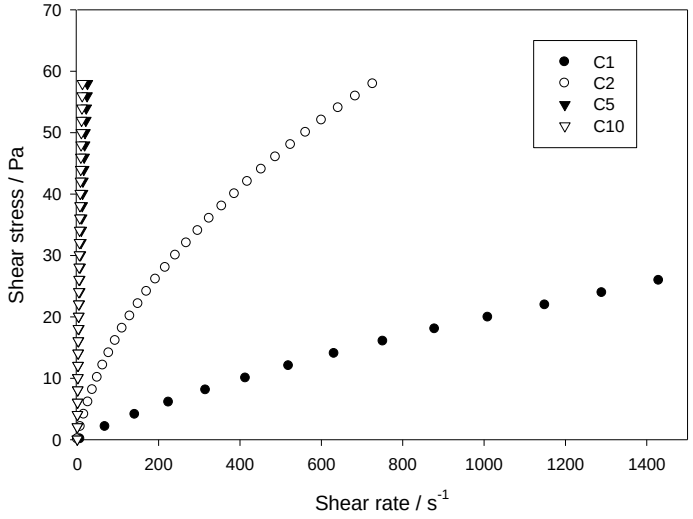

FIGURE 4.23 : The shear rate – shear stress data for 1M PEO solutions

As a method to understand better the viscosity of the single molecular weight PEO's the peak shear rate, that is the shear rate relating to a shear stress of 60 Pa, can be taken as a single figure, and compared to the same value for other samples. Figure 4.24 shows the peak shear rates of the PEO samples in decreasing order of viscosity. This method is capable of ordering the samples by viscosity without the need for actually calculating viscosity values. By calculating viscosity data from the shear rate-shear stress data however, produces full viscosity curves that include shape variation between samples, not just the magnitude. Figures 4.25-4.26 show the viscosity plots for single molecular weight PEO samples.

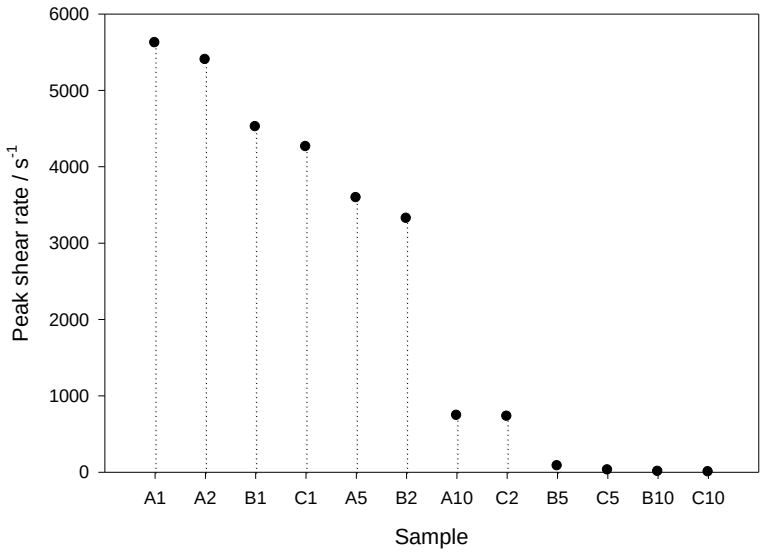

FIGURE 4.24 : Peak shear rates of samples at 60 Pa shear stress in decreasing viscosity, allowing for comparison across molecular weights

The viscosity values for the virgin PEO solutions show that increasing molecular weight and concentration decreases the mobility within the system. In order to analyse the effect that addition of fillers has, the same rheology experiments were performed on samples containing MMT, SD, nSD and BO. Comparing the graphs generated for composites with those for the virgin PEO systems, any effects on mobility and chain interactions within the system can then be analysed.

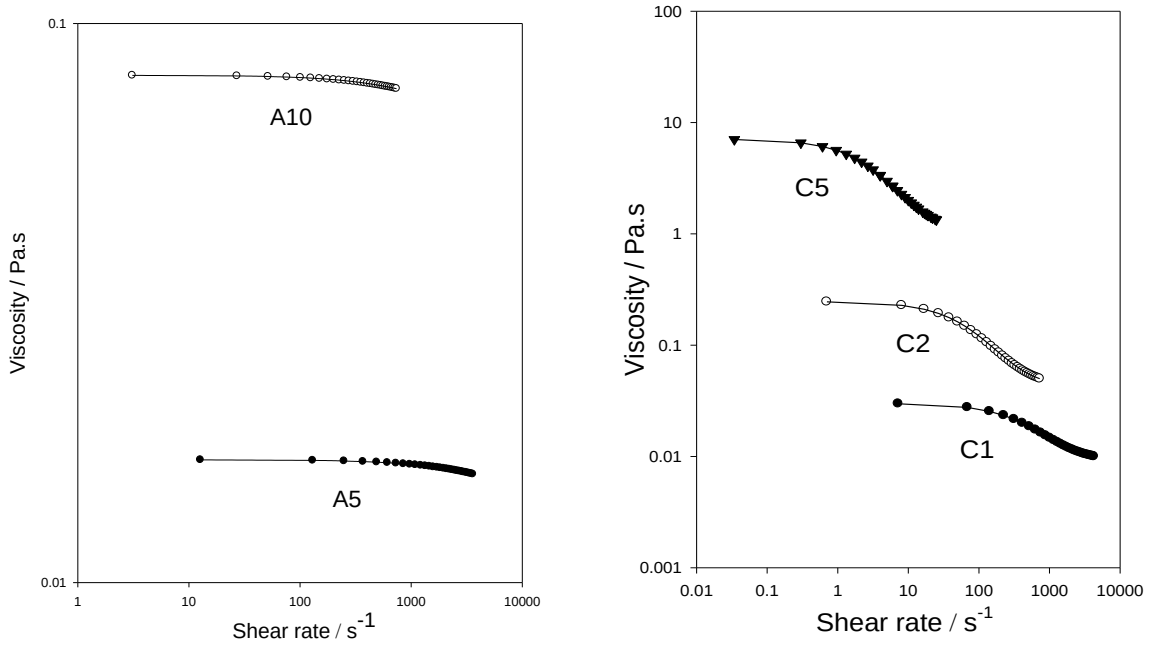

FIGURE 4.25 : Viscosity curves for 5 and 10 PPHW 100k PEO samples (left) and 1, 2 and 5 PPHW 1M PEO samples (right) with fitted De Kee lines

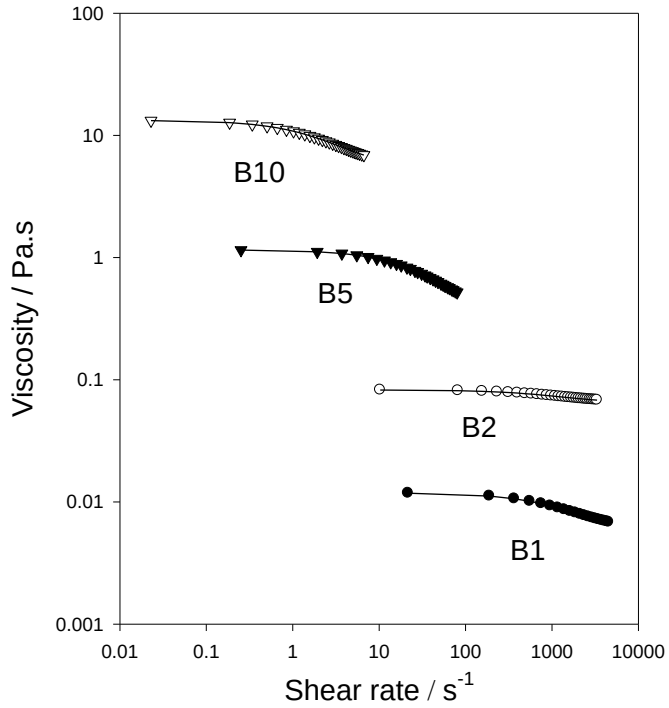

FIGURE 4.26 : The shear rate – viscosity data for 1, 2, 5 and 10 PPHW 400k PEO samples with fitted De Kee lines

4.1.4 Multiple molecular weight PEO blends

One of the major benefits of using PEO is the wide range of available molecular weights, between 200 $gmol^{-1}$ and 8,000,000 $gmol^{-1}$ (although under 100,000 $gmol^{-1}$ it is known as polyethylene glycol, PEG). Therefore testing blends of varying molecular weights might give an insight into the physical flow property dependence of chain length distribution. Along with the previously used 100,000 $gmol^{-1}$, 400,000 $gmol^{-1}$, 1,000,000 $gmol^{-1}$ (100k, 400k and 1M), 20,000 $gmol^{-1}$ and 4,000,000 $gmol^{-1}$ were also used for this part of the investigation. All samples were produced with a total PEO weight-weight ratio to water of 5% and the following blends were mixed;

- 20k with 400k – Particularly short chains with medium length chains
- 100k with 1M – Shorter than average chains with longer than average chains
- 20k with 4M – Particularly short chains with very long chains
- 100k with 400k with 1M – Average chains with slightly shorter and longer chains
- 20k with 100k with 400k with 1M with 4M – Particularly short chains with below average/average/above average and very long chains

It was generally expected that as the ratio of the solution tended towards one of the molecular weights present that the shear rate-shear stress data would also tend towards the behaviour of that molecular weight. Figures 4.27 and 4.28 show that for the 100k-1M and 400k-20k blends, this was indeed the case. However to analyse the transition between the two molecular weight behaviours, viscosity data were calculated as explained previously. The viscosity curves for the 100k-1M and 400k-20k blends are shown in figures 4.29 and 4.30. From these it is clear that the move from one molecular weight to the other has no sudden changes in viscosity, instead representing a smooth transition.

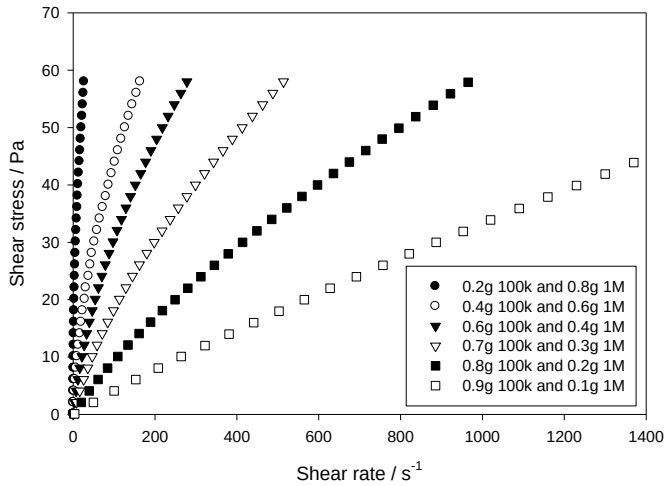

FIGURE 4.27 : Shear rate-shear stress data for the 100k and 1M blend

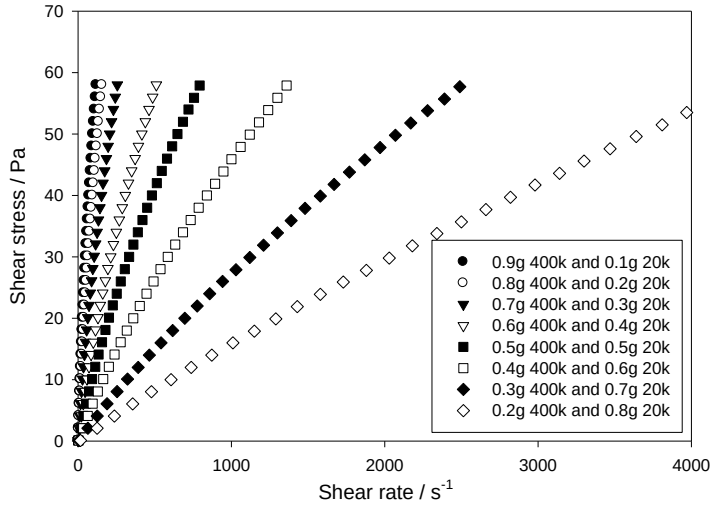

FIGURE 4.28 : Shear rate-shear stress data for the 400k and 20k blend

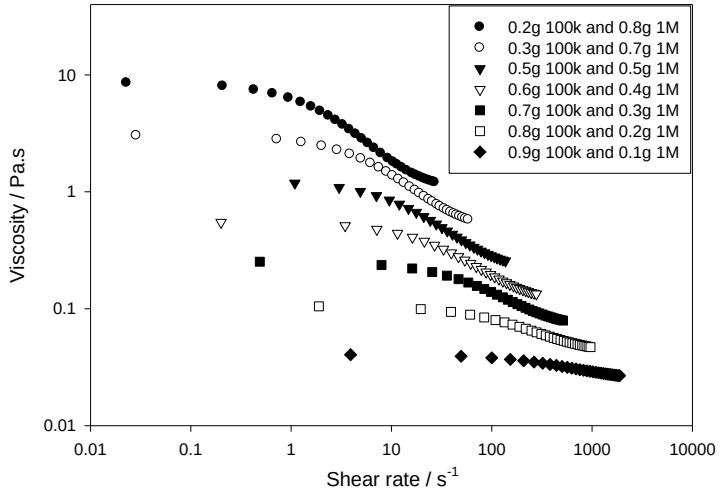

FIGURE 4.29 : Shear rate-viscosity data for the 100k and 1M blend

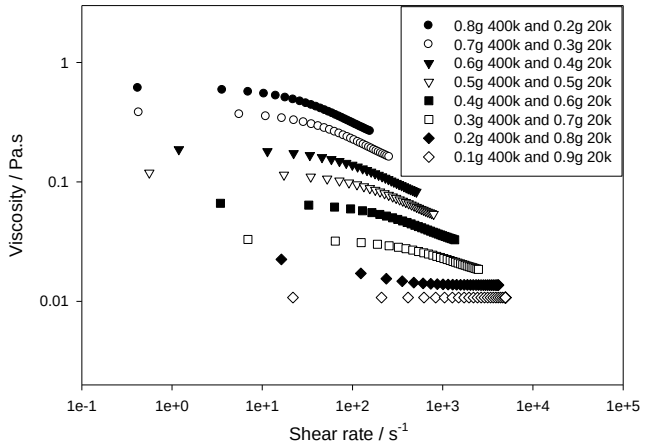

FIGURE 4.30 : Shear rate-viscosity data for the 400k and 20k blend

Previous work into observing the viscosity dependence on molecular weight has found that two regimes exist dependent on the concentration of the system [49]. These two regimes are shown in figure 4.31 below, based upon the figures found at [49], and the point at which they meet is referred to as the entanglement limit. Here regime 1 represents dilute systems and regime 2 represents concentrated ones. Analysis of the viscosity behaviour of equivalent single component systems suggests that, in the low shear rate limit, the viscosity η_0 varies with the quoted molar mass, M, according to equation 4.4, which is a form of the Mark-Houwink-Sakurada equation (MHS), equation 4.5.

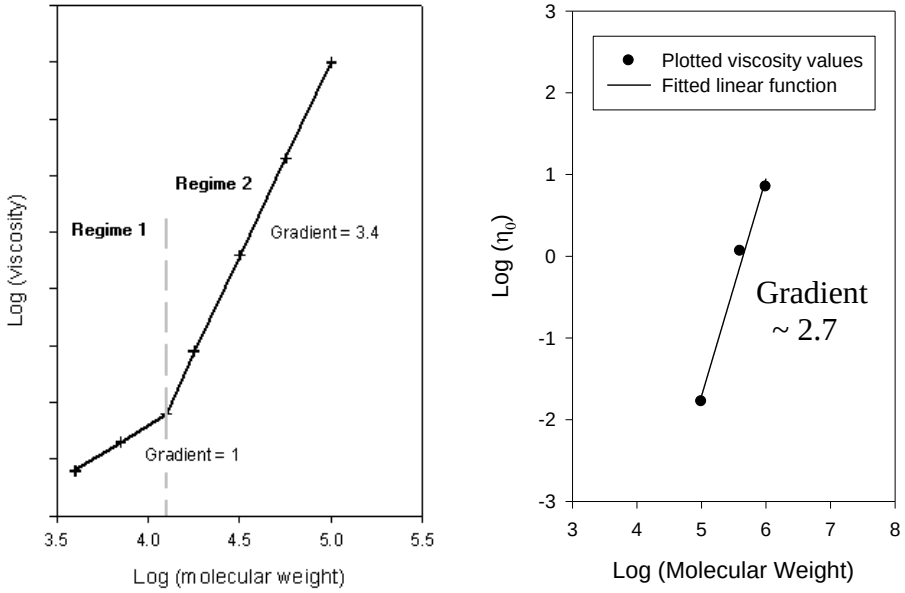

FIGURE 4.31 : Viscosity as a function of molecular weight, based upon [49] (Left) and plotted data from this investigation showing a gradient of 2.7 (Right)

$$\eta_0 \propto M^{2.7} \tag{4.4}$$

$$[\eta] = KM^{\alpha} \tag{4.5}$$

Here, η_0 and $[\eta]$ are both deemed to be the viscosity at a zero shear rate, M is the molar mass, K is an unknown and α is a parameter related to the size of the polymer coil in solution.

This value of 2.7 suggests a fairly concentrated system when compared to literature [49]. This relationship works well and can be applied for single molecular weight systems, however to test this for the blended samples an average molecular number or weight is needed. The number average molar mass for n molecules with molar mass M_i is shown in equation 4.6. Similarly the weight average molecular weight is shown in equation 4.7, where w_i is the fraction by weight of molecules having a molar mass M_i.

$$\overline{M}_n = \frac{\sum n_i M_i}{\sum M_i} \tag{4.6}$$

$$\overline{M}_w = \frac{\sum w_i M_i}{\sum w_i} \tag{4.7}$$

For the more complex blends, such as those with viscosity curves shown in figure 4.30, it is possible to infer effective average molar masses for each blend, and hence calculate values of the a parameter with equation 4.8.

$$\overline{M}_a = \left[\frac{\sum_{i=1}^{i=n} M_i^{1+a} N_i}{\sum_{i=1}^{i=n} M_i N_i} \right]^{1/a} \tag{4.8}$$

Here $\overline{M}_a$ is interpreted as the viscosity average molar mass, *a* conforms to the exponent in the MHS equation which, for the PEO water system, is reported to be ~0.8 [211]. Therefore, values of *a* close to 1 equate to values of $\overline{M}_a$ and are comparable to the number average molar mass of the system, while values close to 1/2 are comparable to the mass average molar mass. Using this approach experimentally derived *a* values were found to vary from 0.2 for the 20k-4M blend, through to 0.45 for the 20k-100k-400k-1M-4M blend, and 0.7 for the 100k-400k-1M system. The physical interpretation of these values are that the rheological behaviour of the 100k-400k-1M blend is characteristic of a system whose molar mass is close to the anticipated viscosity average molar mass of a system with a MHS *a* exponent of 0.7; that is, a value comparable to published values for the PEO/water system. This is despite this investigation involving materials that exist above the entanglement threshold and the strict inapplicability of MHS theory to such systems, the reasoning behind the values for the other two blends not being physically reasonable.

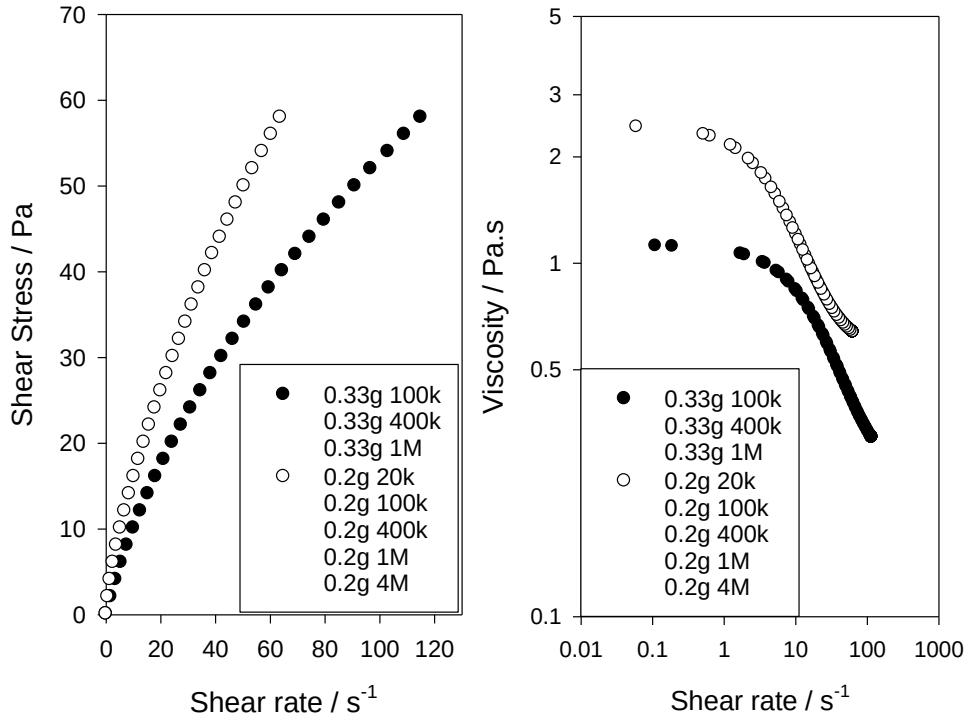

FIGURE 4.32 : Shear rate-shear stress curves (left) and shear rate-viscosity curves (right) for the 100k-400k-1M and 20k-100k-400k-1M-4M blends

4.2 Differential Scanning Calorimetry

After calibration, values of T_c and T_m were recorded for unfilled PEO samples, shown in figure 4.33. The transition temperatures do not appear to follow an obvious trend with increasing molecular weight. The T_g of polymers is said to be highly dependent on molecular weight [212-213], whereas the melting and crystallisation transitions dependence on molecular weight is less clear. At higher chain lengths it has been seen in polymers, such as poly(trans-1,4-isoprene and poly(3,3'-diethyl oxetane), the growth rate is essentially independent of chain length [214]. For PEO the T_m has been observed to increase from 51 ^{0}C to 64 ^{0}C when increasing the molecular weight 1500 – 300000 [215]. From this it was expected that the thermal transitions would increase with higher molecular weights. However, it was observed using the method outlined in figure 4.33, that the 100k samples had the lowest transitions and 400k had the highest.

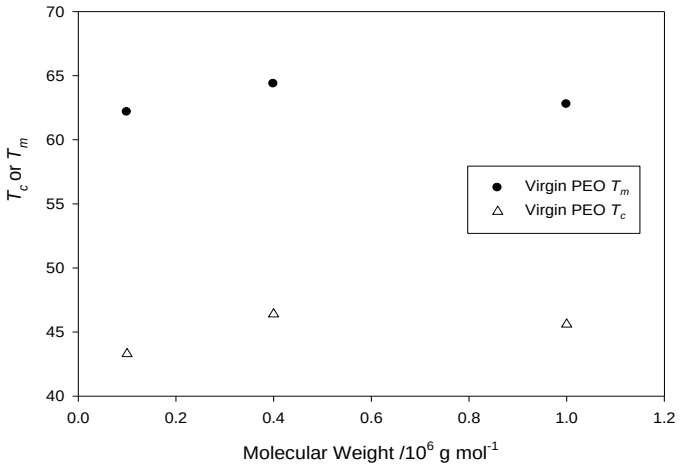

Experiment Settings	
Type of scan	Non-isothermal
Scan settings for T_c	80-20 ^{0}C at 10 ^{0}C/min
Scan settings for T_m	20-80 ^{0}C at 10 ^{0}C/min

FIGURE 4.33 : Transition temperatures, T_m and T_c in ^{0}C for unfilled PEO samples

This suggests that increasing the molecular weight from 100k to 400k has increased the transition temperatures, however since the 1M PEO does not exhibit an increase in transition temperatures that this is possibly due to the nucleation density or the growth rate being independent of chain length at such a high molecular weight [214]. Since all three molecular weight samples have approximately the same thermal transition temperatures, it was not deemed beneficial to test any copolymer blends.

Having collected curves for the melting and crystallisation of the polymer samples with varying T_c it was possible to evaluate the associated $\Delta H_c'$ and $\Delta H_m'$ by calculating the area under the heat flow curves. This provides the raw data, however they must be corrected to take into account the fraction of polymer present in the material and the weight of the sample, shown in equation 4.9. Therefore the $\Delta H_c'$ and $\Delta H_m'$ values for the 25 PPHP filled systems, which contain a polymer to filler weight ratio of 4:1, were divided by 0.8 to represent only the polymer crystallising within the system. These corrected values are referred to as ΔH_c and ΔH_m. Using the same logic, the $\Delta H_c'$ and $\Delta H_m'$ values for the 50 PPHP filled systems, with a polymer to filler ratio of 2:1, were divided by 0.66 while the 100 PPHP filled systems, with a ratio of 1:1, were divided by 0.5. A further correction is then applied when samples differ in mass to give ΔH_c and ΔH_m values per gram. The unfilled PEO and thermally aged PEO samples require no correction since 100% of the material is deemed to be polymer.

$$\Delta H_m = \frac{\Delta H_m'}{mf} \qquad \Delta H_c = \frac{\Delta H_c'}{mf} \tag{4.9}$$

Here, $\Delta H_c'$ and $\Delta H_m'$ are the raw data values, ΔH_c and ΔH_m are the corrected values, f is the fraction of polymer (ie. 0.8, 0.66 or 0.5) and m is the mass of the sample. It should be noted that ΔH_m should always be greater or equal to ΔH_c since the amount of crystals being melted cannot be less than the amount of crystals that were formed. Using equation 4.10 below it is possible to calculate crystallinity values, χ_c, where ΔH_{fus} is the heat of fusion of 100% perfectly crystallised PEO, taken as 216 Jg^{-1} for this investigation [216-217].

$$\chi_c = \frac{\Delta H_m}{\Delta H_{fus}} \tag{4.10}$$

Crystallinity values for the 100k, 400k and 1M samples were calculated to be 84.7, 73.4 and 66.9 % with errors of ± 5, ± 3 and ± 3 respectively. These values appear reasonable when compared to literature, with previous values of 78 % ± 5 for 180,000 $gmol^{-1}$ [218] and 74 % for 1,000,000 $gmol^{-1}$ [219]. The trend of increasing crystallinity with lower molecular weight is understandable since the smaller chains

would be able to crystallise more easily on kinetic grounds. Figures 4.34-4.35 below show the ΔH_m and ΔH_c values for the unfilled PEO systems as a function of T_c, showing that the 100k PEO sample has the largest, followed by 400k then 1M. This also confirms that the 100k has the highest crystallinity.

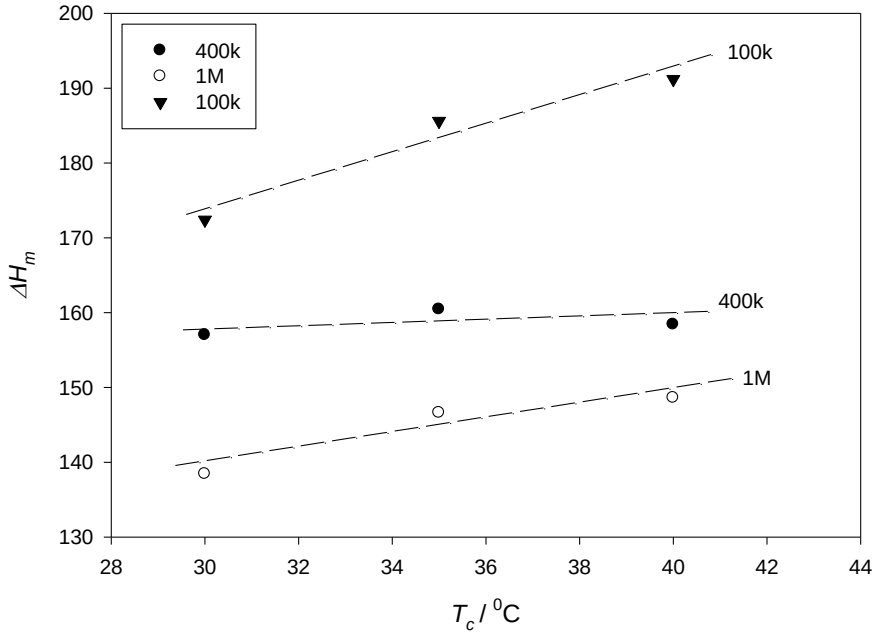

FIGURE 4.34 : ΔH_m values for unfilled PEO samples

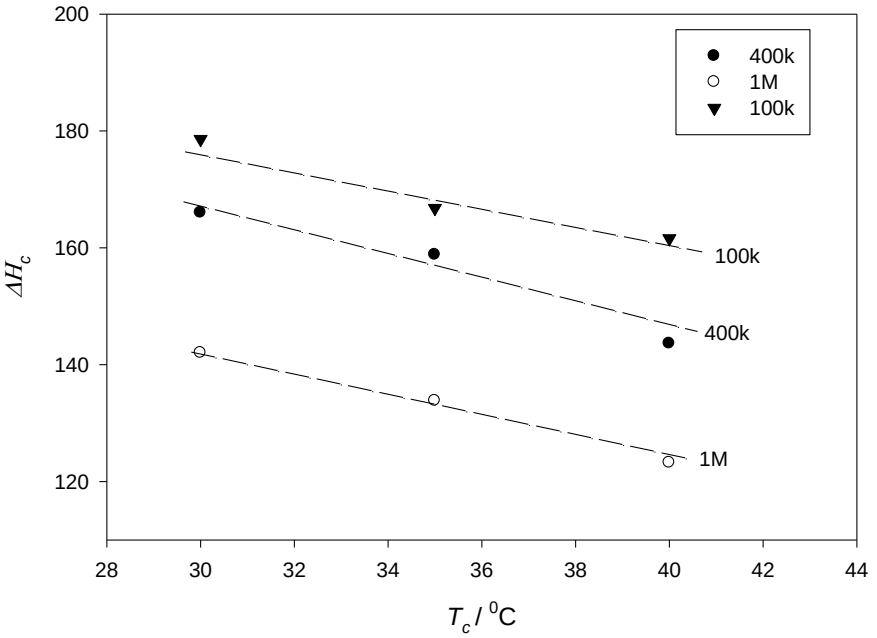

FIGURE 4.35 : ΔH_c values for unfilled PEO samples

4.2.1 Avrami analysis

With isothermal crystallisation curves for all molecular weight PEO samples it was possible using the method detailed in section 3.5 to generate curves, such as those shown in figure 4.36 below. These figures show data collected for the 100k and 400k PEO molecular weights with varying T_c from 30-40 ^{0}C. Fitting the Avrami equation to these data produced an accurate fit and generated *n*, *k* and *T* values, shown in table 4.2. The data can also be represented as a constant crystallisation temperature while observing different samples, shown in figure 4.37, with the onset of crystallisation varying with molecular weight From this it is clear that the 400k sample requires less time to crystallise, followed by the 1M, with the 100k taking the longest to crystallise. This is noted to be the same molecular weight order observed in the non-isothermal DSC tests.

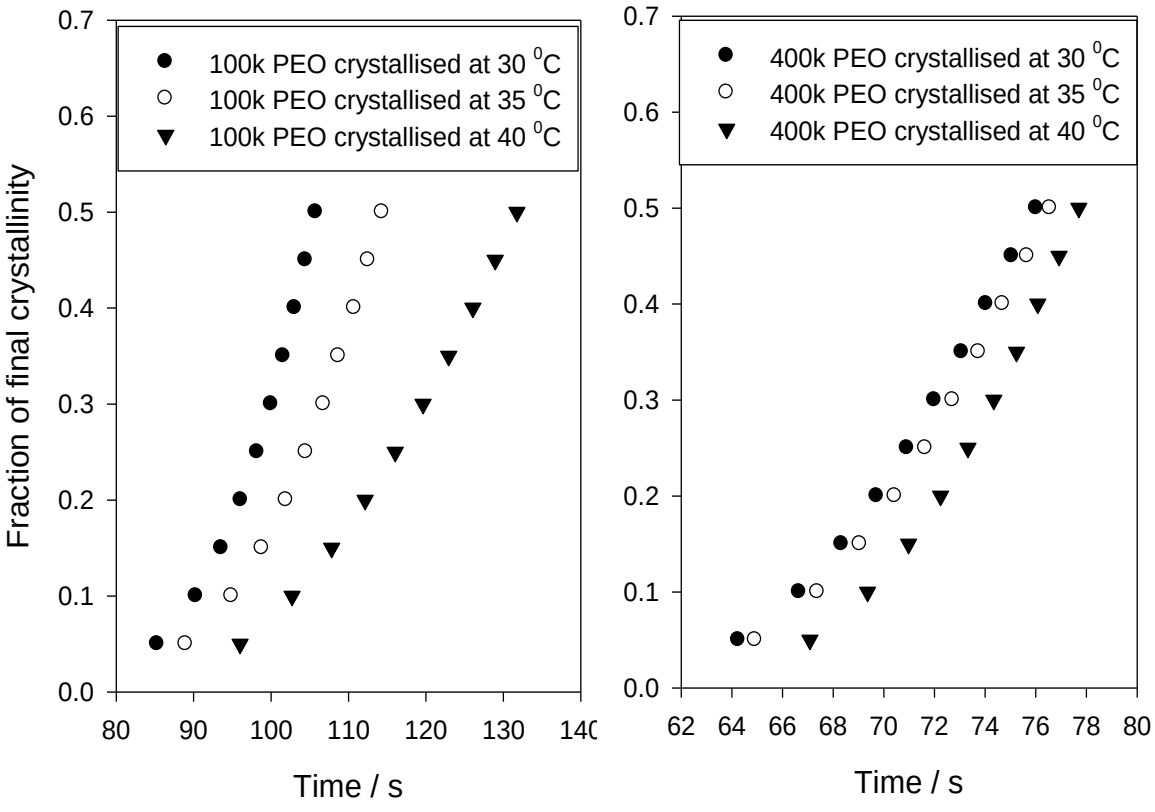

FIGURE 4.36 : Crystallisation data collected for the 100k PEO (left) and 400k PEO (right) samples

Sample	T_c / ^{0}C	Avrami parameters			
		n	k (s^{-1})	R^2	K_3
100k PEO	30	4.575	1.83×10^{-8}	0.9990	8.44×10^{-6}
100k PEO	35	4.304	2.32×10^{-8}	0.9997	4.77×10^{-6}
100k PEO	40	3.098	1.76×10^{-8}	0.9998	2.67×10^{-6}
400k PEO	30	4.127	7.01×10^{-5}	0.9999	8.28×10^{-5}
400k PEO	35	3.455	1.62×10^{-5}	0.9999	6.92×10^{-5}
400k PEO	40	3.053	1.74×10^{-6}	0.9999	6.51×10^{-5}
1M PEO	30	4.58	1.35×10^{-8}	0.9966	7.02×10^{-6}
1M PEO	35	4.011	1.20×10^{-7}	0.9998	6.65×10^{-6}
1M PEO	40	2.328	1.21×10^{-5}	0.9994	4.59×10^{-7}

TABLE 4.2 : The Avrami parameters generated for the unfilled PEO

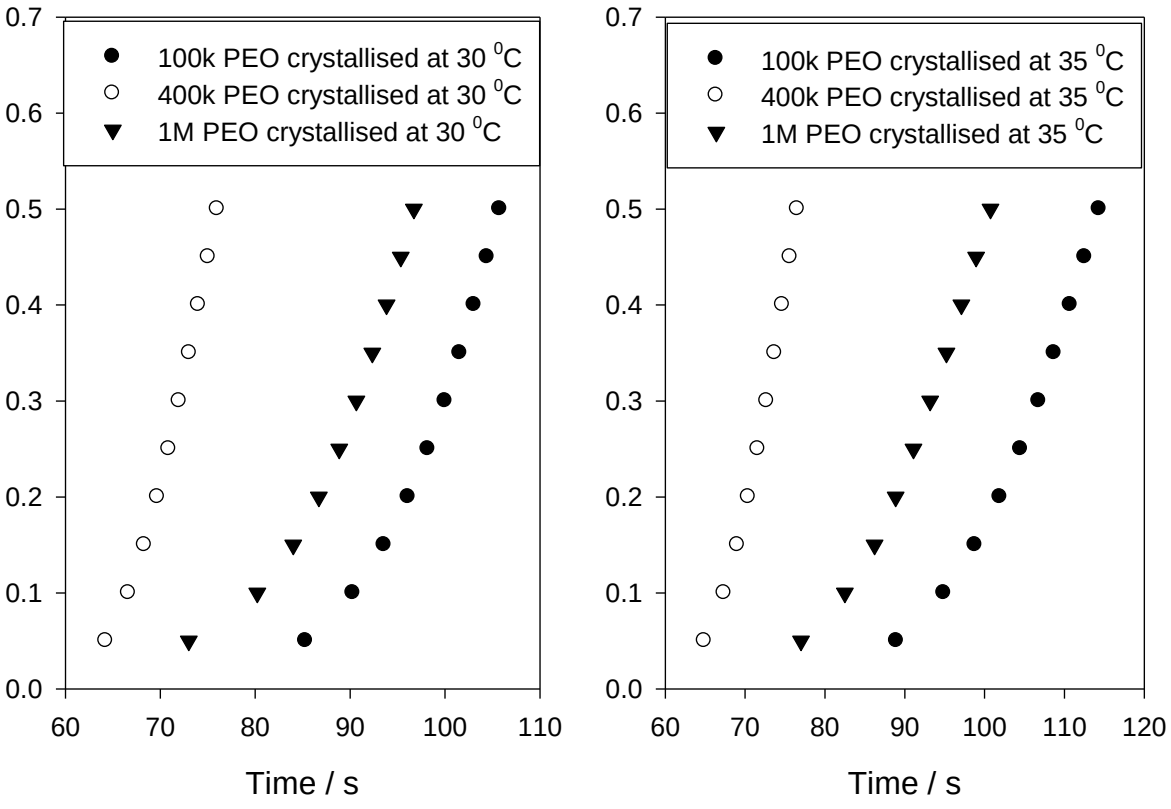

FIGURE 4.37 : Avrami curves for the three molecular weight PEO samples all crystallised at 30 ^{0}C (left) and 35 ^{0}C (right)

Table 4.2 shows the calculated Avrami *n* and *k* values for the PEO samples, along with the R^2 value, which provides an evaluation of the accuracy of the values to fitting the experimental data. The *n* parameter is said to represent the nucleation and dimension of the forming crystals, covered in section 2.2.3, therefore the data here suggests that as T_c increases the growth and nucleation of the polymer are being affected, resulting in a decrease in Avrami *n* value [220]. Varying the molecular weight of the PEO appears to have little effect on the *n* value, as could be expected from previous investigations, such as Imai et. al. [221].

As mentioned in section 2.2.3, the Avrami *k* value cannot be compared across samples (its units are min^{-n}), therefore using equation 2.14, K_3 values were calculated for all samples. The K_3 values represent the nucleation and mobility within the systems and appear slightly higher for the 400k than those for the 100k and 1M. In general though, the K_3 values all decrease with increasing T_c. This is expected since the *n* values were seen to decrease with increasing T_c, an effect seen previously [222]. The *n* values are noted to deviate from the theoretical 3-4 values for spherulitic crystallisation.

Figure 4.38 shows the calculation of T_m^0 values for the 100k, 400k and 1M PEO samples using the theory from section 2.2.3. The intercepts are shown to be 61.6 ^{0}C, 60.9 ^{0}C and 58.4 ^{0}C respectively. The extrapolation may be of questionable accuracy due to a limited data range, therefore a second method of calculating T_m^0 along with the associated errors was used, details of which are in Appendix 6. Table 4.3 shows the corresponding values and errors associated. Beech et. al. [223] define the T_m^0 as "the melting point of a perfect crystal of infinite dimensions composed of polymer of infinite chain length" and discuss the thermodynamic melting point in detail. They summarise the values from several authors and find the average to be 69 ^{0}C for low molecular weight PEO.

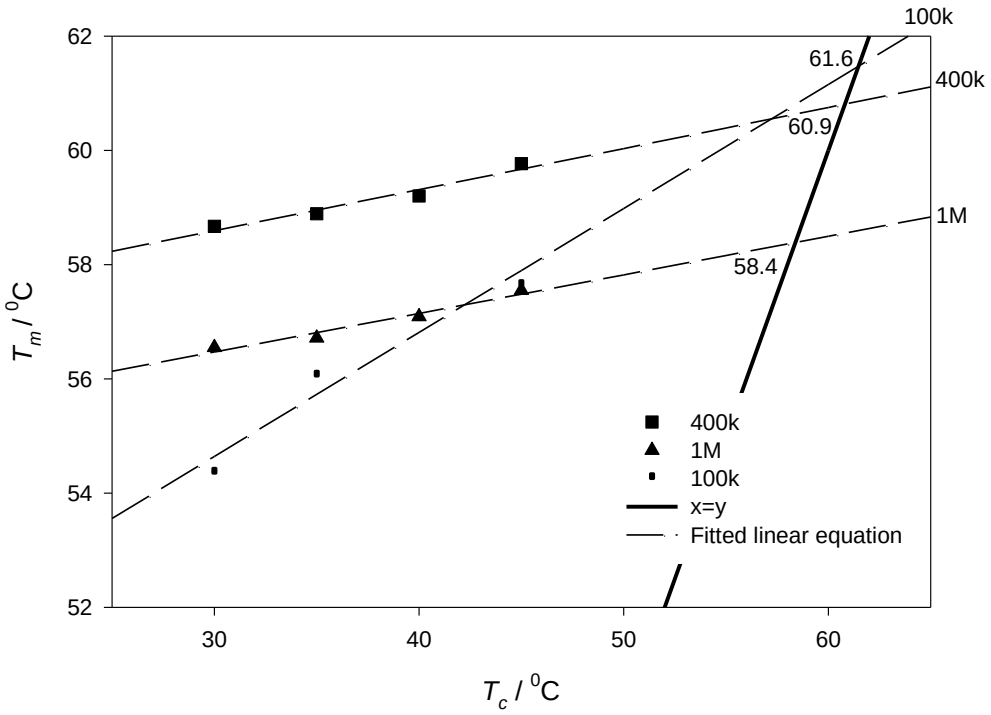

FIGURE 4.38 : T_c vs T_m plots for the unfilled PEO systems along with the T_c=T_m intercept values in ^{0}C

Sample	T_m^0 / ^{0}C	
	T_m vs T_c	**T_c vs T_m-T_c**
100k	61.6	61.4 ± 1.2
400k	60.9	60.8 ± 1.2
1M	58.4	58.4 ± 1.0

TABLE 4.3 : T_m^0 values using both methods with the associated error

Comparing these values to those collected by Beech et. al. [223], it appears that these values are around 8 ^{0}C lower. Work by Broadhurst [224-225] into normal-paraffins has shown a relationship between T_m^0 and molecular weight, shown in equation 4.11, where n is the number of carbon atoms per molecule, T_m is the melting temperature and a and b are constants. This equation fits data such as those collected by Imai et. al. [221] for low molecular weight PEO samples, shown in figure 4.39. Since these data are approximately 8 ^{0}C lower and also show the opposite trend to the data collected by Imai et. al. [221] this suggests that the extrapolation method could be at fault.

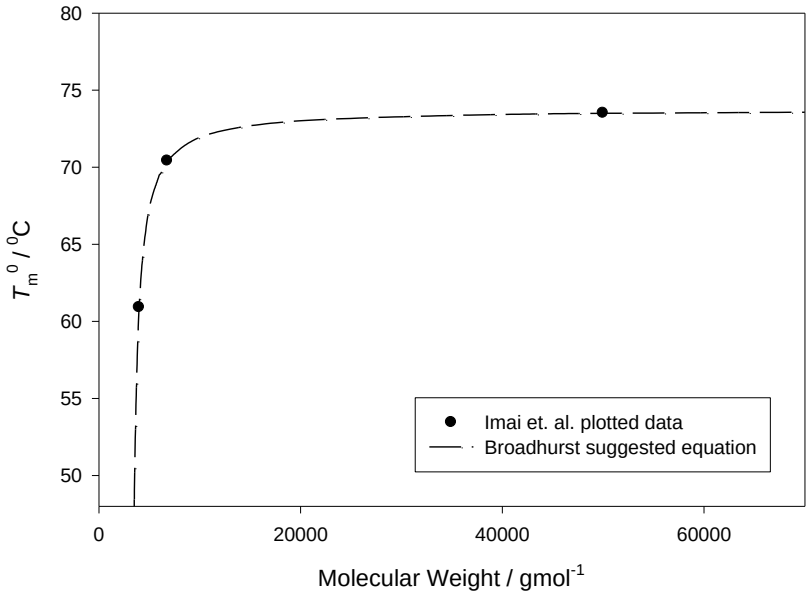

$$T_m = T_m^0\left(\frac{n+a}{n+b}\right) \quad (4.11)$$

FIGURE 4.39 : Plotted Imai [221] data with the Broadhurst equation 4.11

Marand et. al. [226] provide an excellent overview of the linear and non-linear extrapolations for use with the hoffman-weeks method for calculating the equilibrium temperature. In summary, their work shows that often a linear extrapolation is simply not accurate, instead a curve that appears linear for lower T_c values before curving up as it nears the T_m = T_c line. Figure 4.40 below shows an example non-linear extrapolation for the 400k PEO data found in this investigation that provides a T_m^0 value close to that found by Beech et. al. [223]. Future work into collecting data at higher crystallisation temperatures is required to confirm or dispute this.

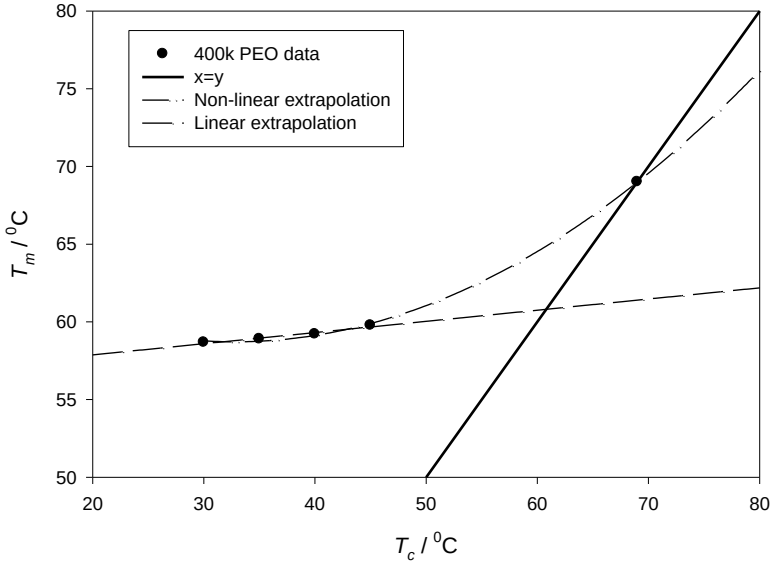

FIGURE 4.40 : An example non-linear extrapolation for the 400k data

4.3 Electrical Results

Figure 4.41 shows the real relative permittivity of the unfilled PEO samples with varying molecular weight. It is clear that the two curves have similar shapes, both showing a large steep increase at low frequencies, initiating at ~ 1Hz. The curve levels off for the mid-range frequencies between 1-100 Hz before dropping again and levelling off for the higher frequencies. Previous work by Se et. al. [227] has confirmed that the difference in molecular weight is unlikely to produce a vast difference in either the tan δ, real or imaginary relative permittivity, confirmed by these data. An investigation by Porter et. al. [228] on polyethylene oxide and polyoxymethylene highlighted the same large increase of real relative permittivity at low frequencies as that seen in figure 4.41, which they believed was not due to a low frequency α dielectric dispersion but due to low frequency loss, possibly due to conduction. Figure 4.42 shows the loss tan delta for both molecular weight samples, with both exhibiting a distinct peak at 1000 Hz. The equipment is seen to reach its limit for accurate data shortly after reaching 1 x10^4 Hz.

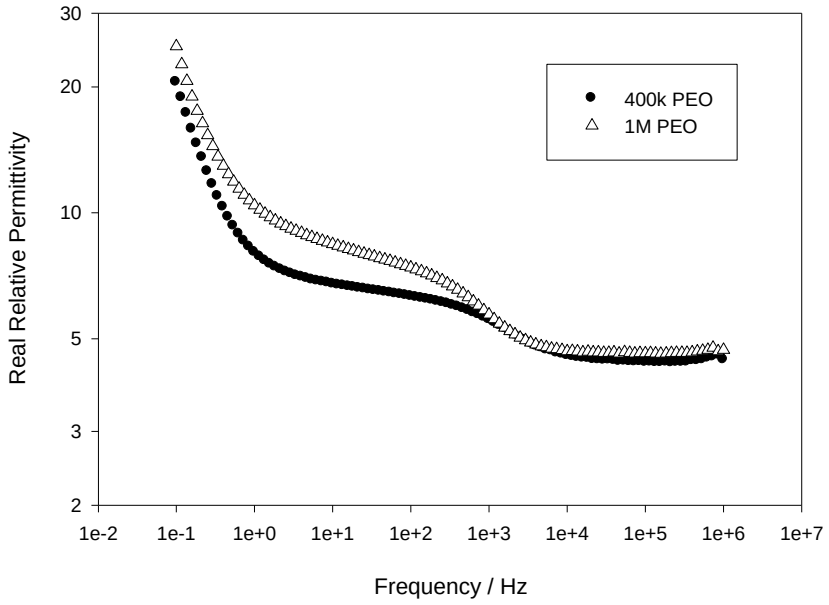

FIGURE 4.41 : Real relative permittivity curves for unfilled PEO samples

Porter et. al. [228] and Arisawa et. al. [229] produced similar curves to those in figure 4.41, also showing the steep gradient at low frequencies, which is thought to be a Maxwell-Wagner interfacial effect caused by charge build-up at the electrode-sample boundary. They also produced a dielectric loss curve like that seen in this investigation, including a peak similar to that seen in figure 4.42 but at lower frequencies, believed to be a γ relaxation. However their data were taken at 0 ^{0}C and 15 ^{0}C, with a large shift of the peak to a higher frequency between the two, suggesting that a further temperature increase to room temperature would have presented them with the same peak position observed here. These beliefs, and these peak positions, were also confirmed by an investigation by Jin et. al. [230] in 2002 who found the peak to exist at approximately 1000 Hz for their 2.16 x 10^5 gmol^{-1} PEO sample.

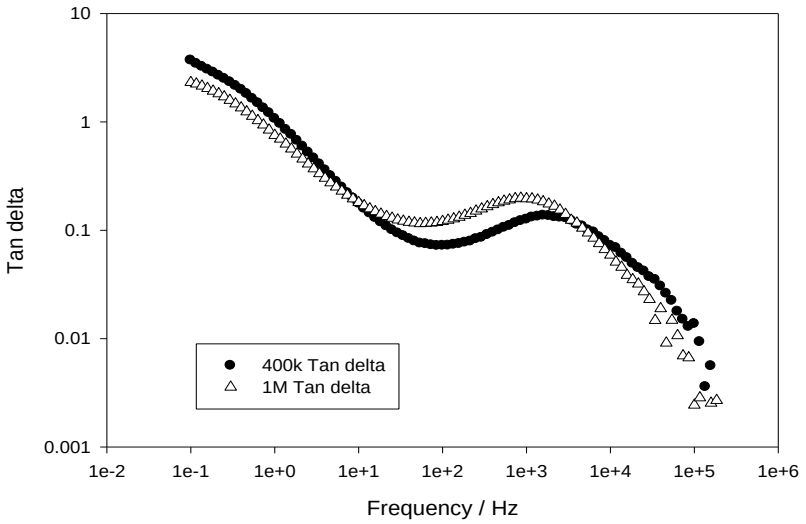

FIGURE 4.42 : Tan delta curves for unfilled PEO samples

The general shape of the real relative permittivity, imaginary relative permittivity and loss tan δ seen for samples in this investigation are confirmed by several authors [231-232]. It should be noted that the general shape of these curves are confirmed by literature, however the exact values differ across the literature, although the values in this investigation seem comparative to several others. The variation is considered to be due to different equipment and sample processing.

4.3.1 AC Electrical Breakdown

Figure 4.41 shows the electrical breakdown strength of the 400k and 1M PEO samples, with both falling in the range 50-70 kV/mm, a value around half that of a reference PE sample, reinforcing its use as a model system rather than a commonly used industrial insulator. This variation is possibly due to the materials having different electrical breakdown mechanisms. For example, if PEO has a breakdown mechanism that involves a thermal contribution, it's relatively low thermal transition temperatures would relate to its low breakdown strength. Despite the two molecular weights having similar breakdown ranges, they are quite clearly not identical, with the increase in molecular weight apparently leading to a decrease in electrical breakdown strength. The data are not conclusive however, since the 90% confidence bounds overlap considerably. Previous investigations into molecular weight dependence of polymer breakdown strengths, such as that by Claude et. al. [233] into poly(vinylidene fluoride-chlorotrifluoroethylene), have found the opposite behaviour with breakdown strength increasing with molecular weight.

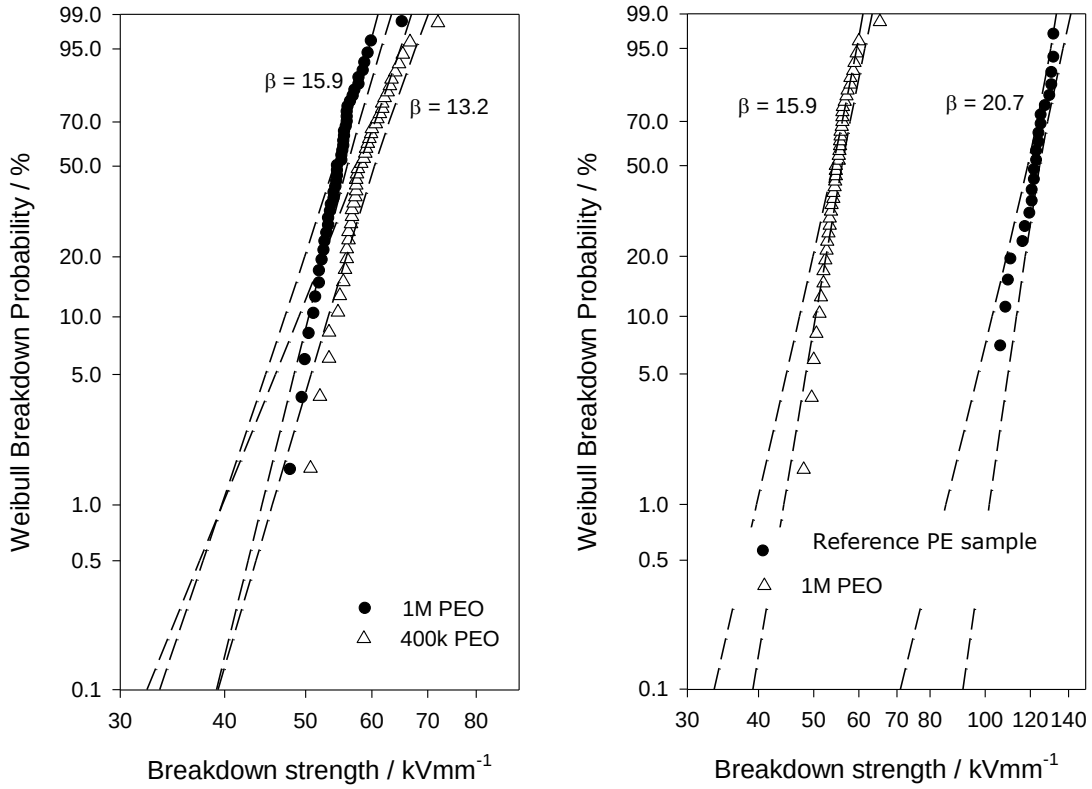

FIGURE 4.43 : Breakdown plots of PEO's (left) and a reference PE sample (right) with 90% confidence bounds

4.4 Structure and Composition using Optical imaging, SEM and etching

It has been seen previously that crystallising PEO produces spherulites [234-236]. A main feature of PEO is its low nucleation rate, allowing the growth of extremely large spherulites, up to 1 cm in diameter [237]. Using optical microscopy, images of samples were possible in transmission for thin film samples and reflection for thicker samples. Figures 4.44-4.46 below were taken with the Leitz optical microscope. In figure 4.44 (right) the larger spherulites began growth at around 46 ^{0}C with smaller spherulites nucleating as the temperature decreased. By using a polariser it was possible to observe the images in several ways. An example of this is shown in figure 4.46, producing colours in the Maltese cross [238].

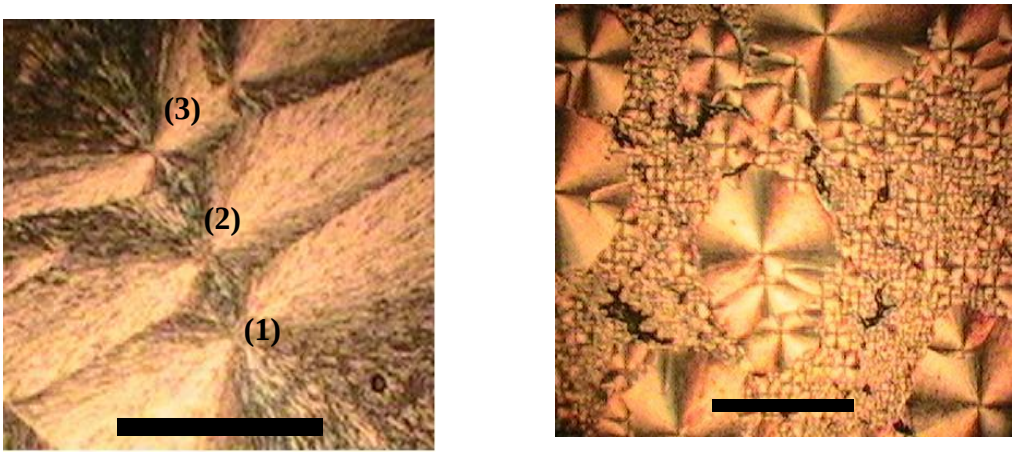

FIGURE 4.44 : Three points of nucleation in a PEO sample melted to 80 ^{0}C then crystallised at 40 ^{0}C (left) and a varying T_c sample with varying size spherulites melted at 80 ^{0}C then cooled to 30 ^{0}C at 50 ^{0}C/min (right). Scale bar = 250 μm

Using imaging techniques such as optical microscopy, such as that detailed above, and scanning electron microscopy (SEM) will aid in providing an analysis of the structure and composition of the material in question. At the simplest level, large agglomerations of fillers or distinct structural changes, such as observing a change in spherulite growth rate, can be observed. SEM is viewed as a more complete procedure than basic optical microscopy, mostly due to it's capability for higher magnification, therefore an investigation into imaging the PEO composite samples was performed.

This involved assessing the feasibility and practical application of etching techniques, the subsequent SEM procedure and use of EDAX, all detailed in Appendix 5. In summary it was found that etching and imaging of the PEO composites was more complex than originally realised, with the investigation concluding that further work is needed to refine the processes.

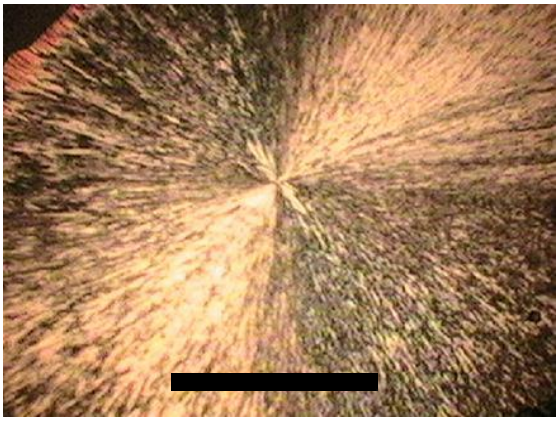

FIGURE 4.45 : A particularly large single spherulite in 400k PEO melted at 80 ^{0}C then crystallised at 50 ^{0}C for 48 hours. Scale bar = 250 μm

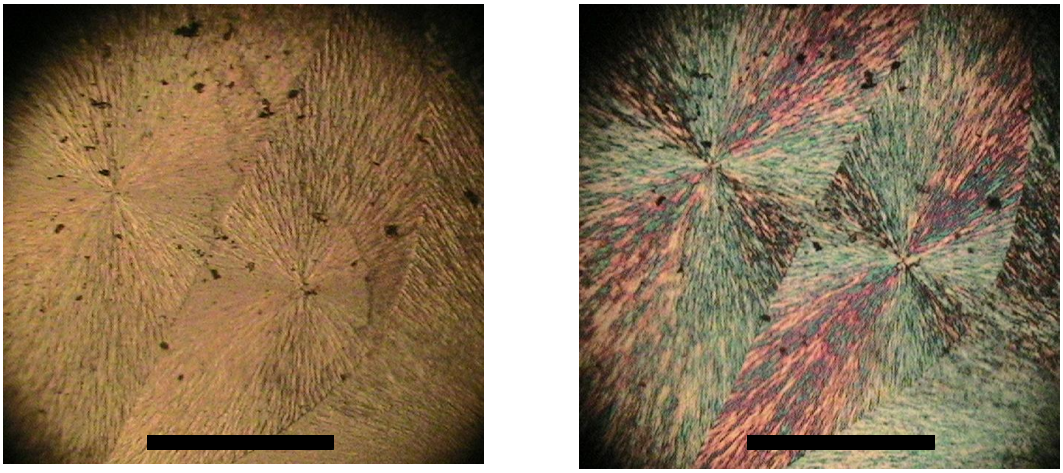

FIGURE 4.46 : Spherulites viewed without a polariser (left) and with a polariser (right) showing a characteristic Maltese cross.
Sample was melted at 80 ^{0}C then crystallised at 35 ^{0}C. Scale bar = 250 μm

4.5 Chapter Summary

The strong flow property dependence of PEO solutions with respect to volume and temperature was observed and care was therefore taken to maintain the same conditions. The limitations of the rheometer were discussed, resulting in the A1, A2, B1 and C10 samples all being omitted due to the low associated accuracies, with the remaining samples said to have an accuracy of 1%. It was also observed that the initial ramp up data varied from that of the final ramp down data, initially thought to be shear re-dispersion as seen in previous investigations, but for this investigation was found to be the achievement of a state of further dispersion. The Ostwald de-Waele and three parameter hyperbolic functions were fitted to data, with the former found to well represent data for low viscosity samples but less accurately at high viscosities, with the latter providing an accurate fit for all viscosities.

The rheometer software was found to be calculating the coefficient of viscosity, however differential viscosity data was calculated by fitting and differentiating the 3 parameter hyperbolic. The Carreau and De Kee models were then fitted to the data, with the latter producing a good fit at all viscosities, whereas the Carreau model was found to be poor at low viscosities. Using MHS theory an α value of 2.7 was calculated, suggesting a concentrated system. DSC showed that the 400k had the highest thermal transition temperatures, followed by 1M and then 100k. Crystallinity values were calculated from corrected enthalpy data collected producing values of 84.7%, 73.4% and 66.9% for 100k, 400k and 1M respectively. Avrami curves were collected, with little variation between molecular weights as expected, and followed a trend of decreasing K_3 with increasing T_c. Calculation of T_m^0 was performed using two methods but values were found to be lower than those in the literature, thought to be due to an incorrect extrapolation method.

Dielectric spectroscopy produced permittivity and tanδ curves like those seen in the literature with a γ relaxation. Also, a Maxwell-Wagner interfacial effect at low frequencies was observed. The breakdown strength of the PEO used in this investigation was found to be 50-70 kV/mm and that, arguably, increasing molecular weight causes a decrease in breakdown strength.

Chapter 5: THERMALLY AGED POLYETHYLENE OXIDE

5.1 Rheometry

Having observed the susceptibility of PEO to thermal ageing, found during the de-gassing process performed to create thin film samples detailed in section 3.7, an aged 100k PEO sample was characterised using the same rheometry, thermal DSC and electrical techniques to gauge the effect that ageing has on such properties. This should aid in identifying the thermal ageing process, related property effects and help to identify possible ageing in other samples. Therefore a 100k sample, since this molecular weight was the most susceptible, was aged at 80 ^{0}C for 8 hours and rheometry data collected. The table in figure 5.1 shows the peak shear rates of the thermally aged 100k and the unaged 100k PEOs. From this it is clear that the ageing process has altered the polymer and subsequently the behaviour in solution; showing an increase in peak shear rate. Figure 5.1 confirms the decrease in viscosity, of approximately 50% in the viscosity values. The thermal process is believed to be inducing chain scission, a process whereby the long polymer chains break down into smaller chains [81,239-240].

PEO / PPHW	Peak Shear Rate	
	Aged 100k	Unaged 100k
5	4820 s^{-1}	3590 s^{-1}
10	1850 s^{-1}	739 s^{-1}

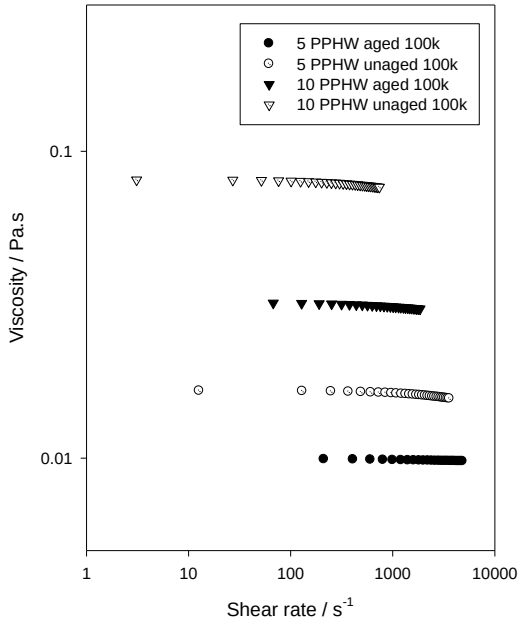

FIGURE 5.1 : Shear rate – viscosity data for aged and unaged 100k samples (left) and a table showing the peak shear rates for the aged and unaged samples

Using the theory previously applied in section 4.1.4 it should be possible to infer an average molecular weight for the thermally aged PEO. In an ideal situation we can assume that the new chain length distribution is the same as that for the unaged 100k, hence the ageing process is affecting all chains equally. If the ageing is effecting only a portion of the total chains present then the inferred average molecular weight will still represent the molecular weight of PEO associated to that viscosity behaviour. Equation 5.1 below represents the relationship between viscosity, η, and molecular weight, *Mw*, where *m* and *c* were constants found to be 2.7 and -15.02 respectively.

$$\log(\eta) = m * \log(Mw) + c \tag{5.1}$$

Substituting in the oberved viscosity value for the thermally aged PEO, the inferred representative molecular weight of the aged PEO system is approximately 77,500 $gmol^{-1}$. This suggests that the thermally ageing process has reduced the average molecular weight by 22,500 $gmol^{-1}$ by chain scission. Figure 5.2 shows this point added to the viscosity-molecular weight distribution line previously seen in figure 4.31. This is only an estimate and assumes that the viscosity regime, mentioned in section 4.1.4, has not changed.

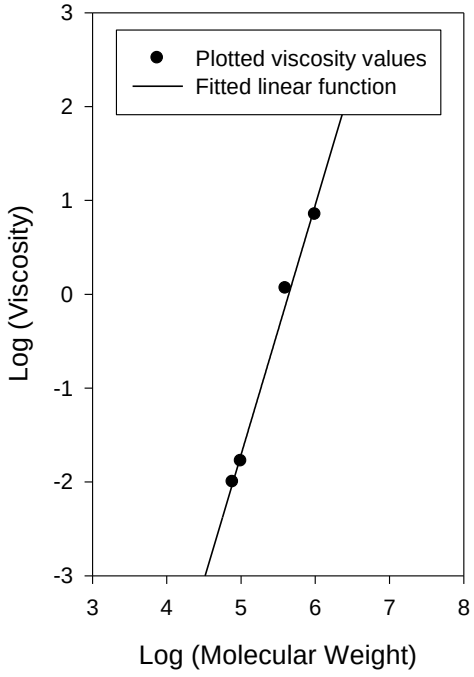

FIGURE 5.2 : The molecular weight – viscosity relationship with the thermally aged PEO representative molecular weight added

5.2 Differential Scanning Calorimetry

Following on from the rheology of the thermally aged 100k PEO in section 5.1, having observed that aged PEO has a lower viscosity in solution, figure 5.3 shows the thermal transitions of the aged 100k PEO sample. Comparing this value to the unaged PEO sample it is clear that the ageing process has caused the thermal transition temperatures to decrease. This suggests that the molecules in the thermally aged sample may be crystallising less readily on cooling. However later, Avrami *n* and *k* values suggest that the thermally aged samples actually crystallise more readily than the unaged samples. Therefore the decrease in thermal transition temperatures observed here for non-isothermal crystallisation could actually be related to thermodynamic factors (such as the introduction of defects into the molecules) or kinetics (the aged samples crystallise more slowly).

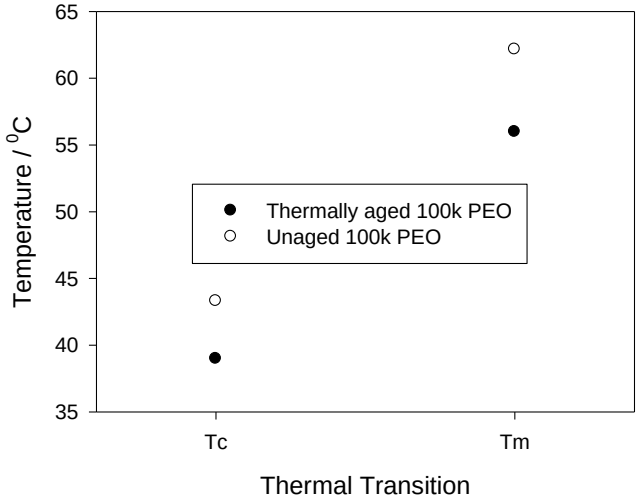

FIGURE 5.3 : The T_c and T_m values for aged and unaged 100k PEO

As figure 5.3 shows, the thermal ageing process has produced lower melting and crystallisation temperatures, possibly as a consequence of thermal chain scission [241], having observed the drop in transition temperatures from 400k down to 100k PEO previously. It is known that polyethers, such as PEO, are subject to oxidation [242], where the polymer degrades forming hydro-peroxides that decompose and cause chain scission [243]. Scheirs et. al. [244] explain that low melting peaks in crystalline polymers can sometimes be caused by such thermal oxidation. Work by

Bigger et. al. [245] and Scheirs et. al. [244] into thermal oxidation of PEO showed the main melting peak to move to lower temperatures after being thermally aged in air at 60 ^{0}C. The change appears slight in their investigation, in contrast to the 5/6 ^{0}C drop seen here. The increase however can be attributed to a higher ageing temperature. However, Scheirs et. al. [157,244] showed that lower molecular weights were more resistant to oxidation, contrary to the findings of this investigation, where the 100k PEO aged far more easily than the 400k and 1M. This could suggest the 100k sample contains impurities which may be acting as a catalyst for chain scission, which might be detected by using a technique such as FTIR.

A further indicator of thermal oxidation is said to be a reduction in the area under the melting and crystallisation curves, ΔH_m and ΔH_c. Sepe [246] showed that a thermally aged polyacetal sample exhibited such a decrease in T_c and curve area, ΔH_c. Coleman et. al. [247] explain that polymer oxidation is based upon free-radical reactions initiated by dissolved oxygen that cause degradation of polymer chains. Previous work by Shlyapnikov et. al. [248] has shown the sensitivity that polymers have towards oxygen. Due to the polymer's self-catalytic nature, this type of oxidation is often referred to as autoxidation [249]. These reactions are said to have a negative effect on the mechanical properties of polymers, being a major reason for polymeric failure [250]. Looking at the area under the crystallization curves for aged and unaged samples, plotted as ΔH_m and ΔH_c values in figures 5.4 and 5.5, they were seen to decrease with ageing. It should be noted that if chain scission is occurring, leaving the sample with shorter chains, it might be expected to exhibit higher, rather than the observed lower, ΔH_m and ΔH_c values when compared to the unaged 100k, following on from the molecular weight trend observed in figures 4.34 and 4.35. A crystallinity value of 73.2 % ± 5 (unaged 84.7 %) was calculated using equation 4.10. The 100k, 400k and 1M crystallinity values all fit with the trends observed by Saboormaleki [251], however the aged sample does not, suggesting other effects may be the cause, such as the introduction of chemical defects that may be confirmed by using FTIR.

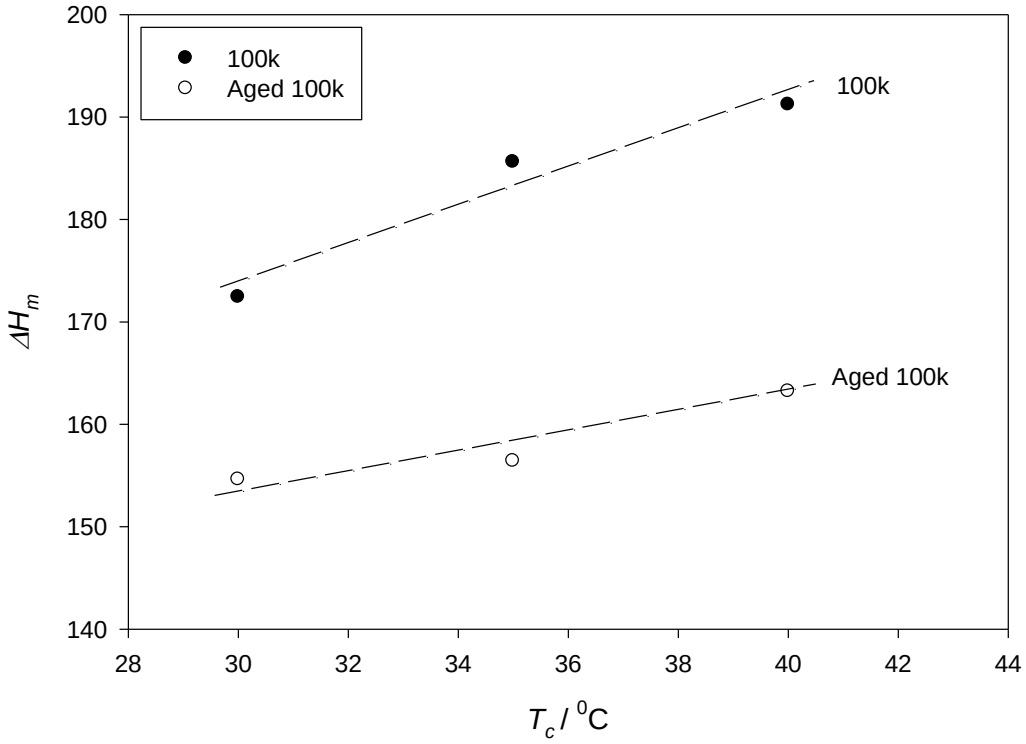

FIGURE 5.4 : ΔH_m values for the aged 100k and unaged 100k PEO samples

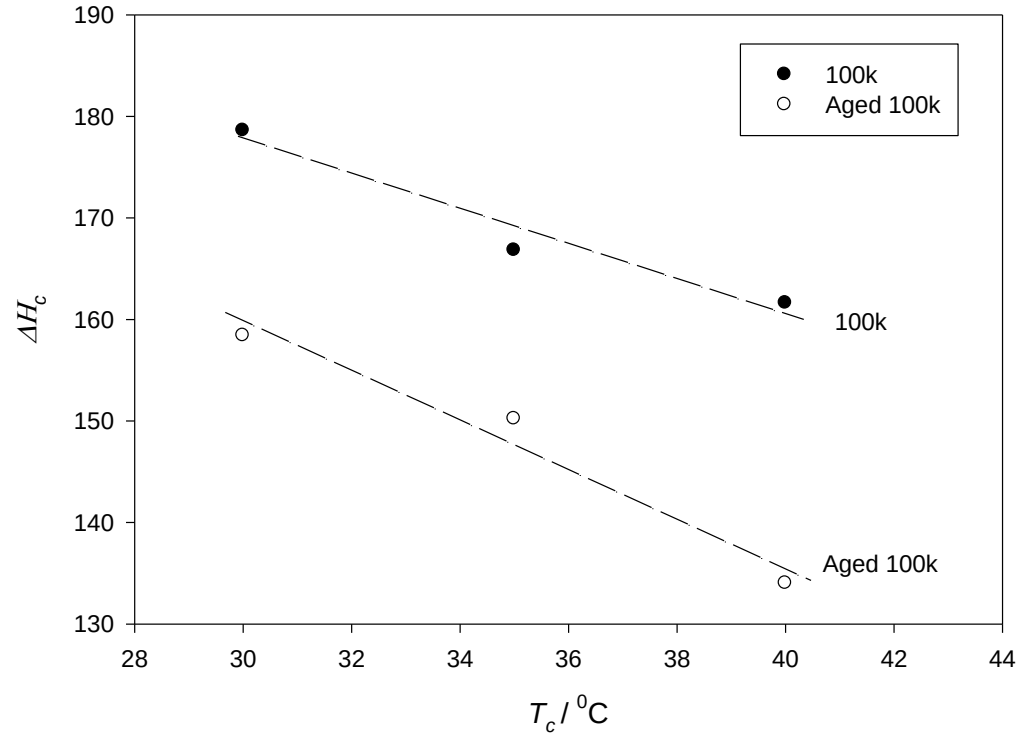

FIGURE 5.5 : ΔH_c values for the aged 100k and unaged 100k PEO samples

5.2.1 Avrami analysis

Having hypothesised that the thermal transitions have moved to lower temperatures for the thermally aged PEO sample due to the introduction of chemical defects or due to the samples crystallising more slowly, it was expected that the Avrami curves might move to lower times, suggesting the sample is crystallising more readily, but with a decrease in the gradient of the avrami curve, suggesting a slower crystallisation process. This was confirmed by the data collected, representative examples of which are shown in figure 5.6. When crystallised at 30 ^{0}C and 40 ^{0}C it is clear that the thermal ageing process has caused a drop in the time required before crystallisation begins. Interestingly however, when moving to a higher T_c, the gradient of the Avrami curve does not appear to decrease, as is observed for most samples, being indicative of slower crystallisation. Instead, the curve is as steep, if not steeper, than the 30 ^{0}C sample. Even with repeat testing this was still found to be the case. Fitting the Avrami equation to the curves produced values for the Avrami parameters, shown in table 5.1.

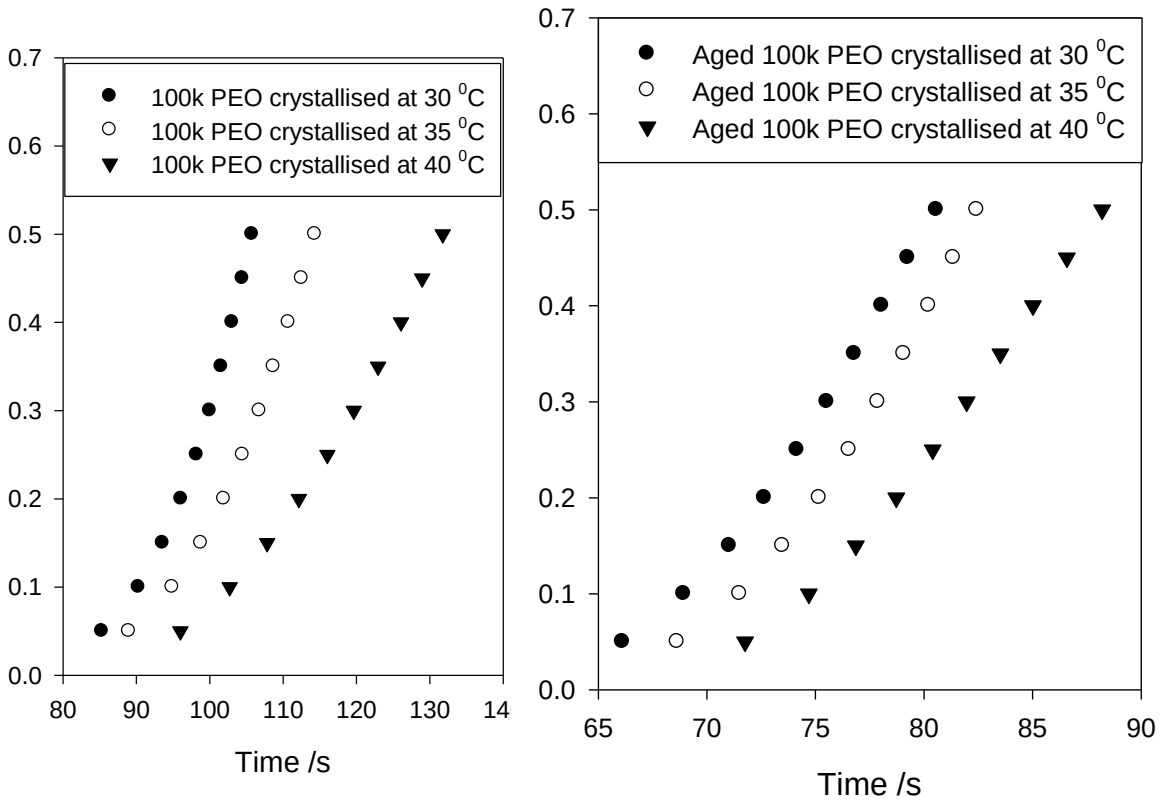

FIGURE 5.6 : Crystallisation data collected for the unaged 100k PEO (left) and the thermally aged 100k PEO (right) samples

100k PEO Sample	T_c / ^{0}C	Avrami parameters			
		n	k (s^{-1})	R^2	K_3
Unaged	30	4.575	1.83×10^{-8}	0.9990	8.44×10^{-6}
Unaged	35	4.304	2.32×10^{-8}	0.9997	4.77×10^{-6}
Unaged	40	3.098	1.76×10^{-8}	0.9998	2.67×10^{-6}
Aged	30	3.023	3.749×10^{-5}	0.9999	4.05×10^{-5}
Aged	35	2.994	5.295×10^{-5}	0.9998	5.19×10^{-5}
Aged	40	2.581	2.170×10^{-4}	0.9999	5.52×10^{-5}

TABLE 5.1 : Avrami parameters generated for the aged and unaged samples

With ageing the Avrami *n* and *k* values are observed to decrease and increase respectively, although the dependence on crystallisation temperature of these parameters does not appear to have changed from that of the unfilled samples. Figure 5.7 shows the ageing process has caused the onset of crystallisation to occur sooner for the whole T_c range.

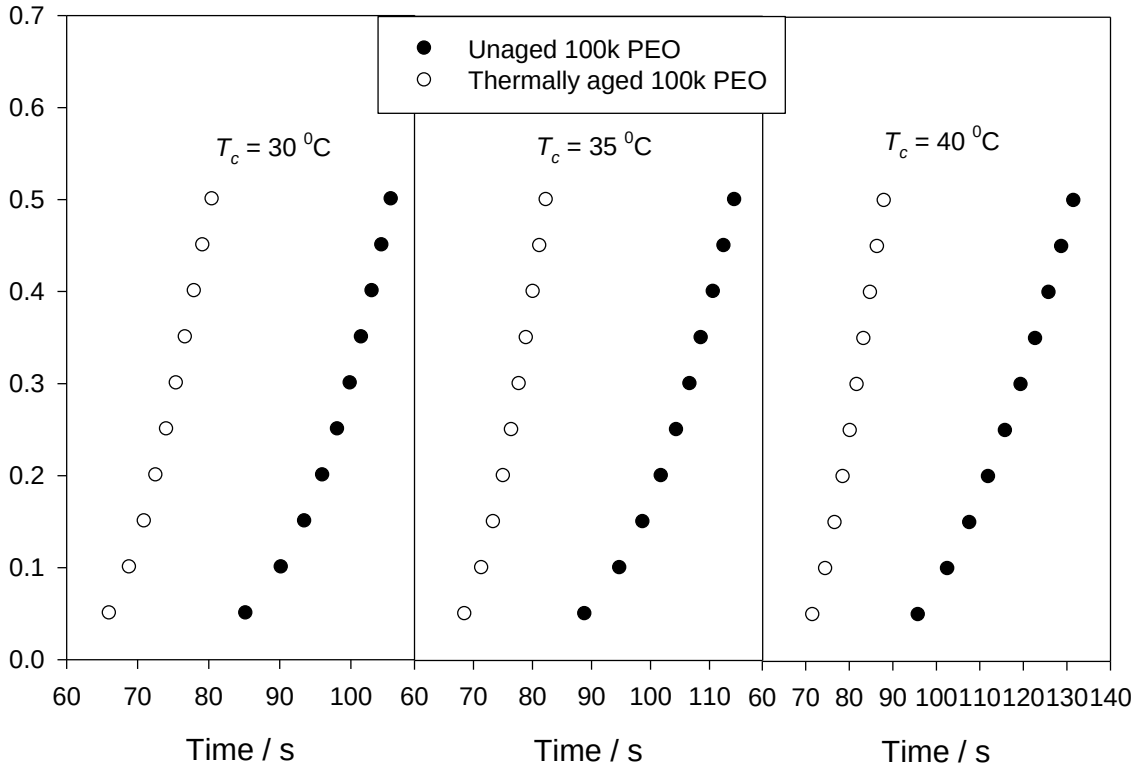

FIGURE 5.7 : Avrami curves for the unaged and thermally aged 100k PEO samples crystallised at 30 ^{0}C (left), 35 ^{0}C (centre) and 40 ^{0}C (right)

Using equation 2.14 again, K_3 values were generated, shown in table 5.1, and the aged samples are seen to have higher K_3 values by approximately an order of magnitude, suggesting that it is crystallising less readily. Previous investigations into aged PEO have shown a similar relationship between ageing and increased n – K_3 values [252]. This suggests that the thermal ageing process has caused a change in the nucleation and mobility within the system. Figure 5.8 then shows the T_m values for aged and unaged samples with respect to T_c and the T_m=T_c intersect, hence the T_m^0, which shows that the aged sample value appears to have decreased. The values are noted to be within the ± 1.0 ^{0}C error, calculated using the method detailed in Appendix 6 and referred to in section 4.2.1. Figure 4.38 however, suggests that an increase would be observed if chain scission was occurring and hence leaving the PEO with shorter chains, which was not the case. Instead this decrease could be due to the defects within the thermally aged system dominating.

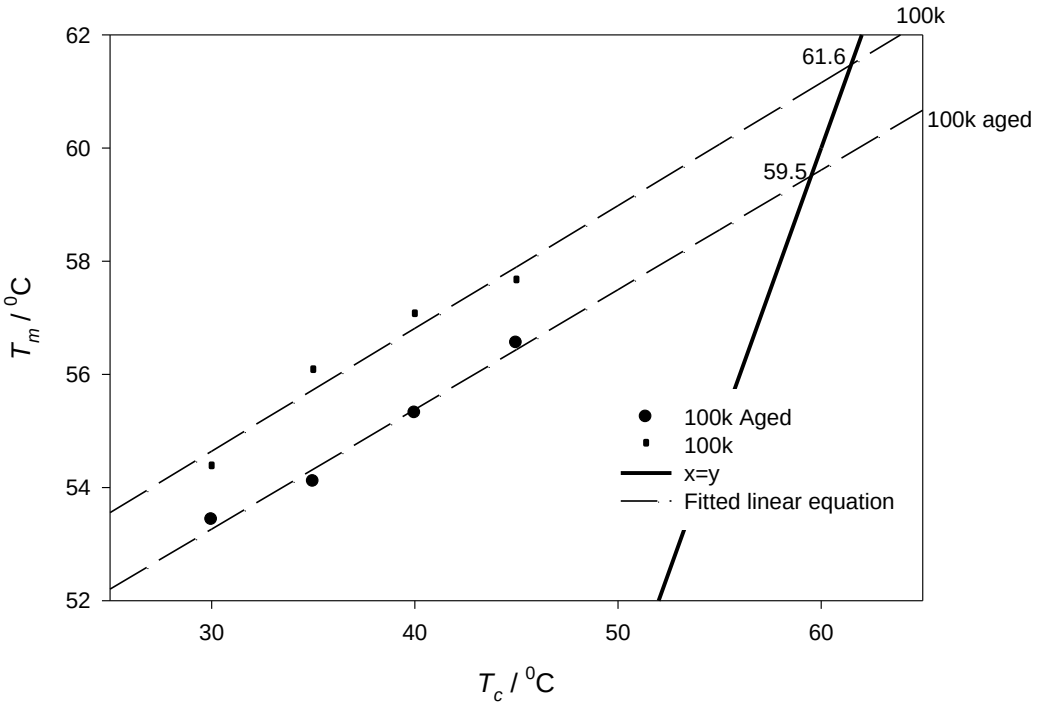

FIGURE 5.8 : T_c vs T_m plots for the aged and unaged 100k PEO systems along with the T_c=T_m intercept values in ^{0}C

5.3 AC Electrical Breakdown

Previous work into breakdown strength of aged polymers and polymer composites has often found the breakdown strength to decrease [253-254]. An example of this is work by Ehsani et. al. [255] who found that thermally ageing their ethylene-propylene-diene system (EPDM) produced a drop of around 10 kV/mm. Other research by Katakai et. al. [256] showed that thermally ageing their low density polyethylene samples induced oxidation and rearrangement of chains, initially introducing deep traps for electronic carriers. This caused an increase in breakdown strength at first, while further thermal degradation caused the carbonyl groups to act as electron hopping sites decreasing the breakdown strength dramatically. Figure 5.9 below shows the thermally aged 100k PEO, compared to the unaged 400k PEO sample (since no 100k sample could be produced without air bubbles or thermal ageing). The ageing process may appear to have caused a minor increase in breakdown strength, however the confidence bounds overlap and the variation is most likely a molecular weight effect following on from the effect seen for 400k and 1M samples in figure 4.41 in section 4.3.1. Therefore a speculative assumption is that the thermal ageing has had no effect on the breakdown strength on the 100k PEO.

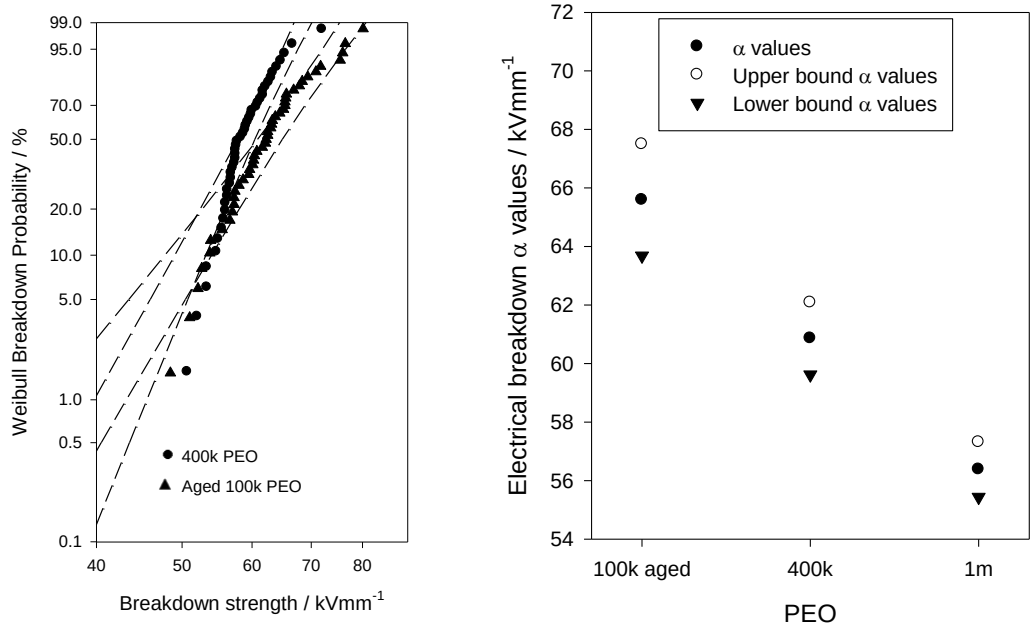

FIGURE 5.9 : Electrical breakdown plots of unaged 400k PEO and thermally aged 100k PEO (left), and α values for unfilled PEO molecular weights (right)

5.4 Fourier Transform Infra-red

To further investigate the structural changes and the altered form of the thermally aged 100k PEO, FTIR was employed. Previously FTIR has been successfully used to quantify material degradation [257-259] and oxidation [260-263] by comparing spectra of aged and unaged samples. In specific, work by Ramirez et. al. [264] used FTIR to observe the carbonyl, aldehyde and methylene bending spectral regions to analyse the thermo-oxidation in their polyoxymethylene copolymer samples. They observed that the copolymer exhibited higher absorption values at wavenumbers 1430 and 1470, than that of the homopolymer and spectral bands were observed to increase with increasing degradation, allowing analysis of the chemical changes taking place.

To investigate the aged 100k PEO, first a background scan was taken to improve the accuracy of sample scans, an example is shown in figure 5.10. Absorbance and transmittance data were then taken and plotted as a function of wavenumber. Figure 5.11 shows that varying the molecular weight results in no major change to the position or amplitude of the absorption peaks. The small variations seen, the most prominent of which are at markers A and B, are believed to be within error.

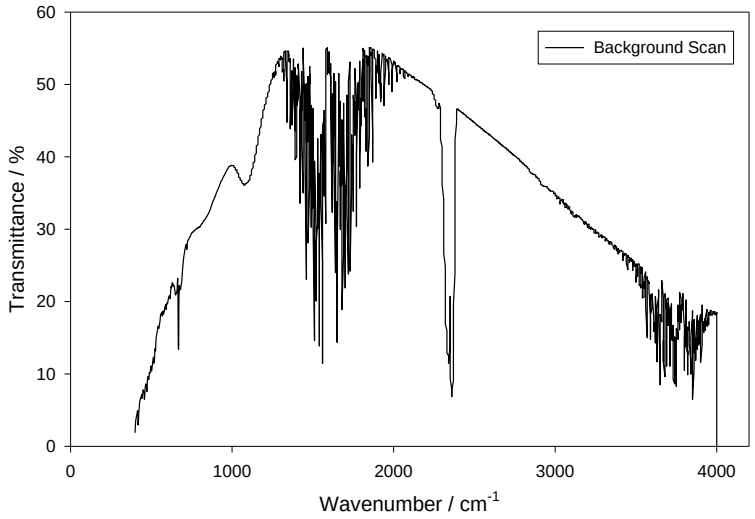

FIGURE 5.10 : A background scan of transmittance % as a function of wavenumber

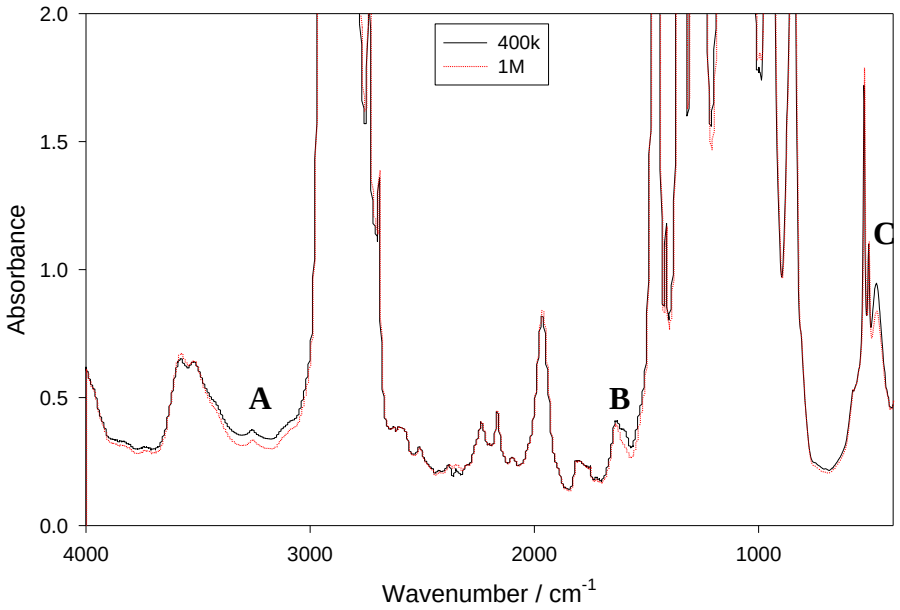

FIGURE 5.11 : An absorption spectrum of 400k and 1M PEO as a function of wavenumber

Previous work by Cardenas et. al. [265] into Chitosan polymer composites showed that only a slight difference was noted between the low and high molecular weight samples, however the relatively low chitin level may not reveal the full effect. Another study into the molecular weight effect was performed by Su et. al. [266] using PEO-PPO triblock copolymers. They summarised work by Dissanayake et. al. [267] and Kimura et. al. [268], showing the assignment of bands for PEO and used their FTIR apparatus to show that increasing molecular weight caused the peaks to shift to slightly higher wavenumbers. They found no significant evidence supporting the belief that molecular weight affects the absorbance values.

The collected FTIR spectra data for PEO correlated well when compared to regions collected by other authors; 700-1500 cm-1 [267], 0-4000 cm-1 [269], 0-3000 cm-1 [270], 700-1400 cm-1 [271], 40-140 cm-1 and 800-1500 cm-1 [153], 400-3500 cm-1 [272] and 0-4000 cm-1 [273]. To represent the main peaks and associated interactions for the entire wavenumber range, table 5.3 has been formed. The first two columns label regions and interactions from the above authors, with the third and fourth columns reprinting data from Bailey et. al. [243] who performed extensive research into FTIR of PEO. Bailey's work is now considered to be dated, but still shows correct classification of many of the peaks.

Wavenumbers (cm^{-1})	**Description of Vibration**	**Wavenumbers ($cm^{-}1$) [243]**	**Desciption of Vibration [243]**
2800-2935	CH stretching	2939, 2890	CH_2 antisymmetric stretching, CH_2 symmetrical stretching
1950-1970	Asymmetric CH_2 stretching	-	-
1465-1485	CH_2 scissoring	1484	CH_2 scissoring
1450	Asymmetric CH_2 bending	1449	CH_2 scissoring
1325-1350	CH_2 wagging	1398, 1364	CH_2 wag and C-C stretch
1242-1297	CH_2 twisting	1282, 1235	CH_2 twisting
-	-	1143	C-O stretch, CH_2 rocking
-	-	1126	CH_2 rocking, C-C stretch
996-1060	CH_2 rocking	1064	C-O, C-C stretch, CH_2 rocking
991	CH_2 twisting	-	-
949-946, 962	CH_2 rocking	-	-
950-1250	C-O-C stretching	-	-
842	CH_2 wagging	537	C-C-O, C-O-C bend, CH_2 rocking
-	-	279, 363	C-C-O, C-O-C bend, C-C internal rotation
-	-	216	C-O-C bend, C-O internal rotation
-	-	160	C-C, C-O internal rotation

TABLE 5.3 : Wavenumbers and related vibrations compiled from many sources - [266-267,269-278]

Having established the peaks and associated interactions for PEO, comparison of the thermally aged and unaged 100k PEO samples was possible. Figure 5.12 shows the absorption data collected. From this it is shown that overall the ageing effect has not changed the position of the peaks, suggesting that all of the vibrational modes remain. The amplitude of the majority of the peaks appears unchanged, although in the region **A**, wavenumbers 3000-4000 cm^{-1}, a decrease in absorbance is seen for the thermally aged sample. A smaller increase was also observed at region **B**, 1600 cm^{-1}, which was deemed to suggest a molecular weight effect (when compared to region **B** in figure 5.11), possibly confirming that chain scission has indeed occurred. The variations observed were all confirmed after repeat experiments. If the ageing process was causing a significant chemical change we would expect to see movement in the peaks, or a severe decrease/increase in some peaks representing the loss/gain of vibrational modes [260,263-264], however this is not the case. Minor amplitude variations however, such as those seen at **A** in figure 5.11, may suggest the introduction of minor chemical defects. This FTIR data has suggested that chain scission is indeed occurring and that some minor chemical defects may be present, although no significant chemical changes have taken place.

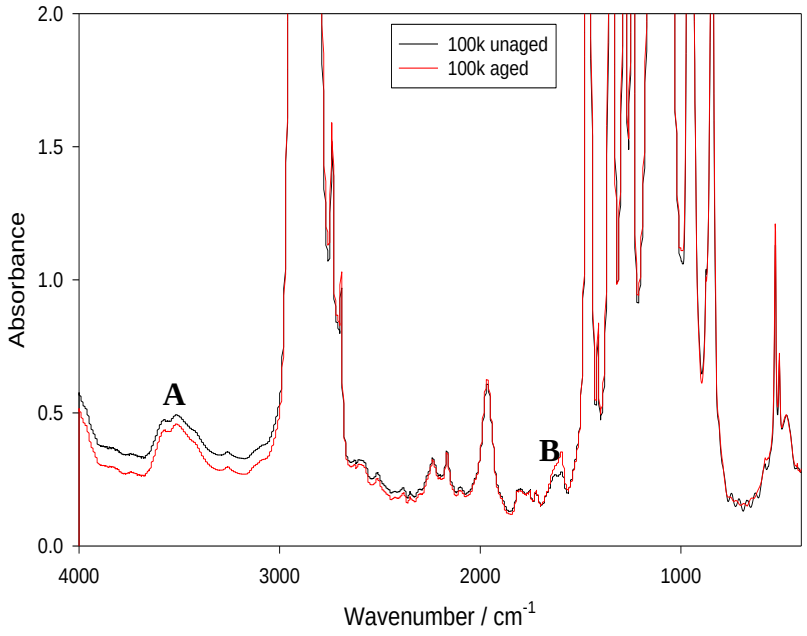

FIGURE 5.12 : The absorbance (left) and transmittance (right) spectrums from thermally aged and unaged 100k PEO as a function of wavenumber

5.5 Chapter Summary

In solution the thermally aged 100k PEO was found to have a differential viscosity around 50% that of the unaged 100k. The DSC also revealed lower thermal transition temperatures. It was hypothesised that this could be due to oxidation or chain scission during the thermal process. Enthalpy values were also observed to decrease, a known sign of chain scission. However, it was noted that the crystallinity decreased with thermal ageing, which does not support chain scission. This drop in crystallinity was thought to be due to the introduction of minor chemical defects. Avrami analysis showed that with ageing the n and k values were seen to increase, the onset of crystallisation occurring sooner and calculated K_3 values were seen to be higher, suggesting a change in the nucleation and/or mobility within the system.

No variation was observed during dielectric spectroscopy and although the breakdown strength was seen to be lower for the thermally aged 100k PEO when compared to 400k, this is likely just a molecular weight effect. FTIR revealed no major peak shifts or amplitude variations, although some smaller variations were observed which also suggested chain scission and that some minor defects may be present.

Chapter 6: PEO-MONTMORILLONITE COMPOSITES

6.1 Rheometry

Since dispersion is of particular importance to the properties of a material, it seems obvious to check that the particles are as dispersed as much as possible. Table 6.1 shows the peak shear rate values for PEO-MMT composite solutions. Again, just like the single molecular weight solutions in section 4.1.3, a further state of dispersion was achieved after the first set of processes. If the MMT platelets hinder the mobility of the polymer chains or cause more interactions these would be seen as the peak shear rate value decreasing. However for addition of up to 10 PPHP MMT this was not the case, with all peak shear rate values for unfilled, 5 PPHP filled and 10 PPHP filled being similar. The lack of effect that addition of up to 10 PPHP MMT has is unlikely to continue to much higher filler loadings.

Sample	Peak Shear Rate 5 PPHP MMT Filler	Peak Shear Rate 10 PPHP MMT Filler
A1	5880	5730
A2	5700	5670
A5	3650	3860
A10	793	802
B1	4960	5350
B2	1600	2710
B5	78.4	86
B10	16.9	14.8
C1	4590	4510
C2	740	711
C5	34	48

TABLE 6.1 : Peak shear rate values for PEO-MMT composite samples

Figure 6.1 shows the peak shear rates for all samples and is comparable to figure 4.24 in section 4.1.3. The addition of up to 10 PPHP MMT has had no effect on the order

of the samples. To analyse any shape changes in the viscosity curves, values were calculated using the hyperbolic equation as before, with some data shown in figures 6.2 and 6.3. As stated previously, the increasing viscosity with molecular weight is as expected when observing work by Lewandowska [70] and Ma [67]. Ramesh et. al. [279] also investigated viscosity of PEO solutions using two different molecular weights, finding higher molecular weights displaying higher viscosities during tests with butanol, pentanol and hexanol-PEO solutions. The shape of the viscosity curves appears unchanged with MMT addition and no different to that for the unfilled PEO samples. This suggests that up to 10 PPHP clay has been well dispersed with no effect on the flow behaviour or mobility of the chains within the solution.

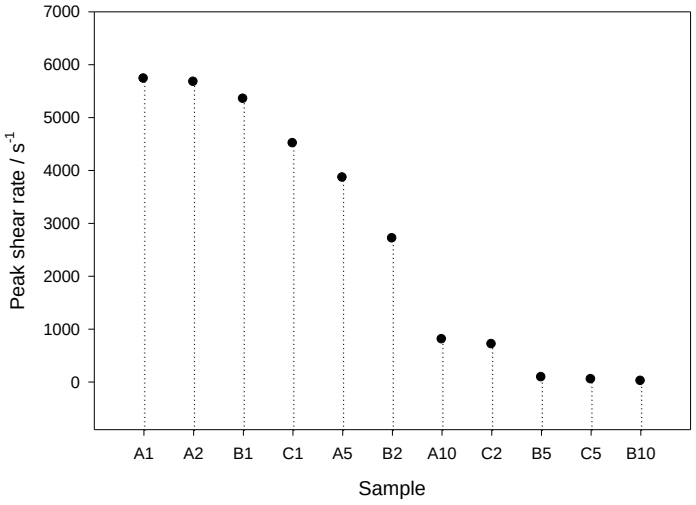

FIGURE 6.1 : Peak shear rate values of all 10 PPHP MMT filled samples

For higher loading samples however, the MMT was seen to affect the flow within the system, shown in figure 6.4. Here the density of MMT platelets is deemed too high for even the best dispersed system. With addition of 50 PPHP MMT the viscosity is seen to increase by up to double the value for unfilled and 10 PPHP filled samples. It should be noted that the increase with MMT addition is not linear.

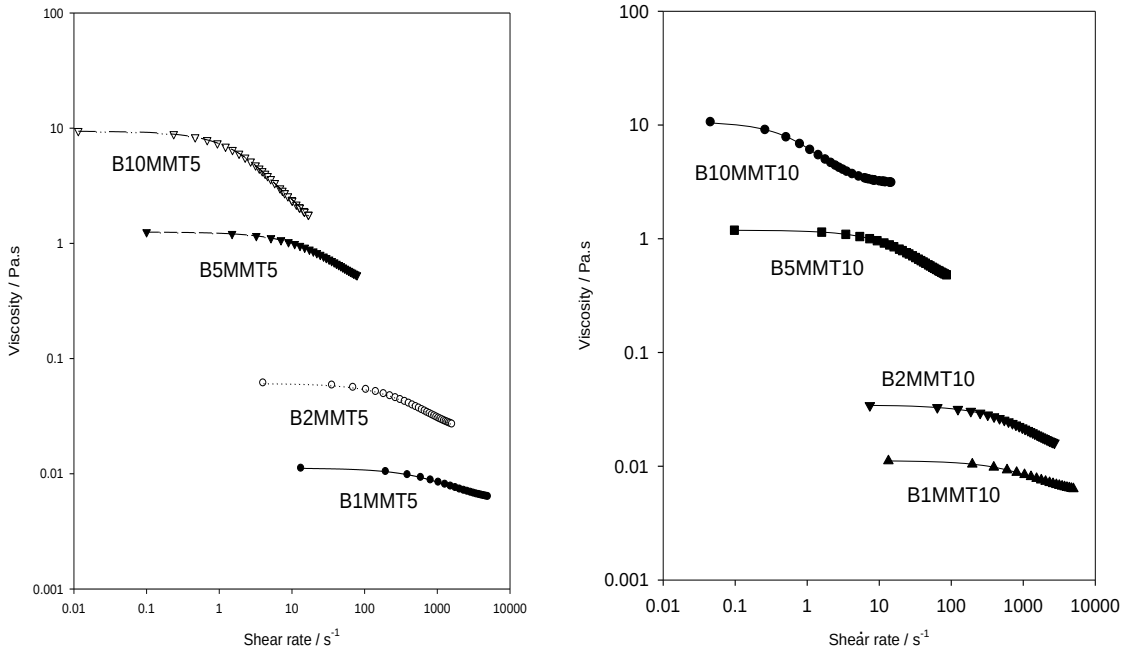

FIGURE 6.2 : Viscosity curves of 1, 2, 5 and 10 PPHW 400k PEO samples with 5 PPHP MMT filler (left) and 10 PPHP MMT filler (right)

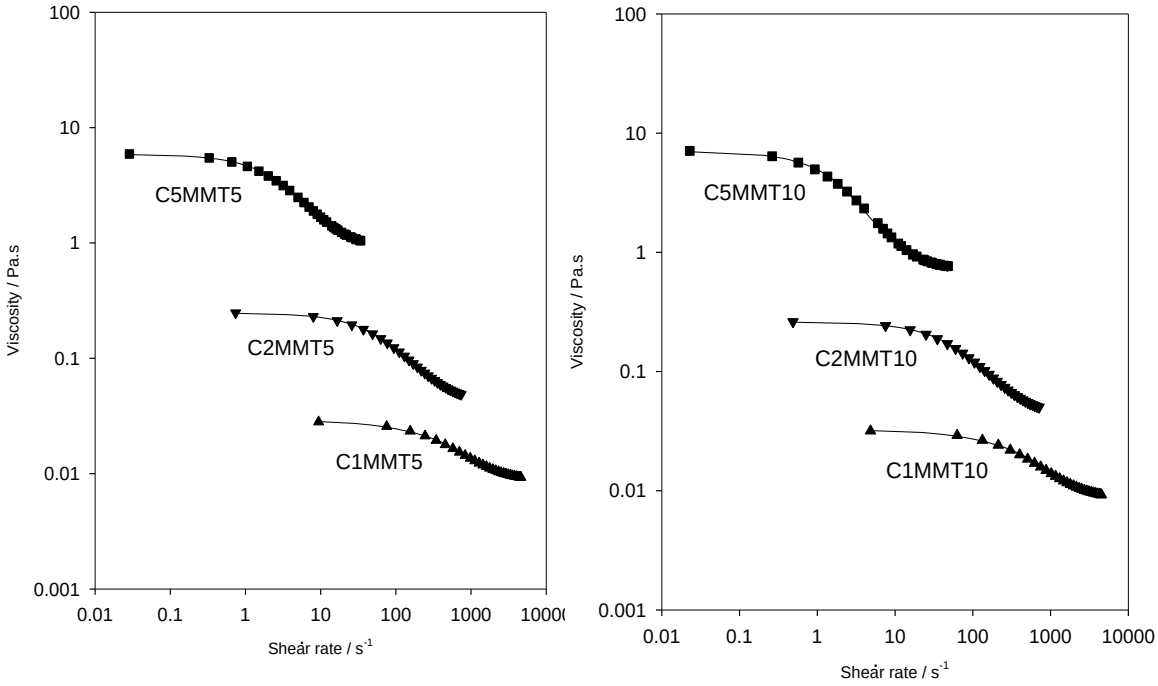

FIGURE 6.3 : Viscosity curves of 1, 2 and 5 PPHW 1M PEO samples with 5 PPHP MMT filler (left) and 10 PPHP MMT filler (right)

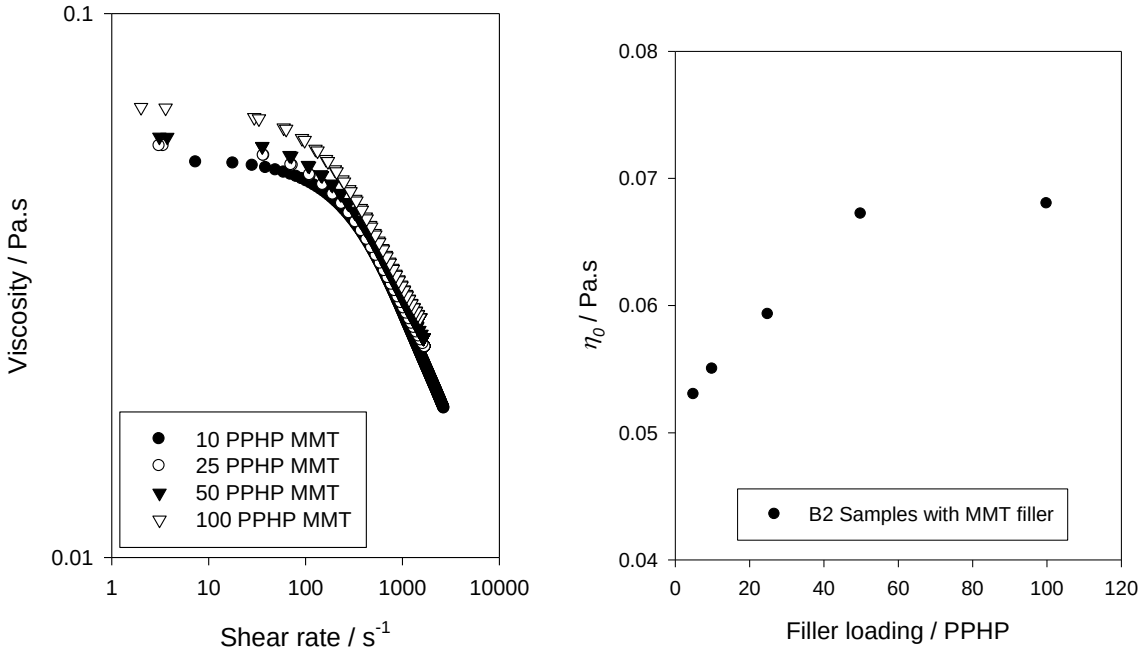

FIGURE 6.4 : Viscosity curves for higher filler loadings of MMT (left) and viscosity values at the zero shear rate as a function of filler loading (right)

The trend observed in the peak viscosity points of figure 6.4 show that the viscosity increases steadily with further addition of MMT, however this was not the case for the 100 PPHP loading. This suggests that a limit has been reached or that there is too much MMT for it to remain dispersed and is instead agglomerating.

6.2 Differential Scanning Calorimetry

Figure 6.5 shows the thermal transitions of PEO-MMT composites of varying filler loadings. It was noted that addition of 5 PPHP MMT provided little if any variation in both T_m or T_c values, suggesting that the MMT platelets are dispersed to such an extent that they have no effect on the crystallisation or melting processes. The crystallisation graph in figure 6.5 appears to show the same lack of variation with 10 PPHP filler loading, however looking at the melting graph it is clear that the MMT platelets are beginning to effect the melting process. At a filler loading of 25 PPHP and above this effect becomes much more prominent, in both T_m and T_c values. Addition of 50 PPHP MMT is noted to decrease the transition temperatures by as much as 14 ^{0}C.

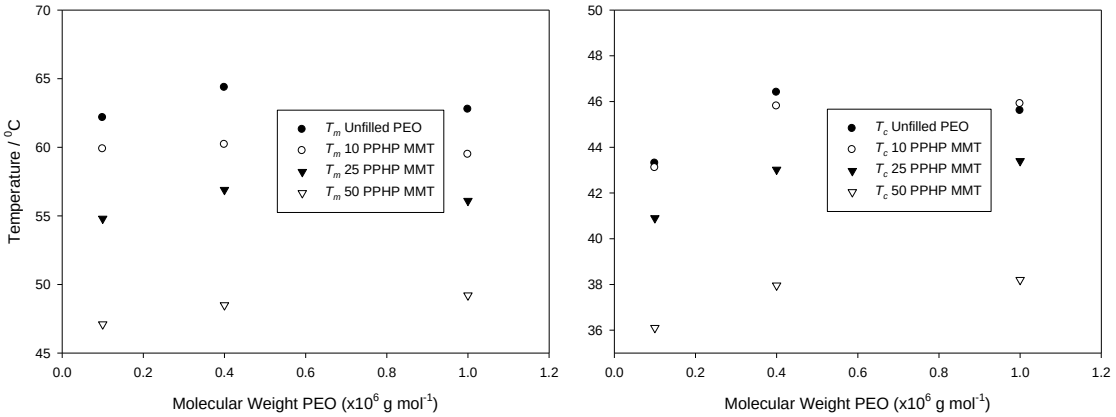

FIGURE 6.5 : The melting (left) and crystallisation (right) transition temperatures for PEO-MMT composite samples

Figures 6.6 and 6.7 show the ΔH_m and ΔH_c for the MMT filled samples. The 25 PPHP MMT had the largest values, followed by 50, then 100, PPHP. Using equation 4.10 from section 4.2.1, crystallinity values of 57.3 %, 30.6 % and 17.8 % were calculated with errors of ± 6, compared to the unfilled value of 73.4 % ± 5. This drop is particularly large, even more so than Saboormaleki et. al. [251] who saw a drop from 85 % down to 35 % for their PEO-lidocaine hydrochloride-propylene glycol samples.

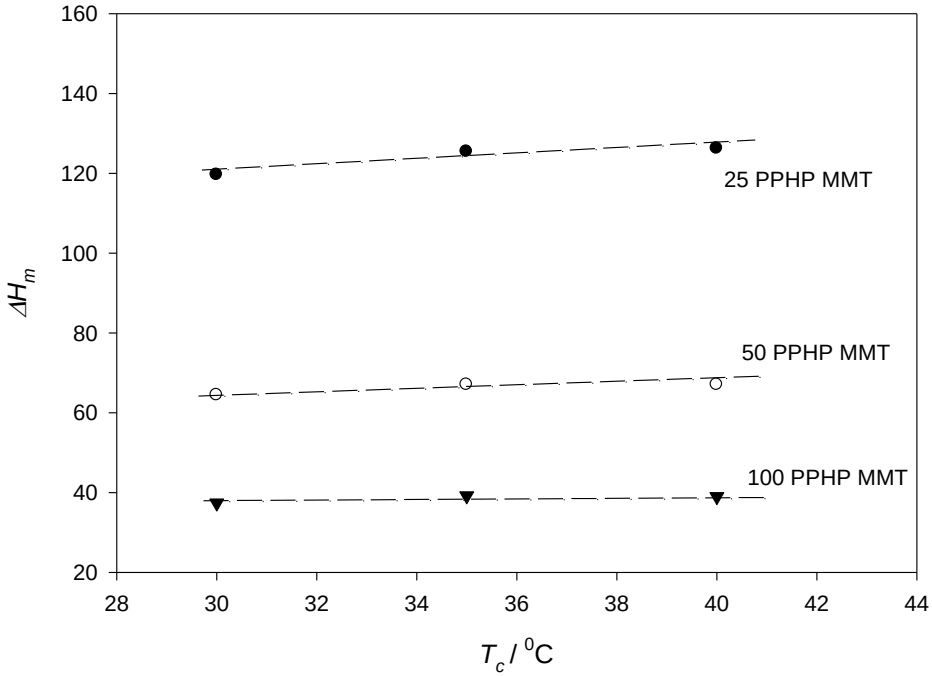

FIGURE 6.6 : ΔH_m values for the 25, 50 and 100 PPHP filled MMT 400k PEO

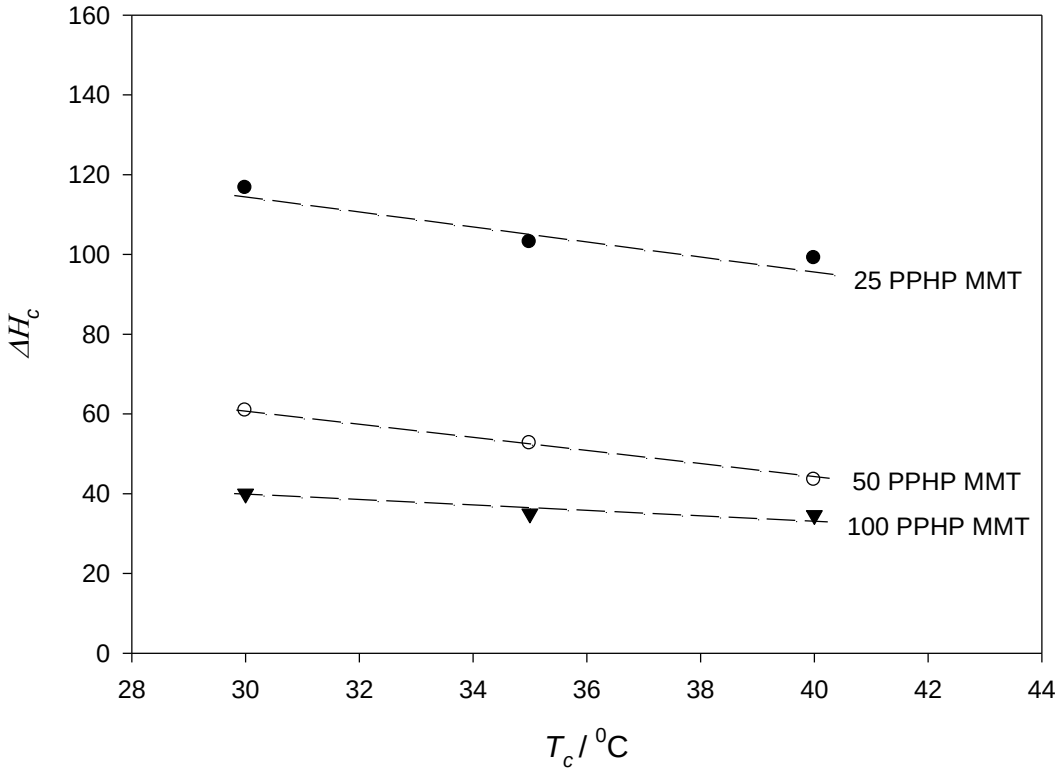

FIGURE 6.7 : ΔH_c values for the 25, 50 and 100 PPHP filled MMT 400k PEO samples

Previous investigations have often found that the PEO crystallinity is reduced for samples with plasticisers, fillers and for blends [280-281]. Work by Fan et. al. [282] into $(PEO)_{16}LiClO_4$ electrolytes showed that addition of MMT caused a drop from approximately 71 % to 50 % with a filler loading of only 30%. This decrease is comparable to the 25 PPHP filled sample from this investigation (57.3% crystallinity) suggesting that if they had continued to higher filler loadings they may have observed similar values to ours.

Work by Hikosaka et. al. [160] into PEO-MMT nanocomposites was of particular interest. They produced composites of 2,000 $gmol^{-1}$ PEO and MMT using two methods, which they refer to as 'wet' and 'dry' techniques. For the dry technique they melted the PEO at 80 ^{0}C and mixed in the MMT powder and stirred for an hour. Using this process they observed that the crystallinity of the resulting sample dropped from 95% for the unfilled PEO, down to 87% with 2% MMT filler loading. Further addition of MMT up to a loading of 25 PPHP caused no further drop in crystallinity. For the 'wet' technique, which is more comparable to the technique used in this

investigation, they dispersed the MMT in water and then mixed the solution into melted PEO at 80 ^{0}C and stirred until complete water evaporation had occurred. Using this process they observed a drop from 95% crystallinity down to 81% for 2% filler loading, a distinct change from the previous method they used. This decrease then continued in a linear fashion, with the 25 PPHP filled sample having a crystallinity of 40%. This decrease is even more than that seen in this investigation and they attributed this behaviour to the very high level of dispersion of MMT within the polymer and the interactions between the two.

6.2.1 Avrami analysis

Figure 6.7 shows the Avrami curves for the 50 and 100 PPHP MMT filled samples when crystallised at 30, 35 and 40 ^{0}C. As expected, the crystallisation times respond to the T_c in the same way as the unfilled PEO samples. Addition of MMT from 50 PPHP to 100 PPHP is seen to have little effect on the onset time for crystallisation, although up to 50 PPHP the crystallisation onset was observed to decrease with addition of filler suggesting a less extensive crystalline structure had formed due to the MMT platelets. It is worth noting that the form of the 40 ^{0}C curves appears to differ from that of the 30 ^{0}C and 35 ^{0}C. Whereas the lower two T_c curves produce the expected initial Avrami shape, the 40 ^{0}C data appear to curve in the opposite direction. There is no physical reasoning or precedent behind this behaviour, however repeat results produced the same curve.

The Avrami *n* and *k* values, shown in table 6.2, appear more erratic for these samples than the unfilled, SD, nSD and BO samples. Whereas for the previous unfilled and aged samples the *n* value has decreased with T_c, here the 25 PPHP sample follows this trend but the 50 and 100 PPHP do not, with 35 ^{0}C values that appear too large. Using equation 2.14 to calculate K_3 data, also shown in table 6.2, has produced values again showing a decrease with increasing T_c as seen before. The values appear reasonable when compared to those for unfilled and aged, although the decrease for 100 PPHP MMT may be considered slightly too large. In general the K_3 values for MMT filled samples and unfilled samples show no defining difference.

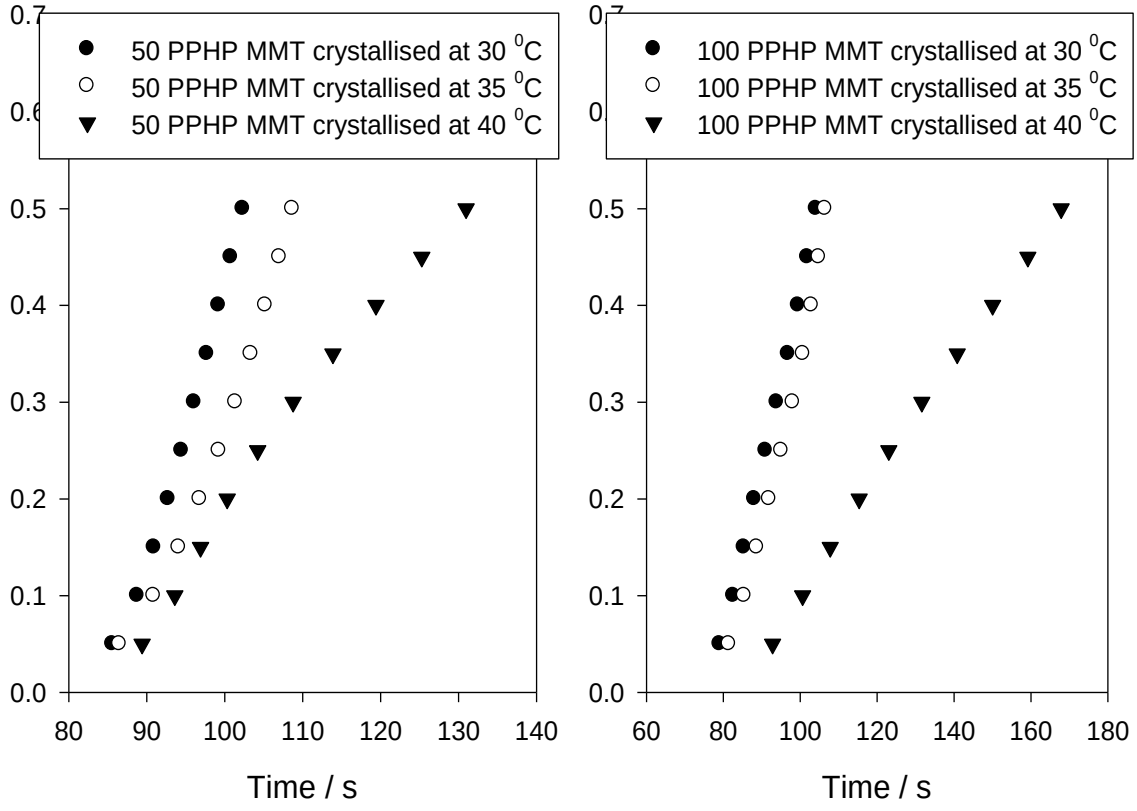

FIGURE 6.7 : Crystallisation data collected for the 50 PPHP (left) and 100 PPHP (right) MMT filled 400k PEO samples

Sample / PPHP	**T_c / ^{0}C**	**Avrami parameters**			
		n	**k (s^{-1})**	**R^2**	**K_3**
25 MMT	30	4.279	1.239×10^{-6}	0.9999	7.22×10^{-5}
25 MMT	35	1.729	2.815×10^{-3}	0.9996	3.75×10^{-5}
25 MMT	40	1.406	6.011×10^{-3}	0.9996	1.82×10^{-5}
50 MMT	30	2.236	5.683×10^{-4}	0.9999	4.42×10^{-5}
50 MMT	35	3.52	1.224×10^{-6}	0.9999	9.14×10^{-6}
50 MMT	40	0.97	1.751×10^{-2}	0.9992	3.73×10^{-6}
100 MMT	30	1.642	2.283×10^{-3}	0.9988	1.49×10^{-5}
100 MMT	35	3.021	6.332×10^{-6}	0.9969	6.88×10^{-6}
100 MMT	40	1.151	4.15×10^{-3}	0.9996	6.19×10^{-7}

TABLE 6.2 : The Avrami parameters generated for the MMT filled 400k PEO samples

The T_c vs T_m data collected using the method detailed in section 2.2.3 is represented in figure 6.8. The 50 and 100 PPHP samples provide very similar T_m^0 values within the associated error of 1 ^{0}C of each other. Table 6.3 below shows the T_m^0 values calculated using both methods, mentioned in section 4.2.1, along with the associated errors. Despite a difference of around 7 ^{0}C between the unfilled and MMT filled samples it is clear that the variation between the different filler loadings is well within error. Since the T_m value is related to the growth rate, this suggests that the MMT is indeed affecting the growth rate, but this is independent of filler loadings between 25-100 PPHP.

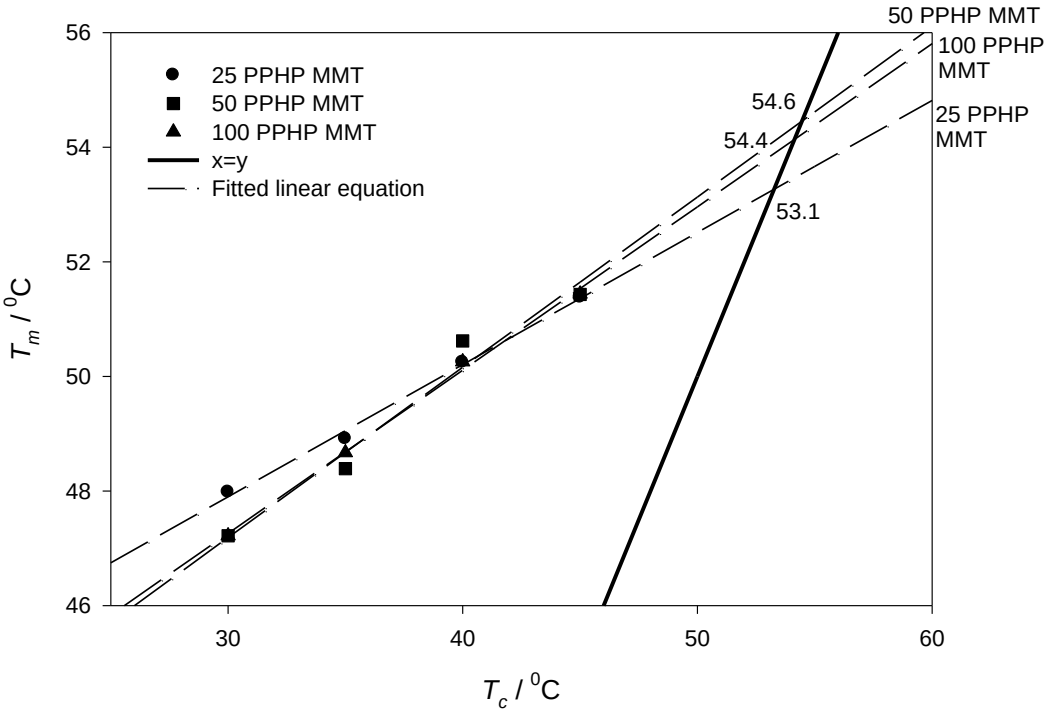

FIGURE 6.8 : T_c vs T_m plots for the MMT filled 400k PEO systems along with the T_c=T_m intercept values in ^{0}C

Sample / PPHP	**T_m^0 (^{0}C)**	
	T_m vs T_c	**T_c vs T_m-T_c**
Unfilled	60.9	60.8 ± 1.2
25 MMT	53.1	53.3 ± 1.0
50 MMT	54.4	54.4 ± 1.6
100 MMT	54.6	54.1 ± 1.0

TABLE 6.3 : T_m^0 values using both methods with the associated error

6.3 AC Electrical Breakdown

Figure 6.9 shows that addition of up to 10 PPHP MMT has produced no change in breakdown strength, with confidence bounds overlapping considerably. Therefore any effects caused by addition of a small amount of MMT are too small to be realised. This suggests that the dispersion achieved within the system is fairly high at these filler loadings. This is supported by previous work by Vaughan et. al. [50] on the breakdown strength of polyethylene-MMT composites, where a good example of dispersion dependence is given. Figure 6.10 shows a quenched material E, pure polyethylene, compared to a material C, polyethylene with poorly dispersed MMT, reprinted from [50]. A drop in breakdown strength was seen along with a much wider range. Comparing this to material B, a well-dispersed PE-MMT sample, a much smaller drop in breakdown strength was observed, suggesting a high level of dispersion can lead to little or no decrease in breakdown strength.

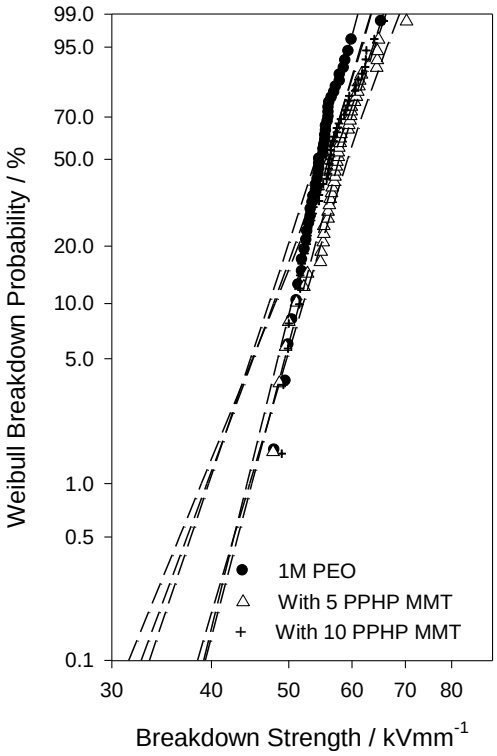

FIGURE 6.9 : Breakdown plots of 1M PEO with up to 10 PPHP MMT

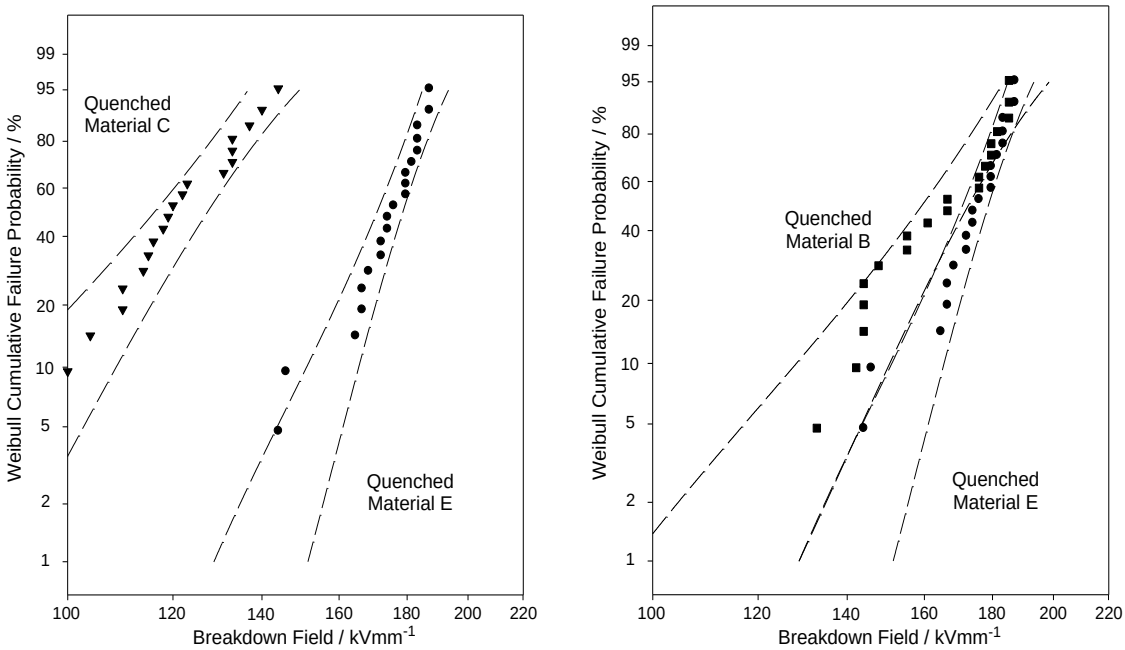

FIGURE 6.10 : Material E, polyethylene, compared to material C, a poorly dispersed PE-MMT composite and material B, a well dispersed PE-MMT composite. Reprinted from [50]

With addition of 25 PPHP MMT and higher, shown in figure 6.11, the breakdown strength of the material is actually seen to increase, appearing to reach a value of approximately 150% of the unfilled breakdown strength at the highest 100 PPHP loading. Figure 6.12 shows the α values and Weibull associated uncertainties for the filled samples along with the generated β values. This increase in breakdown strength is surprising, since in most cases the breakdown strength of polymer composites is seen to increase at low percentages before decreasing. For example, work by Wu et. al. [283] into Al_2O_3/polyimide films showed that addition of 2% filler produced an increase of approximately 10 kV/mm, with the breakdown strength decreasing with further addition of filler, dropping by approximately 30 kV/mm for the 20% filled sample. Most previous investigations have found that addition of filler can increase the breakdown strength at low filler loadings, such as work by Hu et. al. [284], who found that their epoxy DC and AC breakdown strengths could be improved by 18% and 9% respectively with addition of nano TiO_2. They believed that the large surface area and improved dispersion method were the reason for the increase. The increase in breakdown strength observed in this investigation is thought to be due to the increased

breakdown path length relative to the filler loading as the breakdown occurs through the poorly insulating polymer rather than the platelet filler.

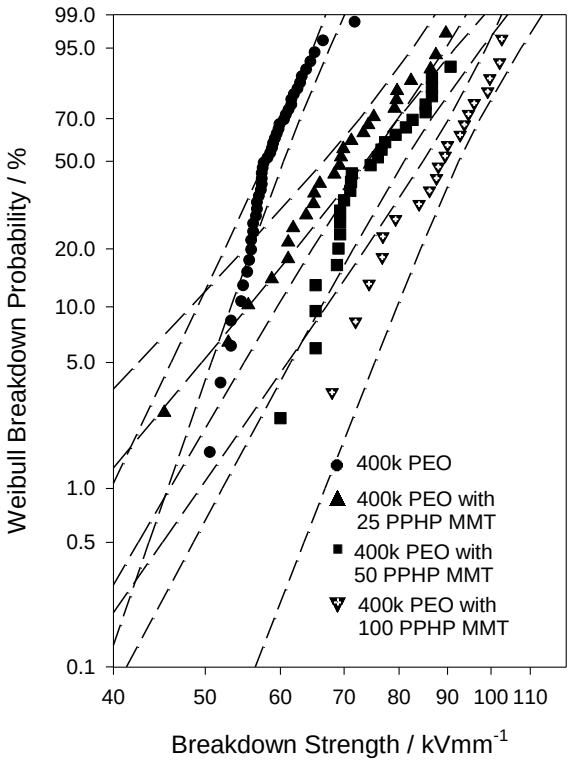

FIGURE 6.11 : Breakdown plots of 400k PEO with up to 100 PPHP MMT filler

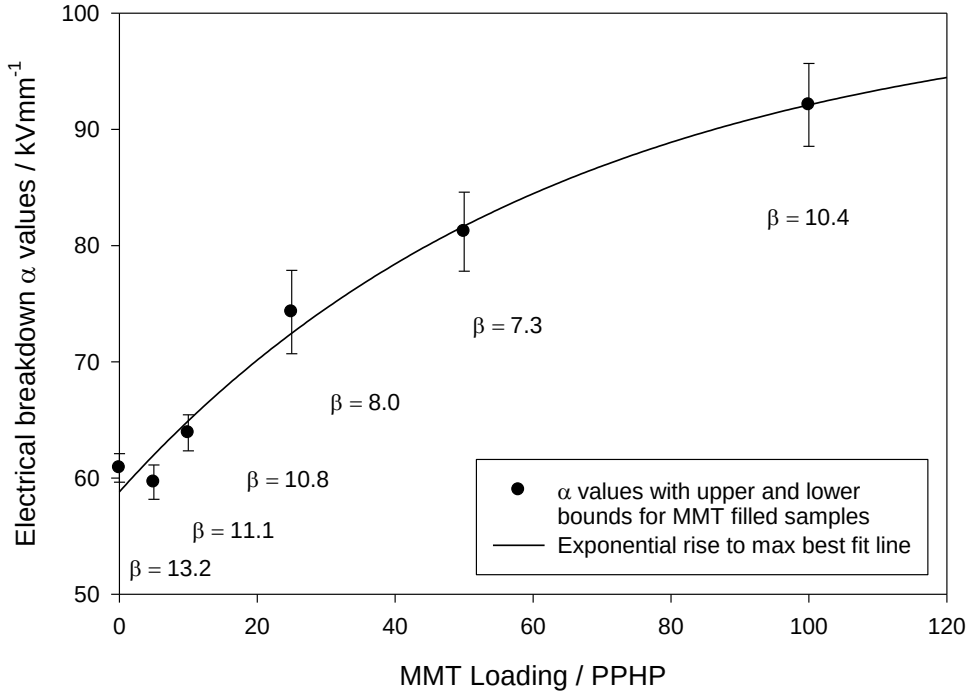

FIGURE 6.12 : α values (with upper and lower values) calculated from the Weibull equation for increasing MMT filler loading

6.4 Chapter Summary

Rheology of the PEO-MMT composites showed that up to 10 PPHP MMT could be added without effecting the flow dynamics and mobility of the chains within the system, attributed to a high level of dispersion. Further addition of MMT up to 50 PPHP produced a steady increase in differential viscosity, whereas addition of a further 50 PPHP, achieving a total concentration of 100 PPHP, showed no further increase in viscosity, attributed to the MMT platelets beginning to agglomerate at such a high filler loading.

Using DSC, addition of up to 5 PPHP MMT caused no change in the thermal transition temperatures, also suggesting that the level of dispersion here is high. Addition of further MMT was found to lower the thermal transition temperatures. From enthalpy data, crystallinity values were calculated to be 73.4%, 57.3%, 30.6% and 17.8% for unfilled, 10 PPHP, 25 PPHP and 50 PPHP respectively. This strongly suggests that the MMT is hindering the crystallisation process. Avrami K_3 values were again seen to decrease with increasing T_c as expected, but in general were not seen to vary much from those for the unfilled sample, suggesting that the nucleation rate was not affected.

The breakdown strength of the PEO-MMT systems was unchanged with up to 10 PPHP, attributed again to the high level of dispersion within the system. Addition of further filler produced a non-linear increase, with addition of more filler having less effect each time, possibly suggesting that the MMT is agglomerating. In general the increase in breakdown strength is thought to be due to the increase breakdown path length.

Chapter 7: PEO-MICRO AND NANO SILICON DIOXIDE COMPOSITES

7.1 Rheometry

In similar fashion to the addition of up to 10 PPHP MMT, addition of up to 10 PPHP SD produced no noticeable effect on the peak shear rate values, shown in table 7.1. A graphical representation of the peak values (similar to figure 4.24), confirms the same sample order. As before, viscosity data were calculated using the hyperbolic function, producing graphs such as figure 7.1. From these it is clear that up to 10 PPHP micro SD has been dispersed well enough into the system that it does not affect the mobility or entanglement of the polymer chains.

Sample	Peak Shear Rate 5 PPHP SD Filler	Peak Shear Rate 10 PPHP SD Filler
A5	3730	3830
A10	832	853
B1	5150	5150
B2	2070	2090
B5	126	98.9
C1	4400	4330
C2	793	826
C5	21.2	21.2

TABLE 7.1 : Peak shear rate values for PEO-SD composite samples

Overall the calculated viscosity data for up to 10 PPHP followed the same trends set by the virgin PEO and PEO-MMT composites. This suggests that the SD particles have not changed the mobility within the system at these low loadings. However with higher loadings, shown in figure 7.2, it was observed that the SD particles do affect the flow and mobility of the chains within the solution. The micro spheres of SD

appear to cause a linear increase in viscosity up to a loading of 100 PPHP at which point the viscosity is almost double that of the unfilled or 10 PPHP filled samples.

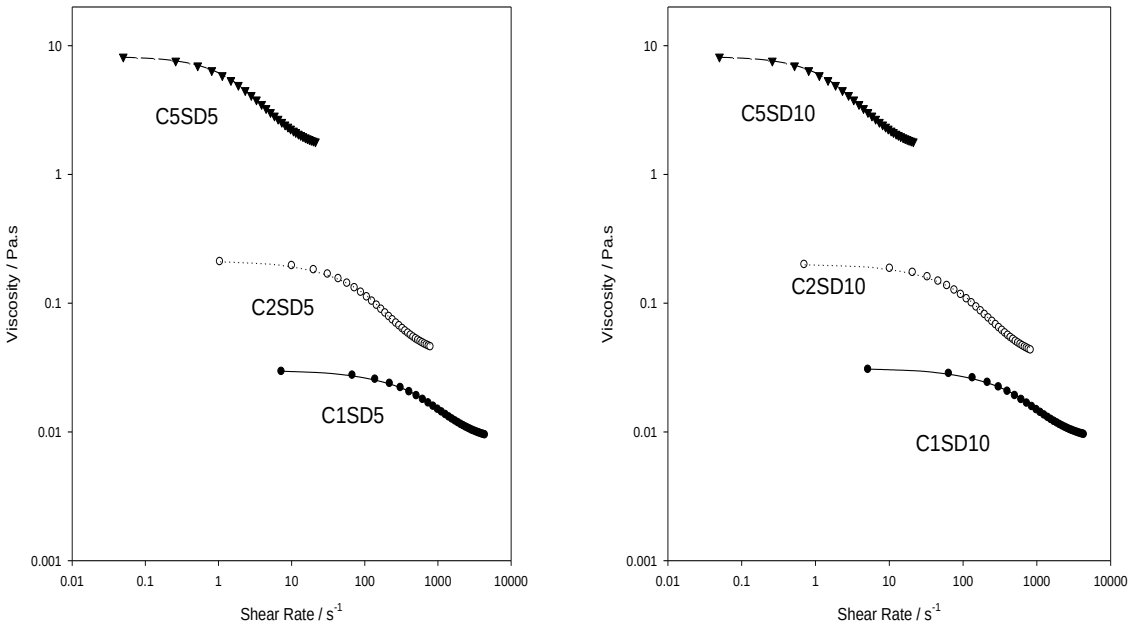

FIGURE 7.1 : Viscosity curves of 1, 2 and 5 PPHW 1M PEO samples with 5 PPHP SD filler (left) and 10 PPHP SD filler (right)

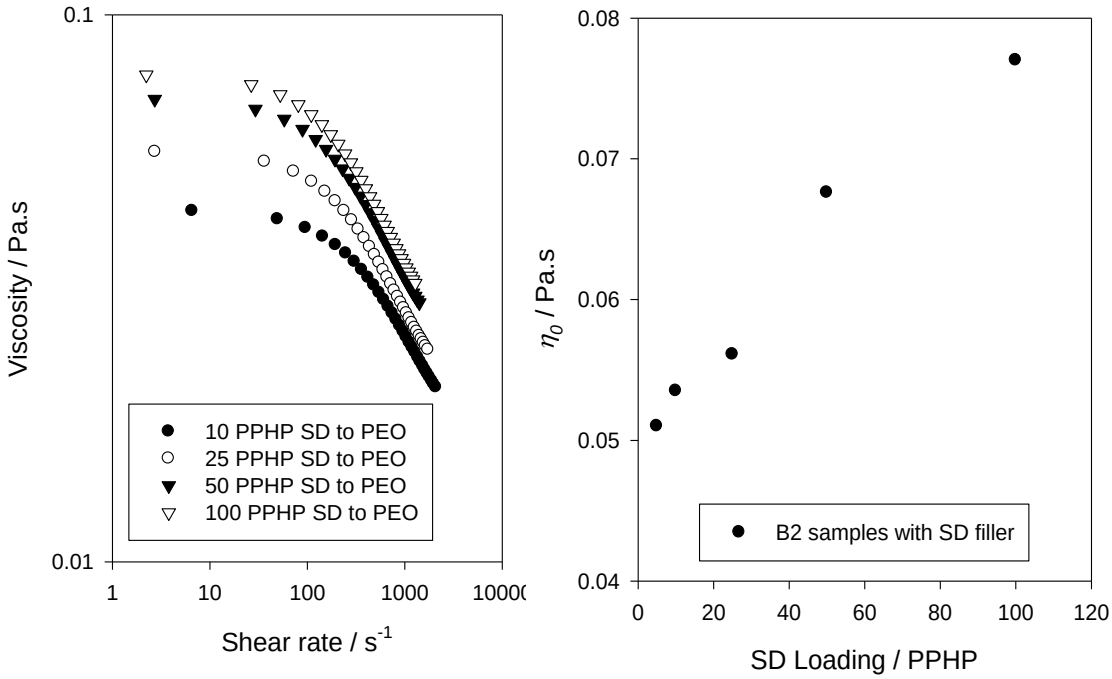

FIGURE 7.2 : Viscosity curves for higher filler loadings of SD (left) and viscosity values at the zero shear rate as a function of filler loading (right)

Many composite material models recognise a difference between adding micro and nano sized particles to a polymer matrix. Despite chemically being the same material, the particles are far smaller and may interact with the polymer in a completely different way. Having observed that up to 10 PPHP SD could be added with no physical effect on the viscosity or flow dynamics, it might be expected that addition of smaller particles of the same material would produce the same result. This was not the case however, as table 7.2 shows, addition of up to 5 PPHP nSD provides no major change to unfilled samples, however addition of 10 PPHP shows a drop in almost all values.

Sample	Peak Shear Rate 5 PPHP nSD Filler	Peak Shear Rate 10 PPHP nSD Filler
A5	3690	3210
A10	802	756
B2	1580	1570
B5	119	83.1
B10	8.46	4.25
C1	3610	3630
C2	1300	759
C5	24.4	9.8

TABLE 7.2 : Peak shear rate values for PEO-nSD composite samples

This suggests that the viscosity has increased, a belief confirmed by viscosity plots, such as those in figure 7.3. From these plots it is clear that the nano-sized particles are disrupting the flow dynamics of the system a great deal more so than the micro-sized particles. This emphasises the understanding that particle size is extremely important when choosing additives for composites. It should be noted that the increase in viscosity due to further addition of filler is more evident for higher PEO loading samples, which is understandable since the nSD particles have more chains to interrupt. In some cases, such as the C2 PEO sample, the addition of a further 5 PPHP nSD causes the viscosity to double. With addition of up to 100 PPHP nSD filler, shown in figure 7.4, it is observed that the viscosity rises as expected.

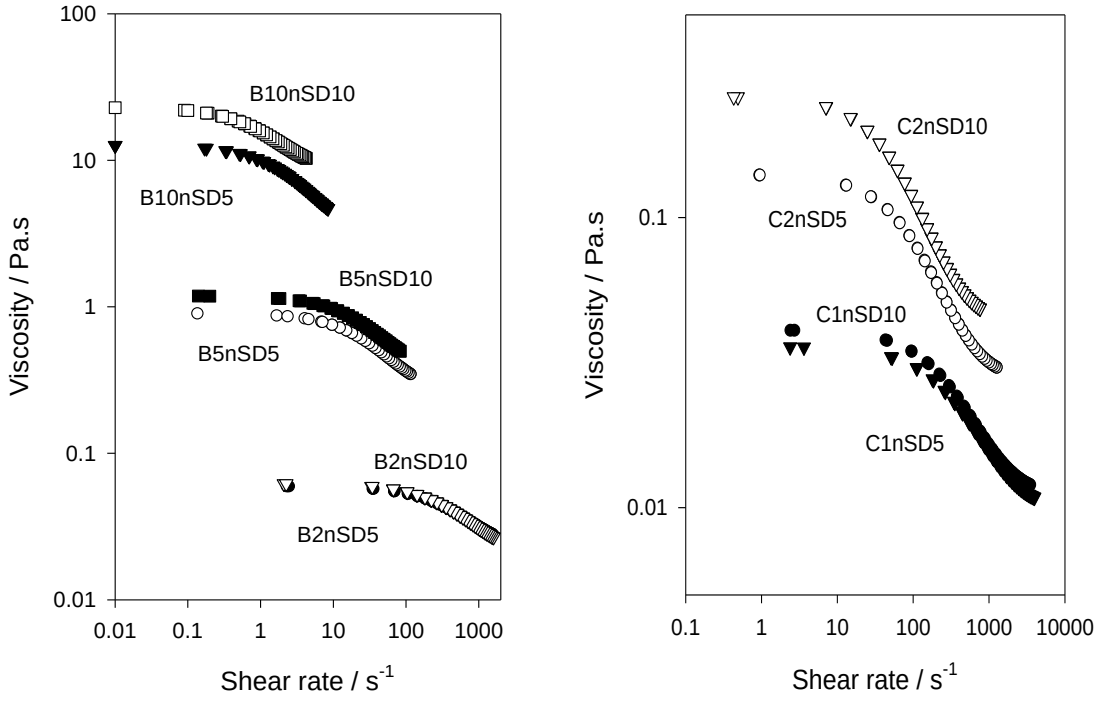

FIGURE 7.3 : Viscosity curves for 400k PEO (left) and 1M PEO (right) samples with up to 10 PPHP nSD filler

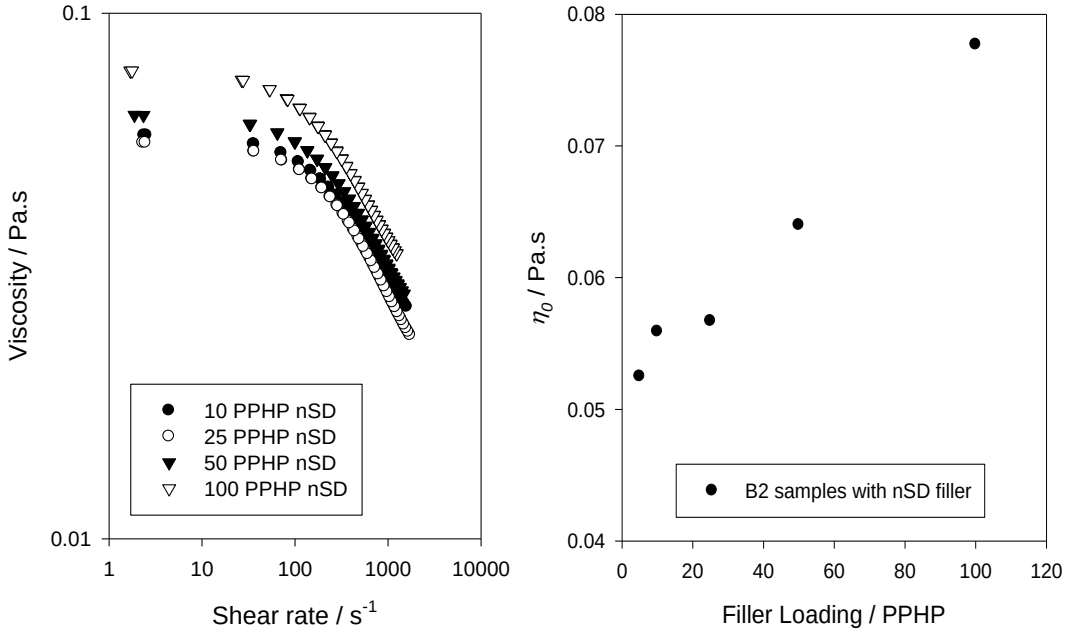

FIGURE 7.4 : Viscosity curves for higher filler loadings of nSD (left) and viscosity values at the zero shear rate as a function of filler loading (right)

Comparing the viscosity response to increased filler loadings, the graphs on the right in figures 7.2 and 7.4, it is seen that the viscosity increase for loadings of 25 PPHP – 100 PPHP appear independent of particle size. Both micro and nano fillers provide similar peak viscosity values for all loadings. Apart from the earlier onset of viscosity

increase (at 5 PPHP for nSD rather than 10 PPHP for SD) the particle size appears to be generally irrelevant. This suggests that the two fillers are behaving in the same way and that the nSD may be agglomerating, due to the cohesive forces between same-type molecules, into larger forms and mimicking the microSD at loadings of 25 PPHP and above, hence the similar rheometric response. To check this, techniques such as etching and SEM could be employed, however etching of PEO is still relatively un-tested, as discussed in Appendix 5.

Previous work by Dorigato et. al. [285] into linear low-density polyethylene – silica nanocomposites analysed the effect of filler size on rheology from large 50 μm microspheres to nanoparticles. They tested four silica fillers in total with surface areas; 0.5 m^2/g (microspheres), 168.3 m^2/g (silica microparticles), 196.6 m^2/g (fumed silica nanoparticles) and 320.8 m^2/g (also fumed silica nanoparticles). They believed that a direct relationship between surface area and rheological response would be observed. Using a parallel plate viscometer and filler loadings up to 4% they observed very little change in the largest particle size (lowest surface area) samples. For the silica micro and nanoparticles however, a massive increase in viscosity was observed, almost 2 orders of magnitude for the 4% loading. This increase in viscosity became larger as the particle size became smaller, indeed suggesting a direct relationship to the surface area. These findings support those from this investigation and it is easy to see how their microspheres and the microSD used here behave similarly, showing no viscosity increase at 5 PPHP filler loading, as well as their nanoparticles and the nSD used here showing an increase at 5 PPHP.

Zhang et. al. [286] created PEO-nanosilica solutions of 0.2%, 1%, 1.5% and 2% filler loadings, which they tested using a Paar Physica MCR300 rheometer. Their data revealed a large increase in viscosity at even the lowest filler loading of their 12 nm silica particles, showing a massive increase to around 600% zero-shear viscosity value when compared to the unfilled sample. For their surface modified 12 nm silica and 100 nm silica however, the increase was significantly lower, although an increase did exist. This supports the behaviour of the nSD samples here having increasing viscosities at the lowest filler loading, however it is still possible that at higher loadings the nanoparticles are agglomerating and behaving more like microparticles.

7.2 Differential Scanning Calorimetry

The thermal transitions of the PEO-SD composites are shown in figure 7.5. Similarly to the addition of up to 5 PPHP MMT, 5 PPHP SD samples produced little change to the thermal transitions, suggesting the micro SD spheres were dispersed well enough to have negligible effect thermally. The 10 PPHP samples produced little change in T_m but the effect was more visible in the T_c, and became much more obvious at loadings of 25 PPHP and above. At a loading of 25 PPHP the T_c and T_m are seen to decrease by as much as 10 ^{0}C and 12 ^{0}C respectively. Comparing this to the MMT composites shows that the MMT platelets are having more of an effect than the SD spheres.

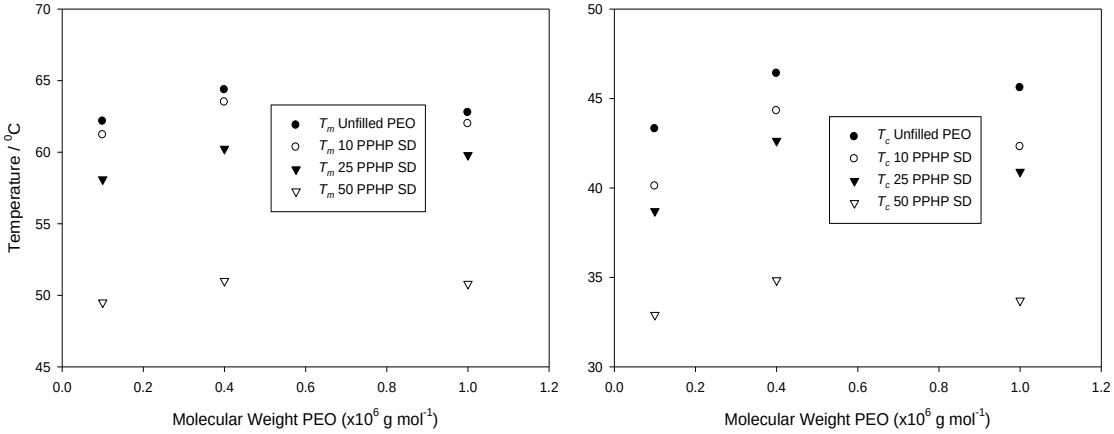

FIGURE 7.5 : The melting (left) and crystallisation (right) transition temperatures for PEO-SD composite samples

With addition of up to 5 PPHP nSD no real difference in transition temperatures was detected. Addition of a further 5 PPHP produced a similar response to that of micro SD, a sharp drop in T_m and a small drop in T_c. At a filler loading of 25 PPHP the T_c and T_m are both seen to decrease substantially. As seen with the other fillers, addition of 50 PPHP produces a further decrease, but on a far smaller scale. Comparing these values to that of the PEO-SD composite it is seen that the nSD is also affecting the thermal transitions, but to a smaller extent. Whereas 50 PPHP SD filler reduced the T_m and T_c to 51 ^{0}C and 35 ^{0}C respectively, the 50 PPHP nSD only reduced the transitions to 53 ^{0}C and 39 ^{0}C. This is assumed to be directly related to the size of the

SD particles, with the nano size spheres having less effect on the melting and crystallising processes.

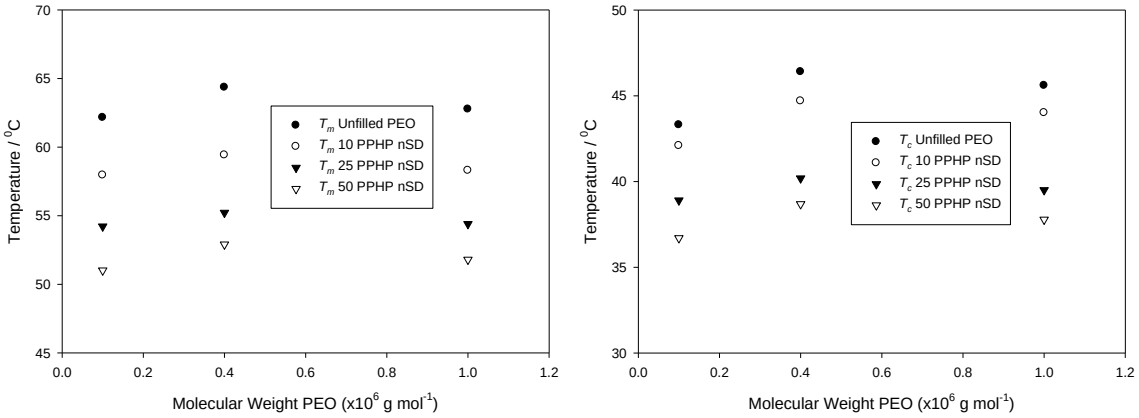

FIGURE 7.6 : The melting (left) and crystallisation (right) transition temperatures for PEO-nSD composite samples

Figures 7.7 and 7.8 show the ΔH_m and ΔH_c for microSD filled samples. Similarly to the MMT samples, the 25 PPHP filler loading has the highest ΔH_m and ΔH_c values, dropping for the 50 and 100 PPHP samples. When comparing these to the values calculated for the nanoSD filler samples, shown in figures 7.9 and 7.10, a drop in all values is observed. This suggests that the crystal structure being formed in the sample during crystallisation is less extensive, thus less energy is required to melt the sample. Calculated crystallinity values, shown in table 7.3, should confirm this belief.

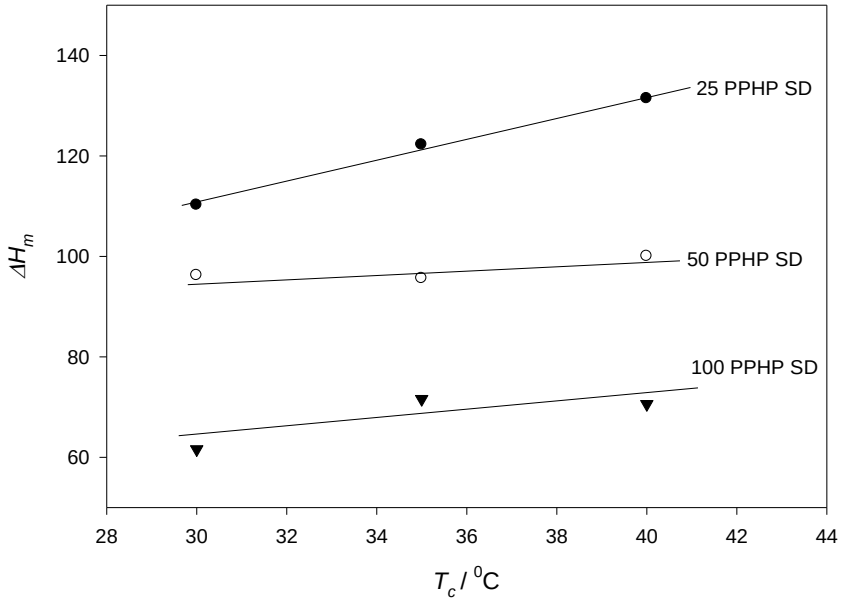

FIGURE 7.7 : ΔH_m values for the 25, 50 and 100 PPHP filled SD 400k PEO samples

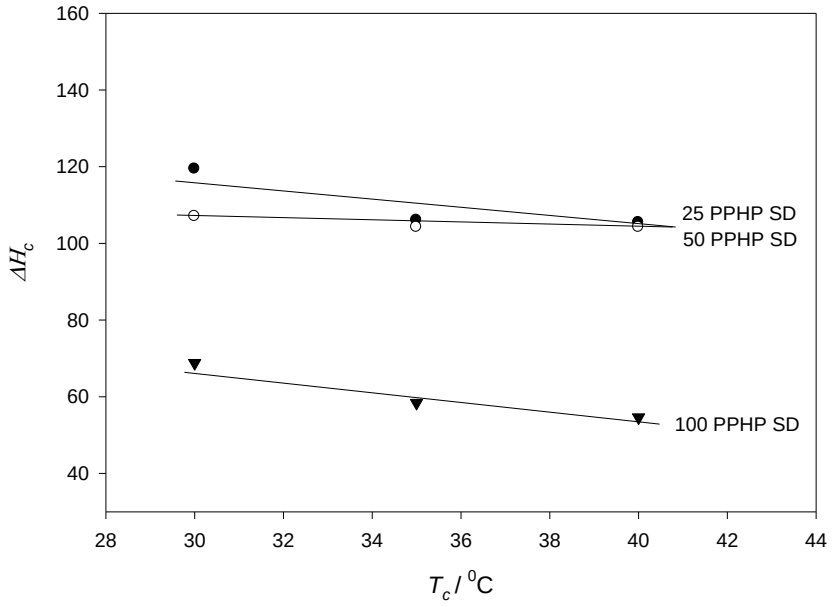

FIGURE 7.8 : ΔH_c values for the 25, 50 and 100 PPHP filled SD 400k PEO samples

Crystallinity %				
Samples	Unfilled	25 PPHP	50 PPHP	100 PPHP
SD	73.4	56.1	45.0	31.4
nSD	73.4	82.8	71.1	61.5

TABLE 7.3 : Calculated crystallinity values for SD and nSD samples

From these data it is clear that addition of micro SD reduces the crystallinity of the sample. The nSD however, is observed to initially increase the crystallinity at 25 PPHP, possibly acting as nucleation sites, before also causing a decrease in crystallinity. At the 50 and 100 PPHP loadings the micro-sized filler seems to hinder crystallisation much more than the nano-filler, with a crystallinity of around half the initial value at a 100 PPHP loading. SD has been seen to decrease crystallinity before [287] and a linear decrease has been observed when using nSD [288]. The variation in crystallinity between the micro and nano fillers could be due to the dispersion and interactions between the filler-polymer in a similar response as that seen by Hikosaka et. al. [160] for their further dispersed MMT samples.

These data suggest that the micro SD is more disruptive to the crystallisation process than the nSD. This is unexpected since the interactions are related to the filler surface

area, suggesting that the nSD here has less surface area than the micro SD. This could suggest that the nSD is agglomerating to produce fewer groups of particulates that represent a lower surface area. If the nSD particles are agglomerating, this suggests that the rheometer is unable to disperse the nSD particles within the solution at a 25 PPHP concentration and higher, relating to the very small particle size.

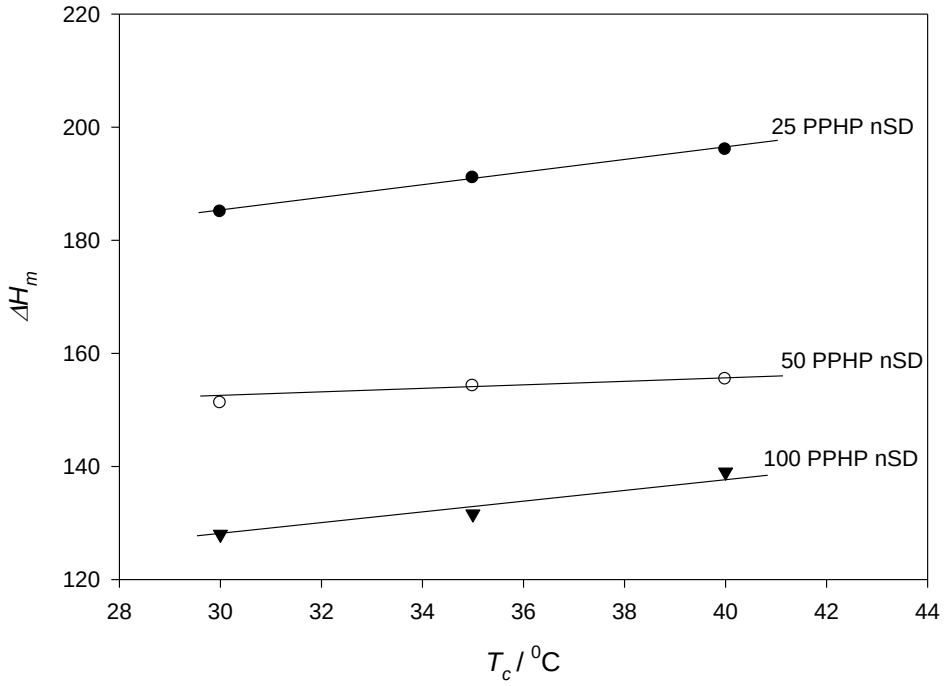

FIGURE 7.9 : ΔH_m values for the filled nSD 400k PEO samples

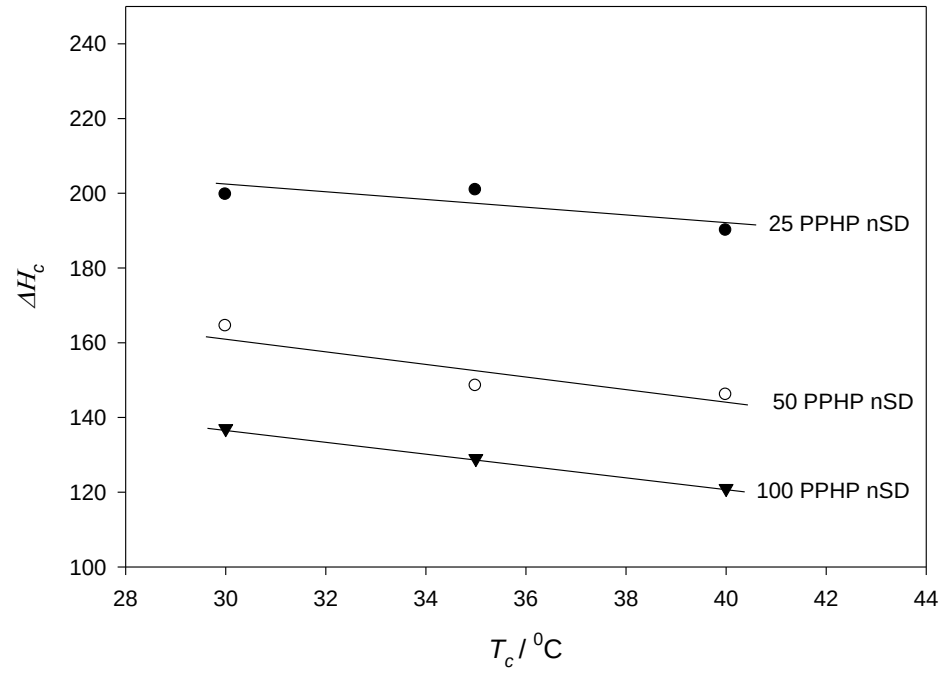

FIGURE 7.10 : ΔH_c values for the filled nSD 400k PEO samples

7.2.1 Avrami analysis

Figure 7.11 below shows the Avrami curves for the 50 and 100 PPHP SD samples crystallised at 30-40 ^{0}C. The curves show predicted behaviour except for the 100 PPHP loading at 40 ^{0}C which appears to show a large increase in crystallisation time and variation in form, similar to that seen in section 6.2.1 for the 100 PPHP MMT sample at 40 ^{0}C. The data were retaken several times and this behaviour remained. The general shape of the other curves collected for SD were in line with the data for unfilled, aged and MMT. The Avrami curves for the 50 and 100 PPHP filled nSD samples are shown in figure 7.12. The 100 PPHP sample shows the expected trend of increasing time with increasing T_c however there again appears to be a large increase in crystallisation time for the 50 PPHP sample at 40 ^{0}C. It is hard to define the cause for this behaviour in several of the samples tested, but for the samples exhibiting this increase in crystallisation time a decrease in K_3, shown in tables 7.4 and 7.5 is observed, as expected.

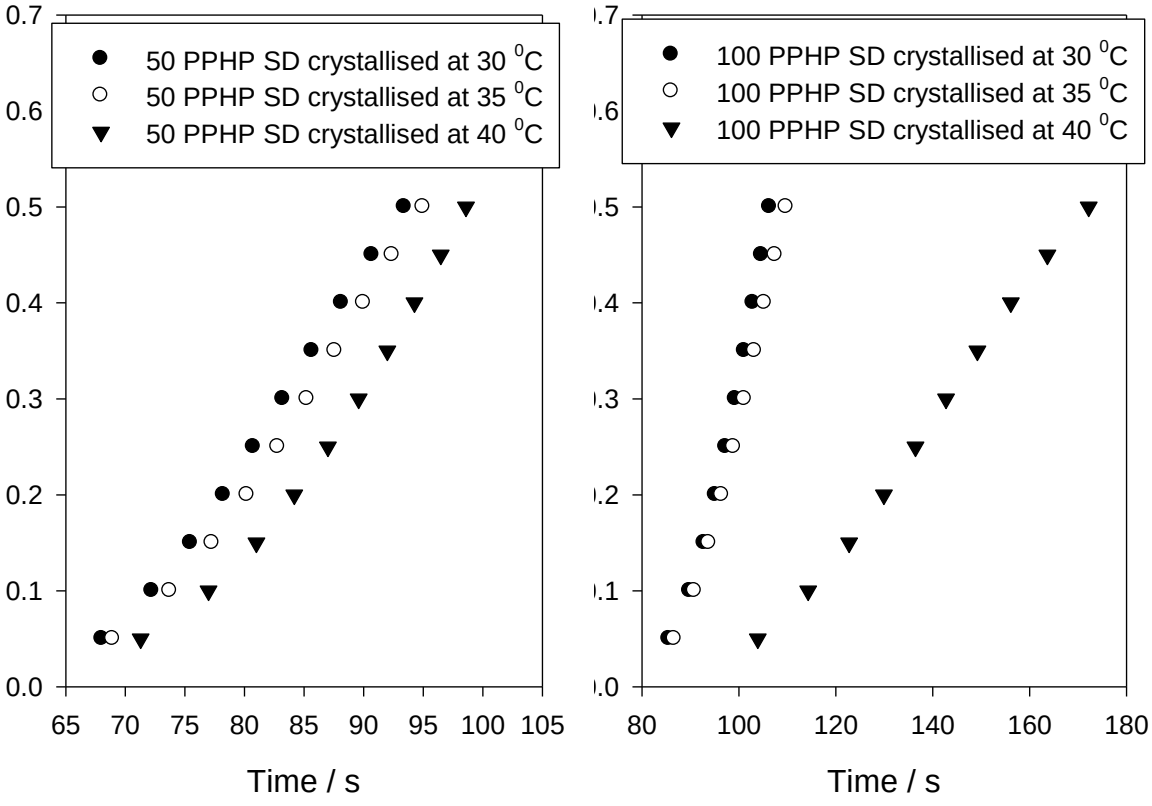

FIGURE 7.11 : Crystallisation data collected for the 50 PPHP (left) and 100 PPHP (right) SD filled 400k PEO samples

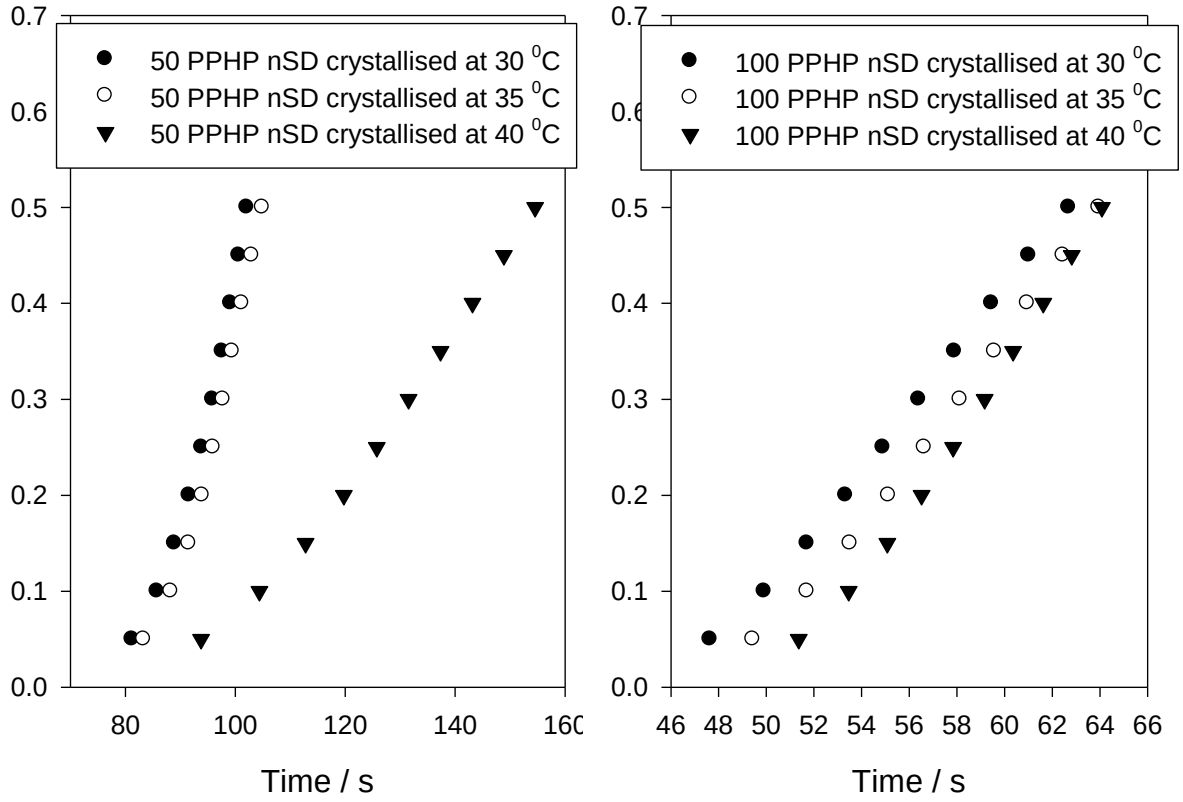

FIGURE 7.12 : Crystallisation data collected for the 50 PPHP (left) and 100 PPHP (right) nSD filled 400k PEO samples

Sample / PPHP	T_c / ^{0}C	Avrami parameters			
		n	k (s^{-1})	R^2	K_3
25 SD	30	3.075	9.153×10^{-5}	0.9999	1.15×10^{-4}
25 SD	35	3.105	9.291×10^{-5}	0.9999	1.27×10^{-4}
25 SD	40	3.163	8.274×10^{-5}	0.9999	1.34×10^{-4}
50 SD	30	1.849	1.076×10^{-3}	0.9998	1.53×10^{-5}
50 SD	35	2.265	1.896×10^{-4}	0.9998	1.17×10^{-5}
50 SD	40	3.456	8.410×10^{-7}	0.9999	5.33×10^{-6}
100 SD	30	3.017	1.427×10^{-5}	0.9999	1.52×10^{-5}
100 SD	35	2.217	2.97×10^{-4}	0.9999	1.69×10^{-5}
100 SD	40	1.59	6.263×10^{-4}	0.9991	9.04×10^{-6}

TABLE 7.4 : The Avrami parameters generated for the SD filled 400k PEO samples

Sample / PPHP	T_c / ^{0}C	Avrami parameters			
		n	k (s^{-1})	R^2	K_3
25 nSD	30	4.464	1.604 x10^{-8}	0.9993	5.78 x10^{-6}
25 nSD	35	4.277	2.339 x10^{-8}	0.9988	4.44 x10^{-6}
25 nSD	40	2.295	5.065 x10^{-5}	0.9999	2.43 x10^{-6}
50 nSD	30	4.393	3.219 x10^{-8}	0.9996	7.65 x10^{-6}
50 nSD	35	3.433	2.412 x10^{-6}	0.9989	1.23 x10^{-5}
50 nSD	40	2.194	3.884 x10^{-5}	0.9999	9.31 x10^{-7}
100 nSD	30	1.656	5.38 x10^{-3}	0.9999	7.75 x10^{-5}
100 nSD	35	1.82	3.259 x10^{-3}	0.9999	7.96 x10^{-5}
100 nSD	40	1.988	2.373 x10^{-3}	0.9999	1.09 x10^{-4}

TABLE 7.5 :The Avrami parameters for the nSD filled 400k PEO samples

The Avrami parameters *n* and *k*, in tables 7.4 and 7.5 for the SD and nSD samples respectively, show the same general behaviours as those for the unfilled and MMT samples. Again, the majority of the K_3 values decrease with increasing T_c as expected. A trend of decreasing K_3 values with increasing filler loading is observed for SD samples as the filler is believed to hinder the crystallisation. The nSD however, has K_3 values much lower than that of the micro SD for the lowest filler loading, suggesting less hindrance to the crystallisation process. As the filler loading increases however, the K_3 value also increases. This behaviour suggests that the 25 PPHP nSD sample is well dispersed with low K_3 values, while increasing the filler loading to 100 PPHP produces much higher values indicative of either; phase separation in the melt or nSD aggregation during the crystallisation, which explains why the K_3 values for the 100 PPHP nSD sample appear very similar to the values for the 25 PPHP micro SD.

Figures 7.13 and 7.14 show the T_m^0 calculated values using the theory detailed in section 2.2.3. All values for both fillers appear to have decreased from that of the unfilled PEO, with a value of 60.8 ^{0}C. The SD values are fairly close to some of those collected for the MMT samples, while the nSD samples are 3 ^{0}C higher. The variation between nSD and microSD samples is observed between all comparable filler loading samples. The values within each figure differ by much more than the associated 1 ^{0}C

error, and are therefore deemed to be genuine. The increasing T_m^0 with increasing nSD filler content suggests the system is becoming more PEO-like with less filler effect, again supportive of phase separation.

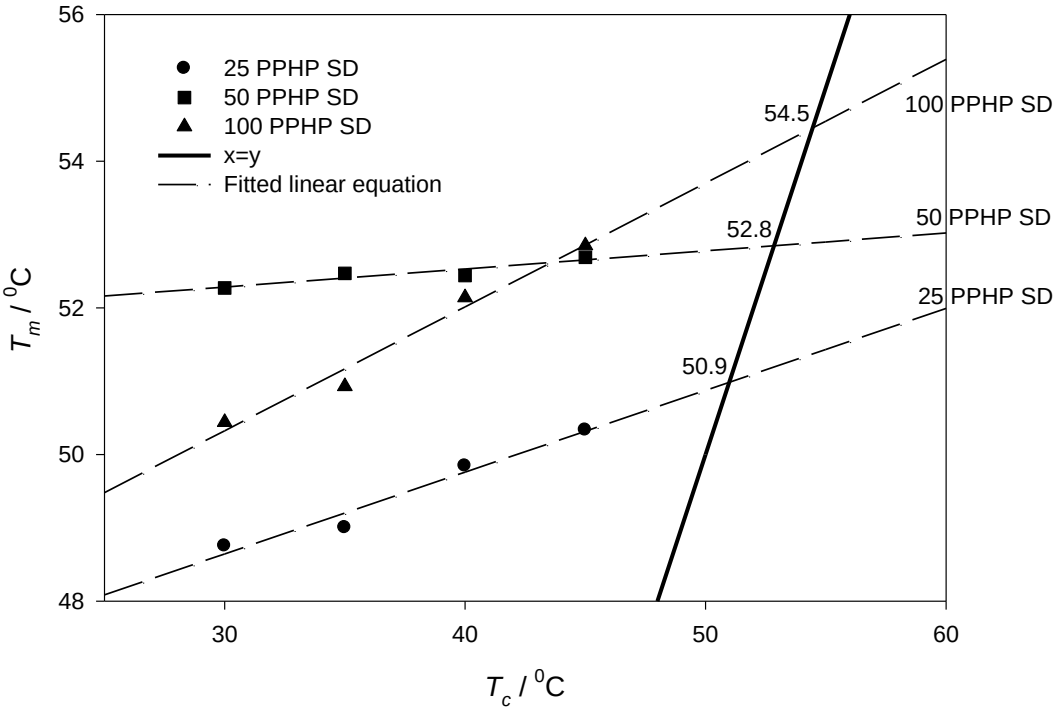

FIGURE 7.13 : T_c vs T_m plots for the SD filled 400k PEO systems along with the T_c=T_m intercept values in ^{0}C

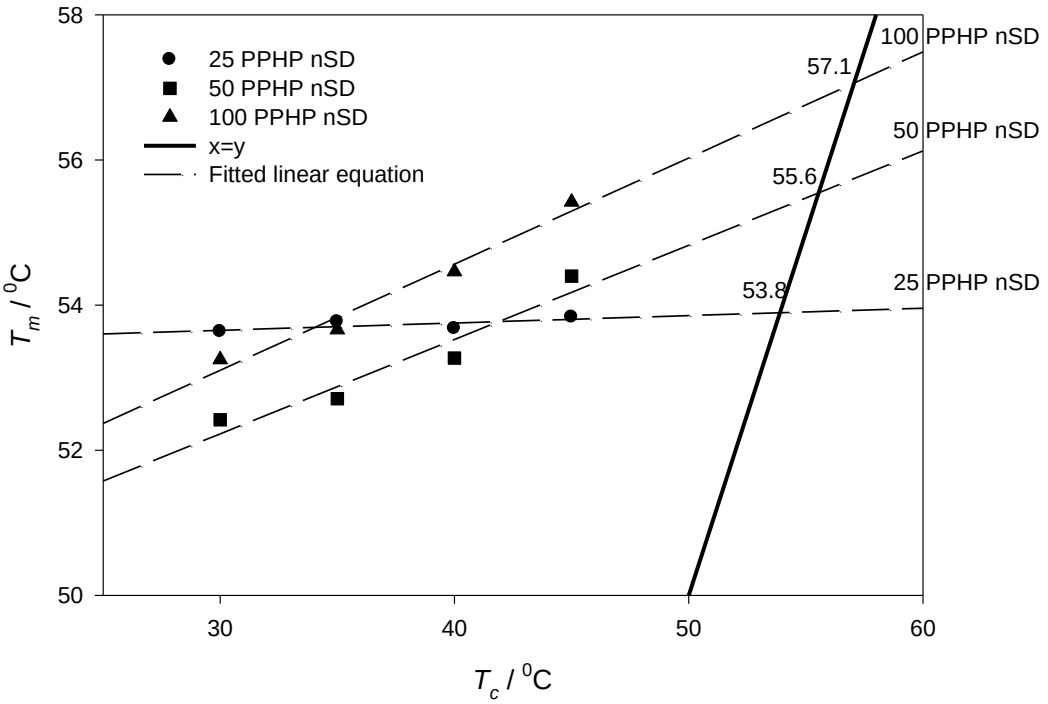

FIGURE 7.14 : T_c vs T_m plots for the nSD filled 400k PEO systems along with the T_c=T_m intercept values in ^{0}C

7.3 AC Electrical Breakdown

Figure 7.15 shows the electrical breakdown strength of 400k PEO samples with up to 10 PPHP micro SD filler. It is clear that the breakdown strength has hardly changed, with the data and confidence bounds consistently overlapping. This suggests that the SD either has no effect on the breakdown strength, or is well dispersed enough that the amount currently present is insufficient to provide any increase or decrease. The graph of the right in figure 7.15 shows that further addition of SD increases the breakdown strength, similarly to that shown by MMT. At 100 PPHP the SD is seen to have increased the breakdown strength by approximately 20 kV/mm. Figure 7.16 shows the α values of the SD filled samples and from this it is believed that addition of further SD causes an increase in breakdown strength at a linear rate. This is in contrast to the MMT filled materials, shown in figure 6.12, which exhibited an exponential rise to maximum increase of approximately 30 kV/mm.

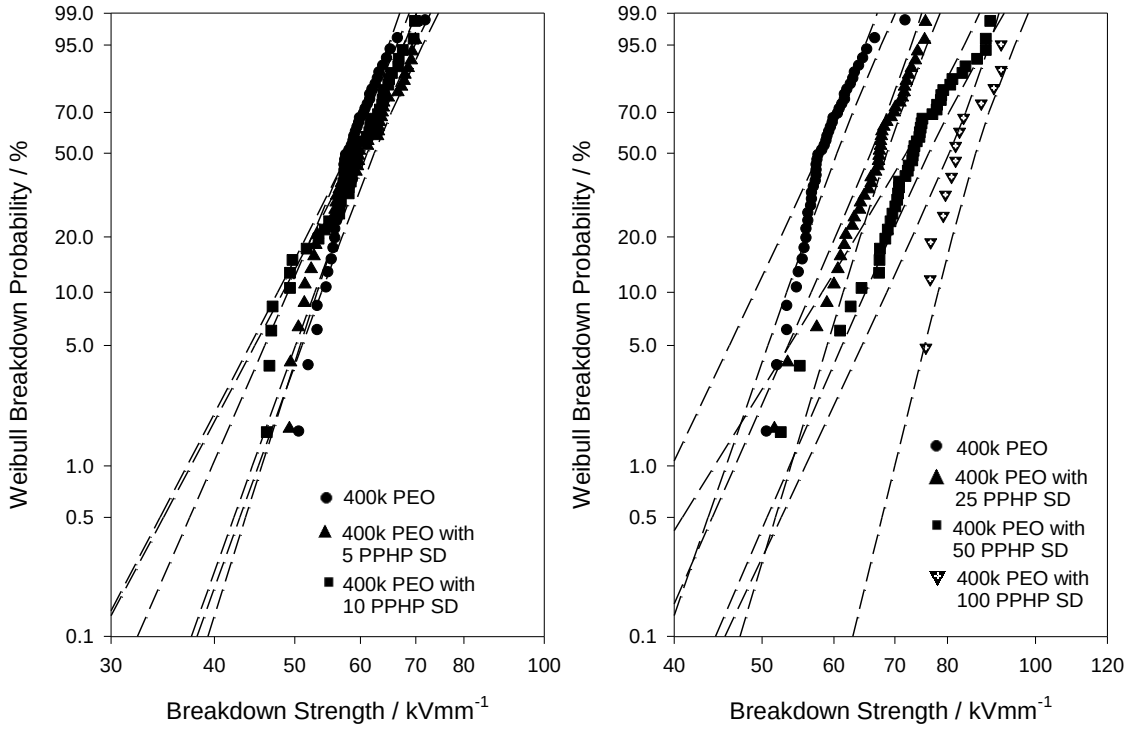

FIGURE 7.15 : Breakdown plots of 400k PEO with up to 10 PPHP SD filler (left) and up to 100 PPHP SD filler (right)

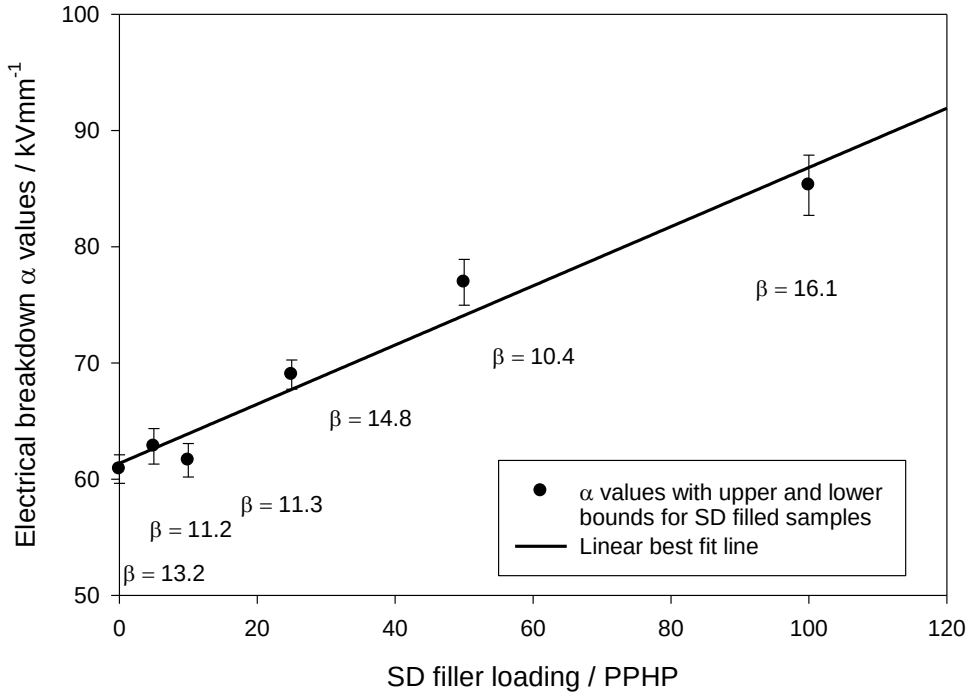

FIGURE 7.16 : α values (with upper and lower values) calculated from the Weibull equation for increasing SD filler loading

Having previously observed that SD has the ability to increase the breakdown strength of PEO considerably (almost double with 100 PPHP loading) it was of great interest to see how the same filler, with nanoscale particles would effect the breakdown strength. Figure 7.17 shows PEO-nSD samples with up to 10 PPHP nSD loading. Unlike the MMT and micro SD, the nSD has had an immediate effect on the breakdown strength with a loading of only 5 PPHP. The increase is quite marked given the small quantity added to PEO, suggesting a very high level of dispersion to achieve such an increase. Addition of a further 5 PPHP provides a similar increase. Figure 7.18 shows the PEO-nSD samples with up to 100 PPHP filler. Similarly to the micro SD samples, the breakdown strength increases with addition of filler, however unlike the SD filled samples, this increase is represented by an exponential rise to maximum rather than a linear relationship. The breakdown strength is therefore still seen to have increased, but at a faster rate initially before settling at approximately the same value for the 100 PPHP loading. This suggests that dispersed nanofiller has a much greater effect at lower loadings before the filler starts to agglomerate and behave in a similar way to the micro SD.

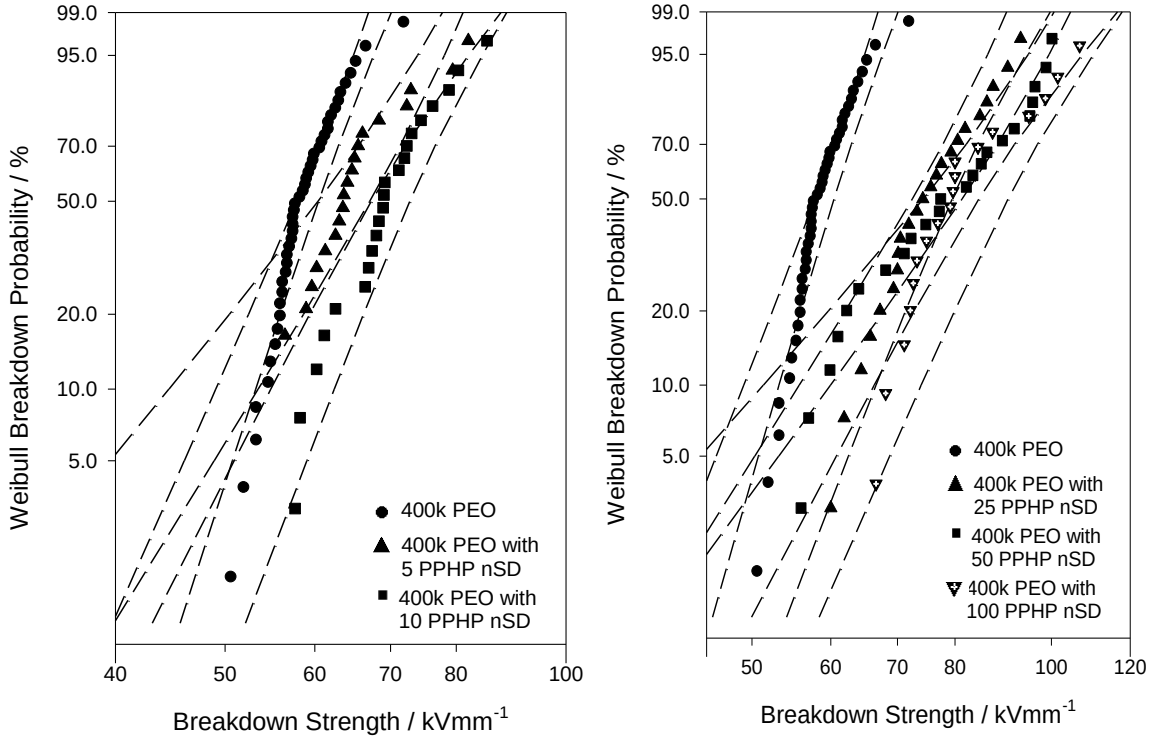

FIGURE 7.17 : Breakdown plots of 400k PEO with up to 10 PPHP nSD filler (left) and up to 100 PPHP nSD filler (right)

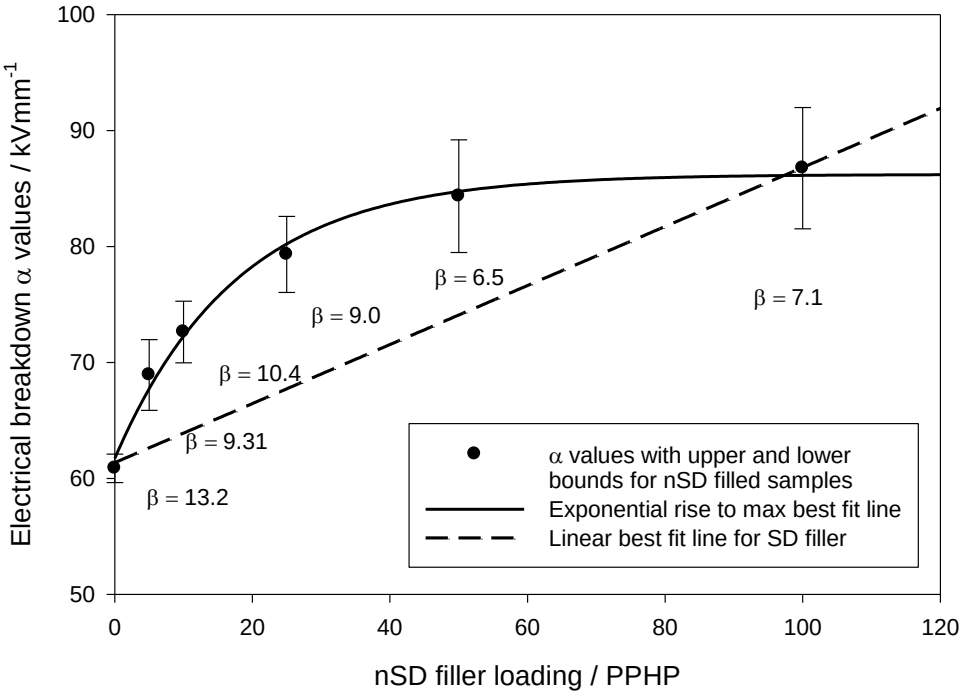

FIGURE 7.18 : α values (with upper and lower values) calculated from the Weibull equation for increasing nSD filler loading

7.4 Chapter Summary

During rheology, up to 10 PPHP of the microSD filler could be added without having any effect on the flow dynamics of the system, however only 5 PPHP of the nSD could be added without an effect. Further addition of both the micro and nano SD fillers produced an increase in viscosity. In fact, the shape and final viscosity values were particularly similar between the two systems. It was noted that, at lower loadings, larger increases in viscosity are seen at different stages, the larger being seen at 10 – 25 PPHP for the SD and 5 – 10 PPHP for the nSD. This suggests that although the solutions have the same viscosity at the highest loading, they reach that state in different ways.

DSC revealed that up to 5 PPHP of both fillers could be added before the thermal transition temperatures were affected, with further addition being noted to cause a decrease. Interestingly, both the micro and nano fillers had the same approximate transition temperatures at the highest filler loading, but similarly to the rheology data, they reached this value in different ways. A large drop was observed for the 50-100 PPHP region for SD and the 25-50 PPHP region for nSD, suggesting that the variation in particle size, is having an observable effect. Crystallinity values showed that the micro SD particles hindered the crystallisation process more than the nSD, with the variation attributed to the dispersion and interactions between the filler-polymer during crystallisation. Avrami analysis showed that for the SD samples, the K_3 value decreased with increasing filler content, confirming it's hindrance of the crystallisation. The nSD K_3 values were noted to be much lower at low filler loadings, suggesting a less prominent effect on the crystallisation process. At increasing nSD loadings the K_3 value was seen to increase to values more comparable to those for SD.

With addition of SD and nSD up to 100 PPHP the breakdown strength of the material was observed to increase greatly. Again however, the two materials had very similar breakdown strengths at the highest filler loading but reached this in very different ways. The micro SD had no effect up to 10 PPHP before increasing linearly, whereas the nSD had an immediate effect before tailing off at 50 PPHP, again supporting the belief that the nanoparticles are agglomerating.

Chapter 8: PEO-BOEHMITE COMPOSITES

8.1 Rheometry

Since the Boehmite used in this investigation is water-soluble, it was expected that addition to a PEO based solution would produce an increase in viscosity. Table 8.1 shows that even addition of as little as 5 PPHP boehmite caused an obervable change in flow properties from unfilled samples. Addition of a further 5 PPHP clearly interrupts the flow dynamics and causes a further increase in viscosity. This increase is greater for higher PEO loading, hence higher initial viscosity, samples as also seen for addition of nSD.

Sample	Peak Shear Rate 5 PPHP BO Filler	Peak Shear Rate 10 PPHP BO Filler
A5	3020	2800
A10	718	576
B2	1610	1300
B5	62.4	51.3
B10	8.72	2.28
C1	3710	3690
C2	741	669
C5	14.3	12.4

TABLE 8.1 : Peak shear rate values for PEO-BO composite samples

Since this filler is particularly hydrophilic it was hypothesised that this may be affecting the interactions with the PEO/water solution. Boehmite-water solutions were generated, the curves of which are shown in figure 8.1. From this it is clear that a large increase in viscosity occurs at ~18 PPHW (c.f. the data for the 16.8 PPHW and 19.3 PPHW). This value is deemed to represent a ‘percolation limit’ for the system, where the nanofiller loading is sufficiently high that nanoparticles begin to interact with one another. A similar situation is found when adding carbon black to an insulating matrix [289-290], where a percolation threshold has to be reached before

conduction occurred. Producing and mixing samples is therefore noted to become significantly more difficult where the final PEO/boehmite composition requires the processing of solutions where the boehmite:water ratio approaches ~18 PPHW.

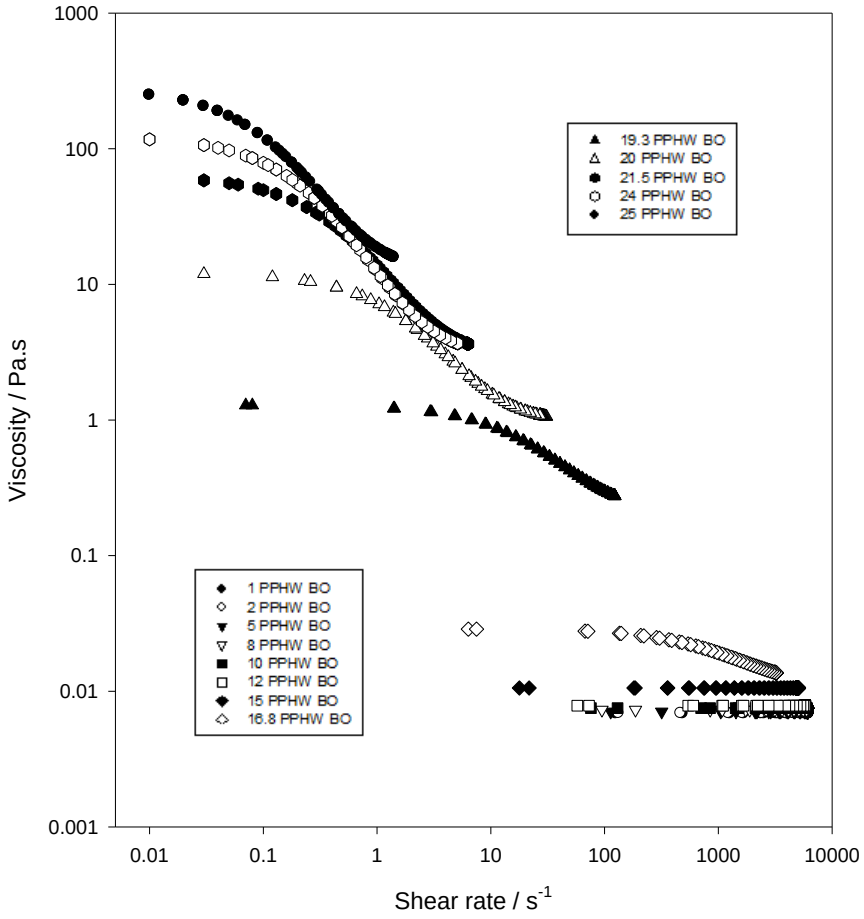

FIGURE 8.1 : Viscosity curves for boehmite-distilled water solutions

At higher concentrations of boehmite, some further dispersion was observed during repeated shear cycles, since data obtained from consecutive runs differed. For water/PEO/boehmite systems with high filler loadings, the observed equilibrium behaviour either conformed to that shown in figure 8.3, where the boehmite dictates the viscosity when a low percentage of PEO is present, or else the system was too viscous to measure. It should be noted that to create the 25, 50 and 100 PPHP loading samples for thermal and electrical testing, each sample was produced from 2 or more diluted versions that were suitable for the rheometer. By using such diluted systems the ratio of boehmite to PEO could be maintained but also dispersion of the filler could be achieved using the rheometer before recombining the solutions.

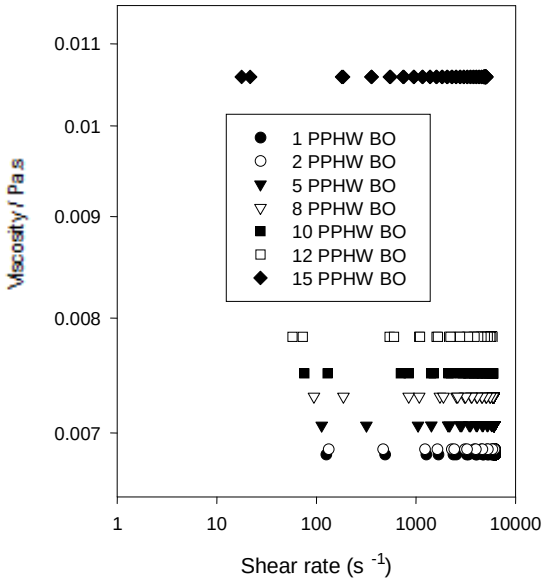

FIGURE 8.2 : Viscosity curves for low percentages showing Newtonian behaviour

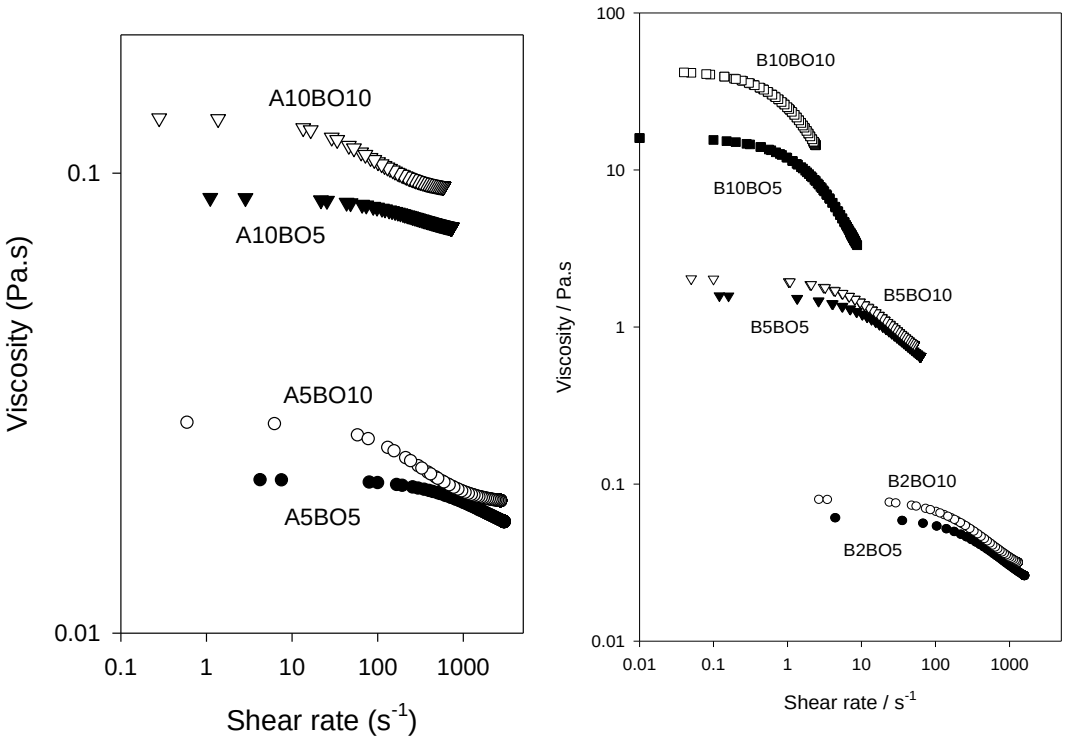

FIGURE 8.3 : Viscosity curves for 100k PEO (left) and 400k PEO (right) samples with up to 10 PPHP BO filler

Figure 8.4 better shows the increasing effect of the filler with a higher percentage of PEO present. Also, by plotting the log of the boehmite-water percentage ratio against the log of the viscosity it is clear to see the large increase in viscosity at the 18 PPHW threshold, shown in the right graph of figure 8.4. This relates to the theory in section 4.1.4 where the newtonian-like data produces a small gradient, in this case 0.05, showing a very dilute system. Then once the entanglement limit has been reached a new regime begins, in this case with a gradient of 21.59. The occurrence of such an entanglement limit is not too surprising, however the magnitude and sudden onset is of particular interest. Figure 8.5 shows an example of a viscosity curve from one of the more concentrated systems. Fitting a De Kee equation, defined in section 2.1.1, a good fit is observed, however at higher shear rates the experimental data appears to drop below the predicted De Kee line. A free fit model was then used to test the accuracy of the De Kee model for this type of system. It was observed that the free fit model, hence ignoring the $1/10^{th}$ relaxation dependency previously mentioned and tested in section 4.1.2, actually provided a significant improvement in representing the data at the previous 'problem region' at the higher shear rates.

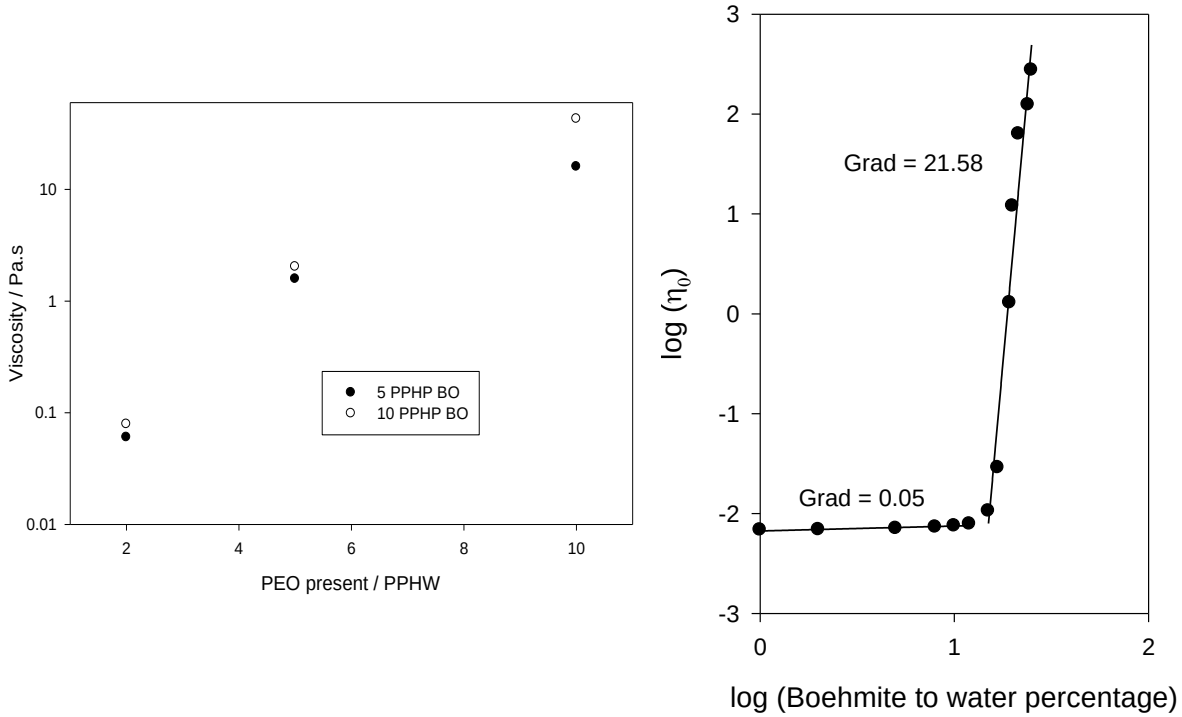

FIGURE 8.4 : Viscosity values for 400k PEO samples with Bo filler on a log scale (left) and a log-log plot of peak viscosity vs filler amount

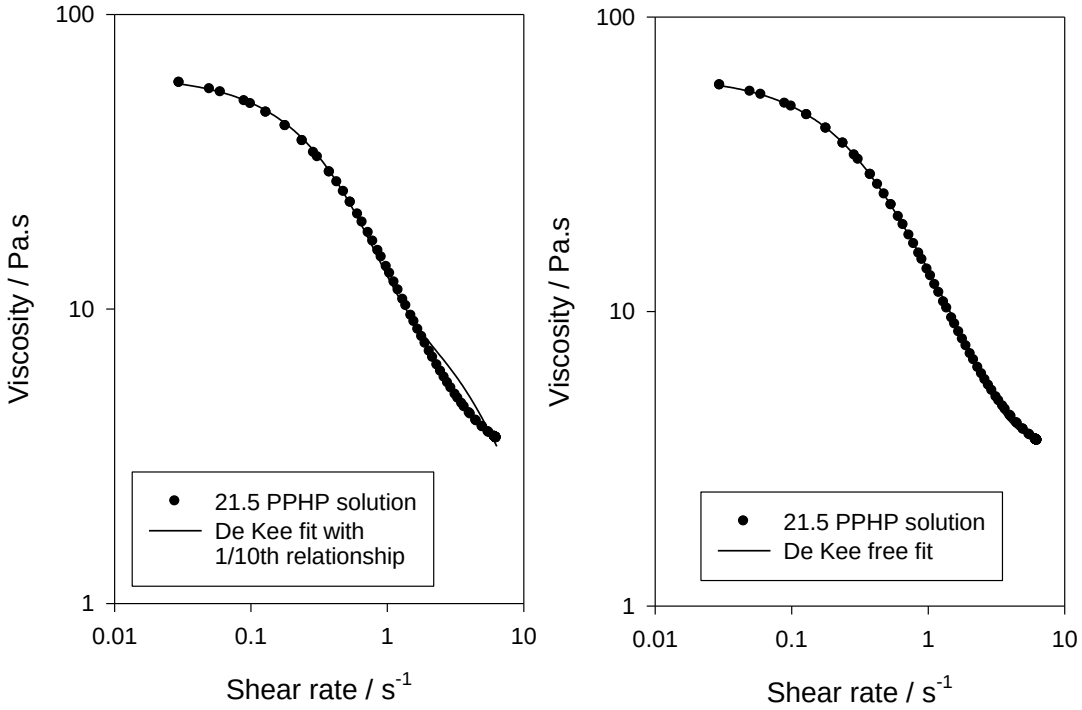

FIGURE 8.5 : De Kee fits to the BO-water solutions with the $1/10^{th}$ relationship (left) and a free fit model (right)

8.2 Differential Scanning Calorimetry

Having observed that the nanofiller strongly affects the viscosity of the PEO solutions, evidence for solid state interactions was sought via DSC. If the boehmite particles enhance nucleation or inhibit the growth of PEO crystals, then this should be revealed through, for example, an elevation of the non-isothermal crystallization temperature, T_c, or depression of the melting enthalpy ΔH_m. Previous work by Kozako et. al. [291] into boehmite-epoxy nanocomposites found that the boehmite had either no effect or a slight decrease on the thermal transitions. Kozako in particular found that addition of up to 7% 10 nm boehmite particles to their epoxy produced a 4 ^{0}C drop in T_g, a value they deem to be within the errors of the data collection. Other authors have found similar behaviour when using boehmite fillers, such as Sugama [292] who saw no change in the thermal transition temperatures of their polyphenylenesulfide samples with addition of boehmite, despite seeing a decrease in ΔH_m and ΔH_c with increasing boehmite content.

Despite authors such as Ozdilek et. al. [190] observing a slight decrease in thermal transitions with addition of boehmite, in their case to polyamide, some authors actually saw an increase. Work by Marcincin et. al. [188] found that addition of Sasol Disperal boehmite (the same supplier of boehmite as used in this investigation but not the same exact boehmite) to their polypropylene fibres caused an increase in melting temperature initially for low filler loadings. However when reaching a filler loading of 1% the melting temperature had returned to the T_m for the unfilled sample, and then started to decrease up to a 3% filler loading. This suggests that higher filler loadings may result in a further decrease in thermal transitions. Some authors, such as Streller et. al. [293], actually found the T_c to increase by 14 ^{0}C with a 10% filler loading. It should be noted that direct comparison to previous investigations is not possible since none of the boehmites tested in the above mentioned previous investigations were the same modified version as used in this investigation.

The graphs in figure 8.6 show T_m and T_c transition temperatures respectively for up to 50 PPHP BO loadings. From these it is clear that the filler is reducing the temperature of all transitions, possibly acting to inhibit crystal formation. Even with a filler loading as low as 5 PPHP, a sharp decrease in T_m is observed, dropping by as much as 12 ^{0}C for the 100k PEO sample. Similar to the MMT and SD filled samples, the ΔH_m and ΔH_c values were highest for the 25 PPHP filled sample, then decreasing with higher filler loadings, shown in figures 8.7 and 8.8. The crystallinity values for the 25, 50 and 100 PPHP samples were 49.6%, 38.3% and 26.2% respectively.

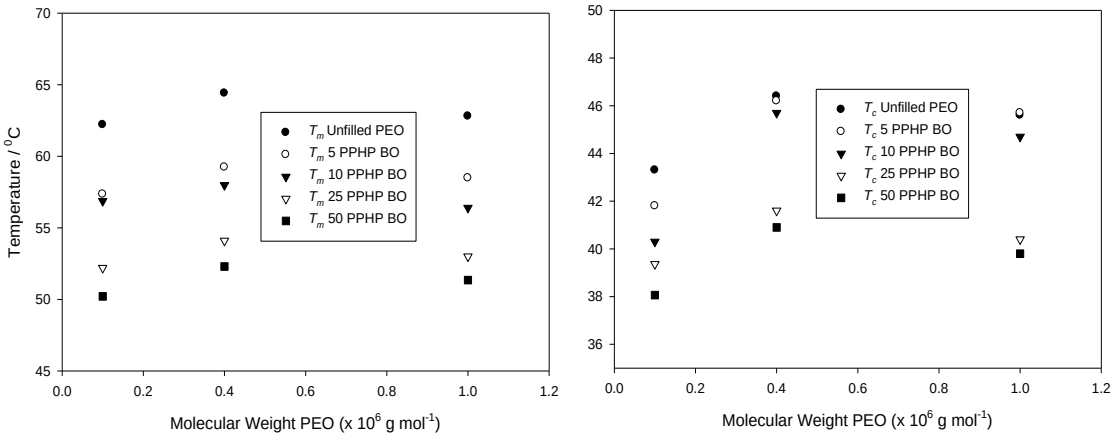

FIGURE 8.6 : The melting (left) and crystallisation (right) transition temperatures for PEO-BO composite samples

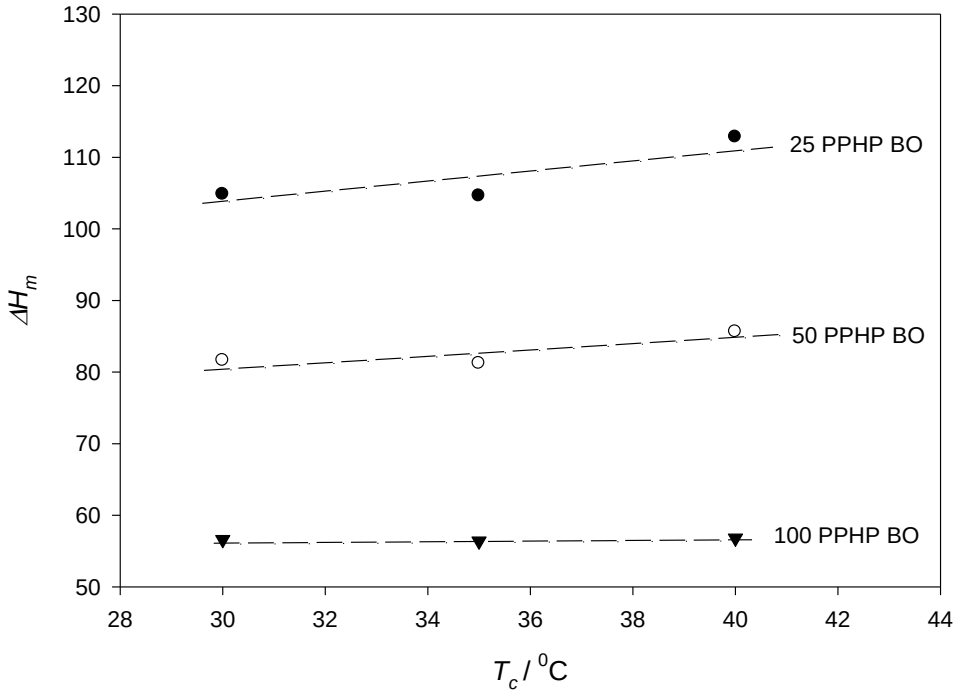

FIGURE 8.7 : ΔH_m values for the 25, 50 and 100 PPHP filled BO 400k PEO samples

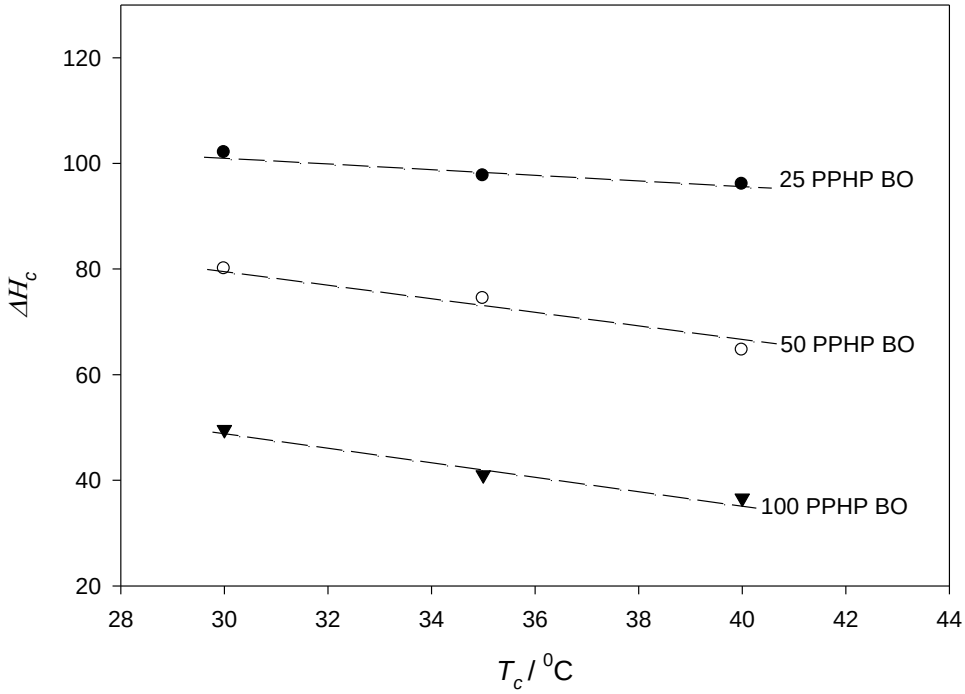

FIGURE 8.8 : ΔH_c values for the 25, 50 and 100 PPHP filled BO 400k PEO samples

The crystallinity drop seen for boehmite filled samples is more severe for the 25 PPHP sample than for MMT, but decreases less for the 50 and 100 PPHP samples,

with a final value 8% higher than the 100 PPHP MMT. Previous work has revealed a decrease in crystallinity with boehmite filler [294] and the significant increase seen here is probably due to the high dispersion that results from using a solution-phase as discussed in section 7.2 for SD/nSD and section 6.2 for MMT.

8.2.1 Avrami analysis

Figure 8.9 shows the crystallisation times for 25 and 50 PPHP boehmite samples crystallised at 30-40 ^{0}C. As before, the times increase with increasing crystallisation temperature as expected and again, like the 50 PPHP MMT 40 ^{0}C, the 100 PPHP MMT 40 ^{0}C, the 100 PPHP SD at 40 ^{0}C and the 50 PPHP nSD at 40 ^{0}C, a particularly large increase is unexpectedly observed in the 25 PPHP BO 40 ^{0}C sample. Interestingly all samples that exhibit this phenomena were taken at 40 ^{0}C, possibly suggesting that the issue may be with collecting experimental results at this temperature, where crystallisation occurs relatively slowly.

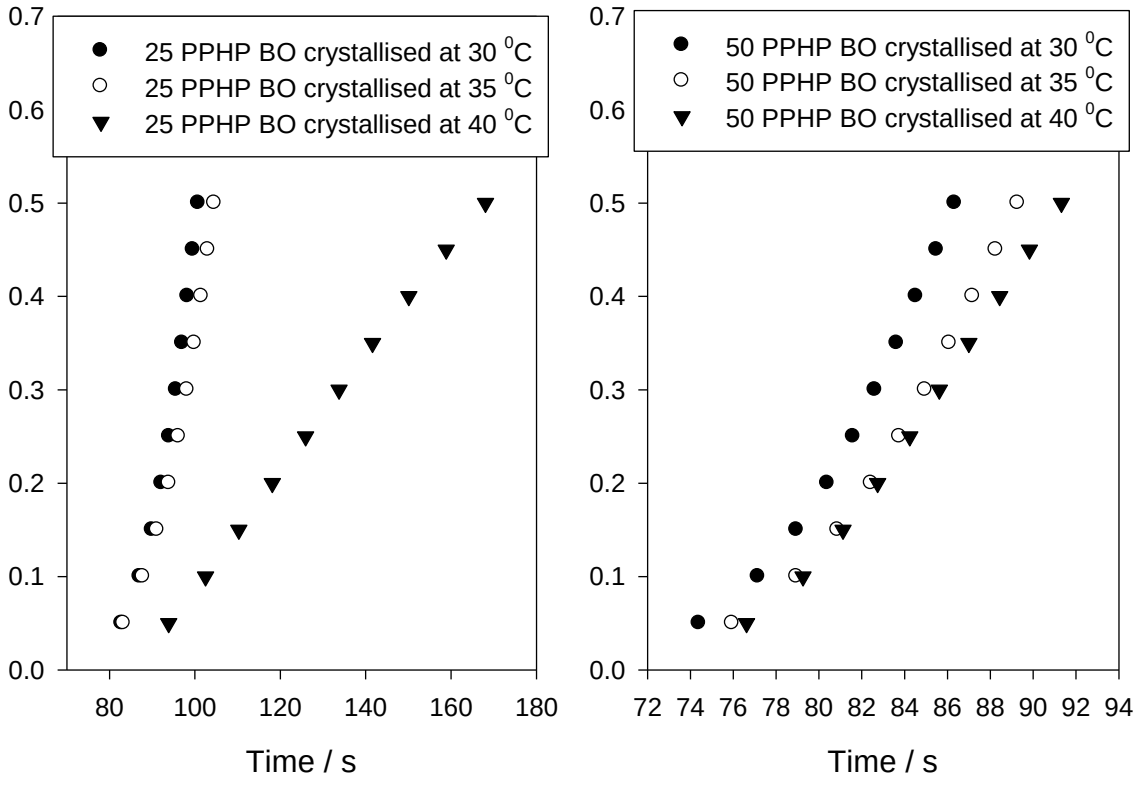

FIGURE 8.9 : Crystallisation data collected for the 25 PPHP (left) and 50 PPHP (right) BO filled 400k PEO samples

Table 8.2 shows the Avrami *n*, *k* and calculated K_3 values for the boehmite samples. As before, the *n* values are seen to decrease with increasing T_c. In general the addition of boehmite appears to have lowered the *n* values for the samples, having an increased effect for the higher T_c values. The 25 PPHP loading sample produced K_3 values that decrease with increasing T_c as expected, however the 50 and 100 PPHP values actually appear to increase, possibly indicative of phase separation as discussed in section 7.2.1 for nSD. The reason for this is not apparent and repeat tests revealed approximately the same values and trends, suggesting that either the variation is within error, thus the values are not changing, or that this increase is genuine. The 50 PPHP sample variation is arguably within error, however the 100 PPHP is not.

Sample / PPHP	**T_c / ^{0}C**	**Avrami parameters**			
		n	**k (s^{-1})**	**R^2**	**K_3**
25 BO	30	4.663	2.159×10^{-8}	0.9994	1.17×10^{-5}
25 BO	35	4.529	1.577×10^{-8}	0.9996	6.79×10^{-6}
25 BO	40	1.297	2.157×10^{-3}	0.9999	6.81×10^{-7}
50 BO	30	4.587	1.794×10^{-7}	0.9999	3.87×10^{-5}
50 BO	35	3.691	4.194×10^{-6}	0.9999	4.26×10^{-5}
50 BO	40	2.03	1.591×10^{-3}	0.9998	7.32×10^{-5}
100 BO	30	4.265	1.711×10^{-8}	0.9983	3.44×10^{-6}
100 BO	35	1.645	2.968×10^{-3}	0.9998	2.46×10^{-5}
100 BO	40	1.755	4.263×10^{-3}	0.9999	8.88×10^{-5}

TABLE 8.2 : The Avrami parameters generated for the BO filled 400k PEO samples

Figure 8.10 shows the calculated T_m^0 values for the boehmite samples, all of which appear to vary significantly. For the SD and nSD samples it was observed that the T_m^0 increased with increasing filler loading, however for boehmite the order appears to be: 25 PPHP, 100 PPHP and 50 PPHP. Even accounting for the associated errors, calculated using the method detailed in section 4.2.1, the values vary enough to be considered genuine. However, it was noted that the 25 PPHP sample in figure 8.10 behaves differently than the 50 and 100 PPHP samples, which was also the case for

K_3 values in table 8.2. This could suggest these variations are related to the increase from 25 to 50 PPHP filler loading.

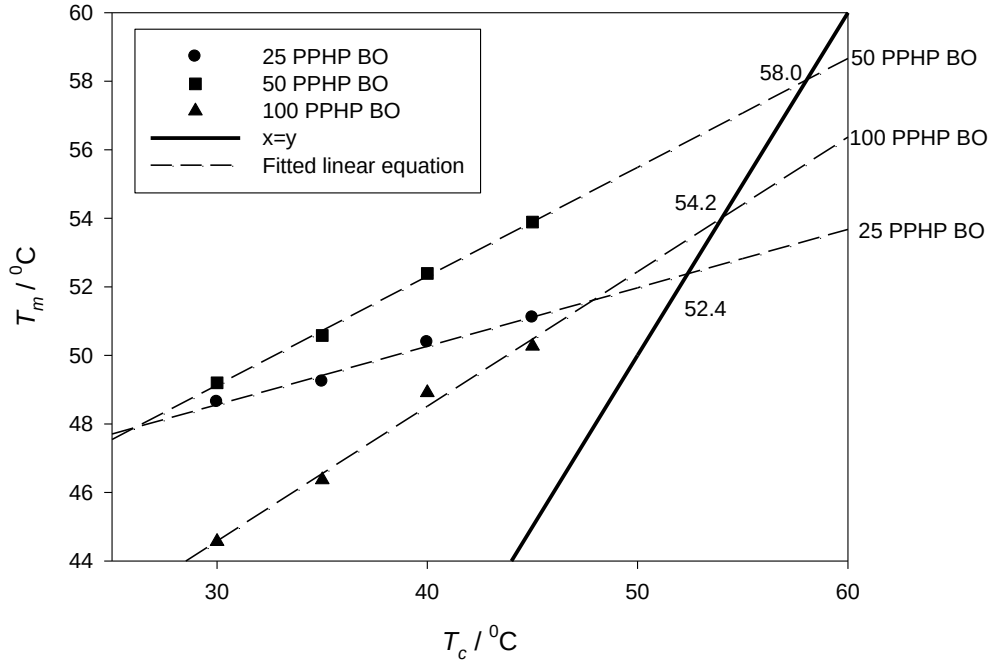

FIGURE 8.10 : T_c vs T_m plots for the BO filled 400k PEO systems along with the T_c=T_m intercept values in ^{0}C

8.3 AC Electrical Breakdown

Having seen that boehmite affects the flow properties of PEO solutions and restricts the formation of ordered crystals in the solid state, the effect on breakdown strength was investigated. Figure 8.11 shows PEO-BO composites with up to 100 PPHP filler loadings. From this it is evident that increasing the filler loading massively decreases the breakdown strength, the magnitude of which is surprisingly large and unlikely to be associated solely with the filler. Since the boehmite is particularly hydrophilic, it was hypothesised that the decrease could relate to retention of water from the processing phase which, in turn, adversely affects the breakdown strength. To test this, a range of samples were heated at 40 ^{0}C in a vacuum oven for up to a week, in an attempt to remove any residual moisture. The samples were then removed and tested. This revealed that after 48 h of drying, significantly higher breakdown strengths were observed, also shown in figure 8.11. Longer drying times of more than 48h provided

no further change. Therefore the decrease in breakdown strength observed in post-drying samples is deemed to be due to the boehmite itself and not free water.

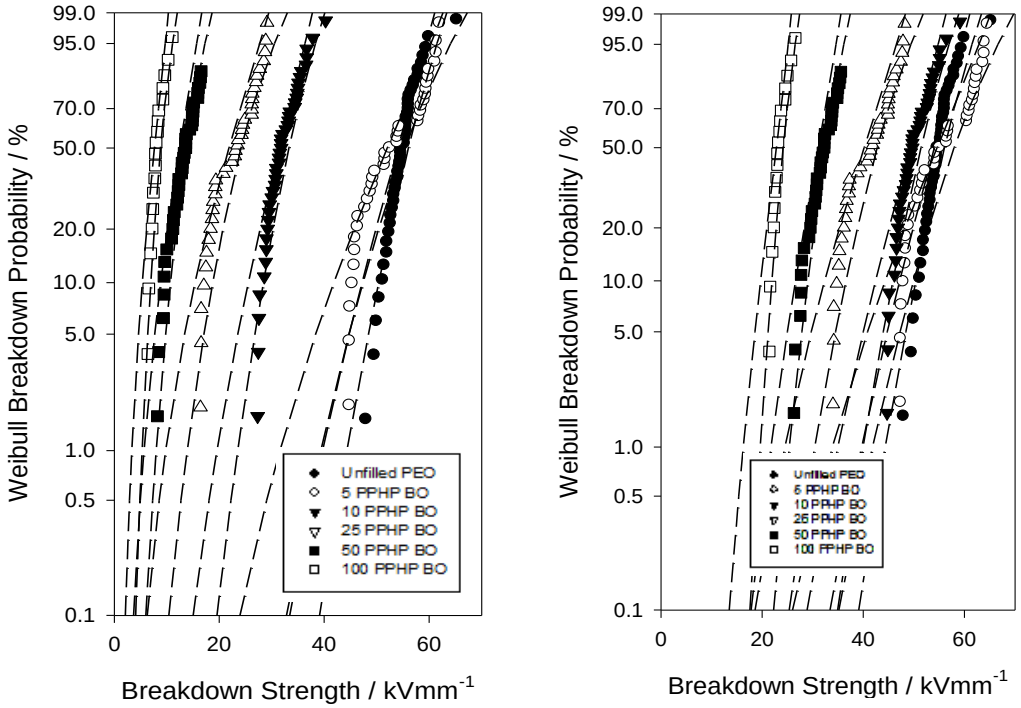

FIGURE 8.11 : Breakdown plots of 400k PEO with up to 100 PPHP Bo filler, before drying (left) and after drying (right)

With reference to figure 8.11, this decrease in breakdown strength with increasing filler content is the opposite trend to that seen for the other fillers. This could be related to the insulating properties of the filler. Previously the breakdown mechanism is thought to have been occurring through the PEO, with the filler causing an increased breakdown path length resulting in higher breakdown strengths. However, since the breakdown strength is decreasing here, the boehmite filler may actually be acting to shorten the breakdown path length due to a lower breakdown strength than the surrounding polymer. Further work into the chemistry and breakdown characteristics of this particular boehmite filler would be required to determine the exact cause of the increase.

Figures 8.12 and 8.13 show the breakdown strength values to decrease with addition of boehmite. Figure 8.12 shows that before drying the samples, the breakdown strength rapidly drops with addition of 10 PPHP filler, continuing to decrease to the 100 PPHP filler loading sample with a breakdown strength around 15% of the unfilled

value. Figure 8.13 shows the α values for the same samples after drying. It is clear that the breakdown strength still decreases with addition of further boehmite, however the magnitude of the drop is far lower. The 100 PPHP boehmite filled sample had a breakdown strength of around 40% that of the unfilled sample.

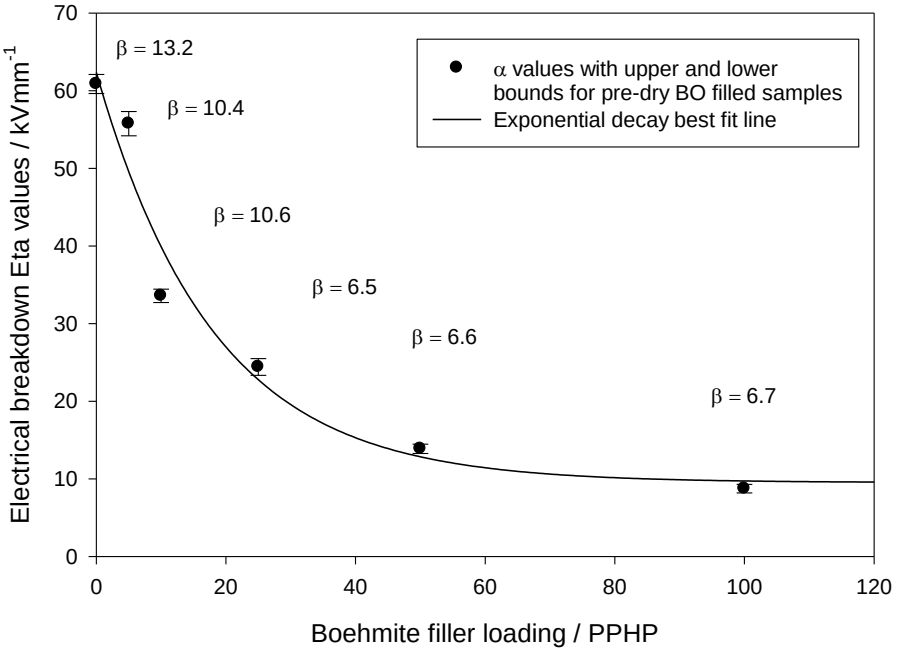

FIGURE 8.12 : α values (with upper and lower values) calculated from the Weibull equation for increasing BO filler loading before drying

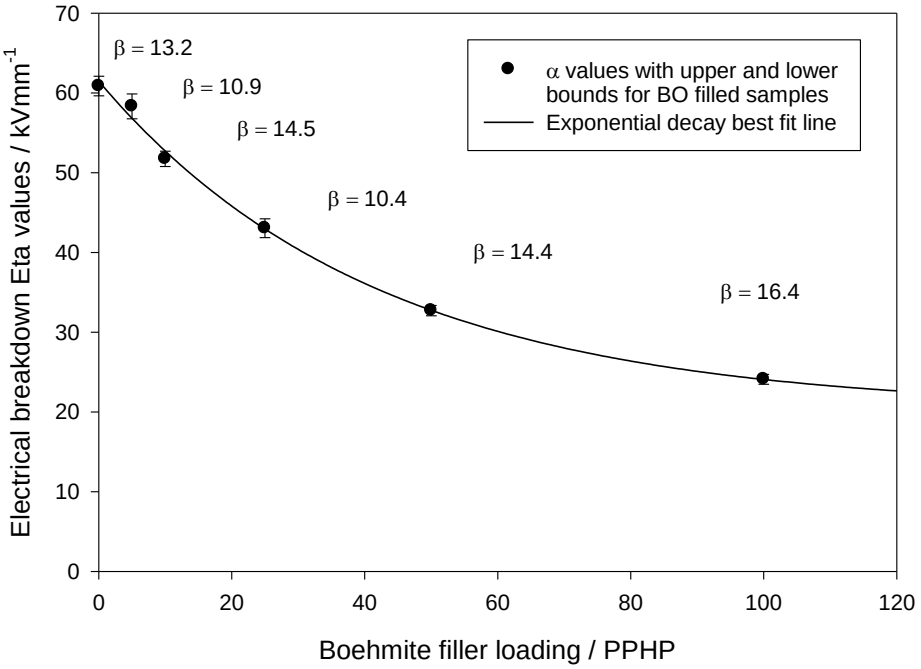

FIGURE 8.13 : α values (with upper and lower values) calculated from the Weibull equation for increasing BO filler loading after drying

8.4 Dielectric Spectroscopy

Having further dried the samples to remove the extra moisture detected during AC breakdown, they were tested using dielectric spectroscopy to further probe the PEO-boehmite electrical interactions. The curves of the dried samples showed no variation from those for unfilled PEO, shown in section 4.3, suggesting the filler has no effect on the relaxations. When testing the initial samples however, the real relative permittivity was seen to massively increase with filler content, shown in figure 8.14 as would be expected with water retention. The increasing effect with increasing filler loading confirms the relation between the boehmite acting to withhold the water. It was also noted that the shape of the curve changes, with the broad peak previously found to be around 100 Hz for pure PEO being visible in lower loadings but completely lost with higher loadings. Tan δ data also changes significantly with addition of the nano filler, as shown in figure 8.15. The 5 and 10 PPHP BO filled samples mimicked the pure 400k PEO curve [7] with two relaxation peaks evident at ~1 Hz and 104 Hz. At higher boehmite loading levels, these appear to be broadened such that the data exhibit a much flattened overall form. The overall loss consequently increases at high frequencies and decreases at low frequencies.

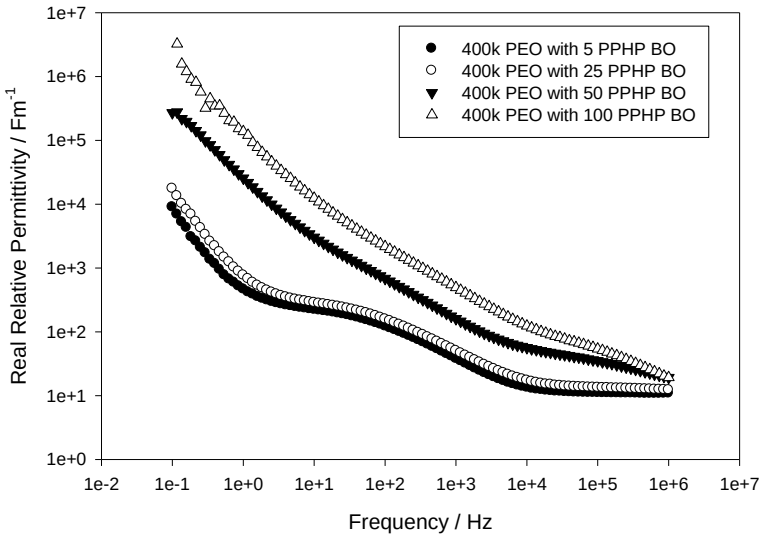

FIGURE 8.14 : Real relative permittivity for PEO-Bo composites with up to 100 PPHP BO filler

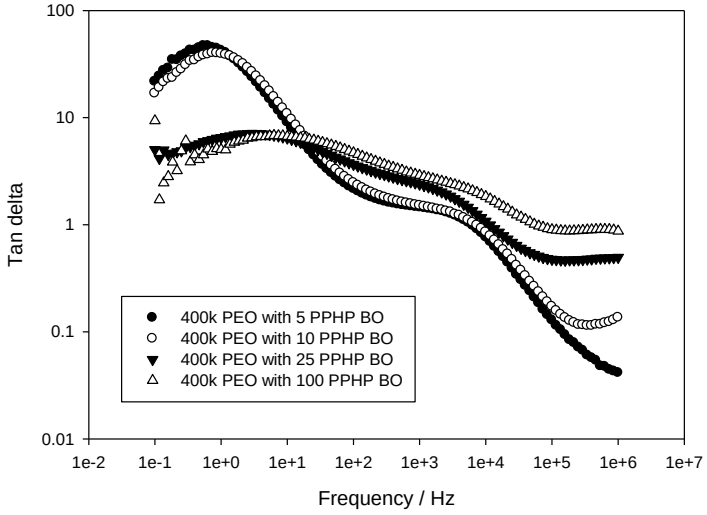

FIGURE 8.15 : Loss tan δ curves for PEO-Bo composites with up to 100 PPHP BO

From figures 8.14 and 8.15 it is clear that the boehmite filler water retention is having a major effect on the dielectric relaxations within the samples. For the 50 and 100 PPHP samples the real relative permittivity is rapidly seen to increase, along with the loss tan δ curves showing variation. Using the Cole-Cole plotting technique, mentioned in section 3.6, makes it easier to analyse the dielectric effect that the boehmite and water are having. Figure 8.16 below is the Cole-Cole plot of real against imaginary relative permittivities for the unfilled, 25 PPHP and 50 PPHP samples.

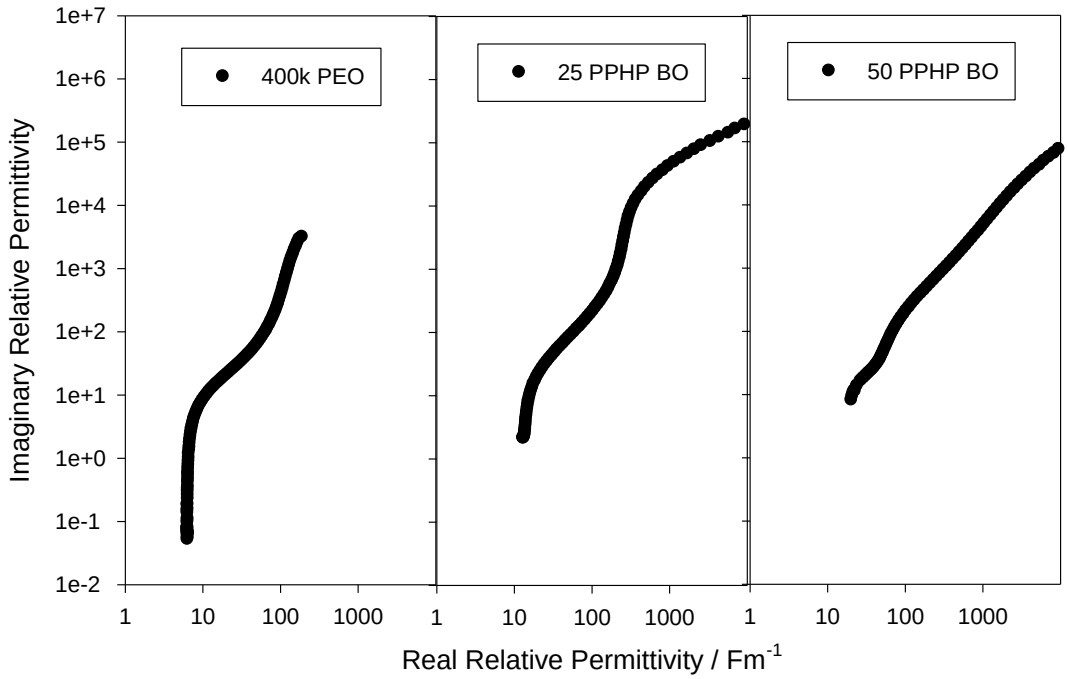

FIGURE 8.16 : Cole-Cole plots for the unfilled (left), 25 PPHP BO sample (centre) and 50 PPHP BO sample (right)

From figure 8.16 it is seen that the addition of filler appears to cause a large increase in conduction compared to the unfilled sample. Using equation 2.27 from section 2.3 it was possible to calculate conductivity values for the entire range of frequencies for the boehmite filled samples. Having observed a large rise in real relative permittivity with addition of boehmite, it was unsurprising to also see a large increase in the conductivity of these materials. Figure 8.17 shows the increase in conductivity at a frequency of 0.14 Hz. Such a large increase in conductivity suggests that water maybe indeed be present in the system, since the conductivity of water is usually between 5 $x10^{-4}$ and 5 $x10^{-2}$ S/m.

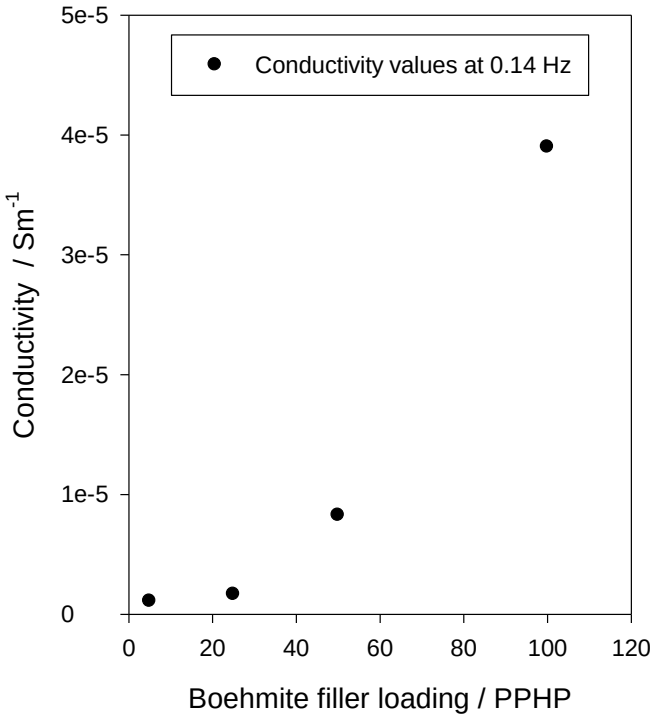

FIGURE 8.17 : Conductivity values at 0.14 Hz for 5-100 PPHP BO samples

8.5 Chapter Summary

During rheology it was found that the boehmite caused a massive increase in viscosity at the lowest filler loadings. It was found that the boehmite rods suddenly form a gel with water at a concentration of 18 PPHP. This behaviour affected the PEO-BO samples as the boehmite rods are believed to act as physical entanglement points. Creation of higher loading boehmite samples was not possible since the rheometer could not mix such viscous solutions, therefore these were diluted, mixed and

recombined. Fitting a De Kee function found a good relationship to the data, with the $1/10^{th}$ dependence shown in be inappropriate.

DSC showed that the boehmite filler decreased the thermal transition temperatures just like the MMT and SD/nSD, suggesting hindrance of the crystallisation. Crystallinity values confirmed this with values of 49.6%, 38.3% and 26.2% for the 25, 50 and 100 PPHP filled samples respectively. Avrami data showed much variation in K_3 trends with increasing filler content, possibly indicative of phase separation at higher loadings.

The AC breakdown strength of the BO filled samples was seen to drastically drop with increasing filler content. The decrease was particularly large and using dielectric spectroscopy was found to be due to water retention throughout the sample processing. Additional drying for 48 hours produced samples with similar dielectric curves to those for unfilled PEO, but still resulted in a drop in breakdown strength thought to be due to the BO particles acting as conductors and shortening the breakdown path length within the material.

Chapter 9: CONCLUSIONS AND FUTURE WORK

9.1 Conclusions

The aim of this thesis was to investigate the use of rheology as a method to gauge the dispersion and resulting effects of nanoparticle and microparticle filled polyethylene oxide. In chapter 1 a brief introduction to the field of polymer nanocomposites was given, along with the aims of this thesis. In chapter 2 all theory behind the experimentation and observed effects was covered along with some initial experiments. In this chapter the previous use of rheometers to aid in dispersion was discussed, along with the expectation of shear thinning to be present in the PEO solutions and the ability for many shear rate-shear stress/shear rate-viscosity models to represent the data. It was concluded that the two most promising models to continue forward for each were the Ostwald de Waele, 3 parameter hyperbolic, Carreau and De Kee models respectively. This chapter also covered the reasons for choosing a 2 parameter Weibull distribution to represent AC breakdown data and the use of Avrami theory to analyse the crystallisation kinetics of the PEO composite materials. Chapter 3 described the experimentation procedures used and details about the materials themselves.

In chapter 4 the rheological, thermal and electrical properties of pure polyethylene oxide and some polyethylene oxide blends were investigated. It was observed that the Ostwald de Waele model for shear rate-shear stress data provided a good overall fit to data, performing better when applied to lower viscosity samples, such as B2, but was found to produce relatively large residuals. The 3 parameter hyperbolic provided a far superior fit to all data sets, with small residuals. Having established that the rheometer software was calculating the coefficient of viscosities, the 3 parameter equation was differentiated and used to generate differential viscosity data with the benefit of knowing the mathematical method used. Analysis of the Carreau and De Kee models revealed that both accurately represented the high viscosity samples. However, the Carreau model failed completely for near-Newtonian solutions, whereas the De Kee model excelled, a finding that was demonstrated through the use of fractional viscosities based on the residuals. As expected increasing viscosity samples exhibited

increased amounts of shear thinning. It was shown that two regimes exist, the point at which they meet being the entanglement limit. Comparison with data from this investigation showed that all of the solutions fell within the second regime; the exponent in the viscosity molar mass relationship was found to be 2.7, compared to 3.4 from the literature. Using MHS theory, an α value of 2.7 was calculated, suggesting a concentrated system when compared to literature.

Using an indium calibrated DSC the thermal transitions of the 100k, 400k and 1M samples were estimated, showing an interesting trend as the thermal transition temperatures increased when increasing the molecular weight from 100k to 400k. However this rise did not continue, with the 1M PEO transitions arguably decreasing. This behaviour was believed to be due to the nucleation density or growth rate being independent of chain length at such a high molecular weight. Corrected ΔH_m and ΔH_c were calculated for the 100k, 400k and 1M samples along with crystallinity values, χ_c, of 84.7% ± 5, 73.4% ± 3 and 66.9 ± 3 respectively. Avrami curves produced the expected trends, such as increasing crystallisation time with increasing T_c and provided *n*, *k* and subsequently K_3 values. Varying the molecular weight had little effect on the *n* values, as expected from the literature, while the K_3 values decreased with increasing T_c. Two methods were employed to calculate T_m^0 values and associated errors, producing values of 61.4 ^{0}C ± 1.2 for the 100k, 60.8 ± 1.2 for the 400k and 58.4 ± 1 for the 1M. These values are all lower than would be expected from literature, probably as a result of the extrapolation routine used.

Dielectric spectroscopy confirmed the shape and approximate values of real relative permittivity and $tan\delta$ previously seen in the literature, including a steep negative gradient attributed to Maxwell-Wagner charge build-up at the electrode-sample interface. A peak in the $tan\delta$ curve was also observed, related to a γ relaxation. AC breakdown showed that PEO has a breakdown strength around half that of PE, in the range 50-70 kV/mm. Using optical imagery large spherulites were observed, up to 1 cm in diameter, in crystallised samples of PEO. Etching of PEO samples was attempted using a sodium ethoxide-ethanol mixture reported in the literature, all detailed in appendix 5. However, this showed that the samples were much more

susceptible to the etchant and required a much lower concentration/exposure time to reach an acceptable etch than previously found.

In chapter 5 the thermally aged 100k sample, detailed in section 3.7, was investigated. The ageing process was found to reduce the viscosity of the PEO solution by around 50% as well as showing a decrease in the thermal transition temperatures suggesting a less extensive crystal structure was formed. Thermal oxidation or chain scission were considered to be the cause, although previous work found in the literature suggested that lower molecular weights were more resilient to such oxidation, contrary to the findings from this investigation. The T_m and T_c transitions were seen to move to lower temperatures, consistent with previous investigations. This decrease is thought to be primarily a consequence of thermodynamic factors associated with the introduction of defects in the PEO chain on ageing. These result in the aged samples crystallising less readily on cooling.

The ΔH_c and ΔH_m values were also seen to decrease with ageing, a known sign of chain scission. The generated Avrami curves produced *n*, *k* and calculated K_3 values. Both *n* and *k* values were seen to increase and the onset of crystallisation was seen to occur sooner. The aged samples were also seen to have higher K_3 values, suggesting a change in the nucleation and/or molecular mobility within the system. The T_m^0 value was seen to decrease, rather than increase as would have been expected for a lower molecular weight system, again suggesting that ageing-induced defects exist. No changes were observed during dielectric spectroscopy and despite observing a decrease in breakdown strength, this was considered to be an expected molecular weight effect. FTIR revealed no major peak shifts but was mostly inconclusive. Overall the effect is most likely chain scission and using the theory depicted in section 4.1.4 an estimate of the average molecular weight was inferred to be close to 77,500 $gmol^{-1}$.

Rheology of the PEO-MMT, PEO-SD, PEO-nSD and PEO-BO samples was observed to produce a state of further dispersion after the initial run, proven not to be shear re-dispersion – an effect seen in the literature. Up to 10 PPHP MMT filler could be added to the solutions without significantly affecting the flow dynamics of the system;

the MMT was seen to have the same effect on all molecular weight PEO's. This was also the case for the SD filler, although only 5 PPHP of the nSD could be added before an increase in viscosity was observed. This suggests that the smaller particles could be dispersing much further into the polymer matrix causing a drop in mobility. The boehmite filler, being the most hydrophilic, produced a response at the lowest filler loading of 5 PPHP. Further addition of all fillers produced increases in viscosity, the most prominent of which was for PEO-BO composites, which was so large that data collection was impossible above 25 PPHP loadings. To investigate this, boehmite-distilled water solutions were generated with boehmite loadings between 1-25 PPHW. The samples containing up to 16.8 PPHW boehmite were seen to be near-Newtonian; however, at around 18 PPHW a large viscosity increase was observed. This threshold was believed to be a threshold limit for the water-boehmite solutions. However, the 25 PPHP boehmite-PEO loaded solutions, representing only a 1.25 PPHW boehmite-to-water ratio, were seen to exhibit an unexpectedly high viscosity. It is believed that since PEO-water and boehmite-water solutions separately do not exhibit such a response at these loadings that a combined effect must be the cause; one possible interpretation of this synergistic behaviour is that the PEO interacts strongly with the boehmite in the solution such that the boehmite particles act as physical entanglement points and the overall solutions then responds as a gel. The increase in viscosity for higher filler loadings for MMT was observed to peak at 50 PPHP filler loading, at which point the MMT was believed to be agglomerating and causing no further detrimental effect on the flow of the solution. For the nSD and SD samples further addition again caused an increase in viscosity, during which the data for both were fairly similar. This could be interpreted as nSD agglomerating at high loadings and behaving more like micro particles.

Addition of up to 5 PPHP MMT, 5 PPHP nSD and 5 PPHP SD filler had no noticeable effect on the thermal transitions of the materials. Higher loadings of all fillers caused a decrease in temperature for the thermal transitions. In particular, for MMT a decrease of 14 ^{0}C at the 50 PPHP loading was observed. Increasing the loading to 10 PPHP for the nSD and SD samples produced a noticeable decrease, an effect much more prominent in nano filled specimens. Interestingly, both fillers appeared to show a single region where the drop in temperature for thermal transitions was considerably larger than the others, found to be 50-100 PPHP for the microSD

and 25-50 PPHP for the nanoSD, again believed to be due to the nanoparticles dispersion. Both fillers exhibited similar 100 PPHP filler values, again suggesting that the nano particles were agglomerating and effectively behaving as larger micro particles. The boehmite was observed to decrease the thermal transitions temperatures even at the lowest 5 PPHP loading, an effect likely caused by the boehmite inhibiting crystal formation, causing a drop in T_c by as much as 12 ^{0}C at the 100 PPHP loading.

Using Avrami analysis, *n* and *k* parameters were generated for the MMT, SD, nSD and BO filled samples that were all theoretically acceptable. The *n* values were mostly seen to decrease with increasing T_c as expected and K_3 values were calculated. For the MMT samples the K_3 values were seen to decrease consistently with increasing filler loading, but were numerically similar to those for the unfilled PEO sample suggesting that the MMT has no major effect on the nucleation or crystal growth. The SD samples produced a similar response, although the absolute values were slightly higher, suggesting more of an effect. For nSD however, the K_3 values were actually seen to increase with filler loading. The low initial values suggested a high level of dispersion within the system having little effect on the crystal formation, however at higher loadings the value was deemed similar to the 25 PPHP SD sample, again suggesting that the nSD is agglomerating at such high loading levels. The K_3 values for boehmite were seen to vary the least, although it was thought that some increasing values might suggest phase separation at higher loadings. T_m^0 values for the MMT samples were all within error, but noted to be 7 ^{0}C below the unfilled values. The SD values were similar to those collected for boehmite, however showed a distinct increase with increasing filler loading. A similar effect was observed for nSD, however these values were 3 ^{0}C higher than for the SD, suggesting the system was becoming more PEO-like with less filler effect, suggesting phase separation. The boehmite values were noted to be rather unpredictable, covering a large range of values with no particular order.

During electrical breakdown tests the MMT samples containing up to 10 PPHP filler produced no effect on the breakdown strength values. However, higher loadings produced a large monotonic increase in breakdown strength up to 90 kV/mm. Similarly, up to 5 PPHP SD could be added without causing a change in breakdown strength, although a further increase in filler loading was noted to cause a linear

increase. The nSD samples were seen to increase the breakdown strength at even the lowest filler loading of 5 PPHP. Addition of further filler produced an exponential rise-to-max form, an effect attributed to the smaller filler size, hence larger surface areas. As the filler loading reached 100 PPHP however, both SD and nSD samples had approximately the same breakdown strength. That is, the nano and micro filled samples behave in a similar manner. This suggests that at this loading the nSD has indeed agglomerated and is behaving more like a micro-composite. With addition of boehmite; a filler loading as low as 5 PPHP caused a drop in breakdown strength before causing a massive decrease for 10 PPHP filler loadings and higher. The literature shows previous investigations where the breakdown strength decreased with addition of boehmite, but the observed magnitude of the decrease was considered to be too much to be caused by the filler alone. It was therefore proposed, and subsequently shown using drying methods, that water still remained in these samples due to the extreme hydrophilic properties of the boehmite. The dried samples still showed a large decrease in breakdown strength, with α values at approximately 50% of the unfilled α values at the 100 PPHP filler loading, but were considered to be more realistic despite still being larger than the decreases seen in the literature.

Dielectric spectroscopy revealed no change in the relaxations with addition of MMT, SD or nSD. When testing the boehmite samples however, the real relative permittivity was seen to largely increase, along with a rise in conductivity. From the literature it was apparent, even without the knowledge from the electrical breakdown data, that the samples still contained water. Cole-Cole plots were used to show the conduction mechanism taking over with increasing filler loadings. For the post-dry samples the real relative permittivity and tanδ values were seen to return to those seen for unfilled PEO.

9.2 Future work

Several areas of this investigation have the potential to be continued by further research and experimentation, some of which is detailed below.

- Having observed the apparent agglomeration of nSD particles at higher filler loadings this hypothesis was tested using etching, which would enable real space information to be gained via SEM. However, as detailed in Appendix 5 this was largely unsuccessful. Improvement on this is definitely an area that could be worked on in the future to gain information on the structure and aggregation state of the materials.

- Having observed the apparent inaccuracy in the linear extrapolation method used to calculate T_m^0 values it would be beneficial to collect more data at higher crystallisation temperatures. This should provide a better idea of the real curvature of the data away from the linear trend line observed.

- With the observation of thermal ageing in the 100k PEO samples it would be beneficial to produce more samples and investigate further to better understand the ageing process and its effect on the material. By ageing different molecular weight samples for varying times it should be possible to understand why the lower molecular weight samples were more susceptible to ageing in this investigation, contrary to literature.

Appendix 1: ELECTRICAL BREAKDOWN THEORIES

AP 1.1 Electric Impact Ionisation Theory

Work by Von Hippel [295-296] has led to the creation of an electrical ionisation model that is currently one of the most popular models, despite its age. Von Hippel states that solid insulators have positive ions that are strongly fixed in position and cannot be affected by the application of an electric field. However, the electrons are not and are therefore swept out by the electric field towards the anode and leaving behind corresponding positive space charge. This space charge perturbs the field distribution and weakens the structure of the material, thus leading to an ionisation process. Similar to other theories, in simple terms the electric field applied becomes high enough that electrons travelling through the crystal have sufficient chance to traverse the maximum value of the excitation function. Von Hippel showed that;

$$e.E_{max}.\frac{a\omega}{2} \quad \rightarrow \quad C.h\nu_{max} \qquad \text{(AP 1.1)}$$

Here E_{max}= breakdown field strength, $e.E_{max}.(a\omega/2)$ is the energy and $(a.\omega/2)$ is the distance between 2 neighbouring ions, hence is the distance between two successive impacts. $C.h\nu_{max}$ corresponds to the maximum of the integral excitation function. The left hand side of equation AP 1.1 must reach the value of the right hand side if impact ionisation and breakdown shall occur. Von Hippel showed that *C* must lie between 1.4 and 2 for the theory to work, which for his investigations into alkali-halides, it did [297-298].

Here the principle breakdown phenomenon is termed cumulative impact ionisation. As multiple ionisations take place, so does destruction of the material, thus degrading its insulating properties. Von Hippel strongly objected to the belief that a form of "heat breakdown" takes place to explain the decrease of electrical breakdown strength with increasing temperature. He suggests this is simply due to the increased mobility

of the ions leading to the recombination of ions with electrons. This recombination is said to cause an electronic emission from the cathode causing a crack to start.

Blythe and Bloor [26] state that electric breakdown is caused by small numbers of electrons, which are available for acceleration by the applied field. For electric breakdown band theory to apply, the breakdown is said to be localised, sudden and catastrophic. This sudden failure is often termed "Avalanche" breakdown. The exact course of the breakdown is determined by localised imperfections or the non-uniformity of the material. Before breakdown, the energy gained by the electrons from the applied field is said to be shared amongst the conduction and trapped electrons through electron-electron collisions.

AP 1.2 Electromechanical Theory

Many properties of materials have dependence on the structure of the system; for example, such as mechanical properties depending on the crystallised structure. It was suggested that electrical breakdown should also depend on the physical structure of the material. Blok et. al. [299] showed along with others [300-302] that such a model could exist and could explain electrical breakdown. Based on dielectric slabs, the electromechanical theory suggests that a "thinning" force (electromechanical force) exists on the dielectric due to the applied electric field. The initial theory produced equation AP 1.2.

$$f = A(\frac{K\varepsilon_0}{2})(\frac{V}{d})^2 \qquad \text{(AP 1.2)}$$

Here f = compressive force on the slab, A = sample area under stress, K = relative permittivity of the dielectric, V = voltage applied, ε_0 = permittivity of free space and d = sample thickness. Another equation was generated to represent the mechanical restoring force of the polymer.

$$\frac{f}{A} = Y\log(\frac{d_0}{d}) \qquad \text{(AP 1.3)}$$

Here Y = Young's modulus, d_o = thickness before, d = thickness after and all other parameters are the same as above. Blok showed that combining these equations gave a d_o/d value of $e^{-0.5}$ which equates to 0.606. Continuing these equations to calculate field strength gives equations AP 1.4 and AP 1.5.

$$F_c = \frac{V_c}{d} = \left(\frac{Y}{\varepsilon}\right)^{\frac{1}{2}} \qquad \text{(AP 1.4)}$$

$$F_n = \frac{V_c}{d_o} = 0.606\left(\frac{Y}{\varepsilon}\right)^{\frac{1}{2}} \qquad \text{(AP 1.5)}$$

Here F_c is the corresponding field strength and F_n is the nominal field strength. Further investigations into this model and these equations proved non-conclusive with mixed agreement. Charlesby et. al. [303] showed that for their investigations into polyethylene the electromechanical model showed excellent correlation with experimental data. However similar analysis performed on polystyrene and poly(methyl methacrylate) showed poor agreement. Charlesby suggested the need for a better or revised model.

Stark et. al. [304] similarly believed that an electromechanical model should represent the data, but perhaps not the same as the one suggested by Blok. Their investigations in thick PE also led them to believe that the mechanism of electrostatic force between the electrodes would cause a yielding within the dielectric. In equilibrium they proposed that the mechanical stress caused by the electrostatic attraction would be equalled by residual elastic stress. Their version of the electromechanical model is shown below.

$$\frac{\varepsilon_o \varepsilon_r}{2}\left[\frac{V}{\omega}\right]^2 = Y \ln\left[\frac{\omega_o}{\omega}\right] \qquad \text{(AP 1.6)}$$

Here V = voltage applied, Y = Young's modulus and $\varepsilon_o\varepsilon_r$ = the dielectric permittivity. However for real values of V this does not produce stable $\frac{\omega_o}{\omega}$ values. An amended equation was then suggested.

$$V_{em} = \omega_o \left[\frac{Y}{e\varepsilon_o \varepsilon_r} \right]^{\frac{1}{2}} \qquad \text{(AP 1.7)}$$

Here V_{em} is the electromechanical breakdown voltage. Some clear similarities exist between this and the previous suggestion from Blok. However, when Stark compared the collected data to this model the fit showed poor agreement. It is now believed that electromechanical theories simply cannot fully explain the electrical breakdown effect, but may contribute to it.

Later Blythe and Bloor [26] commented on the electromechanical breakdown theory renewing the interest in it. They expressed that the compressive force exerted by the electrodes would be due to mutual Coulombic attraction between the electrodes as a voltage was applied. They also derived an equation to represent the equilibrium between the electric force causing the compression and the elastic restoring force, shown as equation AP 1.8. Clearly, increasing V above this point would cause the compression force to outweigh the restoring force and begin mechanical collapse.

$$\frac{1}{2}\varepsilon_0 \varepsilon' \left(\frac{V}{d} \right)^2 = Y \ln \left(\frac{d_0}{d} \right) \qquad \text{(AP 1.8)}$$

Here, Y is the young's modulus for the material and d_0 is the initial thickness.

AP 1.3 Electrofracture Theory

With the observation that materials tend to form cracks when placed under mechanical stress and that this is soon followed by critical failure, this idea was soon applied to electrical breakdown. Fothergill [305] proposed a filamentary-shaped crack that propagates through the dielectric. This is said to release both electrostatic energy and electromechanical strain energy stored in the material due to the applied electric field. The basic theory builds on the electromechanical model. Fothergill suggests electrical breakdown strength has a 4th root dependence on the Young's modulus. He

goes on to suggest that the time taken to complete the breakdown is comparable to the time taken for sound waves to cross the dielectric.

Fothergill's beliefs were tested by Hikita et. al. [306] during their work on polyethylene thin films. Using up to 500 Vs^{-1} ramp dc on 25 μm thick low density PE at varying degrees of crosslinking with silane they observed the breakdown strength and Young's modulus. By varying the temperature and current before breakdown they collected a sizeable data set that proved to show very good agreement with Fothergill's 4^{th} root dependence theory. However, unlike the electromechanical model they believed that there should also be a more electrical component involved.

Work by Mizutani et. al. [307] confirmed that Fothergill's method was appropriate but the accuracy had room for improvement. They noticed that just prior to breakdown in their polyimide films, approx. 10^{-3} seconds before, the current increased. Further investigations by Hikita et. al. [308] showed this to be the case for LDPE as well, which could not be explained by the electromechanical theory. For this theory to advance, a further electrical effect would be needed to explain the rise in current.

Zeller et. al. [309-310] then introduced some new ideas to this Young's modulus dependence theory, creating the electrofracture model. Similarly, the model is based on the idea of a filamentary crack growing through a dielectric due to the electrostatic force. However Zeller states that the model is operative at higher local electric fields and the breakdown process is different to ageing processes. He suggests an analogy to the mechanical crack propagation in brittle materials where the crack grows if the strain energy is greater than that required to overcome the toughness of the material. The envisaged crack is considered in one dimension for now, but is said to be propagating in a similar fashion to a two dimensional mechanical crack.

At the tip of the filament there is said to be an enhanced electrostatic field which gives rise to electrostatically stored energy in the dielectric causing significant mechanical stress if the field is sufficiently high. By considering the electromechanical energy and

electrostatic separately, equation AP 1.9 was obtained, which can be re-written as equation AP 1.10.

$$W_{es} + W_{em} = \left[\frac{1}{2} \varepsilon_o \varepsilon_r E^2 + \frac{\sigma^2}{2Y} \right] \pi r^2 \delta l \qquad \text{(AP 1.9)}$$

$$W_{es} + W_{em} = \left[\frac{1}{2} \varepsilon_o \varepsilon_r E^2 + \frac{\varepsilon_o{}^2 \varepsilon_r{}^2 E^4}{8Y} \right] \pi r^2 \delta l \qquad \text{(AP 1.10)}$$

Here W_{es} is the electrostatic energy, W_{em} is the electromechanical energy, r is the radius of the tubular crack, and $\pi r^2 \delta l$ is the volume displaced. In Zeller's version, the electrostatic energy dominates the electromechanical energy. Comparing this model with Fothergill's theory treated the same way it is seen that Fothergill's theory differs in several key areas. His adapted theory equation is shown below.

$$E_{fem} = \left[\frac{16GY}{\varepsilon_o{}^2 \varepsilon_r{}^2 r} \right]^{\frac{1}{4}} \qquad \text{(AP 1.11)}$$

Here G is the toughness and Y is the Young's modulus. Clearly Fothergill's model still suggests a 4th root dependence but also contradicts Zeller who used a smaller value of surface tension in place of G. This model, with the applied voltage being proportional to the electrostatic field at the tip of the filament, shows excellent agreement to data taken by Fothergill as well as that of Hikita. Fothergill's model is currently at the forefront of the electrofracture theory for electrical breakdown, although Zeller clearly provided the necessary foundations to create the model.

AP 1.4 Thermal Breakdown Theory

Many dielectrics are highly temperature dependent during crystallisation, dielectric loss, relative permittivity and physical experimentation. This soon developed the idea that perhaps electrical breakdown may also be temperature dependent, or at least it may contain a thermal process. Nagao et. al. [311] subsequently performed research into the possibility of thermal effects within electrical breakdown within polyethylene.

Nagao observed local Joule heating in the PE films at room temperature when breaking down the films with a dc electric field. By mapping the Joule spots they observed high temperature points appearing in the film. At these points it was discovered that the conduction current was increasing with time. The final breakdown of the film then occurred at the point of highest temperature. These results strongly suggest that a thermal process is dictating the breakdown. Nagao's conclusions contradicted several other investigations that stated that at room temperature PE breakdown was a completely electronic process [312]. One such contradiction was by Miyauchi et. al. [313] during their investigations into PE film breakdown around room temperature.

From these pockets of Joule heating, Nagao realises that weak points within the films must exist. These could be due to impurities, pores or possibly the ISS (see Impurities in Dielectrics Theory and Interspherulitic Space Theory (ISS) sections). To observe the thermal spots a thermograph was used during the build-up to and during electrical breakdown. Nagao hypothesised that the heating simply allows the dielectric molecules to shift away from the electrode region, hence the dielectric becomes thinner at these points and thus breakdown occurs here. With the current suspected as being thermally activated, the charging current can be expressed as follows.

$$I = I_o \exp^{\left(\frac{-H}{kT}\right)} \qquad \text{(AP 1.12)}$$

Here I_o is a constant, H is the activation energy, k is the Boltzmann constant, T is the absolute temperature and I is the charging current. Some doubts about the effective magnitude of the thermal process still exist. Hikita et. al. [314] had previously observed that, above 50 ^{o}C, their PVDF breakdown strength decreased inversely with temperature. This decrease appeared dependent on the rate of the electric field rise and was not dependent on thickness. This suggests temperature dependence for higher temperature breakdown but it was still believed in this case that ionic conduction was the dominating mechanism of breakdown.

Theories revolving around electrical breakdown dependence on thermal effects have been suggested by many researchers. The main question is whether the overheating of the breakdown site is caused by increasing current or whether the increase in current has occurred due to an increase in temperature. A majority believe that the overheating is caused by the increase in current, such as Wagner [315], Hayden et. al. [316] and Gunther et. al. [317]. Following on from Hikita's work, Buehl et. al. [318] graphically imagined the temperature dependence of the breakdown voltage of a dielectric. Again, further evidence is needed to make an accurate model incorporating the suspected thermal effect.

AP 1.5 Percolation Theory

Another simple model proposed by Kai et. al. [319] is based on percolation theory. The first assumption is that the electron migration in polymers should be electron-hopping or tunnelling conduction between the localised states. Hopping/tunneling conductivity makes charge transport possible when band conduction no longer occurs and requires the charge carriers to jump across/tunnel through the energy barrier. Kai analysed photoelectric data of polymers using classical band theory and concluded that the conduction band is very close to the vacuum level and sometimes above it. Kai reasons that this could mean polymers have no conduction band. Previous research into disordered systems by Anderson [320] and Thouless [321] suggested that there was no apparent conduction band where an electron wave function is localised. Therefore Kai could be correct for some, or perhaps all, polymers.

The application of this idea clearly depends on the degree of disorder in the polymer. Kai stated that, in general, polymers can be considered to have a higher degree of disorder than amorphous semiconductors. This suggests that electrons in the polymers are localised with electron conduction in the form of hopping between the localised states. Kai predicts that the "avalanche" phenomenon is simply down to the electron free path not being long enough to induce collision ionisation. The electrons in the localised states have an equal probability to "hop" in all directions, until the electric field is applied, when the localised states are said to stretch as shown below.

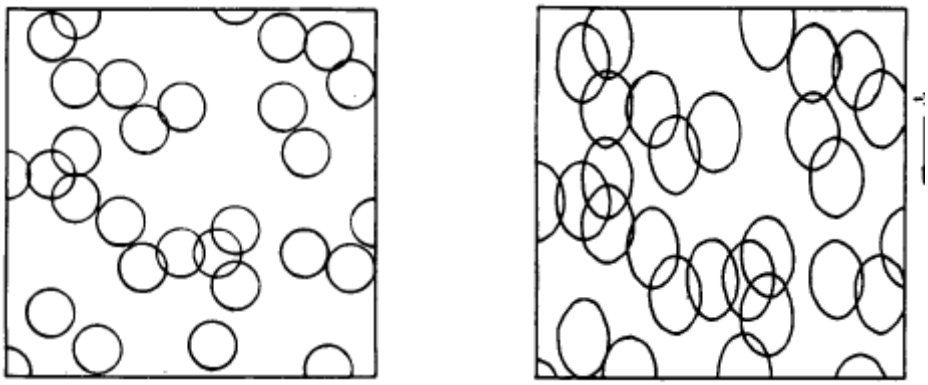

FIGURE AP 1.1 : Shows the distribution of localised states at low field strength (left) and at high field strength (right) Reprinted from Kai et. al. [319]

As the localised states stretch and overlap they form a "percolation" path. Current theory suggests that band structure cannot be changed in materials; although Kai thinks this is true for conduction at low field strength, he believes that in insulating polymers the strength of the field is so high that the probability of electron hopping is far greater and that this could lead to the band structure changing. Above the electrical breakdown voltage, the current is said to increase violently, represented by this model as more and more localised states overlap and the "percolation" paths increase in number. Kai defined the breakdown to occur when the probability of electron hopping reached a certain value.

$$n(E_b) = e^{-\frac{U - eR\frac{E_b}{2}}{KT}} = p \qquad \text{(AP 1.13)}$$

Here $n(E_b)$ is the probability of hopping from one local state to a neighbour, p is the threshold taking a value 0.1-1, R is the average distance between localised states and U is the barrier potential between the localised states. Kai considered U as the width of the forbidden band, a value of around 8 eV. Kai also produced a much simplified version of the equation shown below. When comparing this model to collision theory the breakdown strength was seen to be double that of the actual and collision theory values. This theory is currently very inaccurate, although with consideration of the tunnel effect and weak points in the polymer is believed to be capable of producing a very competitive model.

AP 1.6 Avalanche and a Unified Avalanche/Bubble Theory

Possibly the most popular current theories regarding electrical breakdown involve some kind of avalanche theory. Forster [322] explained the five main steps of an avalanche electrical breakdown; 1) Initiation of a partial discharge (PD), 2) Growth of the PD, 3) Forming of a conducting channel, 4) Electrical breakdown occurs, 5) Post-breakdown effects. The first two steps are considered to be the most sensitive to experimental conditions, as shown by McGrath et. al. [323] in their liquid dielectrics investigations, and others [324-325]. In previous work conducted by Forster, he stated that the formation of the conducting channel, the third step, is so fast that it's difficult to ascertain what is happening [326].

Forster [327] described the fourth step of his theory to be the creation of a plasma state brought about by the flow of very large currents. The fifth step is where the system returns to its original conditions. However Forster [326] stresses that the state of the system's chemistry is permanently changed after each breakdown and does not return to its original state. Forster's 5-step avalanche theory has been widely accepted; an advancement to which has been proposed by Sharbaugh et. al. [328], who blended the ideas from avalanche theory and bubble theory together. Using avalanche theory by Forster [327] and Yamashita et. al. [329], they reasoned on the co-existence of this theory with previous work by Sharbaugh into a bubble theory. By creating a unified model suggesting the dominance of one theory in a particular region it was hoped that accurate explanations of electrical breakdown behaviour could be obtained.

With regard to bubble theory, the dielectric strength is clearly much lower than that of solid insulators, with the discharges believed to be damaging to the solid and eventually leading to failure of the dielectric. Discharges in these bubbles are extinguished as charges are deposited on the walls of the cavity, hence reducing the field inside. These uniform field gas discharges cause breakdown in the form of a cumulative electron avalanche process. Discharges in cavities can also result in tubular channels forming in the dielectric in the direction of the field. These can often branch out and form a pattern commonly referred to as an electrical tree.

Sharbaugh suggested that the avalanche model proposed by Yamashita et. al. that worked so well at low pulse durations would be dominating until passing into a higher pulse duration region where the dominating effect would change. The second dominating effect selected by Sharbaugh, almost as a transition effect, was the avalanche streamer proposition from Forster [330]. This multiple avalanche theory allowed for the unified theory to move from avalanche based to include the bubble theory proposed by Watson et. al. [331] at high pulse duration. Sharbaugh shows that these two theories can co-exist, although more experimental evidence is needed to be sure.

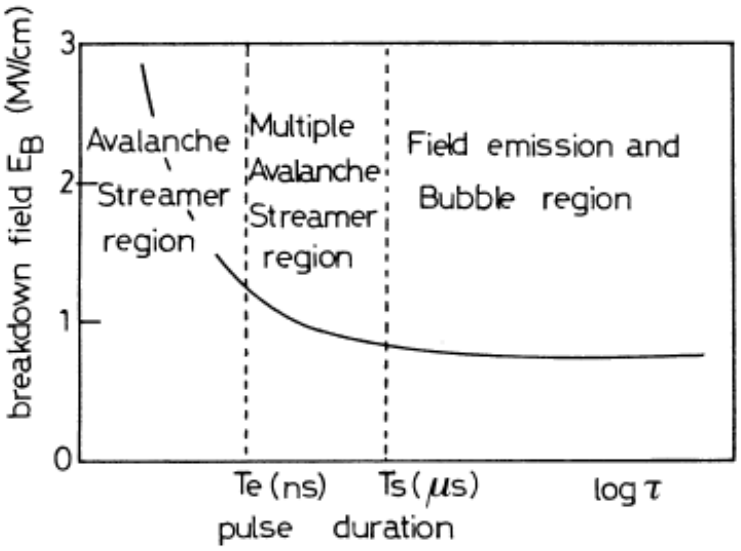

FIGURE AP 1.2 : The effect of pulse duration on breakdown field and breakdown mechanism. Reprinted from Sharbaugh et. al. [328]

AP 1.7 Planckton based Unified Theory

Prevenslik [332] introduced a theory in 1999 building upon the idea that dielectric materials may contain sub microscopic bubbles. His work follows on from Pashen's [333] building on a proposed mechanism for liquid breakdown, based on growth of vapour bubbles by electrical heating accompanying electron avalanche. This theory is extended to solids on the basis that bubbles could exist in the liquid phase and remain as the solid phase forms. Prevenslik defines the sub microscopic bubbles as "Plancktons" due to its later seen roots in Planck theory of sonoluminescence. These "Plancktons" are said to grow from random density functions.

In Planckton unified theory, the electrons within the polymer are free to accelerate under the applied electric field and exceed the 5 eV needed for the ionisation of the dielectric molecules in the Planckton wall. Therefore the material is said to undergo electrical breakdown as the electron avalanche cascades through other Plancktons in the dielectric. Work by Forster et. al. [334-335] led to a theory based on the discovery of regions of low density in a dense medium. This discovery was thought to be the missing link to unify electrical breakdown theory in liquids and solids.

Forster's theory states that a vapour bubble is formed as successive electrons are trapped and the local region is electrically heated, leading to breakdown by electron avalanche. Prevenslik went on to compare the Planckton model to work by Sharbaugh et. al. [336] and Bragg et. al.[337]. He concluded that one major objection to the collision ionisation ideal is its inability to account for the pressure dependence of the breakdown strength, as the mean free path of an electron in dense media is essentially independent of hydrostatic pressure.

Prevenslik therefore believes that work by Sharbaugh and others favours bubble involvement, possibly such as his Planckton theory. Sharbaugh's bubble theory is also based on the creation of vapour bubbles leading to electrical heating induced electron avalanche. Prevenslik proposes that to satisfy both vapour bubble theory and Paschen's law, the vapour bubbles must pre-exist in the solid, supposedly formed from collision ionisation in the liquid phase, later confirmed by Beroual and Tobazeon [338-339].

In the Planck theory of sonoluminescence (SL) previously proposed by Prevenslik [340], standing UV waves exist in resonance with the bubble's dimensions due to induced spontaneous UV emission. As the bubble collapses the wall molecules are said to absorb the energy from these standing waves and UV emission halts, leading to a Stokes' shift from UV to visible photons or to the UV being converted to electrons via the photoelectric effect.

The Planckton bubbles are said to grow until equilibrium is found with the surface tension. Under an applied electric field the electrons are then accelerated inside the

plancktons and collide with the molecules of the bubble walls. The planckton diameters are said to exceed the mean free path of the electrons in dense media, and therefore the electrons can accelerate to energy levels high enough to ionise the dielectric molecules lining the planckton walls.

$$V_{bd} \propto Pd \qquad \text{(AP 1.14)}$$

Looking back to the simple Paschen's law model, the breakdown voltage of a gas in a gap under a uniform electric field is said to be a unique function of the product of the gas' pressure and gap separation, as shown in equation AP 1.14 [341]. Paschen's law describes the region $Pd > (Pd)_{min}$ where electrons collide with gas molecules in the gap and these molecules undergo ionisation. For the region $Pd < (Pd)_{min}$ the breakdown is said to be caused by electrons moving across the gap, not colliding with gas molecules and, instead, colliding with and ionising the electrodes.

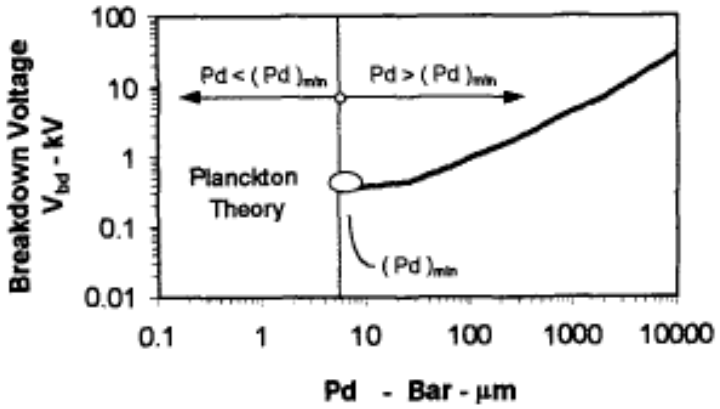

FIGURE AP 1.3 : Regions of Pashcen's law and planckton theory.
Reprinted from Prevenslik [332]

Relating this to the Planckton theory, plancktons with diameters of *2R* will be analogous to a gap *d*. Assuming plancktons pre-exist throughout the dielectric at a pressure *P*, with the dielectric forming the Planckton walls being analogous to metal electrodes. However, with $2R < d_{min}$ the breakdown in the $Pd > (Pd)_{min}$ region by ionisation of gas doesn't happen. This leaves only the region $Pd < (Pd)_{min}$ with breakdown occurring by ionisation of the dielectric wall molecules. Overall the Planckton Unified theory seems feasible and has been shown to correlate with data

from Forster [334-335], however further investigation would be needed since there is no current evidence for such structures.

AP 1.8 Electric and Thermal Unified Theory

Frohlich [342-343] has performed in depth research into the theory of dielectric breakdown in crystals and solids, leading to a unified theory of electric and thermal effects [344]. Frohlich's original theory [345] published in 1937 was later built upon to include a critical temperature. The theory is based on breakdown observations at high temperatures for highly temperature dependent samples, and the near-independence of breakdown strength on temperature at low temperatures. He theorised that at temperatures higher than the lattice temperature T_o, where the breakdown strength F decreases rapidly with temperature, a thermal breakdown effect is in action. At temperatures lower than T_o little temperature dependence an electrical breakdown process is assumed.

$$I = \frac{\left(e^2 \tau\right) F}{Vm} \qquad \text{(AP 1.15)}$$

Equation AP 1.15 shows Frohlich's theory, where I = current density per electron, τ = time of relaxation, F = field strength, V = volume of the crystal. Frohlich continues to define the energy transferred per second from the field to the electron as;

$$A = IFV = e^2 F^2 \tau / m = C\left(F^2 E^{\frac{3}{2}} \right) \qquad \text{(AP 1.16)}$$

Here A = energy transferred to electron by field per second, C = a constant and E = kinetic energy of an electron in the conduction level. This can then be compared to the energy transferred per second from the electron to the lattice, shown in equation AP 1.17. Therefore, to calculate the rate of loss of energy, one is simply subtracted from the other, as in equation AP 1.18.

$$B = C_2 E^{-\frac{1}{2}} \qquad \text{(AP 1.17)}$$

$$B - A = C_2 E^{-\frac{1}{2}} - CF^2 E^{\frac{3}{2}} \qquad \text{(AP 1.18)}$$

Here B = energy per second transferred to the lattice from the electron and C_2 is a constant. From this it can be seen that for low energies, where $E<E^*$, the electron will lose energy and for high energies where $E>E^*$ it gains energy. Frohlich defines E^* as the point at which $A=B$, where the same amount of energy gained by the electron from the field is transferred to the lattice, suggesting a relationship;

$$E^* \propto \frac{1}{F} \qquad \text{(AP 1.19)}$$

The condition for breakdown is said to be that no stationary state for the electron distribution can be reached, hence an electron with energy less that the ionisation potential, IP, can gain energy from the field but that no reverse process can exist. This suggests that $E^* \leq IP$ and, if not satisfied, the field cannot cause any instability due to its inability to produce any electrons capable of ionisation.

Frohlich's revised version includes a critical temperature, T_c, above which the density of electrons is so high that mutual collisions between electrons are much more frequent than collisions between electrons and lattice vibrations. The equilibrium between the rates of energy transfer from field to electrons and from electrons to lattice is only possible below the critical field F^*. For higher values, the electronic temperature is said to rise steadily until breakdown, explaining the thermal dependence of F^* decreasing exponentially with increasing lattice temperature. Frohlich suggests that the theory also covers the rise observed in breakdown strength at low temperatures as well as decrease at high temperatures.

AP 1.9 Interspherulitic Space Theory (ISS)

Another possible effect on electrical breakdown could be the crystallinity and spherulite properties of polymeric dielectric. Kolesov [346-347] performed in-depth research into breakdown strength dependence on spherulite properties in HDPE and PP. It was observed that electric breakdown strength, *Eb*, increased and the *tanδ*

decreased with decreasing spherulite size samples. This was the case for HDPE, polypropylene and isotactic polystyrene. Kolesov suggested that this was due to the ratio of spherulite volume and the interspherulitic space (ISS) within the dielectric.

Using heat treatment, Kolesov varied spherulite sizes in 50 mm diameter discs of thickness 60-70 μm before electrically breaking them down in castor oil. The dielectric loss was measured at 10^6 Hz and the *Eb* decreased as the spherulite size (SS) increased until the mean spherulite diameter *d* became equal to the specimen thickness *h*. Kolesov reasoned that the breakdown must therefore occur in the ISS region and generated the following equation for this. Here *A* is a constant and E_o is the polymers strength when $d \geq h$.

$$Eb = A\left[\sqrt{(d-h)^2} - (d-h) + E_o\right] \qquad \text{(AP 1.20)}$$

Further investigations by Kolesov [348-349] were performed by accurately choosing breakdown sites on samples so that the breakdown strength of the spherulites and ISS could be obtained. Table AP 1.1 shows some of the results from these investigations, clearly showing that the spherulite breakdown strength was approximately double that of the ISS region. Also it was noted that the ISS showed less specimen damage, possibly suggesting a smoother breakdown than a possible catastrophic situation in the spherulites. This lower breakdown strength shown by the ISS could be due to impurities as discussed previously.

Spherulite E_b (kV/mm)		
Maximum	Minimum	90%
690	540	660
Interspherulite space E_b (kV/mm		
Maximum	Minimum	90%
330	120	300

TABLE AP 1.1 : The electric strength of different microvolumes of polypropylene. Reprinted from Kolesov [346]

Wagner [350-351] also observed that most breakdowns occur in the ISS region during his investigations into cross-linked LDPE. Kolesov et. al. [352] performed investigations into ISS theory and with use of SEM found that as the SS increased, the electric strength of the ISS falls rapidly initially before then slowing down eventually reaching a constant value when the mean diameter is the same order as the film thickness.

Kolesov postulated that there may also be defective spherulites within the system but that increasing the SS would cause the number of defective spherulites to increase to a constant value. The electric strength of spherulites without such defects is independent of size and is relatively high, as shown in table AP 1.1 previously. For that specific investigation a value of around 1.2-4 $x10^3$ kV/mm was obtained.

AP 1.10 Impurities in Dielectrics Theory

Apart from the above models and theories, other research has been performed suggesting that slightly different processes were involved in electrical breakdown. One such suggestion was proposed by Zeng et. al. [353] (and Pohanka et. al. [354]) suggesting that dielectric breakdown is caused by weakness in the material such as microscopic pores, cracks and grain boundaries. During their investigations into composites of lead zirconate titante ceramics with SiC they observed a relatively low breakdown strength for samples without SiC. However when diffusing the SiC into the ceramic, most of it settled into the microscopic pores and cracks. Once tested again its breakdown strength was greatly improved, strongly suggesting a relationship between these impurities and breakdown sites and breakdown strength.

Wagner [355] and Maxwell [356] also believed that the electrical breakdown strength was either due to, or severely dependent on, the presence of cracks/voids or impurities. The easiest situation to envisage is an insulator containing dispersed conductive particles, such as a metal. They developed the following equations for a dielectric material of relative permittivity ε_1 with negligible conductivity, containing impurity spheres of volume f, conductivity σ_2 and relative permittivity ε_2.

$$\varepsilon' = \varepsilon_\infty' \left(1 + \frac{k}{1+\omega^2 T^2} \right) \quad \text{(AP 1.21)}$$

$$\varepsilon'' = \frac{\varepsilon_\infty' (k\omega T)}{1+\omega^2 T^2} \quad \text{(AP 1.22)}$$

Where;

$$k = \frac{9f\varepsilon_1'}{2\varepsilon_1' + \varepsilon_2'} \quad \text{(AP 1.23)}$$

$$\tau = \frac{\varepsilon_0 (2\varepsilon_1' + \varepsilon_2')}{\sigma_2} \quad \text{(AP 1.24)}$$

$$\varepsilon_\infty' = \varepsilon_1' \left[1 + \frac{3f(\varepsilon_2' - \varepsilon_1')}{(2\varepsilon_1' + \varepsilon_2')} \right] \quad \text{(AP 1.25)}$$

It was believed that such impurities were the paths that electrical breakdown would follow, however it is unclear in this theory how breakdown would occur if the sample were free of such impurities/defects. This theory can be considered similar to the ISS theory in AP 1.9, as the growth of spherulites could push such impurities into the 'ISS region' causing breakdown there. However a possible flaw in both theories could be shown if a sample consisting of only one large spherulite was created. By both theories the breakdown should only occur at the edges of such a sample and not directly through the spherulite.

AP 1.11 Conclusion

The aim of this appendix was to create a summary of current electrical breakdown theories and provide the basic details and ideas behind them, along with crediting those involved. The most important point to note is that, at this moment in time, no single theory has been fully settled upon. Some theories have more supporting evidence than others but all theories have, at one point or another, been unable to explain an experimental result. The actual cause and processes behind electrical

breakdown could be explained by almost any mixture of the above theories, or even may not have been considered yet. This main body of work does not set out to decide which breakdown process is occurring in the PEO composites, but instead will try to recommend which theories hold and which do not.

Appendix 2: GOLD COATING

To calculate the best set-up for gold coating a preliminary experiment was performed by gold coating glass slides and varying the time/current. The results are shown in table AP 2.1. Based on this short study, several observations were made. As expected, increasing time and/or current increases the thickness of the gold layer and subsequently reduces the surface resistance. Secondly, when increasing the time/current the behaviour observed by the resistance is an exponential/hyperbolic decay as expected when modelling the gold deposition. When multiplying the two factors to provide an arbitrary X value to plot against the resistance, figure AP 2.2 shows the best fit is a simple 2 parameter hyperbolic decay. Thirdly, it appears that neither the time nor current dominates the change in resistance. Figure 2.1 shows the data collected for varying current and time.

Sample	Time /mins	Current /ma	Resistance /ohms
A	2	20	27.2
B	2	30	14.9
C	2	40	11.1
D	2.5	20	12.7
E	2.5	30	7.4 *
F	2.5	40	6 *
G	3	20	11
H	3	30	7.8 *
I	3	40	5.3 *
J	3.5	20	10.7
K	3.5	30	6.1 *
L	3.5	40	5.3 *
M	4	20	7.5 *
N	4	30	4.9 *
O	4	40	4.3 *

* = sample is of acceptable resistance

TABLE AP 2.1 : Test gold coat samples, varying time and current

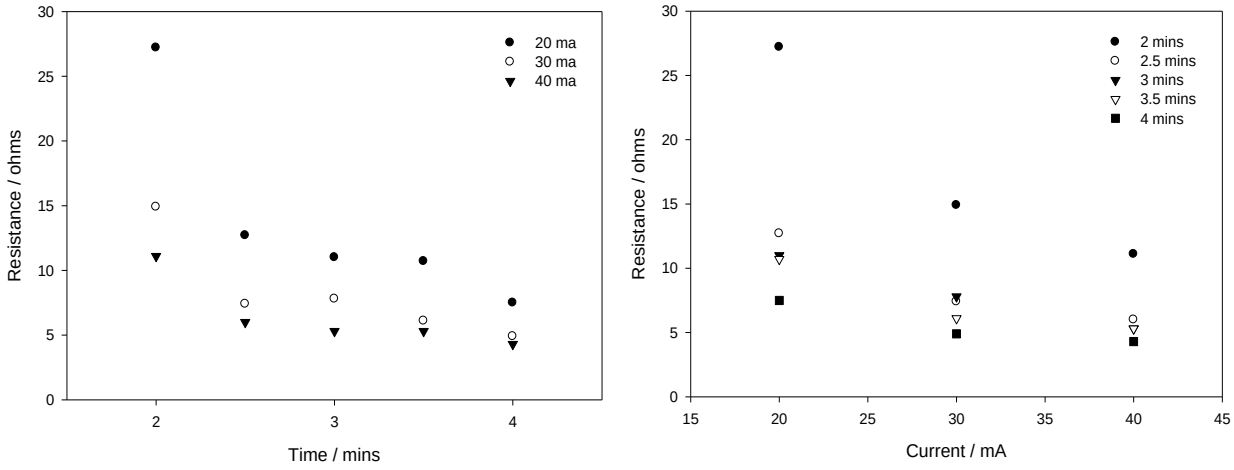

FIGURE AP 2.1 : Varying time and current against resistance

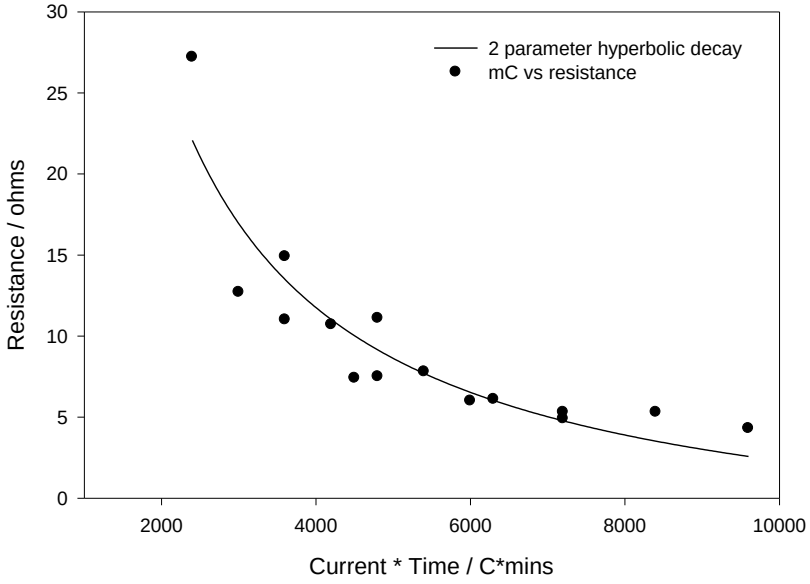

FIGURE AP 2.2 : Combining time and current shows a hyperbolic decay for resistance

These provisional tests provided a much greater understanding of the gold coater and variable dependencies, allowing the best values to be chosen. It was deemed that both current and time values chosen should be in the middle of the equipments range so 30 mA for 3 minutes was chosen, generating a coating with an approximate resistance of 8 ohms.

Appendix 3: RHEOMETER LIMITATIONS

When processing the PEO solutions using the rheometer, many factors were considered to help reduce any errors present, including; temperature, time left standing and volume of solution mixed, some results of which can be seen in the main body of this thesis. However the rheometer itself has an associated accuracy limit, said to be a shear rate of 4000 s^{-1} before data is no longer accurate to the highest possible accuracy of 1%, as quoted in the rheolab manual. Despite this, the rheometer is said to be capable of reaching over 4000 s^{-1} (up to over 5000 s^{-1}), at the cost of reduced accuracy data. Initial investigations showed that for 20 ml samples, data collection failed just below 5000 s^{-1}. Figure AP 3.1 shows the shear rate/shear stress data for a B1 sample reaching the limitations of the rheometer at the marked shear rate.

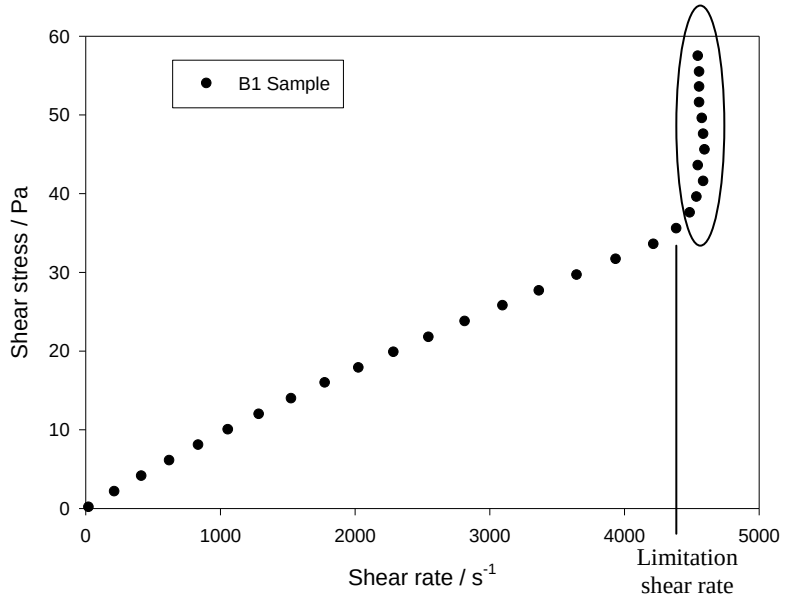

FIGURE AP 3.1 : A 1% 400,000 $gmol^{-1}$ PEO sample highlighting the shear rate limitations of the rheometry system

The corresponding shear rate/viscosity curve also highlights this limitation. From these initial experiments it was clear that for accurate and complete data sets, the shear rate should not exceed 4200 s^{-1}, thus discounting samples: A1, A2 and B1. It was also noted that the C10 samples were too viscous to gain acceptable data and hence was omitted.

Appendix 4: WILLIAMS-LANDAU-FERRY THEORY

The WLF equation, which models the thermal dependence of the viscosity of polymer melts, is an expansion on free volume based kinetic theories. By considering the probability of motion for molecules per unit time, *P*, is associated with an Arrhenius relationship (shown in equation AP 4.1) involving an activation energy, *E*, and the thermal energy *kT* giving equation AP 4.2.

$$k = A \exp^{-E_a / RT} \tag{AP 4.1}$$

$$P = \exp^{-E/ kT} \tag{AP 4.2}$$

From equation AP 4.2, *P* is seen to increase with temperature. By considering the total probability in time *t* to be *Pt* equation AP 4.3 can be formed. When *lnPt* reaches a fixed value for the motion of molecules then, hence *–E/kt + lnt = C*, this then becomes equation AP 4.4, noting that time is inverse to temperature.

$$\ln Pt = \frac{-E}{kT} + \ln t \tag{AP 4.3}$$

$$\ln t = C + \frac{E}{kT} \tag{AP 4.4}$$

The activation energy *E* here is dependent on the free volume in a sample, denoted in equation AP 4.5, where *B* is a constant and *f* is the fraction free volume.

$$\frac{E}{kT} = \frac{B}{f} \tag{AP 4.5}$$

By considering the flow at a ground state time t_0 at a reference temperature of T_0, a 'shift factor' α_T can be applied to represent the difference in natural log values of two times *t* and t_0, with two associated temperatures *T* and T_0, which leads to equation AP

4.6. When the viscosity is inverse to the shear rate, it is therefore proportional to the shift factor, giving equation AP 4.7.

$$\ln \alpha_T = \ln t - \ln t_0 = \Delta \ln t \qquad \text{(AP 4.6)}$$

$$\ln \alpha_T = \ln\left(\frac{\eta}{\eta_0}\right) \qquad \text{(AP 4.7)}$$

This leads to equation AP 4.8, where f_0 is the fraction free volume at a reference temperature, such as T_g and f is the free volume at a desired temperature. From free volume theory, at a temperature f, equation AP 4.9 exists and can be substituted into equation AP 4.8 to create a form of the WLF equation, shown as equation AP 4.10.

$$\Delta \ln t = B\left(\frac{1}{f} - \frac{1}{f_0}\right) \qquad \text{(AP 4.8)}$$

$$f = f_0 + \alpha_f (T - T_0) \qquad \text{(AP 4.9)}$$

$$\ln \alpha_T = -\left[\left(\frac{B}{f_0}\right)(T - T_0)\right] / \left[\left(\frac{f_0}{\alpha_f}\right) + (T - T_0)\right] = -\frac{C_1 (T - T_0)}{C_2 + (T - T_0)}$$

(AP 4.10)

Here, α_T is still the shift factor, C_1 is the first material constant, C_2 is the second material constant and T_0 is the glass transition temperature. The two material constants depend on the definition of T_0 and can be calculated from free volume theory or measured experimentally.

Appendix 5: ETCHING AND SEM

AP 5.1 Etching and SEM Theory

To obtain images of the structure of samples proves difficult when only observing the sample's surface. To get a better image of particle interaction within the system it would be useful to remove surface material to reveal the internal microstructure. This is achieved by chemical etching, defined as the use of a liquid or gas to remove unprotected areas or layers from a material. By submerging the sample into an etchant, the surface layer is 'etched' away leaving a layer more representative of the bulk system. One of the most popular types of etching for polymers, such as polyolefins, is permanganic etching [357-358], where the sample is immersed into an etchant solution of sulphuric acid, orthophosphoric acid and potassium permanganate, for a chosen time period before being placed into a wash solution of methanol. The original permanganic etching method was said to involve; firstly adding 7% potassium permanganate to concentrated sulphuric acid, then treating the specimen for 15 mins at 60 ^{0}C, followed by treatment in a reagent before cooling to 0 ^{0}C and washing in cold dilute sulphuric acid mixture [359]. This whole process removes the low crystallinity surface leaving a high crystallinity layer.

One of the most common polymers, polyethylene, can be etched using fuming nitric acid, as used by Salovey et. al. [360] and others [357,361-362]. Palmer et. al. [363] were the first to etch bulk samples of PE, using 95% fuming nitric acid at 80^{0}C. Later, Hock used a lower concentration of 70% to observe spherulites and lamellar fragments [364]. Like with many etches, a major problem when using nitric acid is the excessive strength. This causes the etchant to not only remove the amorphous surface but also the bulk. Some common solutions are to reduce the etching time or to dilute the etchant.

These etching techniques however cannot be applied to PEO, since a majority of techniques use water to wash away etched debris [365]. Instead, the only documented etchant successfully used on PEO has been sodium ethoxide in ethanol. Used in 1987 by Bu et. al. [366], the PEO is melted for 15 min, cooled to the desired T_c, then cooled

to room temperature. Samples are placed into a 25 ml NaC_2H_5O-ethanol mixture for 10 minutes at around 300 K with agitation. Pure ethanol is then used as a wash to remove etched debris and etchant. They believed that the mechanics of this process were based on an attack on the organic base C-H leading to $–CH=CH_2$ chain scission [365-366]. It was noted that the sodium ethoxide ethanol solution is highly flammable and corrosive, reacting violently in contact with water, suggesting the need for important safety measures. In these previous investigations a 0.21 weight fraction of NaC_2H_5O to ethanol was used.

Scanning electron microscopy is a frequently used technique in materials research, first reported in 1935 by Max Knoll [367]. It allows observation of the surface of a sample down to the nanometer scale, from which the morphology and composition can be identified. Samples for SEM are usually made electrically conductive and grounded to stop charge accumulation at the surface. The SEM apparatus is all contained within a vacuum column during operation. An electron gun at the top creates a stream of monochromatic electrons that pass through a condenser lens, which forms and limits the current in the beam. The beam then passes through the condenser aperture, which eliminates the high-angle electrons from the beam. The beam then passes through a second condenser lens, which forms the electrons into a thin coherent beam, again followed by an aperture to eliminate any high-angle electrons – called the objective aperture. The beam then reaches a set of coils that scans the beam in a grid fashion.

The beam finally passes through an objective lens that focuses the scanning beam onto the area of sample selected. As the beam hits the sample the subsequent interactions are detected. These interactions usually involve secondary electrons, back scattered electrons or X-rays. The most common SEMs observe secondary electrons caused by inelastic scattering. If creating a conducting sample is not possible, environmental SEMs can be used. A chamber at higher pressure than the vacuum in the electron beam column causes beam interactions with the gas to create positive ions that aid in neutralising the negative charge at the surface of the sample. ESEMs are often considered to be superior to regular SEMs, mostly due to the absence of a heavy metal coating that is difficult to reverse and can cover over small features on the surface.

One popular attachment for SEM's is the energy-dispersive X-ray spectroscopy system (EDS). This system analyses x-rays emitted by the target in response to being hit by the electron beam. This incident beam excites electrons into leaving their ground state (lowest shell) and creating an electron hole. Another electron then drops from an outer, higher energy shell, into the hole releasing the energy difference as an x-ray. Analysis of these released x-rays produces a spectrum. Since each element has a unique atomic structure with specific energy gaps between shells, it is possible to identify elements based upon the x-rays emitted.

AP 5.2 Experimental

Three different SEMs were utilised. Initial data were collected on a Cambridge 360 Stereoscan high vacuum SEM, shown in figure AP 5.1, which required samples to be gold coated and an environmental SEM, with no requirement for gold coating. The environmental SEM was a FEI Quanta FEG 600 ESEM. Final images and EDS was performed on a JSM5910 SEM with Cambridge EDS attachment, courtesy of the Science and Engineering Electron Microscopy Centre at the University of Southampton. To organise samples a clockwise system was employed with a gap between the first and last samples, as shown in figure AP 5.2.

FIGURE AP 5.1 : The environmental scanning electron microscope at the Centre for Advanced Microscopy at the University of Reading [368]

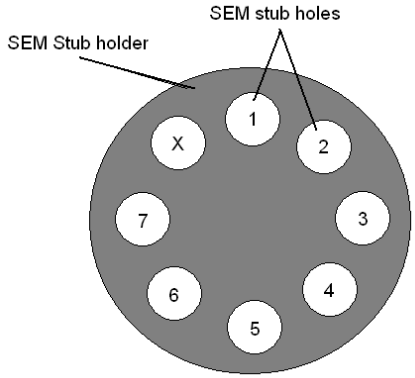

FIGURE AP 5.2 : SEM holder with numbers representing where the corresponding sample went. The X represents a blank

To etch away at the surface lamellar of the PEO samples sodium ethoxide, NaC_2H_5O and ethanol was used as an etchant having seen its use in other investigations. Starting with a concentration of 21% NaC_2H_5O to ethanol, as was used by Bu et. al. [366], before beginning to dilute the etchant after realising that the etch was too aggressive. Table AP 5.1 below shows the concentrations and etching times.

% NaC_2H_5O (remainder is ethanol)	**Etching time, (a) = agitated during etching**	**% NaC_2H_5O (remainder is ethanol)**	**Etching time, (a) = agitated during etching**
0	10 mins	10.5	15 mins
0	15 mins	10.5	10 mins
0	30 mins	10.5	5 mins
21	15 mins	10.5	5 mins (a)
21	10 mins	5.25	15 mins
21	5 mins	5.25	10 mins
21	15 mins (a)	5.25	5 mins
21	10 mins (a)	5.25	5 mins (a)

TABLE AP 5.1 : Etchant concentrations and etching times for samples

AP 5.3 Results

To facilitate higher resolution imaging by scanning electron microscopy, etching was employed, which involved varying the etchant strength and etching time. To analyse the etching effects, images were taken of gold-coated (and uncoated) samples using the microscope in reflection mode. Figure AP 5.3 below shows an unetched 400k PEO sample, both without and with a gold coating. From these it is clear that the surface has not been etched away. Etching in sodium ethoxide for 5 and 15 minutes at a strength of 5.25% produced the images in figure AP 5.4. Here it is clear that the PEO matrix has been etched away, leaving a very rough surface (and leaving filler particles proud of the surface).

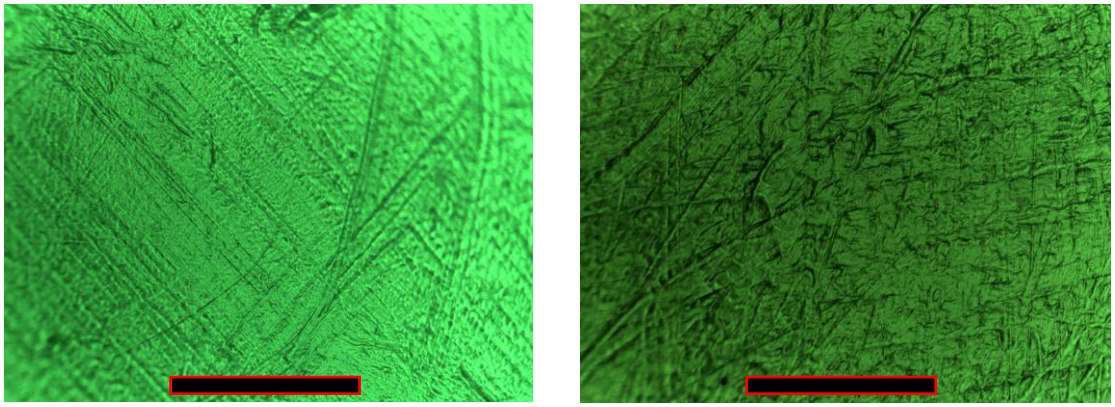

FIGURE AP 5.3 : An unetched 400k PEO sample, uncoated (left) and coated (right). Scale bar = 250 μm

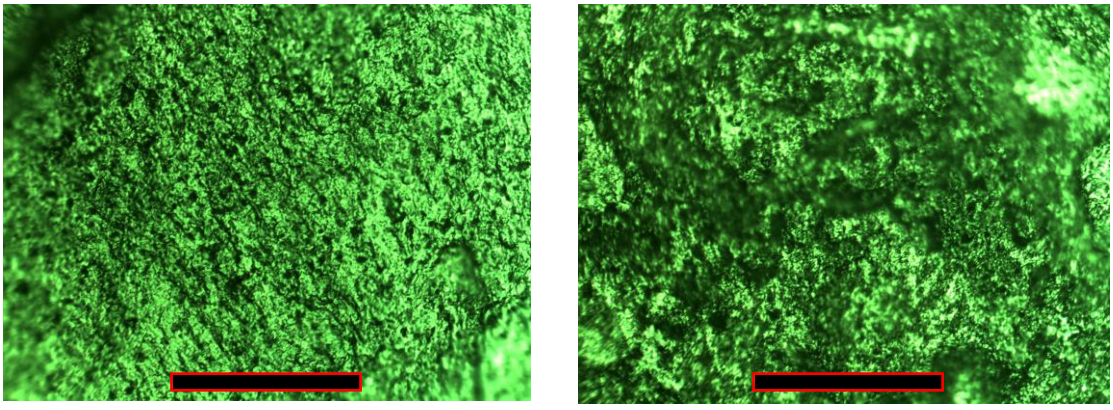

FIGURE AP 5.4 : A PEO-SD sample etched for 5 minutes (left) and 15 minutes (right) at a strength of 5.25%. Scale bar = 250 μm

To ensure that the rinse of ethanol is not etching away at the sample, a test sample was placed into ethanol for 30 minutes, and as can be seen in figure AP 5.5, no etching is observed. Tests into varying the technique for exposing the sample to the etchant were also performed. Previous work by Grosse et. al. [369] into etching of fused silica glass for hollow capillary optical leaky waveguides in microfluidic devices, found that agitation of their samples during etching with hydrofluoric acid, significantly increased the etch rate. Several other investigations into varying etchants for varying samples revealed the same increase in etch rate with agitation [370-371]. This was confirmed in figure AP 5.6, which shows a 21% etch strength for 15minutes with and without agitation. Clearly the agitated sample has been etched much more severely than the stationary sample. This would prove useful if the etchant strength or time could not be increased but a more sever etch was required.

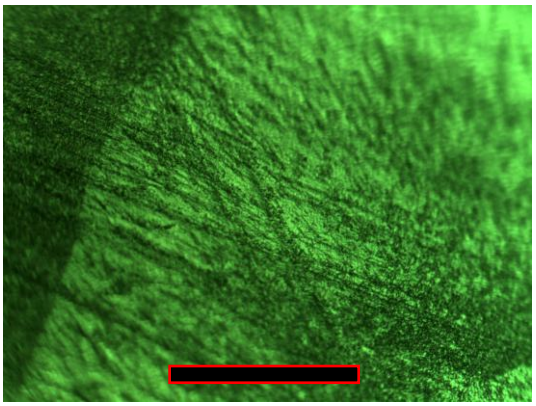

FIGURE AP 5.5 : A 400k PEO sample given 30 minutes in an ethanol rinse. Scale bar = 250 μm

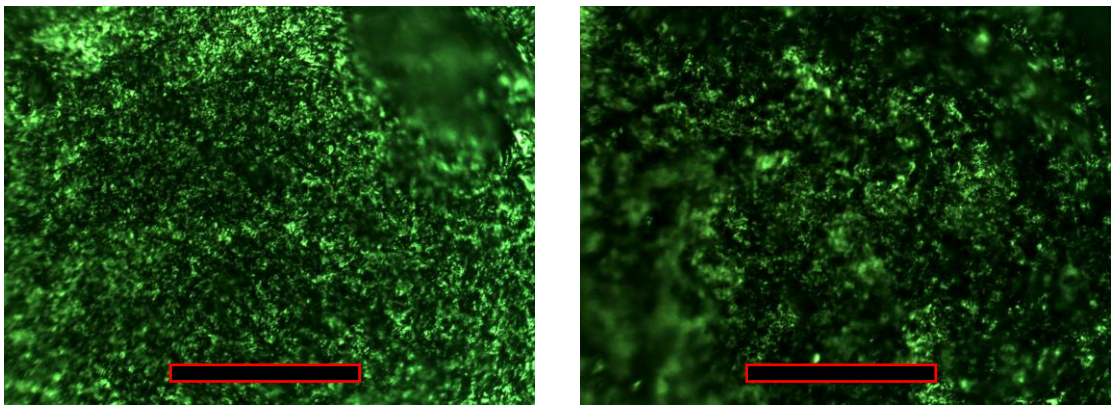

FIGURE AP 5.6 : A 21% strength etch was used for 15 mins on 400k PEO samples with a stationary sample (left) and agitated sample (right). Scale bar = 250 μm

Having established that the rinse of ethanol had no etching effect and that agitation increased the severity of etching, experiments changing etching strength and time were performed. Figure AP 5.7 shows a 10.5% strength etch for 5 (left) and 15 (right) minutes. Figure AP 5.8 shows a 21% etch strength for 5 (left) and 15 (right) minutes. From these it is clear that increasing the etchant strength and etching time increase the severity of the etch as expected. Even the lowest etchant strength of 5.25% (sodium ethoxide to ethanol) for 5 minutes has had a significant etching effect, shown in equation AP 5.9.

This is particularly interesting since previous studies by Bu et. al. [365] claimed a much higher concentration of etchant was needed. In their investigation they used mixtures of high and low molecular weight PEO samples; one with 27.9% of 100,000 $gmol^{-1}$ PEO and 72.1% of 3,500 $gmol^{-1}$ PEO called 2M-1; and the other with 29.9 % of 100,000 $gmol^{-1}$ and 70.1 % 7,000 $gmol^{-1}$ called 2M-7. They used a 21% NaC_2H_5O-ethanol strength etchant, hence the reason to start using this etchant at this concentration, with an ethanol wash for 10 minutes. However their samples appear to withstand the etchant more than ours. In this investigation a much lower etchant concentration was required for a shorter duration to be able to study the internal lamellar of the PEO crystals. This may be associated with the difference in average molecular weight since their samples were blends of two very different molecular weights while the samples tested here have a much more precise M_w.

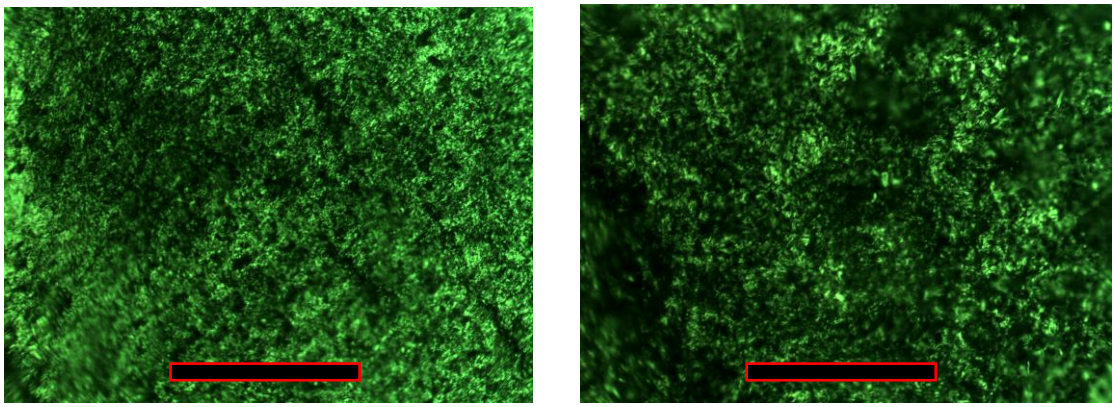

FIGURE AP 5.7 : A PEO-SD sample etched for 5 minutes (left) and 15 minutes (right) at a strength of 10.5%. Scale bar = 250 μm

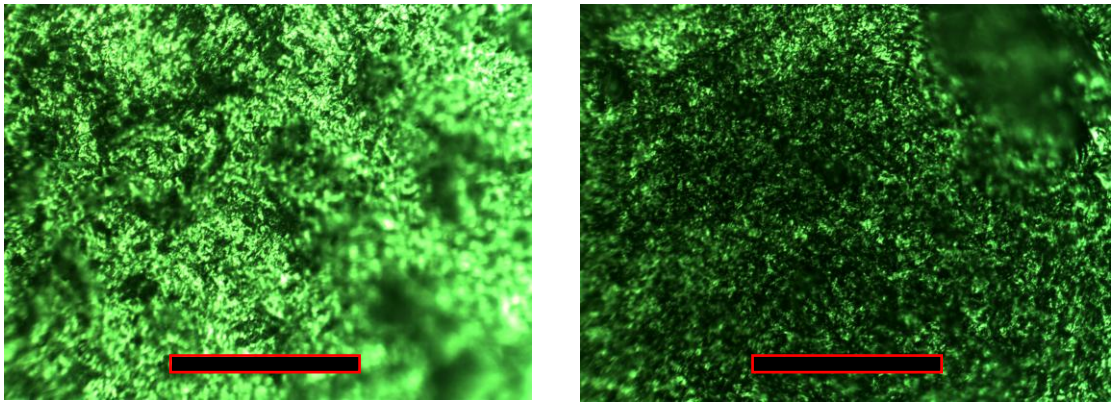

FIGURE AP 5.8 : A PEO sample etched for 5 minutes (left) and 15 minutes (right) at a strength of 21%. Scale bar = 250 μm

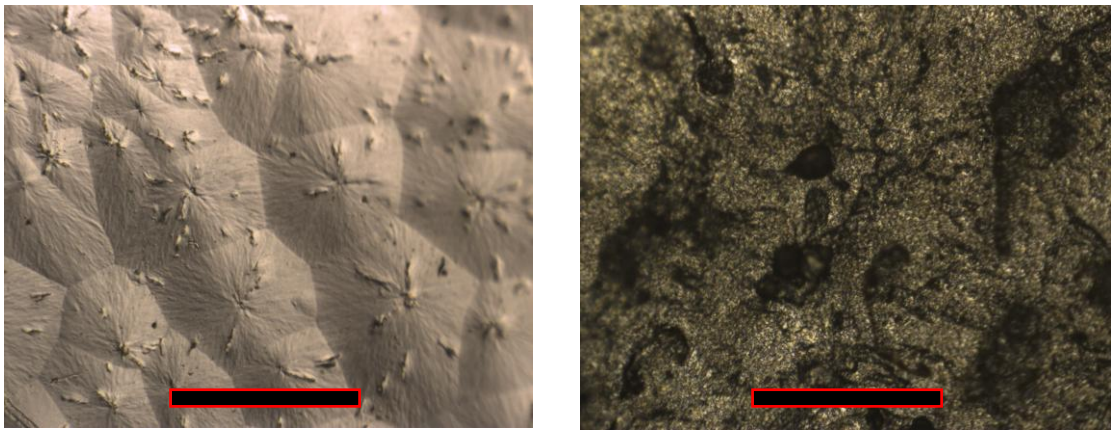

FIGURE AP 5.9 : A 1M-SD unetched sample allowed to crystallise with a free growth surface (left) and a 1M sample etched for 5 minutes in a 5.25% strength etchant (right). Scale bar = 250 μm

SEM images and training was initially undertaken using the facilities provided by the Centre for Advanced Microscopy at the University of Reading. A Cambridge 360 Stereoscan high vacuum SEM, designed for coated and conducting samples, was used at first, mostly for training purposes, but did not possess the ability to take high magnitude images of acceptable quality. Initial images were taken using an environmental SEM, the FEI Quanta FEG 600, designed for examining samples at pressures and humidities which approach normal laboratory conditions.

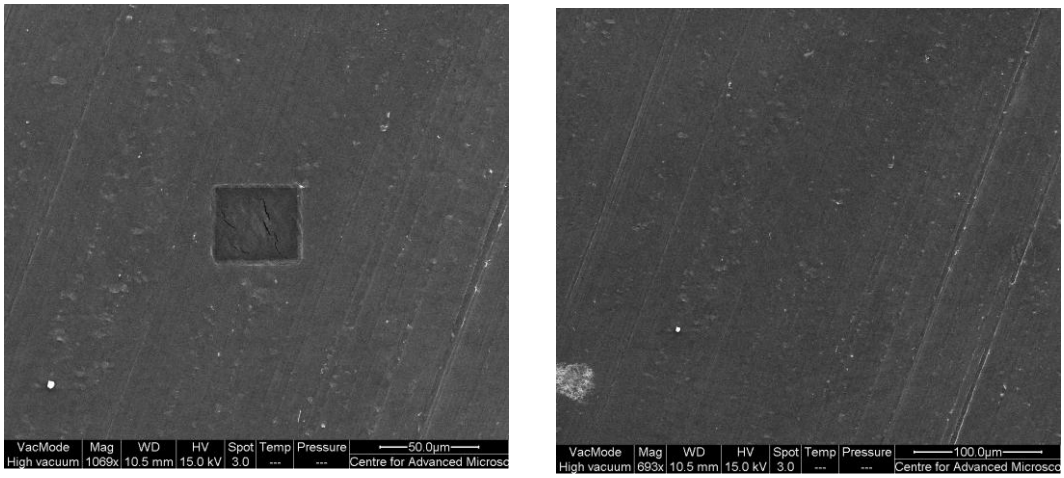

FIGURE AP 5.10 : Preliminary SEM image showing burning of the sample when observed in one position for too long (left) and a preliminary image of 100,000 $gmol^{-1}$ PEO (right)

The Cambridge 360 provided acceptable images from an ageing piece of equipment. It was thought that the newer and more advanced eSEM Quanta would provide superior images without the need for gold coating the sample. However, as can be seen in figure AP 5.10 above, without a coating of gold the sample is particularly susceptible to radiation damage and the image quality improvement over the 360 is less than expected. Therefore for final imaging, a JSM 5910 SEM was used at the Electron Microscopy Centre within the University of Southampton, using JSM 5000 software. This SEM is also fitted with an Oxford Inca 300 energy dispersive x-ray microanalysis (EDAX) system, enabling chemical characterization of samples. This particular EDAX system allows characterization of an area or a point.

Using the JSM SEM it was possible to take images of the gold-coated PEO composites. In the left image shown in figure AP 5.11, spherulites of up to 250 μm can be seen in a 400k PEO sample, using 15kV with a working distance of 11mm at a magnification of x85. The right image shows a sample of 400k PEO with silicon dioxide filler etched for 5 minutes at a low concentration. The PEO matrix has been etched away leaving a particle of silica proud of the surface. Following on from the optical microscopy performed on etched samples, SEM images such as this one confirmed conclusions about concentrations of etchant and etching time.

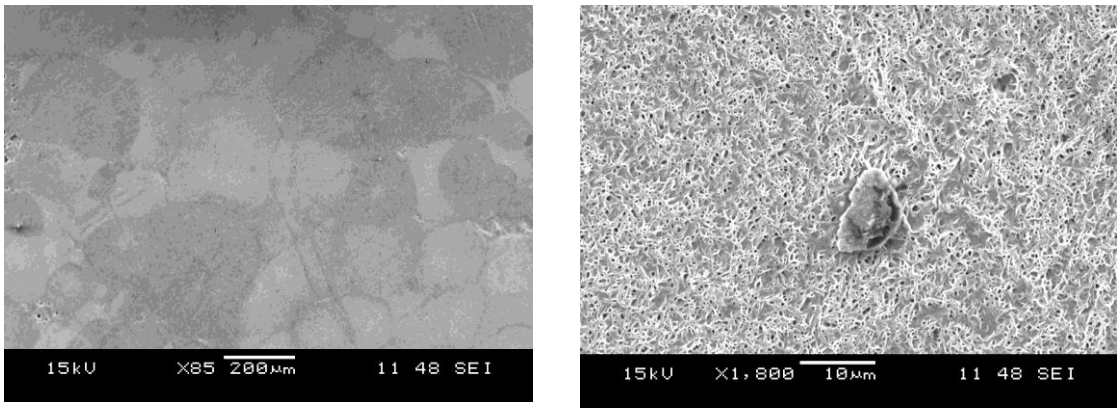

FIGURE AP 5.11 : SEM images of 400k PEO spherulites (left)
and an etched PEO-SD sample (right)

Figures AP 5.12 and AP 5.13 on the following pages were generated by the JSM software and show an image of the area being observed (top left), the area or point that the spectrum is focusing on (top right) and the EDAX characterization underneath. Figure AP 5.12 shows the EDAX result for some carbon conducting cement. The main SEM image was taken at x90 magnification, but to improve the EDAX data a much higher magnification was used, producing the second image. Here the pink box represents the spectrum area, signifying that the spectrum here is comprised of most of the area observed. As would be expected, a large amount of carbon and oxygen are observed.

To further test the EDAX system some dust was analysed, shown in figure AP 5.13. The particle seen here is possibly dust on the surface of the sample since a ‘halo’ is visible, a common sign of electron charging. EDAX confirms this using the point characterization, finding an array of elements present, including sodium, chlorine and potassium – a common indicator of a dust particle.

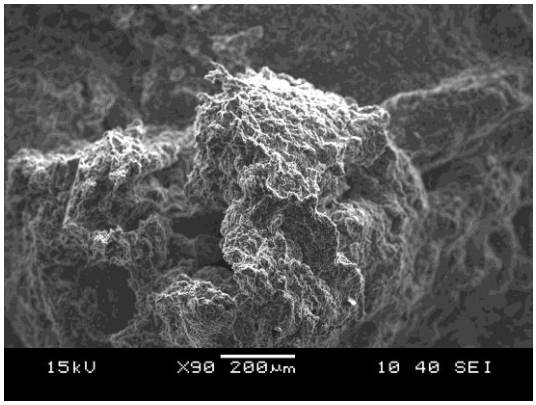

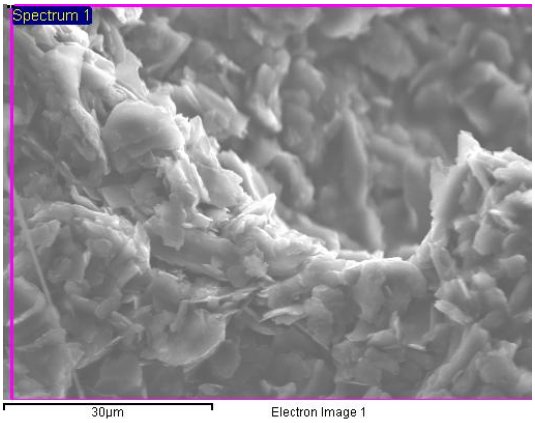

Element	Weight %	Atomic %
C	90.67	92.83
O	9.33	7.17

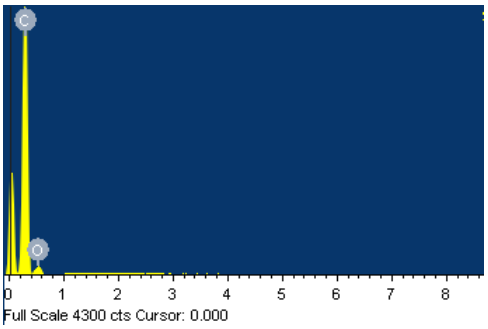

FIGURE AP 5.12 : A SEM image (top left), EDAX image (top right) and subsequent data for carbon conducing cement

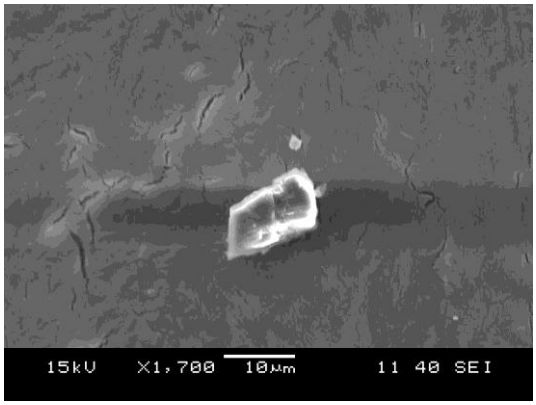

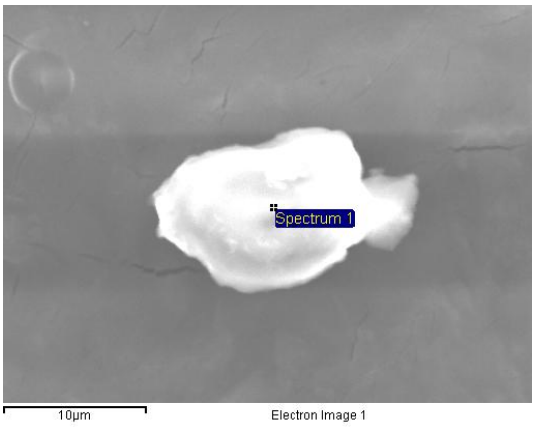

Element	Weight %	Atomic %
C	59.93	72.92
O	18.69	17.07
Na	6.66	4.23
Si	0.55	0.29
S	1.32	0.6
Cl	3.33	1.37
K	4.58	1.71
Ca	4.94	1.80

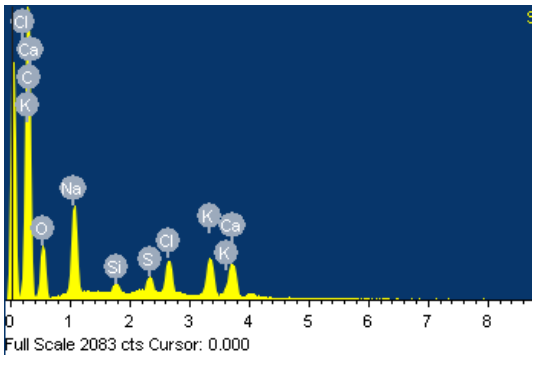

FIGURE AP 5.13 : A SEM image and EDAX data for a dust particulate

Figure AP 5.14 shows an image of an unfilled 400k PEO sample at a magnification of x950. It is expected that EDAX on such a sample should produce a characterization table with only 3 elements- carbon, oxygen and gold. If any other elements are detected this could be due to dirt on the surface of the sample, or suggest that the material is not as pure as previously thought. This was not the case however, as only the 3 elements expected were detected. Overall the EDAX system appears to work well for the three test samples, thus samples containing fillers were tested.

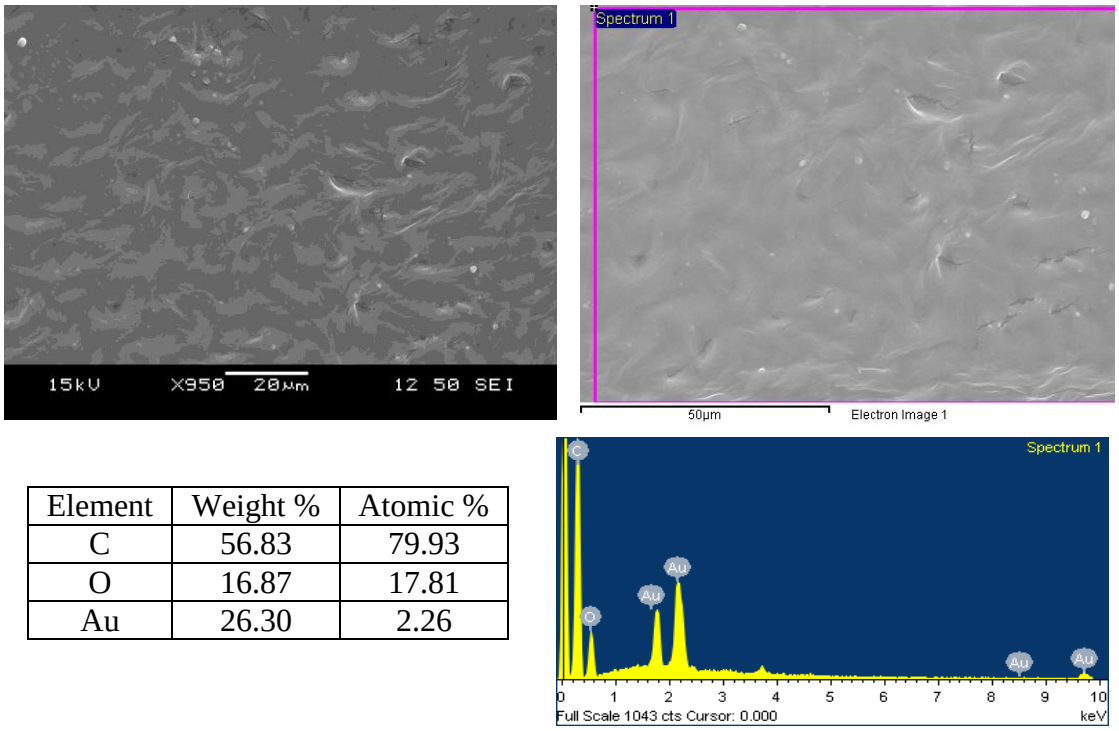

Element	Weight %	Atomic %
C	56.83	79.93
O	16.87	17.81
Au	26.30	2.26

FIGURE AP 5.14 : A SEM image and EDAX data for an unfilled 400k PEO sample

Figure AP 5.15 shows an image at magnification x3700 of a 400k PEO sample with 10 PPHP MMT filler. The filler is clearly visible and an area spectrum using the EDAX should allow characterization of this filler. From this the expected carbon, oxygen and gold are observed, along with aluminium. For aluminium pillared MMT clay, formula shown below, we would expect a large amount of oxygen, some aluminium and a small amount of silicon. From the EDAX results the oxygen and aluminium are clearly present, however no trace of silicon was observed. This is not particularly surprising, since the expected silicon value would be around half that of aluminium, hence 0.36% atomic, a value below the accuracy of the equipment.

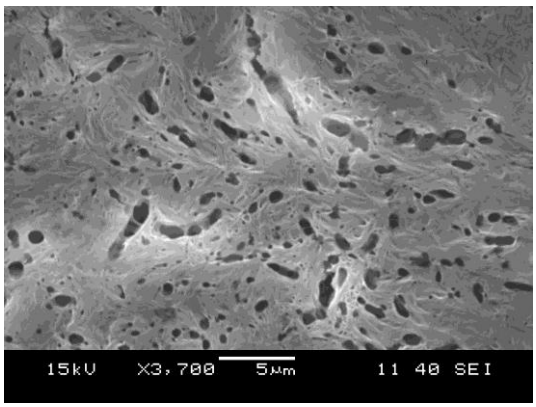

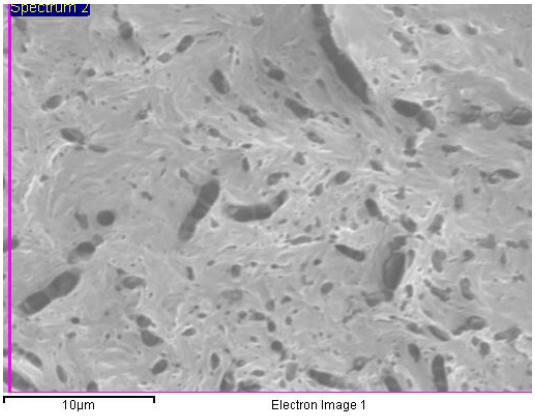

Element	Weight %	Atomic %
C	52.30	89.63
O	4.03	5.18
Al	0.95	0.72
Au	42.73	4.47

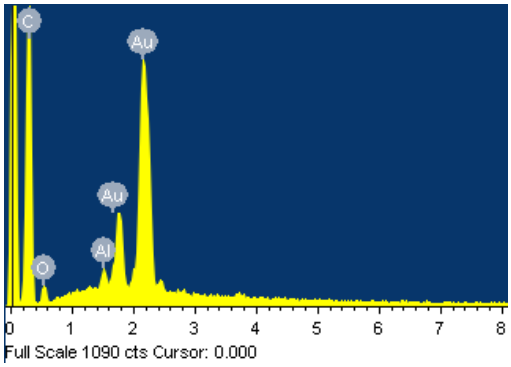

FIGURE AP 5.15 : A SEM image and EDAX data for a 400k PEO sample with 10 PPHP MMT clay

Figures AP 5.16 and AP 5.17 show a sample of 400k PEO with 5 PPHP SD filler. One particle, believed to be silica, has been positioned central to the image. Figure AP 5.16 uses the area spectrum technique, whilst figure AP 5.15 uses point spectrum. The area spectrum EDAX data finds mostly carbon, oxygen and gold as expected, along with 1.77% atomic silicon. To confirm the silicon being detected is the central particle a point spectrum is used, revealing an increase in silicon to 21.63% atomic.

From this we can gather that the particle is indeed silica, however a larger percentage atomic silicon may have been expected. This is due to the EDAX system penetrating into the sample and not just collecting data on the uppermost surface. Therefore the point spectrum collects data from the silicon particle as well as the PEO around and below it, hence collecting higher values for carbon and oxygen than would be expected from a single particle of silica.

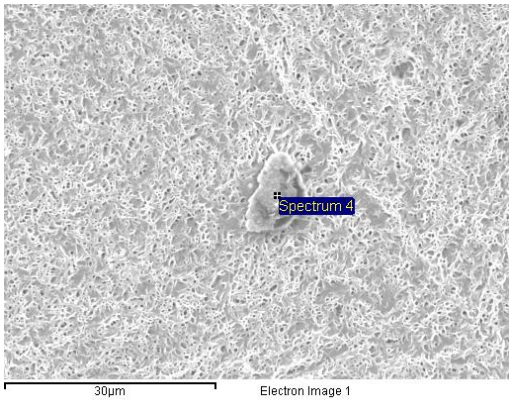

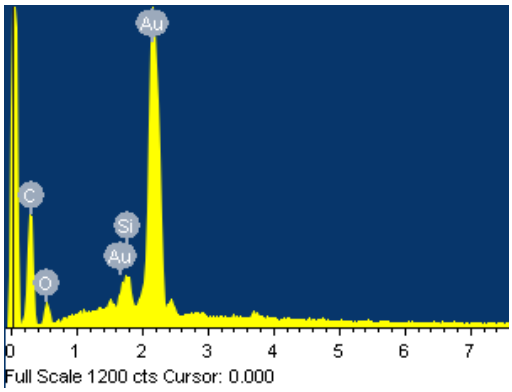

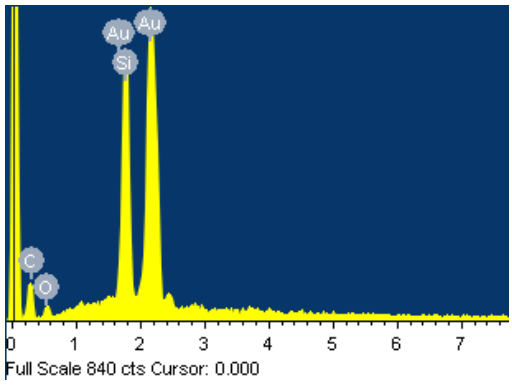

Element	Weight %	Atomic %
C	29.09	76.9
O	5.57	11.05
Si	1.57	1.77
Au	63.78	10.28

FIGURE AP 5.16 : EDAX for a 400k sample with 5 PPHP SD filler using an area spectrum

Element	Weight %	Atomic %
C	14.19	53.23
O	3.32	9.34
Si	13.48	21.63
Au	69.01	15.79

FIGURE AP 5.17 : EDAX for a 400k sample with 5 PPHP SD filler using a point spectrum

Appendix 6: UNCERTAINTY IN T_m^0

The standard method for calculating T_m^0 is to plot T_c vs T_m to find the point at which the best fit line of the data intersects with the y = x line. However, due to the relatively limited data range the accuracy of this extrapolation is questionable in this investigation. To improve the accuracy, another method can be employed to calculate T_m^0. Bassett [372] has previously shown that by substituting equation AP 6.1 for *l*, into the standard equation AP 6.2, produces equation AP 6.3. Rearranging, leading to equation AP 6.4, produces a plot of T_c vs $(T_m - T_c)$ with the y axis intercept being T_m^0.

$$l = \gamma l_g^* \approx \gamma \frac{2\sigma_e T_m^0}{\Delta h\left(T_m^0 - T_c\right)} \qquad \text{(AP 6.1)}$$

$$T_m = T_m^0\left(1 - \frac{2\sigma_e}{l\Delta h}\right) \qquad \text{(AP 6.2)}$$

$$T_m = T_m^0 - \frac{T_m^0}{\gamma} + \frac{T_c}{\gamma} \qquad \text{(AP 6.3)}$$

$$T_c = -\frac{1}{\left(1 - \frac{1}{\gamma}\right)}\left(T_m - T_c\right) + T_m^0 \qquad \text{(AP 6.4)}$$

This provides a graph, such as that shown in figure AP 6.1 below. Confidence bounds can then be calculated to represent the accuracy of the extrapolation. If the confidence bounds overlap considerably then the values are too similar to be considered as varying for the samples.

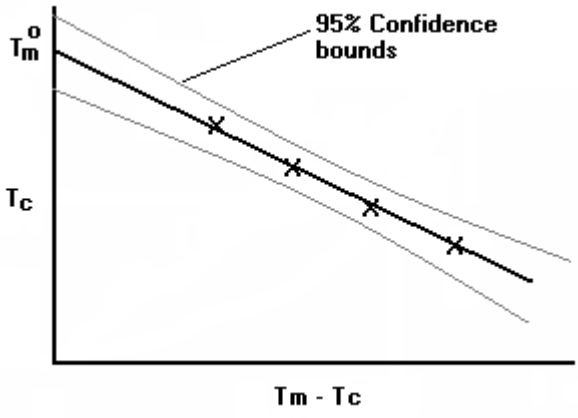

FIGURE AP 6.1 : An example regression plot showing T_m vs $(T_m\text{-}T_c)$ allowing calculation of T_m^0 and the error associated

References

[1] J. Wisniak, "Jons Jacob Berzelius, A Guide to the Perplexed Chemist", ***The Chem. Educ*.,** **5(6):343-350, 2000**

[2] A. Rudin, "The Elements of Polymer Science and Engineering", ***Academic Press,*** **1982**

[3] A. Haque, M. Shamsuzzoha and F. Hussain, "S2- Glass/Epoxy Polymer Nanocomposites: Manufacturing, structure, thermal and mechanical properties", ***J. Comp. Mats.,*** **37(20):1821-1837, 2003**

[4] *When comparing the number of news articles printed containing the word "Nanocomposite" between 1980-2006, using Google Trends at* ***www.google.com/trends.***

[5] X. Huang, S. Lewis and W. J. Brittain, "Synthesis of polycarbonate layered silicate nanocomposites via cyclic oligomers", ***Macromolecules,*** **33:2000-2004, 2000**

[6] C. L. Chiang, C. C. M. Ma, F. Y. Wang and H. C. Kuan, "Thermo-oxidative degradation of novel epoxy containing silicon and phosphorous nanocomposites", ***Euro. Poly. J.,*** **39(4):825-830, 2003**

[7] P. Jawahar and M. Balasubramanian, "Preparation and properties of polyester-based nanocomposite gel system", ***J. Nanomaterials,*** **(1):4, 2006**

[8] P. A. Jarvela and P. K. Jarvela, "Multicomponent compounding of polypropylene", ***J. Mat. Sci.,*** **31(14):3583-3860, 1996**

[9] J. H. Choi, J. Jegal and W. N. Kim, "Fabrication and Characterisation of multi-walled carbon nanotubes/polymer blend membranes", ***J. Membrane Sci.,*** **284(1-2):406-415, 2006**

[10] M. Baibarac, P. Gomez-Romero, M. Lira-Cantu, N. Casan-Pastor, N. Mestres and S. Lefrant, "Electrosynthesis of the poly(N-vinyl carbazole)/carbon nanotubes composite for applications in the supercapacitors field", ***Euro. Poly. J.,*** **42(10):2302-2312, 2006**

[11] P. Calvert, "Potential Applications of nanotubes", ***Carbon nanotubes-preparation and properties,*** **ed. T. W. Ebbesen, CRC Press, 1997**

[12] L. Jun, L. Chang, K. Seon, K. In and K. Sun, "Controlled Nanofiber Composed of Multi-wall carbon nanotubes/poly(ethylene oxide)", ***J. Macro. Sci. Part A: Pure and Applied Chem.,*** **43(4-5):785-796, 2006**

[13] M. Alexandre and P. Dubois, "Polymer-layered silicate nanocomposites: preparation, properties and uses of a new class of materials", ***Mats. Sci. and Engin. R: Reports,* 28(1-2):1-63, 2000**

[14] J. E. Mark, **"**Ceramic reinforced polymers and polymer-modified ceramics**",** ***Poly. Engin. Sci.,* 36(24):2905-2920, 1996**

[15] A. Weisman, "The world without Us", ***St. Martin's Press,* 2007**

[16] A. Keller, "A note on single crystals in polymers – evidence for a folded chain configuration", ***Philosophical Mag.,* 2(21):1171-1175, 1957**

[17] P. H. Till, "The growth of single crystals of linear polyethylene", ***J. Polym. Sci.,* 24:301-306, 1957**

[18] E. W. Fischer, "Stufen-und spiralförmiges Kristallwachstum bei Hochpolymeren", ***Z. Naturforsch,* 12a:753-754, 1957**

[19] G. C. Simon JR, "Imaging cells on polymer spherulites", ***J. Microscopy,* 216(2):153-155, 2004**

[20] F. D. Price, "A theory of spherulite shape", ***J. Polym. Sci.,* 54(160):S40-S46, 1961**

[21] M. Takayanagi and T. Yamashita, "Growth rate and structure of spherulite in fractioned poly(ethylene adipate)", ***J. Polym. Sci.,* 22(102):552-555, 1956**

[22] M. L. Di Lorenzo and C. Silvestre, "Measurement of spherulite growth rates using tailored temperature programs", ***Thermochimica Acta,* 396(1-2):67-73, 2003**

[23] R. Patki and P. J. Phillips, "Nucleation and spherulitic growth rates in thin films with embedded thermocouples", ***J. Plastic Film and Sheeting,* 23(3):221-238, 2007**

[24] K. Wang, J. Wu and H. Zeng, "Radial growth rate of spherulites in polypropylene/barium sulphate composites", ***Euro. Poly. J.,* 39(8):1647-1652, 2003**

[25] U. W. Gedde, "Polymer Physics", ***Kluwer Academic Publishers,* 1995**

[26] T. Blythe and D. Bloor, "Electrical properties of polymers", ***Cambridge University Press,* 2005**

[27] *Airbus, an EADS Company,* ***www.airbus.com***

[28] L. Tong, A. P. Mouritz and M. Bannister, "3D Fibre reinforced polymer composites", ***Elsevier Science*, 2002**

[29] L. Quercis, F. Loffredo and G. Di Francia, "Influence of filler dispersion on thin film composites sensing properties", ***Sensors and Actuators B,* 109(153-158), 2005**

[30] Y. H. Lee, C. B. Park, M. Sain, M. Kontopoulou and W. Zheng, "Effects of clay dispersion and content on the rheological, mechanical properties and flame retardance of HDPE/clay nanocomposites", ***J. App. Poly. Sci.,* 105:1993-1999, 2007**

[31] J. Moczo, E. Fekete, K. Laszlo and B. Pukanszky, "Aggregation of particulate fillers: factors, determination, properties", ***Macromolecules Symposium,* 194:111-124, 2003**

[32] A. S. Vaughan, S. G. Swingler and Y. Zhang, "Polyethylene Nanodielectrics: The Influence of nanoclays on structure formation and dielectric breakdown", ***IEEJ Trans. FM,* 126(11):1057-1064, 2006**

[33] T. Ramanathan, S. Stankovich, D. A. Dikin, H. Liu, H. Shen, S. T. Nguyen and L. C. Brinson, "Graphitic nanofillers in PMMA nanocomposites- An investigation of particle size and dispersion and their influence on nanocomposite properties", ***J. Poly. Sci. Part B,* 45:2097-2112, 2007**

[34] *Image reproduced from – "TRANSPORT PROPERTIES OF HECTORITE BASED NANOCOMPOSITE SINGLE-ION CONDUCTORS" by RUCHI GUPTA SINGHAL as a Thesis at the Graduate Faculty of North Carolina State University*

[35] J. Grunlan, A. Grigorian, C. Hamilton and A. Mehrabi, "Effect of clay concentration on the oxygen permeability and optical properties of a modified poly(vinyl alcohol)", ***J. App. Poly. Sci.,* 93:1102-1109, 2003**

[36] H. S. Katz and J. V. Milewski, "Handbook of Fillers for Plastics", ***Van Nostrand Reinhold,* 1987**

[37] R. J. Young and P. A. Lovell, "Introduction to Polymers 2nd Edition", ***CRC Press,* 1991**

[38] M. A. Al-Nasassrah, F. Podczeck and J. M. Newton, "The effect of an increase in chain length on the mechanical properties of polyethylene glycols", ***Euro. J. of pharmaceutics and biopharmaceutics,* 46(1):31-38, 1998**

[39] H. K. Reimschuessel, "On the glass transition temperature of comblike polymers: effects of side chain length and backbone chain structure", ***J. Poly. Sci. : polymer chemistry edition,* 17(8):2447-2457, 2003**

[40] "Conductive patterns in polymeric films", ***United States Patent 4540620***

[41] "Asymmetric polyisocyanate monomers in urethane polymers and oligomers to reduce crystallinity", ***United States Patent 20050101746***

[42] K. G. McLaren, "Dynamic mechanical studies of irradiation effects in polytetrafluoroethylene", ***Br. J. Appl. Phys,* 16:185-193, 1965**

[43] H. S. Kaufman and J. J. Falcetta, "Introduction to Polymer Science and Technology : An SPE Textbook", ***Wiley & Sons Pub.,* 1977**

[44] International Union of Pure and Applied Chemistry, "Condensation Reaction", ***Compendium of Chemical Terminology,* (66):1099, 1994**

[45] "Encyclopedia of Polymer Science and Engineering – volume 2", ***Wiley and Sons Pub.,* 1987**

[46] J. R. Lee, D. G. Lee, S. M. Hong and H. J. Kang, "Crosslinking Characteristics of High Density Polyethylene by reactive melt processing", ***Polymer Korea,* 29(4):385-391, 2005**

[47] P. C. Powell, A. J. Ingen-Housz, "Engineering with Polymers", ***Stanley Thornes Publishers,* 1983**

[48] M. F. Saettone, G. Perini, P. Rijli, L. Rodriquez and M. Cini, "Effect of different polymer-plasticizer combinations on 'in vitro' release of theophylline from coated pellets", ***Int. J. Pharmaceutics.,* 126(1):83-88, 1995**

[49] G. Allen, J. C. Bevington, C. Booth and C. Price, "Comprehensive polymer science", ***Pergammon Press,* 1989**

[50] C. Green and A. S. Vaughan, "Nanodielectrics – How much do we really understand?", ***IEEE Mag,* 24(4):6-16, 2008**

[51] F. R. Eirich, "Rheology – Theory and Applications", ***Academic Press,* 1956**

[52] G. Matthews, "Polymer Mixing Technology", ***Elsevier Science,* 1982**

[53] C. Feger, J. D. Gelorme, M. McGlashan-Powell and D. M. Kalyon, "Mixing, Rheology, and stability of highly filled thermal pastes", ***IBM J. R&D,* 45(4):339-347, 2005**

[54] S. Bar-Chaput and C. Carrot, "Rheology as a tool for the analysis of the dispersion of carbon filler in polymers", ***Rheologica Acta,* 45(4):339-347, 2007**

[55] H. Zhu and D. De Kee, "A numerical study for the cessation of couette flow of non-newtonian fluids with a yield stress", ***J. Non-newt. Fluid Mech.,* 143(2-3):64-70, 2006**

[56] H. Zhu, Y. D. Kim and D. De Kee, "Non-newtonian fluids with a yield stress", ***J. Non-newt fluid mech.,* 129(177), 2005**

[57] S. Coppola, N. Grizzuti, G. Floudas and D. Vlassopoulos, "Viscoelasticity and crystallisation of poly(ethylene oxide) star polymers of varying arm number and size", ***J. Rheology,* 51(5):1007-1025, 2007**

[58] P. J. Carreau, D. De Kee and R. P. Chhabra, "Rheology of Polymeric systems. Principles and application", ***Hanser Gardner Publications*, 1997**

[59] A. Yahia and K. H. Khayat, "Applicability of rheological models to high performance cement grout containing various supplementary materials and rheology modifying admixtures", ***Concr. Sci. Eng.*, in press.**

[60] A. Yahia and K. H. Khayat, "Analytical models for estimating yield stress of high-performance pseudoplastic grout", ***Cement and Concrete Research,* 31:731-738, 2001**

[61] V. C. Kelessidis and R. Maglione, "Modeling rheological behaviour of Bentonite suspensions as Casson and Robertson-Stiff fluids using newtonian and true shear rates in couette viscometry", ***Powder Tech.,* 168:134-147, 2006**

[62] E. J. Fordham, S. H. Bittleston and M. A. Tehrani, "Viscoplastic flow in centered annuli, pipes and slots", ***Ind. Eng. Chem. Res.,* 30:517-524, 1991**

[63] W. Haige and S. Yinao, "Flow of Robertson-stiff fluids through an eccentric annulus", ***Appl. Math. and Mech.,* 19(10), 1998**

[64] *The Schlumberger oilfield glossary,* ***www.glossary.oilfield.slb.com***

[65] J. G. Krieble and J. C. Whitwell, "The Viscosity of new Newtonian, Pseudoplastic and Dilatant Liquids", ***Textile Res. J.,* 19(5):253-258, 1949**

[66] H. Schlichting and K. Gersten "Boundary Layer Theory", ***Springer,* 1955**

[67] S. X. Ma and S. L. Cooper, "Shear thickening in aqueous solutions of hydrocarbon end-capped poly(ethylene oxide)", ***Macromolecules,* 34(10):3294-3301, 2001**

[68] A. J. McFarlane, J. Addai-Mensah and K. Bremmell "Rheology of flocculated kaolinite dispersions", ***Korea-Australia Rheology J.,* 17(4):181-190, 2005**

[69] A. Gonet, S. Stryczek and J. Pinka, "Analysis of Rheological Models of Selected Cement Slurries", ***Acta Montanistica Slovaca,* 9(1):16-20, 2004**

[70] K. Lewandowska, "Comparative studies of rheological properties of polyacrylamide and partially hydrolyzed polyacrylamide solutions", ***J. App. Poly. Sci.,* 103(4):2235-2241, 2006**

[71] T. Matheson, "Impact of dispersion of interfaces on the rheology of polymeric nanocomposites", ***MPhil. Thesis,* University of Southampton, 2009**

[72] D. G. Harlow and R. P. Wei, "Materials aging and structural reliability", ***J. Materials and Product Tech.,*** **16(4-5):304-316, 2001**

[73] D. L. Allara, "Aging of Polymers", ***Environ. Health Pers.,*** **11:29-33, 1975**

[74] J. Akhavan, E. Koh and E. Kronfli, "Effect of UV and thermal radiation on polyNIMMO", ***Polymer,*** **42(18):7711-7718, 2001**

[75] N. Guermazi, K. Elleuch, H. F. Ayedi and P. H. Kapsa, "Aging effect on thermal, mechanical and tribological behaviour of polymeric coatings used for pipeline application", ***J. Materials Processing Tech.,*** **203(1-3):404-410, 2008**

[76] P. Riha, J. Hadac, P. Slobodian, P. Saha, R. W. Rychwalski, J. Kubat, "Effect of aging time on the volumetric and enthalpic glass transition of a-PMMA upon heating", ***Polymer,*** **48(25):7356-7363, 2007**

[77] I. L. Hosier, A. S. Vaughan, S. J. Sutton and F. J. Davis "Chemical, Physical and electrical properties of aged dodecylbenzene: Thermal aging of mixed isomers in air", ***IEEE Trans. Dielec. Elec. Insul.,*** **14(5):1113-1124, 2007**

[78] M. Lazzari and O. Chiantore, "Thermal-ageing of paraloid acrylic protective polymers", ***Polymer,*** **41(17):6447-6455, 2000**

[79] W Kuhn, "Kinetics of the destruction of high molecular weight chains", ***Ber. Dtsch. Chem. Ges.,*** **63(1503), 1930**

[80] R Simha, "Kinetics of degradation and size distribution of long chain polymers", ***J. Appl. Phys.,*** **12(569), 1941**

[81] L. A. Pinheiro, M. A. Chinelatto and S. V. Canevarolo, "The role of chain scission and chain branching in high density polyethylene during thermo-mechanical degradation", ***Poly. Degrad. and Stability,*** **86:445-453, 2004**

[82] A. Tayal and S. A. Khan, "Degradation of a water-soluble polymer: Molecular weight changes and chain scission characteristics", ***Macromolecules,*** **33:9488-9493, 2000**

[83] A. M. Basedow, K. H. Ebert and H. J. Ederer, "Kinetic studies on the acid hydrolysis of dextran", ***Macromolecules,*** **11(4):774-781, 1978**

[84] J. V. Dawkins, "Developments in Polymer Characterisation", ***Elsevier Science,*** **1986**

[85] N. P. Cheremisinoff, "Polymer Characterisation. Laboratory Techniques and Analysis", ***William Andrew Publishing,*** **1996**

[86] M. Saunders, K. Podluii, S. Shergill, G. Buckton and P. Royall, "The potential of high speed DSC (Hyper-DSC for the detection and quantification of small amounts of amorphous content in predominantly crystalline samples", ***Int. J. Pharmaceutics,*** **274(1-2):35-40, 2004**

[87] R. D. Saklatvala, M. H. Saunders, S. Fitzpatrick and G. Buckton, "A comparison of high speed differential scanning calorimetry (Hyper-DSC) and modulated differential scanning calorimetry to detect the glass transition of polyvinylpyrrolidone : the effect of water content and detection sensitivity in powder mixtures (a model formulation)", ***J. Drug delivery science and tech.,*** **15(4):257-260, 2005**

[88] P. Liu, H. Liu, L. Chen and L. Li, "Glass transition temperature of starch studied by a high-speed DSC", ***Carbohydrate polymers,*** **77(2):250-253, 2009**

[89] A. T. Riga, M. Golinar and K. S. Alexander, "Fast scan differential scanning calorimetry distinguishes melting, melting-degradation/subliation and thermal stability of drugs", ***J. ASTM International,*** **4(3), 2007**

[90] A. T. Lorenzo, M. L. Arnal, J. Albuerne and A. J. Muller, "DSC isothermal polymer crystallization kinetics measurements and the use of the Avrami equation to fit the data: Guidelines to avoid common problems", ***Polymer Testing,*** **26:222-231, 2007**

[91] M. Avrami, "Kinetics of Phase Change 1 General Theory", ***J. Chem. Phys.,*** **7(12):1103-1112, 1939**

[92] A. Keller, G. R. Lester and L. B. Morgan, "Crystallisation Phenomena in Polymers. I. Preliminary Investigation of the Crystallisation Characteristics of Polyethylene Terephthalate", ***Philo. Trans. Royal Soc. London, Series A, Math. and Phy. Sci.,*** **247(921):1-12, 1954**

[93] M. Avrami, "Kinetics of Phase Change 2 Transformation-Time relations for random distribution of nuclei", ***J. Chem. Phys.,*** **8(2):212-224, 1940**

[94] M. Avrami, "Granulation, Phase Change, and Microstructure Kinetics of Phase Change 3", ***J. Chem. Phys.,*** **9(2) :177-184, 1941**

[95] G. Gherbaz, "Nanostructured Polymers: Morphology and Properties", ***PhD Thesis,*** **University of Southampton, 2009**

[96] A. S. Vaughan, "The Structure of Polystyrene crystallized from the melt", ***PhD Thesis,*** **Reading University, 1984**

[97] M. Muchova and M. Lednicky, "Investigation of heterogeneous nucleation using the induction time of crystallisation: 1. theory of induction time", ***Polymer,*** **37:3031-3036, 1996**

[98] T. Kowalewski and A. J. Galeski, "Influence of chalk and its surface treatment on crystallization of filled polypropylene", ***J. App. Poly. Sci.,*** **32:2919-2934, 1986**

[99] S. Vyazovkin and N. Sbirrazzuoli, "Isoconversional approach to evaluating the Hoffman-Lauritzen Parameters (U* and Kg) from the overall rates of nonisothermal crystallisation", ***Macromolecular Rapid Communications,* 25:733-738, 2004**

[100] J. I. Lauritzen, E. A. DiMarzio and E. Passaglia, "Kinetics of growth of multicomponent chains", ***J. Chem. Phys.,* 45(12):4444-4454, 1966**

[101] J. I. Lauritzen and J. D. Hoffman, "Extension of theory of growth of chain-folded polymer crystals to large undercoolings", ***J. Appl. Phys.,* 44(10):4340-4352, 1973**

[102] J. D. Hoffman and R. L. Miller, "Kinetics of crystallisation from the melt and chain folding in polyethylene fractions revisited: theory and experiment", ***Polymer,* 38(13):3151-3212, 1997**

[103] J. D. Hoffman, G. T. Davis and J. I. Lauritzen, "Treatise on solid state chemistry", ***ed. N B Hannay,* Plenum Press, 1976**

[104] J. I. Lauritzen and J. D. Hoffman, "Theory of formation of polymer crystals with folded chains in dilute solution", ***J. Res. Natl. Bur. Stand.,* 64:73-102, 1960**

[105] J. D. Hoffman and J. I. Lauritzen, Crystallisation of bulk polymers with chain folding: Theory of growth of lamellar spherulites", ***J. Res. Natl. Bur. Stand.,* 65:297-336, 1961**

[106] J. I. Lauritzen and J. D. Hoffman, "Formation of Polymer Crystals with folded chains from dilute solutions", ***J. Chem. Phys.,* 31:1680-1681, 1959**

[107] J. D. Hoffman and J. J. Weeks, "Rate of spherulitic crystallization with chain folds in polychlorotrifluoroethylene", ***J. Chem. Phys.,* 37:1723-1741, 1962**

[108] T. Suzuki and A. J. Kovacs, "Temperature dependence of spherulitic growth rate of isotactic polystyrene", ***Polymer,* 1(1):82-100, 1970**

[109] L. H. Sperling, "Introduction to physical polymer science", ***Wiley & Sons Pub.,* 1992**

[110] J. D. Hoffman and J. J. Weeks, "Melting process and equilibrium melting temperature of poly(chlorotrifluoroethylene)", ***J. Res. Nat. Bur. Stand.,* 66A(1):13-28, 1962**

[111] J. D. Menczel and R. B. Prime, "Thermal analysis of polymers, fundamentals and applications", ***Wiley & Sons Pub.,* 2009**

[112] *EM Technologies, Emitech K550X Sputter Coater Instruction Manual. **2003**.*

[113] H. C. Ohanian, "Ohanian Physics – Volume 2", **1989**

[114] P. Hedvig, "Dielectric Spectroscopy of Polymers", ***Akademiai Kiado,* 1977**

[115] C J. F. Bottcher, "Theory of Electric Polarisation", ***Elsevier Science,* 1973**

[116] E. Hecht, "Optics Third Edition", ***Addison Wesley Publishing,* 1998**

[117] N. E. Hill, W. E. Vaughan, A. H. Price and M. Davies, "Dielectric Properties and Molecular Behaviour", ***Van Nostrand Reinhold,* 1969**

[118] L. Lanzi, M. Carla, C. M. C. Gambi and L. Lanzi, "Dielectric spectroscopy by differential measurements in transmission lines on sodium dodecyl sulfate micelles in water", ***J. Non-crystalline solids,* 351(33-36):2864-2867, 2005**

[119] R. Buchner, J. Barthel and J. Stauber, "The dielectric relaxation of water between 0 ^{0}C and 35 ^{0}C", ***Chemical physics letters,* 306(1-2):57-63, 1999**

[120] T. J. Kelleners, D. A. Robinson, P. J. Shouse, J. E. Ayars and T. H. Skaggs, "Frequency dependence of the complex permittivity and its impact on dielectric sensor calibration in soils", ***Soil Sci. Soc. Am. J.,* 69:67-76, 2005**

[121] J. D. Kraus, "Electromagnetics", **McGraw-Hill College, 1984**

[122] P. Salovaara and K. Kannus, "Increasing the Dielectric Breakdown strength of Polypropylene using Polyaniline Additive", ***Energy and Power Systems,* EPS, 2006**

[123] W. J. Weibull, "A Statistical Distribution Function of Wide Applicability", ***J. Appl. Mechs.,* 18:**293-297, 1951

[124] L. A. Dissado and J. C. Fothergill, "Electrical Degradation and Breakdown in Polymers", **Peter Peregrinus, 1992**

[125] *Life Data Analysis Reference, Reliasoft 2005*

[126] H. Pham and C. D. Lai, "On Recent Generalizations of the Weibull Distribution", ***IEEE Trans. Reliability,* 56(3):454-458, 2007**

[127] C. Lu, R. Danzer and F. D. Fischer, "Influence of Threshold Stress on the Estimation of the Weibull Statistics", ***J. Amer. Cer. Soc.,* 85(6):1640-1642, 2002**

[128] R. B. Abernethy, "The New Weibull Handbook", **2004**

[129] *Confidence bounds,* ***www.weibull.com/LifeDataWeb***

[130] A. S. Vaughan, G. Gherbaz, S. G. Swingler and N. A. Rashid, "Polar/non-polar Polymer Blends: On structural evolution and the electrical properties of blends of polyethylene and ethylene – vinyl acetate", ***Annual report of CEIDP,* Kansas city, USA, 2006**

[131] N. Mann and K. Fertig, "Tables for obtaining Weibull confidence bounds and tolerance bounds based on best linear invariant estimates of parameter of the extreme-value distributions", ***Technometrics,* 15(1):87-93, 1973**

[132] J. H. Yun, K. Kuboyama and T. Ougizawa, "High birefringence of poly(trimethylene terephthalate) spherulite", ***Polymer,* 47:1715-1721, 2006**

[133] T. Ikehara, H. Kimura and Z. Qiu, "Penetrating spherulitic growth in poly(butylene adipate-co-butylene succinate/Poly(ethylene oxide) blends", ***Macromolecules,* 38:5104-5108, 2005**

[134] I. L. Hosier, A. S. Vaughan and S. G. Swingler, "Studies on the ageing behavior of various synthetic and natural insulation oils", ***Int. Conf. Dielec. Liquids,* Poitiers, France, s4-07, 2008**

[135] B. C. Smith, "Fundamentals of Fourier transform infrared spectroscopy", ***CRC press,* 1996**

[136] D. I. Bower and W. F. Maddams, "The vibrational spectroscopy of polymers", ***Cambridge solid state science series,* Cambridge university press, 1989**

[137] A. A. Bunaciu, H. Y. Aboul-Enein and S. Fleschin, "FT-IR Spectrophotometric analysis of acetylsalicylic acid and its pharmaceutical formulations", ***Canadian J. Analy. Sci. and Spec.,* 51(5):253-259, 2006**

[138] R. Neubert, B. Colin and S. Wartewig, "Quantitative analysis of drug content in semisolid formulations using step-scan FT-IR photoacoustic spectroscopy", ***Vibrational Spectroscopy,* 13(2):241-244, 1997**

[139] P. Bouguer, "Essai d'Optique sur la Gradation de la Lumiere", ***Gauthier-Villars,* Paris, 1729**

[140] J. H. Lambert, "Photometria sive de mensura et gradibus luminus, colorum et umbrae", ***Translated from latin by David L Dilaura,* 2001**

[141] A. Beer, "Bestimmung der Absorption des rothen Lichts in farbigen flussigkeiten", ***Annal. Phys. Chem.,* 86:78-88, 1852**

[142] C. Zhu and P. R. Griffiths, "Extending the range of Beer's law in FT-IR Spectrometry. Part 1: Theoretical study of Norton-Beer Apodization Functions", ***Applied Spectroscopy,* 52(11):1403-1408, 1998**

[143] *Leif Gerward at Technical University of Denmark,* ***http://www.canberra.edu.au/irps/Archives/vol21no1/blbalaw.html***

[144] M. M. Fares, J. Hacaloglu and S. Suzer, "Characterisation of degradation products of polyethylene oxide by pyrolysis mass spectrometry", ***Euro. Poly. J., 3*0(7):845-850, 1994**

[145] S. Bekiranov, R. Bruinsma, "Solution behaviour of PEO in water as a function of temperature and pressure", ***Physical Review E.*****, 55:577-585, 1997**

[146] D. L. Ho, B. Hammouda and S. R. Kline, "Clustering of PEO in water: revisited", ***J. Poly. Sci. Part B: Pol. Phy.*****, 41:135-138, 2003**

[147] D. B. Shenoy and M. M. Amiji, "Poly(ethylene oxide)-modified poly(ε-caprolactone) nanoparticles for targeted delivery of tamoxifen in breast cancer", ***Int. J. Pharmaceutics.,*** **293(1-2):261-270, 2004**

[148] J. Q. G. Maclaine and C. Booth, "Effect of molecular weight on crystal isotherms of high molecular weight PEO fractions", ***Poly. J.,*** **16:680-684, 1975**

[149] Z. J. Albinska, P. Ulanski and J. M. Rosiak, "Radiation induced degradation and crosslinking of poly(ethylene oxide) in solid state", ***J. Radioanalytical and Nuclear Chemistry,*** **253(3):339-344, 2002**

[150] H. Kaczmarek, A. Kaminska, J. Kowalonek and A. Szalla, "Changes of poly(ethylene oxide) photostability by doping with nickel(II) chloride", ***J. Photochemistry and Photobiology A: Chemistry,*** **128:121-127, 1999**

[151] L. Bowman, "Study on dogs yields hope in human paralysis treatment", ***Seattlepi.com,*** **2004**

[152] T. L. Krause and G. D. Bittner, "Rapid morphological fusion of severed myelinated axons by polyethylene glycol", ***Proc. Natl. Acad. Sci. USA,*** **87(4):1471-1475, 1990**

[153] V. M. Da Costa, T. G. Fiske and L. B. Coleman, "Far-infrared reflection-absorption spectroscopy of thin polyethylene oxide films", ***J. Chem. Phys.,*** **101(4), 1994**

[154] B. Fabre and J. Simonet, "Electroactive polymers containing crown ether or polyether ligands as cation-responsive materials", ***Coordination Chem. Reviews,*** **178-180:1211-1250, 1998**

[155] *Polyethylene glycol,* ***Chemindustry.ru***

[156] F. Fraisse, S. Morlat-Therias, J. L. Gardette, J. M. Nedelec and M. Baba, "In situ kinetics study of the accelerated aging of Poly(ethylene oxide) using photoDSC", ***J. Phys. Chem. B.,*** **110:14678-14684, 2006**

[157] J. Schiers, S. W. Bigger and O. Delatycki, "Characterising the solid state thermal oxidation of PEO powder", ***Poly. J.,*** **32:2014-2019, 1991**

[158] J. Schiers, S. W. Bigger, O. Delatycki, "Effect of Thermal Oxidation on the Spherulitic Morphology of High-Density Polyethylene", ***J. Poly. Sci.: Polymer Physics.,*** **29B(7):795-804, 1991**

[159] *Montmorillonite,* ***Mindat.org***

[160] M. Y. Hikosaka, S. H. Pulcinelli, C. V Santilli, K. Dahmouche and A. F. Craievich, "Montmorillonite (MMT) effect on the structure of Poly(ethylene oxide) PEO-MMT nanocomposites and silica-PEO-MMT hybrid materials", ***J. non-crystalline solids.,*** **352:3705-3710, 2006**

[161] H. I. Inyang, S. Bae, G. Mbamalu and S. W. Park, "Aqueous polymer effects on volumetric swelling of na-montmorillonite", ***J. Mats. Civil Engin.,*** **19(1):84-90, 2007**

[162] *Amethyst Galleries Inc.,* ***http://mineral.galleries.com/***

[163] R. A. Vaia, K. D. Jandt, E. J. Kramer and E. P. Giannelis, "Kinetics of Polymer Melt intercalation", ***Macromolecules,*** **28(24):8080-8085, 1995**

[164] P. Ducrotte, M. Dapoigny, B. Bonaz and L. Siproudhis, "Symptomatic efficancy of beidellitic montmorillonite in irritable bowel syndrome: a randomised, controlled trial", ***Ailment. Pharmscol. Ther.,*** **21(4):435-444, 2005**

[165] J. T. Li, Y. L. Zhang, J. Q. Ma, J. Gao, C. S. Wang, J. Liu and Y. X. Cao, "Montmorillonite absorbs uric acid and decreases the concentration of uric acid in the serum", ***2nd Int. Conf. Bioinform. Biomed. Engin.,*** **iCBBE, (4535118):971-974, 2008**

[166] C. H. Hu, Y. Xu, M. S. Xia, L. Xiong and R. Xu, "Effects of Cu2+- exchanged montmorillonite on growth performance, microbial ecology and intestinal morphology of Nile tilapia (Oreochromis niloticus)", ***Aquaculture,*** **270(1-4):200-206, 2007**

[167] L. Long, Z. Ma, Y. Cao, J. Liu and T. Zhai, "Effect of montmorillonite on diffusion of creatinine between blood vessel and intestine", ***2nd Int. Conf. Bioinformatics and Biomed. Engin.,*** **iCBBE, (4535517):1237-1240, 2008**

[168] Z. Ma, L. H. Long, X. J. Tao, J. Wang, J. Liu, L. Z. Zhou and Y. X. Cao, "Montmorillonite influences the diffusion of uric acid between blood vessel and intestinal tract", ***Chinese Pharma. Bulletin,*** **24(9):1245-1249, 2008**

[169] F. Avalos, J. C. Ortiz, R. Zitzumbo, M. A. Lopez-Manchado, R. Verdejo and M. Arroyo, "Effect of montmorillonite intercalant structure on the cure parameters of natural rubber", ***Euro. Polym. J.,*** **44(10):3108-3115, 2008**

[170] M. Biswas and S. S. Ray, "Recent progress in synthesis and evaluation of polymer-montmorillonite nanocomposites", ***Adv. Poly., Sci.,*** **155:167-221, 2001**

[171] J. Ma, J. Xu, J. H. Ren, Z. Z. Yu and Y. W. Mai, "A new approach to polymer/montmorillonite nanocomposites", ***Polymer,*** **44(16):4619-4624, 2003**

[172] K. E. Strawhecker and E. Manias, "Crystallization behaviour of Poly(ethylene oxide) in the presence of Na+ Montmorillonite fillers", ***Chem. of Mats. J.,*** **15(4):844-849, 2003**

[173] K. E. Strawhecker and E. Manias, "Structure and properties of Poly(vinyl alcohol)/Na+ Montmorillonite nanocomposites", ***Chem. Mats. J.,*** **12(10):2943-2949, 2000**

[174] E. Manias, A. Touny, L. Wu, K. E. Strawhecker, B. Lu and T. C. Chung, "Polypropylene/Montmorillonite nanocomposites. Review of the synthetic routes and materials properties", ***Chem. Mats. J.,*** **13(10):3516-3523, 2001**

[175] *Media resources to accompany Chem Connections Workbooks by W. W. Norton,* **www.wwnorton.com/college/chemistry/chemconnections/index.html**

[176] *USGS Coastal and Marine Geology Program,* ***http://pubs.usgs.gov/of/2001/of01-041/htmldocs/clays/smc.htm***

[177] R. K. Iler, "The Chemistry of Silica", ***Plenum Press,*** **1979**

[178] N. N. Greenwood and A. Earnshaw, "Chemistry of the elements", ***Oxford Butterworth-Heinemann,*** **1997**

[179] A. B. D. Nandiyanto, S. G. Kim, F. Iskandar and K. Okuyama, "Synthesis of silica nanoparticles with nanometer size controllable mesopores and outer diameters", ***Microporous and Mesoporous Mats.,*** **120(3):447-453, 2009**

[180] K. Kihara, "An x-ray study of the temperature dependence of the quartz structure", ***Euro. J. Mineralogy,*** **2(63), 1990**

[181] *Silicon dioxide: Properties and applications,* ***Timedomain CVD, Inc.***

[182] *Harimic Malaysia (Company),* ***www.harimic.com/images/category03_4.jpg***

[183] *Chemistry in Context,* ***www.utas.edu.au/sciencelinks/chemincon/files/s1_grow/s1_soils/bonding/network.html***

[184] ***http://webmineral.com***

[185] University of Colorado, Mineral Structure Data

[186] *The 48 Special Crystal Forms, Steven Dutch, Natural and Applied Sciences, University of Wisconsin,* ***http://www.uwsp.edu/geo/projects/geoweb/***

[187] *External symmetry of crystals, 32 Crystal classes, Prof. Stephen Nelson,* **EENS 211, Mineralogy, Tulane University**

[188] A. Marcincin, M. Hricova, K. Marcincin, A. Hoferikova and J. Legen, "Rheological behaviour of polypropylene/boehmite composites, structure and properties of hybrid fibres", ***Fibres and Textiles,*** **15(5-6):64-65, 2007**

[189] K. G. Gatos, J. G. Martinez Alcazar, G. C. Psarras, R. Thomann and J. Karger-Kocsis, "Polyurethane latex/water dispersible boehmite alumina nanocomposites: Thermal, mechanical and dielectrical properties", ***Comp. Sci. and Tech.,*** **67(2):157-167, 2007**

[190] C. Ozdilek, K. Kazimierczak and S. J. Picken, "Preparation and characterization of titanate-modified Boehmite-polyamide-6 nanocomposites", ***Polymer,*** **46(16):6025-6034, 2005**

[191] T. Klimova, E. Carmona, J. Ramirez and J. Aracil, "Statistical approach prediction of the testural properties of $TiO_2 - Al_2O_3$ mixed oxides modified by organic glycol-type polymers", ***Mater. Sci. and Engin. A,*** **241(1-2):90-98, 1998**

[192] S. Bocchini, S. Morlat-Thrias, J. L. Gardette and G. Camino, "Influence of nanodispersed boehmite on polypropylene photooxidation", ***Poly. Degrad. And Stab.,*** **92:1847-1856, 2007**

[193] T. Mousavand, S. Ohara, M. Umetsu, J. Zhang, S. Takami, T. Naka and T. Adschiri, "Hydrothermal synthesis and in situ surface modification of boehmite nanoparticles in supercritical water", ***J. of Supercritical Fluids,*** **40:397-401, 2007**

[194] D. A. Saville and D. W. Thompson, "Secondary flows associated with the Weisstnberg Effect", ***Nature letters,*** **223:391-392, 1969**

[195] O. Barwart, J. M. Rollinger and A. Burger, "An evaluation of the transition temperature range of super-elastic orthodontic NiTi springs using differential scanning calorimetry", ***Euro. J. Orthodontics,*** **21:497-502, 1999**

[196] K. S. Cole and R. S. Cole, "Dispersion and absorption in dielectrics. 1. Alternating current characteristics", ***J. Chem. Phys.,*** **9:341-351, 1941**

[197] K. S. Kohli, D. V. Rai, V. K. Jindal and N. Goyal, "Electrical characterization of eye lens", ***Biomedical engin. Conf. proc.,*** **15:342-343, 1996**

[198] J. G. Powles, "The Interpretation of dielectric measurements using the Cole-Cole plot", ***Proc. Phys. Soc. B,*** **64:81-82, 1951**

[199] Y. Z. Wei and S. Sridhar, "A new graphical representation for dielectric data", ***J. Chem. Phys.,*** **99(4):3119-3124, 1993**

[200] E. Bormashenko, S. Sutovski, R. Pogreb, A. Sheshnev and A. Shulzinger, "Development of novel binary and ternary conductive composites based on polyethylene, low melting point metal alloy and carbon black", ***J. Thermoplastic Comp. Mats.,*** **17(3):245-257, 2004**

[201] *Washington University in St Louis, Arts and Sciences*, ***www.nslc.wustl.edu/***

[202] I. L. Hosier, A. Guushaa, A. S. Vaughan and S. G. Swingler, "Selection of a suitable vegetable oil for high voltage insulation applications", ***J. Phys. Conf. Series,* 183(012014), 2009**

[203] V. K. Daga and N. J. Wagner, "Linear viscoelastic master curves of neat and laponite-filled poly(ethylene oxide)-water solutions", ***Rheologica Acta,* 45(6):813-824, 2006**

[204] A. R. Rao and M. Mishra, "Peristaltic transport of a power-law fluid in a porous tube", ***J. Non-Newtonian Fluid Mech.,* 121:163-174, 2004**

[205] E. Alvarez, M. A. Cancela, N. Delgado-Bastidas and R. Maceiras, "Rheological Characterization of Commercial Baby Fruit Purees", ***J. Food properties,* 11(2):321-329, 2008**

[206] J. T. C. L. Toneli, K. J. Park, J. R. P. Ramalho, F. E. X. Murr and I. M. D. Fabbro, "Rheological characterization of chicory root inulin solution", ***Braz. J. Chem. Eng.,* 25(3), 2008**

[207] D. G. Regan, K. I. Momot, P. J. Martens, P. W. Kuchel, L. A. Poole-Warren, "NMR measurement of small-molecule diffusion in PVA hydrogels: a comparison of CONVEX and standard PGSE methods", ***Diffusion Fundamentals Online,* 4:1.1-1.8, 2005**

[208] S. M. J. Guzik and C. P. T. Groth, "Comparison of solution accuracy of multidimensional residual distribution and Godunov-type finite-volume methods", ***Int. J. Comp. Fluid Dynamics,* 22(1&2):61-83, 2008**

[209] G. E. J. Langenbach and W. A. Weijs, "Growth patterns of the rabbit masticatory muscles", ***J. Dental Res.,* 69(1):20-25, 1990**

[210] J. M. Franco, C. Gallegos and H. A. Barnes, "On slip effects in steady-state flow measurements of oil-in-water food emulsions", ***J. Food Engin.,* 36:89-102, 1998**

[211] M. S. Khan, "Aggregate formation in poly(ethylene oxide) solutions", ***J. App. Poly. Sci.,* 102:2578-2583, 2006**

[212] C. A. Daniels, "Polymers—structure and properties", ***CRC Press,* 1989**

[213] Y. H. Lin, "Entanglement and the molecular weight dependence of polymer glass transition temperature", ***Macromolecules,* 23(25):5292-5294, 1990**

[214] L. Mandelkern, "Crystallization of polymers", ***Cambridge University Press,* 2002**

[215] J. C. Salamone, "Concise polymeric materials encyclopedia", ***CRC Press,* 1998**

[216] W. Braun, K. H. Hellwege and W. Knappe, "Enthalpie von polyoxyathylenen im temperaturbereich von 15-100 ^{0}C", ***Colloid and Polym. Sci.,* 215(1), 1967**

[217] A. M. Afifi-Effat and J. N. Hay, "Enthalpy and entropy of fusion and the equilibrium melting point of polyethylene oxide", ***J. Chem. Soc., Faraday Trans. 2,* 68:656-661, 1972**

[218] J. M. Marentette and G. R. Brown, "The crystallization of poly(ethylene oxide) in blends with neat and plasticized poly(vinyl chloride)", ***Polymer,* 39(6-7):1415-1427*,* 1998**

[219] V. P. R. Silva, G. G. Silva, V. Caliman, J. Rieumont, C. O. B. De Miranda-Pinto, B. S. Archanjo and B. R. A. Neves, "Morphology, crystalline structure and thermal properties of PEO/MEEP blends", ***Euro. Polym. J.,* 43 :3283-3291, 2007**

[220] M. Lambrigger, "Non-isothermal polymer crystallization kinetics and avrami master curves", ***Polym. Engin. Sci.,* 38(4):610-615, 1998**

[221] S. Imai, S. Shimono, Y. Fukushima, K. Umezaki, M. Okada, M. Takahashi and H. Matsuda, "Activation energy for crystallisation of low molecular weight poly(ethylene oxide) and low molecular weight poly(ethylene oxide)/poly(methyl methacrylate) blends determined by DSC and polarized optical microscopy", ***Thermochimica Acta,* 267:259-268*,* 1995**

[222] M. S. Lisowski, Q. Liu, J. Cho and J. Runt, "Crystallisation behaviour of poly(ethylene oxide) and its blends using time-resolved wide and small angle x-ray scattering", ***Macromolecules,* 33:4842-4849, 2000**

[223] D. R. Beech and C. Booth, "Thermodynamic melting point of poly(ethylene oxide)", ***J. Polym. Sci. Part B: Polymer Letters,* 8(10):731-734*,* 1970**

[224] M. G. Broadhurst, "An analysis of the solid phase behaviour of the normal paraffins", ***J. Res. Natl. Bureau Standards: A, Phys. Chem.,* 66A(3), 1962**

[225] M. G. Broadhurst, "The melting temperatures of the n-paraffins and the convergence temperature for polyethylene", ***J. Res. Natl. Bureau Standards: A: Phys. Chem.,* 70A(6), 1966**

[226] H. Marand, J. Xu and S. Srinivas, "Determination of the equilibrium melting temperature of polymer crystals: Linear and nonlinear hoffman-weeks extrapolation", ***Macromolecules,* 31(23):8219-8229, 1998**

[227] K. Se, K. Adachi and T. Kotaka, "Dielectric relaxations in poly(ethylene oxide) : Dependence on molecular weight", ***Poly. J.,* 13(11):1009-1017*,* 1981**

[228] C. H. Porter and R. H. Boyd, "A dielectric study of the effects of melting on molecular relaxation in poly(ethylene oxide) and polyoxymethylene", ***Macromolecules,* 4(5):589-594*,* 1971**

[229] K. Arisawa, K. Tsuge and Y. Wada, "Dielectric relaxations in polyoxymethylene and polyethylene oxide", ***Jap. J. Appl. Phys.,* 4(2):138-147, 1965**

[230] X. Jin, S. Zhang and J. Runt, "Observation of a fast dielectric relaxation in semi-crystalline poly(ethylene oxide)", ***Polymer,* 43:6247-6254, 2002**

[231] D. K. Pradhan, R. N. P. Choudhary and B. K. Samantaray, "Studies of dielectric relaxation and AC conductivity behaviour of plasticized polymer nanocomposite electrolytes", ***Int. J. Electrochem. Sci.,* 3:597-608, 2008**

[232] J. R. Dygas, B. Misztal-Faraj, Z. Florjanczyk, F. Krok, M. Marzantowicz and E. Zygadlo-Monikowska, "Effects of inhomogeneity on ionic conductivity and relaxations in PEO and PEO-salt complexes", ***Solid State Ionics,* 157:249-256, 2003**

[233] J. Claude, Y. Lu and Q. Wang, "Effect of molecular weight on the dielectric breakdown strength of ferroelectric poly(vinylidene fluoride-chlorotrifluoroethylene)s", ***Appl. Phys. Lett.,* 91(21), id. 212904, 2007**

[234] A. G. B. Pereira, R. F. Gouveia, G. M. de Carvalho, A. F. Rubira and E. C. Muniz, "Polymer blends based on PEO and starch: Miscibility and spherulite growth rate evaluated through DSC and optical microscopy", ***Mater. Sci. Eng. :C.,* 29(2):499-504, 2009**

[235] M. Marzantowicz, J. R. Dygas, F. Krok, J. L. Nowinski, A. Tomaszewska, Z. Florjanczyk and E. Zygadlo-Monikowska, "Crystalline phases, morphology and conductivity of PEO:LiTFSI electrolytes in the eutectic region", ***J. Polym. Sources,* 159(1):420-430, 2006**

[236] S. Jiang, C. He, L. An, X. Chen and B. Jiang, "Crystallization and ring-banded spherulite morphology of poly(ethylene oxide)-block-poly(ε-caprolactone) diblock copolymer", ***Macro. Chem. & Phys.,* 205(16):2229-2234, 2004**

[237] F. P. Price and R. W. Kilb, "The morphology and internal structure of poly(ethylene oxide) spherulites", ***J. Polym. Sci.,* 57(165):395-403, 2003**

[238] D. Bower, "An introduction to polymer physics", **Cambridge University Press, 2002**

[239] Zainuddin, J. Albinska, P. Ulanski and J. M. Rosiak, "Radiation-induced degradation and crosslinking of poly(ethylene oxide) in solid state", ***J. Radioanalytical and Nuclear Chem.,* 253(3):339-344, 2002**

[240] O. Chiantore, S. Tripodi, C. Sarmoria and E. Valles, "Mechanism and molecular weight model for thermal oxidation of linear ethylene-butene copolymer", ***Polymer,* 42(9):3981-3987, 2001**

[241] *IUPAC Compendium of Chemical Terminology,* 2nd edition 1997, **ref: 1996, 68, 2309**

[242] C. W. McGary Jr, "Degradation of polyethylene oxide", ***J. Poly. Sci.,* 46:51, 1960**

[243] F. E. Bailey and J. V. Koleske, "Poly(ethylene oxide)", ***Academic Press,* 1976**

[244] J. Schiers, "Compositional failure analysis of polymers", ***Wiley & Sons Pub.,* 2000**

[245] S. W. Bigger, J. Schiers, O. Delatycki and N. C. Billingham, "Effects of frequency, molecular weight and thermal oxidation on the dynamic mechanical response of poly(ethylene oxide)", ***Polymer,* 26(3):181-186, 2007**

[246] M. P. Sepe, "The use of thermal analysis in polymer characterization" in "Elastomer Technology Handbook" by N. P. Chermisinoff, ***CRC Press* :128, 1993**

[247] M. M. Coleman, M. Mock and P. C. Painter, "Miscible Macromolecular antioxidants for polyethers", ***J. Macromol. Sci.,* B38(4):403-417, 1999**

[248] Y. A. Shlyapnikov, S. T. Kiryushkin and A. P. Mar'in, "Antioxidative stabilization of polymers", ***Taylor and Francis,* 1996**

[249] J. R. Shelton, "Basic oxidation processes in elastomers", ***Rubber Chemistry and Technology,* 45(2):359-380, 1972**

[250] J. Pospisil, "Exploitation of the current knowledge of antioxidant mechanisms for efficient polymer stabilization", ***Polymers for Advanced Technologies,* 3(8):443-455, 2003**

[251] M. Saboormaleki, A. R. Barnes and W. S. Schlindwein, "Characterization of polyethylene oxide (PEO) based polymer electrolytes", ***The electrochemical society inc.,* Abstract 726, 205th meeting, 2004**

[252] F. Fraisse, J. M. Nedelec, J. P. E. Grolier and M. Baba, "Isothermal crystallisation kinetics of in situ photo and thermo aged poly(ethylene oxide) using photodsc", ***Physical chemistry- chemical physics,* 9:2137-2141, 2007**

[253] Y. T. Hsu, K. S. Chang-Liao, T. K. Wang and C. T. Kuo, "Correlation between mechanical and electrical properties for assessing the degradation of ethylene propylene rubber cables used in nuclear power plants", ***Polym. Degrad. and Stability,* 92(7):1297-1303, 2007**

[254] P. A. Roseen, T. Reitberger, S. M. Gubanski and U. W. Gedde, "PD resistance of thermally aged polyethylene and carbonyl-containing model polymers", ***IEEE Trans. Dielec. Elec. Insul.,* 6(2):191-201, 1999**

[255] M. Ehsani, H. Borsi, E. Gockenbach, J. Morshedian and G. R. Bakhshandeh, "An investigation of dynamic mechanical, thermal, and electrical properties of housing materials for outdoor polymeric insulators", ***Euro. Polymer J.,* 40:2495-2503, 2004**

[256] S. Katakai and K. Yahagi, "Effect of thermal aging on breakdown strength of polyethylene", ***Jpn. J. Appl. Phys.,* 24 :441-445, 1985**

[257] A. Neira, M. Tarraga and R. Catalan, "Degradation of acrylic acid-grafted cellulose in aqueous medium with radical initiators", ***J. Chil. Chem. Soc.,* 53(1), 2008**

[258] M. Celina, D. K. Ottesen, K. T. Gillen and R. L. Clough, "FTIR emission spectroscopy applied to polymer degradation", ***Polymer Degrad. and Stability,* 58:15-31, 1997**

[259] E. Pamula, M. Blazewicz, C. Paluszkiewicz and P. Dobrzynski, "FTIR study of degradation products of aliphatic polyesters-carbon fibres composites", ***J. Molecular Structure,* 596:69-75, 2001**

[260] M. Bengisu and E. Yilmaz, "Oxidation and pyrolysis of chitosan as a route for carbon fiber derivation", ***Carbohydrate polymers,* 50:165-175, 2002**

[261] C. Jin, P. A. Christensen, T. A Egerton, E. J. Lawson and J. R. White, "Rapid measurement of polymer photo-degradation by FTIR spectrometry of evolved carbon dioxide", ***Poly. Degrad. and Stability,* 91:1086-1096, 2006**

[262] D. J. Nagle, M. Celina, L. Rintoul and P. M. Fredericks, "Infrared microspectroscopic study of the thermo-oxidative degradation of hydroxy-terminated polybutadiene/iosphorone diisocyanate polyurethane rubber", ***Polymer Degrad. and Stability,* 92(8):1446-1454, 2007**

[263] M. Celina, J. Wise, D. K. Ottesen, K. T. Gillen and R. L. Clough, "Correlation of chemical and mechanical property changes during oxidative degradation of neoprene", ***Polymer Degrad. and Stability,* 68:171-184, 2000**

[264] N. V. Ramirez, M. Sanchez-Soto, S. Illescas and A. Gordillo, "Thermal degradation of Polyoxymethylene evaluated with FTIR and Spectrophotometry", ***Polym. plastics tech. and engin.,* 48:470-477, 2009**

[265] G. Cardenas and S. P. Miranda, "FTIR and TGA studies of chitosan composite films", ***J. Chil. Chem. Soc.,* 49(4);291-295, 2004**

[266] Y. Su, J. Wang and H. Liu, "FTIR spectroscopic investigation of effects of temperature and concentration on PEO-PPO-PEO block copolymer properties in aqueous solutions", ***Macromolecules,* 35(16):6426-6431, 2002**

[267] M. A. K. L. Dissanayake and R. Frech, "Infrared spectroscopic study of the phases and phase transitions in poly(ethylene oxide) and poly(ethylene oxide)-lithium trifluoromethanesulfonate complexes", ***Macromolecules,* 28:5312-5319, 1995**

[268] N. Kimura, J. Umemura and S. Hayashi, "Polarized FT-IR Spectra of Water in the middle phase of triton X100-Water system", ***J. Colloid and Interface science,* 182:356-364, 1996**

[269] K. S. Ji, H. S. Moon, J. W. Kim and J. W. Park, "Role of functional nano-sized inorganic fillers in poly(ethylene) oxide-based polymer electrolytes", ***J. Power sources,* 117:124-130, 2003**

[270] T. Yoshihara, H. Tadokoro and S. Murahashi, "Normal vibrations of the polymer molecules of helical conformation. IV. Polyethylene oxide and polyethylene-d oxide", ***J. Chemical Physics,* 41(9):2902-2911, 1964**

[271] A. Miyake, "CH_2 rocking frequencies of ethylene glycol and its derivatives in relation to the configuration of polyethylene glycol", ***J. Am. Chem. Soc.,* 82(12):3040-3043, 1960**

[272] T. Miyazawa, K. Fukushima and Y. Ideguchi, "Molecular vibrations and structure of high polymers. III. Polarized infrared spectra, normal vibrations, and helical conformation of polyethylene glycol", ***J. Chem. Phys.,* 37(12):2764-2776, 1962**

[273] N. F. M. Nasir, M. G. Raha, N. A. Kadri, S. I. Sahidan, M. Rampado and C. A. Azlan, "The study of morphological structure, phase structure and molecular structure of collagen-PEO 600k blends for tissue engineering application", ***Am. J. Biochem. Biotech.,* 2(5):175-179, 2006**

[274] S. Rajendran, T. Mahalingam and R. Kannan, "Experimental investigations on PAN-PEO hybrid polymer electrolytes", ***Solid state ionics,* 130(1-2):143-148, 2000**

[275] R. P. Chartoff, T. S. K. Lo, E. R. Harrell and R. J. Roe, "Infrared spectral changes with crystallization in poly(vinylchloride): Correlations with x-ray and density data", ***J. Macromol. Sci. Phys. B,* 20(3):287-303, 1981**

[276] D. R. MacFarlane, P. Meakin, A. Bishop, D. McNaughton, J. M. Rosalie and M. Forsyth "FTIR study of ion-pairing effects in plasticized polymer electrolytes", ***Electrochimica Acta,* 40(13-14):2333-2337, 1995**

[277] A. M. Rocco, D. P. Moreira and R. P. Pereira, "Specific interactions in blends of poly(ethylene oxide) and poly(bisphenol A-co-epichlorohydrin): FTIR and thermal study", ***Euro. Poly. J.,* 39(9):1925-1934, 2003**

[278] S. Rajendran, R. Kannan and O. Mahendran, "Ionic conductivity studies in poly(methylmethacrylate)-polyethylene oxide hybrid polymer electrolytes with lithium salts", ***J. Power sources,* 96(2):406-410, 2001**

[279] P. S. Ramesh, D. Geetha and C. Rakkappan, "Ultrasonic studies on aqueous polyethylene oxide in n-alkanols", ***J. Molecular Liq.,* 126(1-3):69-71, 2006**

[280] Y. J. Wang, Y. Pan and D. Kim, "Crystallinity, thermal properties, morphology and conductivity of quaternary plasticized PEO-based polymer electrolytes", ***Polym. Int.,* 56:381-388, 2007**

[281] L. E. Cohen and A. M. Rocco, "Study of the crystallization kinetics of Poly(ethylene oxide) and a blend of poly(ethylene oxide) and poly(bisphenol A-co-epichlorohydrin", ***J. therm. Analy. and calorimetry,*** **59:625-632, 2000**

[282] L. Fan, C. W. Nan and M. Li, "Thermal, electrical and mechanical properties of $(PEO)_{16}LiClO_4$ electrolytes with modified montmorillonites", ***Chem. physics letters,*** **369:698-702, 2003**

[283] J. Wu, S. Yang, S. Gao, A. Hu, J. Liu and L. Fan, "Preparation, morphology and properties of nano-sized Al_2O_3/polyimide hybrid films", ***Euro. Polym. J.,*** **41(1):73-81, 2005**

[284] Y. Hu, R. C. Smith, J. K. Nelson and L. S. Schadler, "Some mechanistic understanding of the impulse strength of nanocomposites", ***CEIDP conf.,*** **Kansas City:31-34, 2006**

[285] A. Dorigato, A. Pegoretti and A. Penati, "Linear low-density polyethylene/silica micro- and nanocomposites: dynamic rheological measurements and modelling", ***eXPRESS Polym. Lett.,*** **4(2):115-129, 2009**

[286] Q. Zhang and L. A. Archer, "Optical polarimetry and mechanical rheometry of poly(ethylene oxide)-silica dispersions", ***Macromolecules,*** **37:1928-1936, 2004**

[287] M. Garcia, W. E. van Zyl, M. G. J. ten Cate, J. W. Stouwdam, H. Verweij, M. S. Pimplapure and G. Weickert, "Novel preparation of hybrid polypropylene/silica nanocomposites in a slurry-phase polymerization reactor", ***Ind. Eng. Chem. Res.,*** **42:3750-3757, 2003**

[288] S. H. Lee, J. E. Kim, H. H. Song and S. W. Kim, "Thermal conductivity of maleated polyethylene/layered silicate nanocomposite", ***15th Symposium on thermophysical properties,*** **Boulder, USA, 2003**

[289] J. Liang and Q. Yang, "Aggregate structure and percolation behaviour in polymer/carbon black conductive composites", ***J. App. Phys.,*** **102(083508), 2007**

[290] F. Gubbels, S. Blacher, E. Vanlathem, R. Jerome, R. Deltour, F. Brouers and P. H. Teyssie, "Design of electrical composites: Determining the role of the morphology on the electrical properties of carbon black filled polymer blends", ***Macromolecules,*** **28:1559-1566, 1995**

[291] M. Kozako, S. Yamano, R. Kido, Y. Ohki, M. Kohtoh, S. Okabe and T. Tanaka, "Preparation and Preliminary characteristic evaluation of epoxy/alumina nanocomposites", ***Proc. Int. Symp. Elec. Insul. Mats.,*** **A4-3, 2005**

[292] T. Sugama, "Nanoscale boehmite filler for corrosion and wear resistant polyphenylenesulfide coatings", ***Office of Geothermal technologies,*** **Informal report, BNL- 71395-2003-IR, 2003**

[293] R. C. Streller, R. Thomann, O. Torno and R. Mulhaupt, “Isotactic poly(propylene) nanocomposites based upon boehmite nanofillers”, ***Macromol. Mater. Eng.*, 293:218-227, 2008**

[294] C. Ozdilek, K. Kazimierczak, D. van der Beek and S. J. Picken, “Preparation and properties of polyamide-6-boehmite nanocomposites”, ***Polymer*, 45:5207-5214, 2004**

[295] A. von Hippel, “Electric Breakdown of Solid and Liquid Insulators”, ***J. Appl. Phys.*, 8:815-832, 1937**

[296] A. von Hippel, “Der mechanismus des elektrischen durchschlages in festen isolatoren”, ***Zeitschrift fur Physik*, 67(11-12):707-724, 1931**

[297] A. von Hippel, “Die elektrische festigkeit der alkalihalogenide und ihre beeinflussung durch Mischkristallbidung und fremdzusatze”, ***Zeitschrift fur Physik*, 88(5-6):358-365, 1934**

[298] A. von Hippel, “Elektrische festigkeit und kristallbau”, ***Zeitschrift fur Physik*, 75(3-4):145-170, 1932**

[299] J. Blok and D. G. LeGrand, “Dielectric Breakdown of Polymer Films”, ***J. Appl. Phys.*, 40(1):288-293, 1969**

[300] W. G. Lawson, “Temperature Dependence of the Intrinsic Electric Strength of Polythene”, ***Nature*, 206:1248-1249, 1965**

[301] E. Sacher, “An attempt to apply the ‘equation for polymer life’ to the dielectric strength of polymers”, ***J. Phys. D: Appl. Phys.*, 13(L21-24), 1980**

[302] N. Parkman, G. F. Goldspink and W. G. Lawson, “Effect of pressure and constraint on the apparent electric strength of polythene”, ***Electron. Lett.*, 1, 98, 1965**

[303] A. Charlesby and N. H. Hancock, “The effect of cross-linking on the elastic modulus of polythene”, ***Proc. Roy. Soc. A.*, 218(1133):245, 1953**

[304] K. H. Stark and C. G. Garton, “Electric strength of irradiated PE”, ***Nature*, 176(4495):1225-1226, 1955**

[305] J. C. Fothergill, “Filamentary Electromechanical breakdown”, ***IEEE Trans. Elec. Insul.*, 26(6):1124-1129, 1991**

[306] M. Hikita, S. Tajima, I. Kanno, I. Ishino, G. Sawa and M. Ieda, “High-field conduction and electrical breakdown of PE at high temperatures”, ***Jap. J. Appl. Phys.*, 24 :988-996, 1985**

[307] T. Mizutani, I. Kanno, M. Hikita and M. Ieda, “Pre-breakdown currents due to filamentary thermal breakdown in polyimide films”, ***IEEE Trans. Elec. Insul.*, 22:473-477, 1987**

[308] M. Hikita, I. Kanno, M. Ieda, I. Ishino, S. Doi and G. Sawa, "Electrical breakdown of ethylene copolymers", ***IEEE Trans. Elec. Insul.,* 22(2):175-179, 1987**

[309] H. R. Zeller, T. Hibma and P. Pfluger, "Electrofracture mechanics of dielectric aging", ***Ann. Rep. CEIDP,* IEEE cat. no. 84, CH 1993-4, :85-88, 1984**

[310] H. R. Zeller, W. R. Schneider, "Electrofracture mechanics of dielectric aging", ***J. Appl. Phys.,* 56 :455-459, 1984**

[311] M. Nagao, T. Kimura, Y. Mizuno, M. Kosaki and M. Ieda, "Detection of Joule Heating before Dielectric Breakdown in Polyethylene Films", ***IEEE Trans. Elec. Insul.,* 25(4):715-722, 1990**

[312] M. Hikita, S. Tajima, I. Kanno, G. Sawa and M. Ieda, "New approach to breakdown study by measuring pre-breakdown current in insulating materials", ***Japan, J. Appl. Phys.,* 23(12):L886-888, 1984**

[313] M. Miyauchi and K. Yahagi, "Electronic breakdown in PE film in room temperature region", ***Trans. IEE Japan,* 92A:36-45, 1972**

[314] M. Hikita, M. Nagao, G. Sawa and M. Ieda, "Dielectric breakdown and electrical conduction of poly(vinylidene-fluoride) in high temperature region", ***J. Phys. D: Appl. Phys.*, 13:661-666, 1980**

[315] K. W. Wagner, "Physical nature of electrical breakdown in solid dielectrics", ***Trans. A. I. E. E.,* 41:1034, 1922**

[316] J. L. R. Hayden and C. P. Steinmetz, "Insulation failure-A pyroelectric effect", ***Elec. World,* 80:865, 1922**

[317] A. Gunther-Schulze, "Die Vorgange an der Kathode des Quecksilbervakuumlichtbogens", ***Zeitschrift fur physik a hadrons and nuclei,* 11(1):74-87, 1922**

[318] R. C. Buehl and A. von Hippel, "The electrical breakdown strength of ionic crystals as a function of temperature", ***Physical Review,* 56:941-947, 1939**

[319] W. Kai, X. Hengkun and G. Jingpang, "Percolation and Dielectric Breakdown", ***Proc. Int. Conf. Props. Apps. Dielec. Mats.,* 4214:49-51, 1994**

[320] P. W. Anderson, "Absence of diffusion in certain random lattices", ***Phys. Rev.,* 109:1492-1505, 1958**

[321] D. J. Thouless, "Anderson's theory of localised states", ***J. Phys. C. Solid State Phys.,* 3:1559-1566, 1970**

[322] E. O. Forster, "Research in the dynamics of electrical breakdown in liquid dielectrics", ***IEEE Trans. Elec. Insul.,* Volume E1-15, number 3, pp. 182-185, 1980**

[323] P. B. McGrath and J. K. Nelson, "Optical studies of pre-breakdown events in liquid dielectrics", ***IBID.,* 124:183-187, 1977**

[324] W. G. Chadband and J. H. Calderwood, "Pre-breakdown events in dielectric fluids", ***Proc. IEE.,* 119:1661-1666, 1972**

[325] E. Morikawa, "Optical observation of pre-breakdown phenomena in dielectric oil", ***Elec. Eng. Japan,* 92:11-17, 1972**

[326] P. P. Wong and E. O. Forster, "The dynamics of electrical breakdown of hydrocarbon fluids", ***J. Electrostatics,* 5:157-168, 1978**

[327] E. O. Forster and P. P. Wong, "High speed laser schlieren studies of electrical breakdown in liquid hydrocarbons", ***IBID,* E1-12:435-442, 1977**

[328] A. H. Sharbaugh, J. C. Devins and S. J. Rzad, "Review of past work on liquid breakdown", ***IEEE Trans. Elec. Insul.,* E1-15(3):167-170, 1980**

[329] H. Yamashita, H. Amano and T. Mori, "Optical observation of pre-breakdown and breakdown phenomena in transformer oil", ***J. Phys. D.,* 10 :1753, 1977**

[330] E. O. Forster, "Research in the dynamics of electrical breakdown in liquid dielectrics", ***US/Japan Seminar on Elec. Cond. Breakdown in Dielec.,* USA, 1979**

[331] P. K. Watson and A. H. Sharbaugh, "High-field conduction currents in liquid n-Hexane under microsecond pulse conditions", ***J. Electrochem. Soc.,* 107:516, 1960**

[332] T. V. Prevenslik, "Plancktons in a Unified Theory of Electrical Breakdown", ***Proc. 13th Int. Conf. Dielec. Liquids,* :290-292, 1999**

[333] F. Paschen, "Uber die zum Funkenubergang in Luft, Wasserstoff und Kohlensaure bei verschiedenen drucken erforderliche potentialdifferenz", ***Annalen der Physik,* 273(5):69-96, 1889**

[334] E. O. Forster and G. J. FitzPatrick, "Electric breakdown in dielectric liquids", ***Physics in Technology,* 16:282-287, 1985**

[335] E. O. Forster, "Electrical breakdown in liquid hydrocarbons", ***J. Electrostatics,* 12:1-12, 1982**

[336] A. H. Sharbaugh, E. D. Cox, R. W. Crowe and P. L. Auer, "Annual report of the conference on electrical insulation and dielectric phenomena", ***US Nat. Res. Coun. Publ.,* 396:16-20, 1955**

[337] J. K. Bragg, A. H. Sharbaugh and R. W. Crowe, "Cathode effects in dielectric breakdown of liquids", ***J. App. Phys.,* 25(3) :382-391, 1954**

[338] A. Beroual and R. Tobazeon, "Propagation et generation des streamers dans les dielectriques liquids", ***Rev. Phys. Appl.,* 22:1117-1123, 1987**

[339] A. Beroual and R. Tobazeon, "Prebreakdown phenomena in liquid dielectrics", ***IEEE Trans. Elec. Insul.,* E1-21(4):613-627, 1986**

[340] T. V. Prevenslik, "Dielectric polarisation in the Planck theory of sonoluminescence", ***Ultrasonics Sonochemistry,* 5(3):93-105, 1998**

[341] E. Kuffel, W. S. Zaengl and J. Kuffel, "High Voltage Engineering: Fundamentals Second Edition", ***Pergamon Press,* 1984**

[342] H. Frohlich, "Dielectric breakdown in ionic crystals", ***Phys. Rev.,* 56(4):349-352, 1939**

[343] H. Frohlich, "Dielectric breakdown in solids", ***Proc. Phys. Soc. B.,* 69 :21-32, 1956, (Nb. With Corrigendum *Proc. Phys. Soc. B.,* 69:866-866)**

[344] H. Frohlich, "On the theory of dielectric breakdown in solids", ***Proc. Roy. Soc. Lond. A.,* 188(1015):521-532, 1947**

[345] H. Frohlich, "Theory of electrical breakdown in ionic crystals", ***Proc. Roy. Soc. Lond. A.,* 160(901):230-241, 1937**

[346] S. N. Kolesov, "The influence of morphology on the electric strength of polymer insulation", ***IEEE Trans. Elec. Insul.,* E1-15(5):382-388, 1980**

[347] S. N. Kolesov, "Effect of supermolecular structure on electrical strength of crystalline polymers", ***Visokomolekulamye Soyedynenya,* BX(8):582, 1968**

[348] S. N. Kolesov, "How the electrical withstand strength of polymer films depends on the size of the spherulite structure", ***Elektrichestvo,* (9):84, 1970**

[349] S. N. Kolesov and L. N. Kheraskov, "Electrical strength of micro-regions in polypropylene", ***Visokomolekularnyne,* BX11(4):266, 1970**

[350] H. Wagner, "Zum elektrischen durkschlay von teilkristallinen polymeren electrotechn", ***Z. A.,* 94(7):436, 1973**

[351] H. Wagner, "Pseudo-spherulite structures in cross-linked LDPE", ***IEEE Trans. Elec. Insul.,* E1-13(2):81, 1978**

[352] S. N. Kolesov, I. A. Kil'deev, I. S. Kolesov and N. P. Balaban, "Electrical strength of micro-sections of polymer films as a function of the size of spherulite structure", ***Izvestya Vuzov,* Physica (12), 1973**

[353] T. Zeng, X. Dong, H. Yang, C. Mao and H. Chen, "Enhancement of mechanical and dielectric breakdown properties by diffusion of SiC into lead zirconate titanate ceramics", ***Scripta Materialia,* 55(10):923-926, 2006**

[354] R. C. Pohanka, R. W. Rice and B. E. Walker, "Effect of internal stress on the strength of $BaTiO_3$", ***J. Am. Ceram. Soc.,* 59(1-2):71-74, 1976**

[355] K. Wagner, “Erklarung der dielektrischen Nachwirkungsvorgange auf grund maxwellscher vorstellungen”, ***Elec. Engin. (Archiv fur elektrotechnik),*** **2(9):371-387, 1914**

[356] J. C. Maxwell, “Electricity and Magnetism”, ***Oxford Clarendon,*** **1892**

[357] A. M. Freedman, D. C. Bassett and R. H. Olley, “An investigation of permanganic etching of linear low-density polyethylene”, ***J. Macromolecular Sci., Part B,*** **27(4):319-335, 1988**

[358] S. J. Sutton and A. S. Vaughan, “A comparison of fracture and permanganic etching of polypyrrole films”, ***J. Polym. Sci., B Polym. Phys.,*** **34(5):837-843, 1996**

[359] L. C. Sawyer and D. T. Grubb, “Polymer microscopy”, ***Chapman and Hall Publishers,*** **1987**

[360] R. Salovey, M. Y. Hellman, W. Matreyek and F. H. Winslow, “Etching of irradiated PE with fuming nitric acid”, ***J. Poly. Sci. B: Poly. Lett.,*** **5(12):1131-1134, 2003**

[361] R. H. Olley, “Selective etching of polymeric materials”, ***Sci. Prog.,*** **70(1) :17-43, 1986**

[362] A. M. Freedman, D. C. Bassett, A. S. Vaughan and R. H. Olley, “On quantitative permanganic etching”, ***Polymer,*** **27(8):1163-1169, 1986**

[363] R. P. Palmer and A. J. Cobbold, “The texture of melt crystallised polythene as revealed by selective oxidation”, ***Die Makromolekulare Chemie,*** **74(1):174-189, 1964**

[364] C. W. Hock, “Selective oxidation with nitric acid reveals the microstructure of polypropylene”, ***J. Poly. Sci. B: Polym. Lett.,*** **3(7):573-576, 1965**

[365] H. S. Bu, S. Z. D. Cheng and B. Wunderlich, “New etching method for poly(ethylene oxide)”, ***Polymer,*** **29:1603-1607, 1988**

[366] H. S. Bu, S. Z. D. Cheng and B. Wunderlich, “A new etching method for the electron microscopy of semicrystalline poly(ethylene oxide)”, ***Polymer Bulletin,*** **17:567-571, 1987**

[367] M. Knoll, "Aufladepotentiel und Sekundäremission elektronenbestrahlter Körper", ***Zeitschrift für technische Physik***, **16:467–475, 1935**

[368] ***http://www.reading.ac.uk/cfam/facilities/low_vacuum_sem.htm***

[369] A. Grosse, M. Grewe and H. Fouckhardt, “Deep wet etching of fused silica glass for hollow capillary optical leaky waveguides in microfluidic devices”, ***J. Micromech. Microeng.,*** **11:257-262, 2001**

[370] N. A. Aziz, M. R. Buyong and B. Y. Majlis, "Process characterization of wet etching for high aspect ratio microneedles development", ***Adv. Materials Res.*, 74:341-344, 2009**

[371] T. G. Park, J. J. Kim, S. H. Jung, H. J. Song, J. K. Chang, D. C. Han and S. S. Yang, "Fabrication of megasonic-agitated module for improving the characteristics of wet etching", ***Jap. J. Appl. Phys.*, 47(6):5262-5269, 2008**

[372] D. C. Bassett, "Principles of polymer morphology", **Cambridge solid state science series, Cambridge university press, 1981**